Title

Physics of Interacting Supernova Light Curves

Author

Khatami, David

Publication Date

2024

Physics of Interacting Supernova Light Curves

by

David Kyle-Lansangan Khatami

A dissertation submitted in partial satisfaction of the

requirements for the degree of

Doctor of Philosophy

in

Astrophysics

in the

Graduate Division

of the

University of California, Berkeley

Committee in charge:

Professor Daniel Kasen, Chair
Professor Raffaella Margutti
Professor Wenbin Lu

Summer 2024

Physics of Interacting Supernova Light Curves

Abstract

Physics of Interacting Supernova Light Curves

by

David Kyle-Lansangan Khatami

Doctor of Philosophy in Astrophysics

University of California, Berkeley

Professor Daniel Kasen, Chair

When a supernova explodes within a dense circumstellar environment, it creates a highly energetic shockwave that can be observed across the entire electromagnetic spectrum. The shockwave emission can be used as an observational probe to infer the properties of the circumstellar medium (CSM), and learn about how the progenitor star lived out its final moments before death. Numerous explanations have been proposed to explain the CSM, with each physical model varying in the amount of expelled mass, its spatial extent, and geometry. Due to the inherent difficulty in modeling the shock emission from circumstellar interaction, simplified analytic and numerical models are widely used to interpret observational data. However, the assumptions made in these simplified models, their range of applicability, and their ability to accurately infer physical quantities is not clear. In this thesis, I have extended the Monte Carlo radiative transfer code Sedona with advanced multi-physics simulation capabilities, including one-dimensional finite-volume arbitrary Lagrangian-Eulerian hydrodynamics, inline multi-group non-LTE opacities, and non-thermal electron populations. I leverage these capabilities to perform extensive radiation hydrodynamics simulations of interacting supernovae, and construct a broad theoretical framework with which to interpret their resulting light curves. I find that CSM interaction can produce a wide range of light curve durations and luminosities, with timescales ranging from hours to months. I demonstrate their viability in powering a broad range of unusual supernovae. In particular, I show how CSM interaction is a plausible explanation for the recently-discovered class of fast blue optical transients, and constrain the CSM properties inferred for this type. For the specific case of the Type II subclass of interacting supernovae, I perform non-equilibrium multi-group radiation hydrodynamics simulations to construct time-dependent panchromatic radio to X-ray spectral energy distributions of the combined supernova and shock emission. I find that analytic expectations used in the literature disagree with the numerical light curves due to an evolving non-thermal electron energy population with contributions from both the forward and reverse shocks, compounded by the effects of inverse Compton scattering and photo-absorption by a cold dense shell.

To my immigrant parents,

who worked hard to support my dream of being a scientist.

Contents

List of Figures

Acknowledgments

I'm extremely grateful for the opportunity to have worked with my PhD advisor Dan Kasen, who gave me both the support and freedom in forming my scientific identity and passion, and provided much-needed space and mental breaks to sort through life hapennings. Additionally, I could not have finished the PhD without Brenna Mockler and the long hours we spent writing hydrocode and playing whack-a-mole with the bugs. Those coding and co-working sessions were a breath of fresh life in the midst of the pandemic. I'm also especially thankful for Nathan Roth, who connected me to the folks at Lawrence Livermore National Laboratory and acted as an amazing sounding board for all of my crazy ideas.

I would like to express my deepest appreciation for the Zwicky Transient Facility Theory Network, which provided me with a space to creatively explore interesting science questions while being supported by a group of amazing astronomers. In particular, I'd like to thank the organizers Lars Bildsten, Eliot Quataert, Sterl Phinney, and Jim Fuller; and participating scientists Samantha Wu, Dillon Dong, Jared Goldberg, Abigail Polin, Yuhan Yao, Benny Tsang, and Hannah Klion. I'd like to give special thanks and appreciation for Anna Ho, who fueled my excitement and scientific curiosity of FBOTs. I'd also like to thank the many scientists I worked with elsewhere, particularly Howard Scott and Hai Le at LLNL; Maria Drout and Niloufar Afsariardchi at University of Toronto; Ann Almgren and Don Wilcox at Lawrence Berkeley National Laboratory; and Wynn Jacobsen-Galan at UC Berkeley.

This work would not have been possible without the abundance of personal support provided by a collection of wonderful people. I'm especially indebted to fellow Nekomini bandmembers LQ, Claude, Michael, and Nic for all the great memories and music we made. I'd also like to thank former roommates Hong Suh, Tom Trieu, and Sam Pollard for putting up with me and all my various shenanigans. I thank my graduate cohort Fatima Abdurrahman, Kareem El-Badry, Kara Kundert, and Ned Molter; and other Berkeley grad students Ellie Abrahams, Wren Suess, and Jason Wang. I'm especially grateful to Sal Fu, who has helped me weather the storm that is grad school. I also give special thanks to my dentist Dr. Bhullar, who helped get rid of a crippling dental emergency right when I was finishing up the thesis writing.

Finally, I acknowledge support from various funding sources including the National Science Foundation through the Graduate Research Fellowship Program; the Gordon and Betty Moore Foundation; the Department of Energy Office of Science through SciDAC and the Exascale Computing Project; and the UC Office of President and Department of Energy National Nuclear Security Administration through the In-Residence Graduate Research Fellowship.

Chapter 1

Introduction

Stars continuously lose mass throughout their lives. The sun steadily expels material from its surface in the form of the solar wind, at a rate of roughly a few times 10^{-14} solar masses per year [1]. Occasionally, the sun will undergo bief eruptive mass loss episodes in what are known as coronal mass ejections [2]. Just like the sun, massive stars ($\gtrsim 8 M_{\odot}$) also expel material in the form of a stellar wind. Given their greater masses, the rates will be larger, typically around $\sim 10^{-9}$-$10^{-6} M_{\odot}/\mathrm{yr}$ throughout their main-sequence lifetime [3].

As massive stars evolve off the main sequence and begin advanced stages of nuclear burning in their cores, they undergo an evolutionary change that significantly alters their stellar structure [4–6]. These structural changes can result in much larger rates of mass loss, e.g. $\sim 10^{-6} M_{\odot}/\mathrm{yr}$ from a red supergiant wind [7]. Over a long enough period, the star may entirely lose its hydrogen envelope through this wind [8].

When stars eventually explode as supernovae, we can get a qualitative idea of how significant the progenitor star's mass loss was by determining the chemical composition of the ejecta from their spectra [9]. If no hydrogen spectral features are present, then the progenitor star must have lost its outermost hydrogen layer by some means. These supernovae are referred to by astronomers as Type I, to distinguish them from supernovae that do show hydrogen in their spectra (Type II). Some observed supernovae display not only a lack of hydrogen, but also no helium features. In some cases, the amount of mass lost can be so significant to only leave behind an "ultra-stripped" progenitor star that has retained only a fraction of the mass it was born with [10, 11].

Different physical mechanisms have been proposed to drive periods of enhanced mass loss, such as through the binary interaction of a nearby companion star gravitationally stripping its outer layers [12, 13]. Very close in binary systems can even undergo stellar mergers, expelling a large fraction of the mass in the process [14–16]. Other explanations that don't invoke a binary companion also exist. For example, when a massive star reaches an advanced evolutionary stage, it will undergo changes in the core due to the nuclear burning of heavier elements (such as carbon and oxygen) [5, 17]. These later burning stages can become unstable, injecting additional energy that exceeds its gravitational binding energy [18, 19].

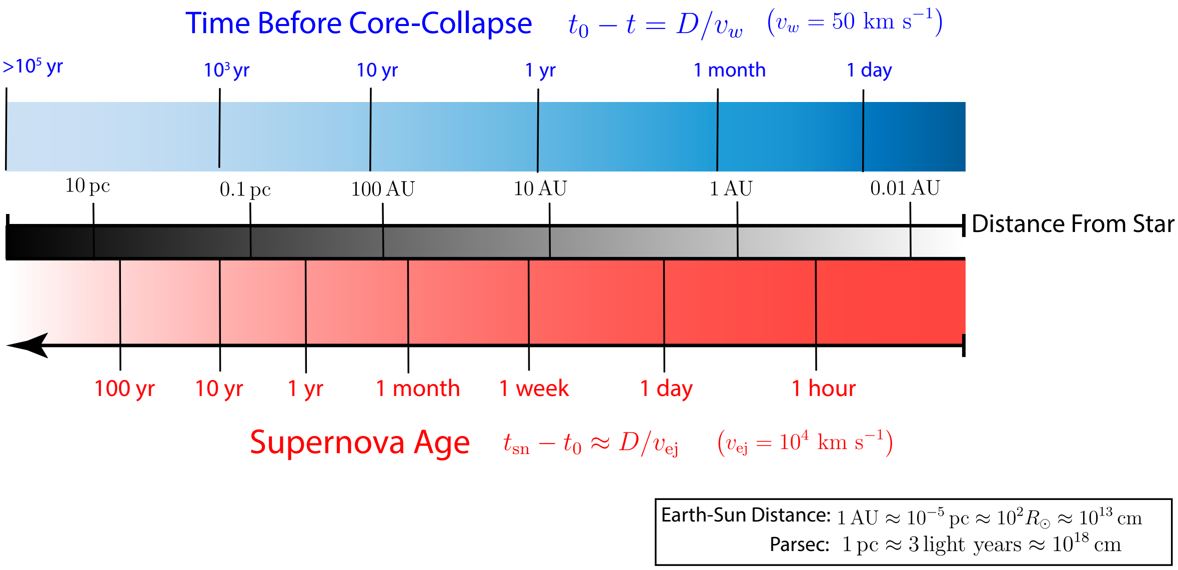

Figure 1.1: Supernova-CSM Interaction diagram. *Blue:* The location of mass lost from the star relative to the surface, as a function of time before supernova explosion and assuming a constant outflow velocity of 50 km/s. *Red*: The location of the edge of the supernova assuming ballistic expansion with constant velocity of 10,000 km/s. The star is located at the right, and the mass loss/supernova move to the left in time.

The common denominator between all of these mass loss mechanisms is the formation of a circumstellar medium (CSM) around the star. Once the star explodes as a supernova, the resulting ejecta (moving much faster than the CSM) will overtake and sweep up mass as it plows outward, forming a shock in the process [20]. This highly energetic shock produces electromagnetic emission that is readily observable by both ground and space-based telescopes [21, 22].

Fig. (1.1) illustrates a rough ejecta-CSM interaction "map" of how long ago before collapse the CSM was ejected from the star; and the location of the outer edge of the supernova ejecta as it expands outwards (ignoring the potential deceleration of the ejecta velocity as it sweeps up mass). For the example velocities given in Fig. (1.1), if shock emission is seen a week after core collapse, then the circumstellar material must have been expelled by the star roughly a year before its death.

Thus, any given physical model invoked to explain the CSM must predict not only the inferred mass-loss rate but also the expected timing relative to the time of supernova explosion. Thus, if we can accurately infer the properties of the CSM from the observed electromagnetic emission, then we will gain insight into how the star lived out its final moments before its eventual demise as a brilliant supernova.

1.1 Modeling Challenges

The physical complexity that makes interacting supernovae so fascinating also makes them extremely challenging to model. The gas temperature and density during CSM interaction span several orders of magnitude. Temperatures can range from $\lesssim 10^4$ K in the inner regions of the supernova ejecta; up to $\gtrsim 10^9$ K in the shocked circumstellar region [23].

We therefore have a radiation hydrodynamics problem at hand. The very same emission that we observe with our telescopes once played an important role in the hydrodynamical and thermal state of the gas, due to the strong radiation generated by the supernova and the shock. Thus, the radiation field must be evolved not just to create synthetic observables, but also to get the hydrodynamics and plasma conditions right.

Radiation hydrodynamics is an interdisciplinary field that plays an important role in other areas of astrophysics, including stellar evolution [24], star formation [25], galaxy evolution [26], and cosmology [27]. It is also important in other areas of physics and engineering, including inertial confinement fusion [28], atmospheric re-entry [29], planetary defense [30], and nuclear weapons research. As such, there exists a vast body of literature and an array of numerical techniques going back decades to accurately simulate radiation hydrodynamics phenomena [31–33].

Even with extensive scientific investment and variety of applications, radiation hydrodynamics remains an active area of research. Computer simulations of radiation hydrodynamical phenomena continue to pose a challenge to do accurately. In multiple dimensions, they can require enormous supercomputing resources to run a single simulation in a reasonable amount of human time [24]. I highlight some of the general challenges the radiation hydrodynamics community continues to tackle, in addition to specific issues in simulating CSM interaction.

Fluid Dynamics

The mathematical description of fluid dynamics consists of five nonlinear hyperbolic partial differential equations, reflecting the conservation of mass, momentum (with three components), and energy. These five quantities are defined as a function of four independent variables: three in space, and one in time. Numerical approaches to solving the fluid dynamics equations generally fall in one of two classes: Eulerian and Lagrangian methods. In the Eulerian approach, the computational mesh stays fixed, while the Lagrangian mesh moves with the fluid flow. Choosing the right method is highly problem-dependent.

The hydrodynamical behavior during CSM interaction poses a unique challenge to both methods. The issue is that we must simultaneously resolve the shocked region *and* the outwardly expanding supernova ejecta. This would seem to favor a Lagrangian approach. However, the extreme compression of the shocked region can result in a severe restriction of the timestep. As such, an Eulerian approach may be better suited. Given that the shocked region can be as thin as 10^{-6} the size of the entire problem domain, advanced techniques such as adaptive mesh refinement (AMR) must be used to strategically put more zones around the shock. However, the expanding nature of the supernova ejecta requires one to continuously enlarge the computational domain, repeatedly restarting and remapping the simulation output to larger grids as the shock moves out.

New techniques have been developed more recently that retain the attractive features of both the Eulerian and Lagrangian approaches, while overcoming each of their shortcomings. These approaches are the class of so-called arbitrary Lagrangian-Eulerian, or ALE, methods. They move the mesh in order to resolve important features, while ameliorating the zone size issue of traditional Lagrangian approaches. Different ALE methods have been used both in astrophysics [34, 35] and other science and engineering fields [36].

Radiation Transport

The radiation field is described by a Boltzmann-type equation, commonly referred to as the radiative transfer equation. However, it is significantly more complicated than the fluid equations, falling into a class known as partial integro-differential equations [37]. The reason it is so difficult to model is its curse of dimensionality: the radiation field is a function of not four but *seven* variables; in addition to space and time, the field is also directionally and energy/frequency dependent. To make matters worse, photons move literally at the speed of light, rendering many standard explicit numerical techniques inefficient.

There are three major numerical approaches to solve the equation of radiative transfer: moments-based, Monte-Carlo, and discrete-ordinates (also known as S_N). The moments-based approach circumvents the curse of dimensionality by taking angular moments of the specific intensity. What we are left with are mean quantities such as the mean intensity (0-th moment) and radiative flux (1-st moment). If only the 0-th moment is retained, then we are effectively replacing the Boltzmann transport equation with a diffusion approximation [38]. This is usually a good approximation in optically thick regions, but fails to get the correct behavior once the gas becomes optically thin and radiation free-streams out (as the signal speed in diffusion is infinite). As such, ad-hoc flux-limiters have been introduced to correct for the optically thin limit [39].

The S_N method discretizes the radiation field along specific directions, and the equation of radiative transfer is solved along these “rays” [37]. The numerical convergence of this approach depends on the number of rays used to model the radiation field. If the angular discretization is too coarse, “ray effects” can appear due to under-resolved solid angle coverage [40]. These methods are also challenging to parallelize as the method is non-local, i.e. the solution in one part of the grid depends on the solution across the whole domain.

Last (but certainly not least), there is the Monte Carlo approach [41]. Of the three methods, it is the closest form of the original kinetic Boltzmann equation. By discretizing the radiation field into individual particles, we retain a continuous representation of the directional and frequency dependence of the radiation field. The optical depth then becomes a random sampling event, and particle histories are tracked until census. Its numerical convergence thus hinges on ensuring the radiation field is well-sampled by a sufficient enough number of particles. Like all Monte-Carlo approaches, it is subject to shot noise that decreases with particle count as $1/\sqrt{N}$, where N is the number of particles. Perhaps the most fatal shortcoming of Monte-Carlo radiation transport is its inefficiency in optically thick regions. In these parts, the extremely small mean free path result in many interaction events, slowing the simulation down to a crawl. Several acceleration techniques have been proposed to alleviate this issue [42–44].

Regardless of the chosen approach, the radiative transfer solution must be coupled to the equations of hydrodynamics that represent the kinetic and thermal state of the gas. As this coupling can be quite stiff, the transport must be solved implicitly using an iterative method. For the moments and S_N methods, these iterations can be slow to converge, especially in scattering-dominated regions. For the "implicit" Monte Carlo approach [45], the particles can become bogged down when there is a tight coupling with the thermal state of the gas. Additionally, when the fluid velocity becomes non-negligible, one has to be particularly careful about keeping track of lab- and comoving-frame quantities [46].

The final straw that breaks the camel's back is the opacity. In the simplest approach, we can use a frequency-integrated, or grey, opacity. This is usually a good approximation for regions where e.g. electron scattering dominates, but breaks down when other sources such as bound-free and line absorption play a role. In the more general case, opacity tables have been generated for a variety of astrophysical conditions by assuming local thermodynamic equilibrium (LTE) conditions, including both mean and multi-group (frequency-dependent) opacities [47, 48]. However, under non-LTE (NLTE) conditions (e.g. during CSM interaction [49]), the opacity becomes dependent on the radiation field as well, making it impossible to tabulate. Instead, the individual atomic level populations must be solved for, resulting in a large system of rate equations [50]. As metals can have thousands of important levels and millions of transition rates to keep track of, these systems quickly become unwieldy and various approximations must be made [51, 52].

1.2 Thesis Overview

The thesis is organized as follows. Chapter 2 gives an overview of "normal" supernova light curves without a circumstellar medium. In it, I discuss the limitations of analytic techniques widely used to infer properties of supernovae from their light curves, such as the ejecta and radioactive masses. Chapter 3 introduces a comprehensive theoretical framework for interpreting interacting supernova light curves. This framework is informed by extensive radiation hydrodynamics simulations of the ejecta-CSM landscape. In Chapter 4, I describe improvements to the Sedona Monte Carlo radiative transfer code, namely the new capability to perform time-dependent non-LTE multi-group radiation hydrodynamics simulations. Finally, in Chapter 5 I leverage the capabilities developed in Chapter 4 to simulate the panchromatic radio to X-ray emission resulting from CSM interaction.

Chapter 2

Physics of Supernova Light Curves

2.1 Abstract

Simplified analytic methods are frequently used to model the light curves of supernovae and other energetic transients and to extract physical quantities, such as the ejecta mass and amount of radioactive heating. The applicability and quantitative accuracy of these models, however, have not been clearly delineated. Here we carry out a systematic study comparing certain analytic models to numerical radiation transport calculations. We show that the neglect of time-dependent diffusion limits the accuracy of common Arnett-like analytic models, and that the widely-applied Arnett's rule for inferring radioactive mass does not hold in general, with an error that increases for models with longer diffusion times or more centralized heating. We present new analytic relations that accurately relate the peak time and luminosity of an observed light curve to the physical ejecta and heating parameters. We further show that recombination and the spatial distribution of heating modify the peak of the light curve and that these effects can be accounted for by varying a single dimensionless parameter in the new relations. The results presented should be useful for estimating the physical properties of a wide variety of transient phenomena.

2.2 Introduction

Wide-field surveys are gathering data on an increasing number of common supernovae (SNe) and related transients such as tidal disruption events, fast-evolving luminous transients, superluminous supernovae, and kilonovae. The general physics controlling the light curves of these events is similar – energy deposited either by a propagating shock (e.g. Type II-P SNe) or a heating source (e.g. radioactivity or a central engine) radiatively diffuses through the optically thick and expanding ejecta, undergoing adiabatic loses until the radiation reaches the surface and escapes. Analysis of the observed light curves can provide information on the ejecta properties and the nature of the powering source.

With the increasing number of observed transients, there is increased need for fast, empirical techniques to infer their physical properties and discriminate between competing theoretical explanations. Simplified analytic models are commonly used to analyze observations and make theoretical predictions (e.g. [53–58]). Most common among these are the Arnett models [59, 60], in which bolometric light curves are calculated through a simple numerical integral. These models also provide several "rules of thumb" for estimating physical properties from the light curve brightness and duration. In particular, "Arnett's rule" states that the instantaneous heating rate at peak is equal to the peak luminosity [60]. For Type I supernovae, this rule in principle allows one to extract the mass of radioactive ^{56}Ni [61–65].

Despite the frequent application of these analytic models and rules, a systematic study of their accuracy and applicability has not been carried out. Previous numerical models of Type Ia SNe have noted that Arnett's rule is usually accurate to $\sim 20\%$ [66–68]. For Type Ib/c SNe Arnett's rule is typically off by $\sim 50\%$ [69, 70], and for Type II SNe like SN1987A the error is a factor of ~ 2 [71]. The reasons for these discrepancies – and why they are more extreme for certain classes of transients – have not been fully spelled out.

In this paper we carry out a systematic investigation of certain analytic models compared to numerical light curve simulations. We find that the main limitations in the Arnett models stem from the assumption that a self-similar temperature profile is immediately established in the ejecta. This fails to account for the time-evolving propagation of a radiative "diffusion wave" from the heating source to the surface. The neglect of the diffusion wave is worse for more centrally concentrated heating sources, which is why Arnett's rule is worse for more stratified Type Ib/c SNe and better for more thoroughly mixed Type Ia SNe.

We derive a new relation between the peak time and peak luminosity of transient light curves which accurately captures the results of numerical models. We study how the relation depends on the spatial distribution of heating as well as the effects of a non-constant opacity due to recombination. The new relation is parameterized by a dimensionless constant β, and works for a variety of assumed heating sources and ejecta characteristics.

In Section 2, we describe the assumptions and limitations of the Arnett light curve models and Arnett's rule. In Section 3, we derive the new peak-time luminosity relation and compare it to numerical simulations. In Section 4, we investigate the relation between the peak and diffusion time. In Section 5, we examine the effects of concentration of the heating source. In Section 6, we look into the effects of a non-constant opacity due to recombination on the light curve and the new relation. Finally, in Section 7, we apply the results and relation to radioactive ^{56}Ni-powered transients. In Appendix A, we provide a table of the new relation for a variety of luminous transients.

2.3 Limitations of Arnett-like Models

The analytic light curve modeling approach of [59, 60] (hereafter A80,A82) is widely used to analyze luminous transients. A closely related "one-zone" modeling approach [56, 72, 73] differs in its mathematical details but results in a similar expression for calculating the light curve.

Assumptions and Light Curve Solution

The Arnett-like models begin with the first law of thermodynamics

$$\dot{\mathcal{E}} = -P\dot{\mathcal{V}} + \varepsilon - \frac{\partial L}{\partial m} \tag{2.1}$$

where $\mathcal{E}$ is the specific (i.e. per unit mass) energy density, P the pressure, $\mathcal{V} = 1/\rho$ is the specific volume, ε is the specific heating rate, and L the emergent luminosity. Several simplifying assumptions are then made: (1) the ejecta is expanding homologously and so the radius evolves as

$$R_{ej}(t) = v_{ej}t \tag{2.2}$$

where v_{ej} is the maximum ejecta velocity; (2) Radiation pressure dominates over the gas pressure and so we can express the specific energy density as

$$\mathcal{E} = 3P/\rho = aT^4/\rho \tag{2.3}$$

where T is the temperature; (3) The luminosity is described by the spherical diffusion equation

$$L(r) = -4\pi r^2 \frac{c}{3\kappa\rho}\frac{\partial e}{\partial r} \tag{2.4}$$

where $e = \rho\mathcal{E}$ is the energy density (per unit volume) and κ the opacity; and (4) the ejecta is characterized by a constant opacity.

The Arnett models make an additional consequential, but often overlooked, assumption: (5) The energy density profile is self-similar, i.e., the spatial dependence is fixed and only the overall normalization changes with time

$$e(x,t) = \frac{E_{int}(t)}{V(t)}\psi(x) \tag{2.5}$$

where E_{int} is the total internal energy of the ejecta and $x = r/R_{ej}(t)$ is the (comoving) dimensionless coordinate. The dimensionless function $\psi(x)$ describes the spatial dependence of the radiation energy density, which by assumption does not change with time. Substituting Eq. 2.5 into the diffusion equation (Eq. 2.4) gives the emergent luminosity at $r = R_{ej}$

$$L = \frac{tE_{int}(t)}{\tau_d^2} \tag{2.6}$$

where

$$\tau_d = \left[\frac{3}{4\pi}\frac{\kappa M_{ej}}{v_{ej}c}\frac{1}{\xi}\right]^{1/2} \tag{2.7}$$

is the characteristic diffusion time through the ejecta with mass M_{ej}. The quantity $\xi = d\psi/dx|_{x=1}$ specifies the energy density gradient at the ejecta surface and is a constant when self-similarity is assumed. The one-zone models make the ansatz $\xi = 1$. [60] uses a more sophisticated separation of variables method to derive a self-consistent solution for $e(x,t)$. This requires making a final assumption: (6) The spatial distribution of the heating is proportional to the energy density. Eq. 2.1 can then be solved to find

$$e(x,t) = \frac{E_{int}(t)}{V(t)}\left[\frac{\pi}{3}\frac{\sin(\pi x)}{x}\right] \tag{2.8}$$

which gives $\xi = \pi^2/3$.

To solve for the light curve, the Arnett models integrate Eq. 2.1 over the entire ejecta and apply the assumptions of homology and radiation energy domination to derive an equation for global energy conservation

$$\frac{dE_{int}(t)}{dt} = -\frac{E_{int}(t)}{t} + L_{heat}(t) - L(t) \tag{2.9}$$

where $L_{heat}(t)$ is the total input heating rate. Using Eq. 2.6 to replace $E_{int} = L\tau_d^2/t$ and rearranging gives

$$\frac{\tau_d^2}{t}\frac{dL}{dt} = L_{heat}(t) - L(t) \tag{2.10}$$

Arnett's rule follows, since the condition of an extremum $dL/dt = 0$ implies $L = L_{heat}$.

The ordinary differential equation Eq. 2.10 can be solved for $E_{int}(t)$ and hence the emergent luminosity

$$L(t) = \frac{2}{\tau_d^2}e^{-t^2/\tau_d^2}\int_0^t t' L_{heat}(t') e^{t'^2/\tau_d^2}\, dt' \tag{2.11}$$

Both the one-zone and the separation of variables approaches result in the same expression for the light curve; the only difference is the value of ξ, which reflects different assumptions about the shape of the self-similar energy density profiles. The diffusion time for the one-zone models is a factor of $\pi/\sqrt{3} \approx 2$ larger. To avoid confusion, we hereafter define a characteristic diffusion timescale without any numerical factors

$$t_d = \sqrt{\frac{\kappa M_{ej}}{v_{ej}c}} \tag{2.12}$$

and so $\tau_d = [3/4\pi\xi]^{1/2} t_d$. Physically, the characteristic diffusion timescale gives the time at which the expansion timescale $t_{exp} = R_{ej}/v_{ej}$ equals the diffusion time $t_{diff} = \kappa\rho R_{ej}^2/c$. The peak time scales with the diffusion timescale $t_{peak} \propto t_d$, but the numerical coefficient relating them depends on the distribution of heating, nature of the opacity, and other effects.

The self-similarity assumption will be shown below to limit the accuracy of the Arnett models. However, this is not a necessary assumption as Eq.2.8 is only the first eigenfunction of the separated spatial equation. The full solution of the energy density can be expressed as an infinite sum of higher order eigenfunctions whose normalization will be set by the spatial distribution of heating and boundary conditions. [74] show how such an approach can be used to relax the assumptions (5) and (6) and produce more accurate light curves. However, due to the more complicated nature of the solution, the full solution with higher-order eigenmodes is rarely used in practice.

Comparison to Numerical Simulations

To assess the accuracy of the Arnett solutions, we compare them to numerical monte-carlo radiation transport calculations run with Sedona [75] .We adopt similar assumptions as A82: homologous expansion, uniform density, and a constant opacity. Non-constant opacity will be considered in Section 6. In this section, the ejecta has a diffusion timescale $t_d = 100$ days and the heating source is at the center and follows $L_{heat}(t) = L_0 e^{-t/t_s}$, where the timescale $t_s = 10$ days.

Fig. (2.1) compares the numerical light curve to the Arnett analytic solution. The numerical models have an initial "dark period" until $t \sim 0.1 t_d$, before which the photons have not had sufficient time to diffuse from the center of the ejecta [76]. In contrast, the analytic solutions predict a steeper rise beginning at $t = 0$, a consequence of the assumption that radiation energy is immediately distributed throughout the ejecta. The A82 solution predicts a peak time a factor of 2 shorter than the numerical result, but gives roughly the correct peak luminosity. The peak time of the one-zone model is closer to the numerical simulation, but under-predicts the peak luminosity and is overall too broad. There is no choice of ξ such that the analytic solution closely matches the numerical light curve.

This inaccuracy of the analytic models is more pronounced for more centrally concentrated heating sources. Fig. (2.2) shows numerical models where the heating source has been uniformly mixed out to dimensionless radius x_s, with $x_s = 0$ corresponding to a central source. The Arnett analytic solution most closely resembles a well-mixed numerical model with $x_s \approx 0.8$. We can define a heating-weighted radius where the bulk of heating occurs as

$$\langle x_s \rangle = \left(\frac{\int_0^1 x^2 \dot{e}_{heat}(x)\, dx}{\int_0^1 \dot{e}_{heat}(x)\, dx} \right)^{1/2} \tag{2.13}$$

where $\dot{e}_{heat}(x)$ is the energy density heating rate at x. For constant heating out to radius x_s, we have the relation $\langle x_s \rangle = x_s/\sqrt{3}$. In the Arnett solution, $\dot{e}_{heat}(x) \propto e(x)$ and using Eq.(2.8) we find that $\langle x_s \rangle \approx 0.4$, which indeed corresponds to $x_s \approx 0.7$.

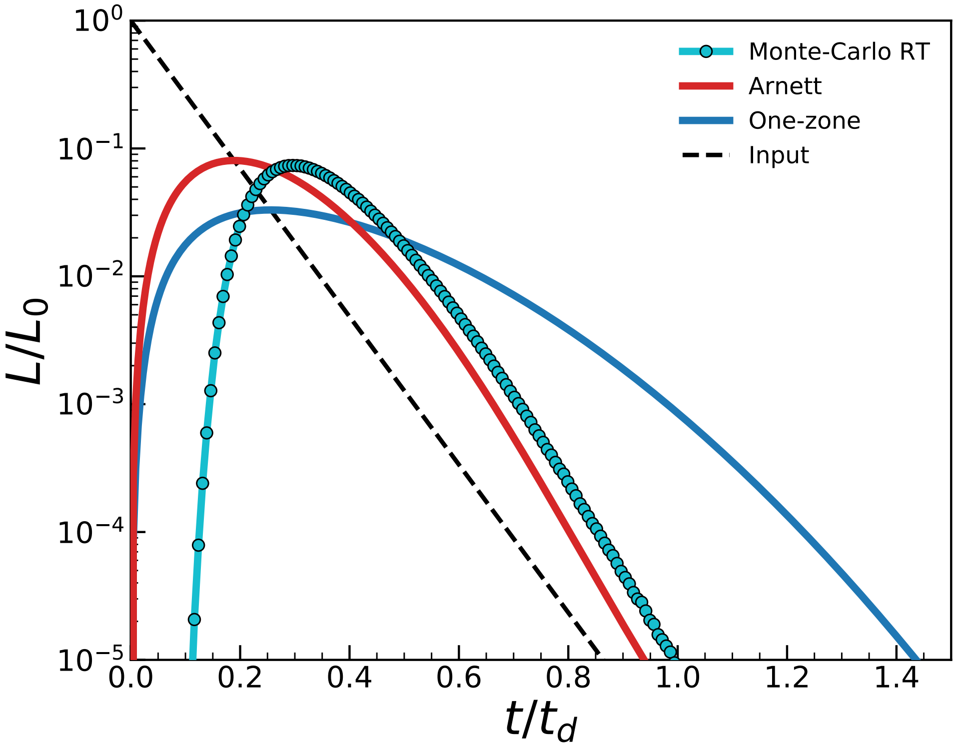

Figure 2.1: Light curves from the Arnett solution Eq.(2.11) with different choice in the diffusion timescale factor ξ (red and blue lines), compared with a numerical monte-carlo radiation transport solution using Sedona (teal line with points). The input heating (dashed black line) consists of a centrally-located exponential source with luminosity $L_{in}(t) = L_0 \exp\left[-t/t_s\right]$ with a timescale $t_s = 10$ days and a characteristic diffusion timescale $t_d = 100$ days.

The limitation of the Arnett models stems from the assumption that the spatial distribution of the radiation field is self-similar. In reality, for central sources a radiation diffusion wave initially propagates outwards, only reaching the surface and establishing a self-similar profile after a timescale $\sim t_d$. In Fig. (2.3), we show the evolution of the energy density profile defined in Eq.(2.8) for a central exponential heating source. At early times, a diffusion wave propagates outwards, and the self-similar assumption fails. By neglecting this diffusion wave, the Arnett-like models overestimate the luminosity at early times. For a more uniformly mixed source, self similarity is established earlier, and so the Arnett models are more applicable.

Thus, it is a common misconception that the Arnett models assume a centrally-located heating source – while the *energy density* increases towards the center, the *heating luminosity*

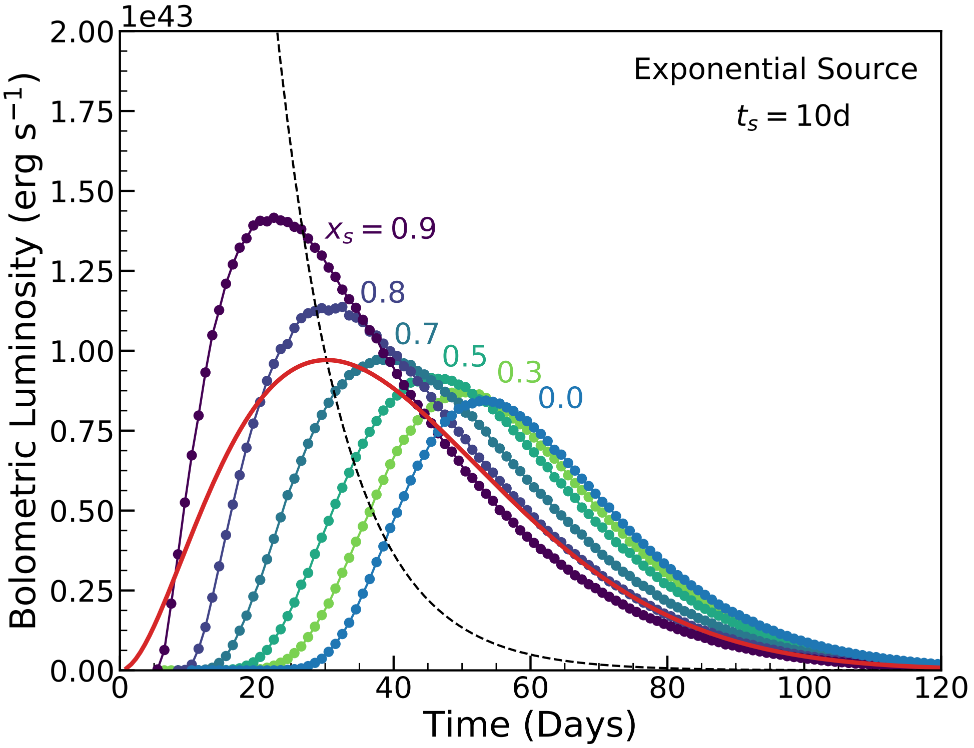

Figure 2.2: Effects of varying concentration, in terms of the dimensionless radius x_s. The heating is uniformly mixed out to x_s. The solution of A82 is shown for comparison (red line), as well as the input heating rate (dashed black line), here an exponential source with timescale $t_s = 10$ days. Arnett's rule, which predicts that the input heating rate should intersect the observed light curve exactly at peak holds only for well mixed sources, $x_s \approx 0.8$.

peaks close to the surface, producing the faster rise and earlier peak compared to the central-heating numerical solution.

This likely explains why the A82 solution more closely predicts Type Ia rather than core collapse SN light curves – Type Ia SN typically have a much larger degree of mixing [66] while core collapse SNe have more centrally concentrated ^{56}Ni. We explore the effects of the spatial distribution of the heating source in more detail in Section 5.

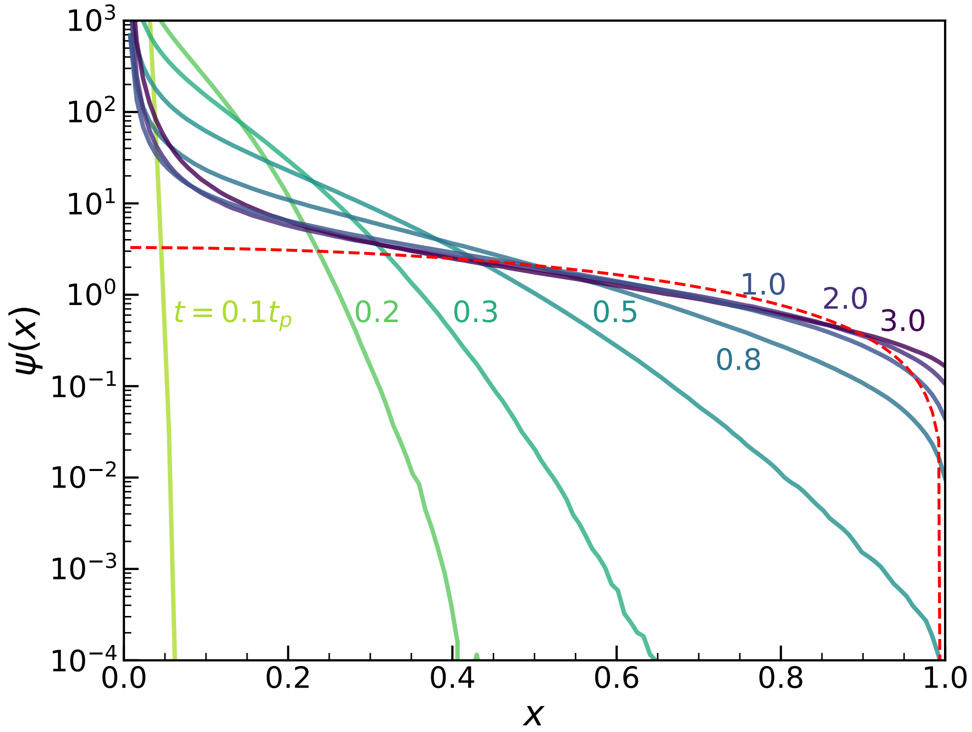

Figure 2.3: Evolution of the energy density profile Eq. (2.5) for a central exponential heating source. Shown are profiles at different times relative to peak, t_p. The self-similar assumption breaks down at early times as the diffusion wave propagates outward. At times $t > t_p$, the profile settles into a self-similar shape. Also shown for comparison is the solution of Arnett in Eq.(2.8) (dashed red line).

Arnett's Rule

A specific prediction of the Arnett models is that the peak luminosity is equal to the heating rate at peak, i.e.

$$L_{peak} = L_{heat}(t_{peak}) \tag{2.14}$$

This is commonly referred to as Arnett's rule (or Arnett's law) and is widely used to infer e.g. the nickel mass in radioactive SNe [61, 62].

We see from Fig.(2.2) that Arnett's rule does not hold in general and that its accuracy depends on the heating source concentration. For centrally concentrated sources ($x_s \lesssim 0.8$) Arnett's law gives an under-estimate of the true peak luminosity, with the error being systematically worse for more centralized heating. For nearly fully mixed heating sources ($x_s \gtrsim 0.8$) Arnett's law is an over-estimate.

The failure of Arnett's rule again stems from the assumption of self-similarity, which implies a proportionality between the luminosity and the total ejecta internal energy, $L \propto Et$. Under this assumption, the light curve has to peak simultaneously with $E(t)$ – i.e., at the time when the rate of energy loss, $L(t)$ equals the rate of energy gain, $L_{heat}(t)$. In reality, the time-dependent propagation of a diffusion wave means that the luminosity does not strictly track the internal energy. For central sources, $L(t)$ generally lags $E(t)$ and the light curve peaks at a time when $L > L_{heat}$. For fully mixed cases, $L(t)$ leads $E(t)$ and the light curve peaks when $L < L_{heat}$. Arnett's law holds only for the case of a specific concentration ($x_s \approx 0.8$) for which the light curve coincidentally peaks at the same time as does the internal energy.

2.4 A New Relation Between Peak Time and Luminosity

Given the limits of Arnett's rule, we look for a more robust relationship between the peak time and peak luminosity of a transient light curve. We proceed by considering the evolution of the global internal energy, E, and rewrite Eq. 2.9 as

$$\frac{d(tE)}{dt} = t[L_{heat}(t) - L(t)] \tag{2.15}$$

which integrates to

$$tE(t) = \int_0^t t' L_{heat}(t')\, dt' - \int_0^t t' L(t')\, dt' \tag{2.16}$$

Eq. (2.16) is similar to the analysis presented in [77], which considers times $t \gg t_{peak}$ when $E(t) = 0$. Here we instead consider times around peak $t \sim t_{peak}$. Furthermore, we assume the initial energy content in the ejecta is zero and ignore the initial stellar radius in our assumption of homology. Thus, the analysis presented here does not necessarily apply to Type IIP/L SNe, whose light curves are dominated by the initial shock-deposited energy.

We rewrite Eq. (2.16) as

$$\frac{t^2}{2} L_{peak} = \int_0^t t' L_{heat}(t')\, dt' + \epsilon(t) \tag{2.17}$$

where

$$\epsilon(t) = \left[\frac{t^2}{2} L_{peak} - \int_0^t t' L(t')\, dt'\right] - tE(t) \tag{2.18}$$

The first term in brackets can be shown to be positive (since $L(t) \leq L_{peak}$) and monotonically increasing (see Appendix B). The second term $tE(t)$ is also positive and is a decreasing function when $L > L_{heat}$, which is typically obtained for $t \gtrsim t_{peak}$. We therefore anticipate there may be a time when the two functions cross and cancel to give $\epsilon(t) = 0$.

We express this time as $t = \beta t_{peak}$ and rearrange Eq.(2.17) to get

$$L_{peak} = \frac{2}{\beta^2 t_{peak}^2} \int_0^{\beta t_{peak}} t' L_{heat}(t')\, dt' \tag{2.19}$$

which is our desired expression for L_{peak}. In Appendix B we show that for common heating functions there is indeed a time when $\epsilon(t) = 0$ for a value of $\beta \sim 1$ that can be calibrated from the numerical simulations and is essentially independent of the heating timescale or functional form.

Eq.(2.19) can be analytically evaluated for certain heating functions. For example, for an exponential heating function

$$L_{heat}(t) = L_0 e^{-t/t_s} \tag{2.20}$$

the peak time-luminosity relation can be evaluated to get

$$L_{peak} = \frac{2L_0 t_s^2}{\beta^2 t_{peak}^2} \left[1 - (1 + \beta t_{peak}/t_s) e^{-\beta t_{peak}/t_s}\right] \tag{2.21}$$

This can be contrasted with Arnett's rule, which predicts $L_{peak} = L_0 e^{-t_{peak}/t_s}$. The two expressions make similar predictions when $t_{peak} \ll t_s$ but increasingly diverges for $t_{peak} \gg t_s$.

In Fig. (2.4) we compare our expression for L_{peak} to those of numerical light curve calculations for a central exponential heating source with $t_s = 10$ days. The numerical models span a wide range of ejecta masses, velocities, and opacities, and hence result in a range of peak times. Eq. 2.21 with $\beta = 4/3$ gives a near-perfect match to the numerical simulations, independent of the ejecta properties. In comparison, Arnett's rule predicts systematically too low values of L_{peak} and becomes progressively worse for larger values of t_{peak}/t_s.

The peak time-luminosity relation Eq. 2.19 with $\beta = 4/3$ applies for most central heating functions, as long as the opacity is constant and the density uniform. In Fig. 2.5, we show the peak time-luminosity relations for both an exponential source and a power-law source appropriate for magnetar energy injection

$$L_{heat}(t) = \frac{L_0}{(1 + t/t_s)^2} \tag{2.22}$$

which can also be analytically evaluated (see Appendix A). Fig. 2.5 shows that the Eq. 2.19 with $\beta = 4/3$ accurately reproduces the numerical calculations. In later sections, we show that the value of β does change if the source heating is spatially mixed or the opacity is non-constant due to recombination, but that β remains largely independent of the heating function, source timescale t_s, or ejecta diffusion timescale t_d.

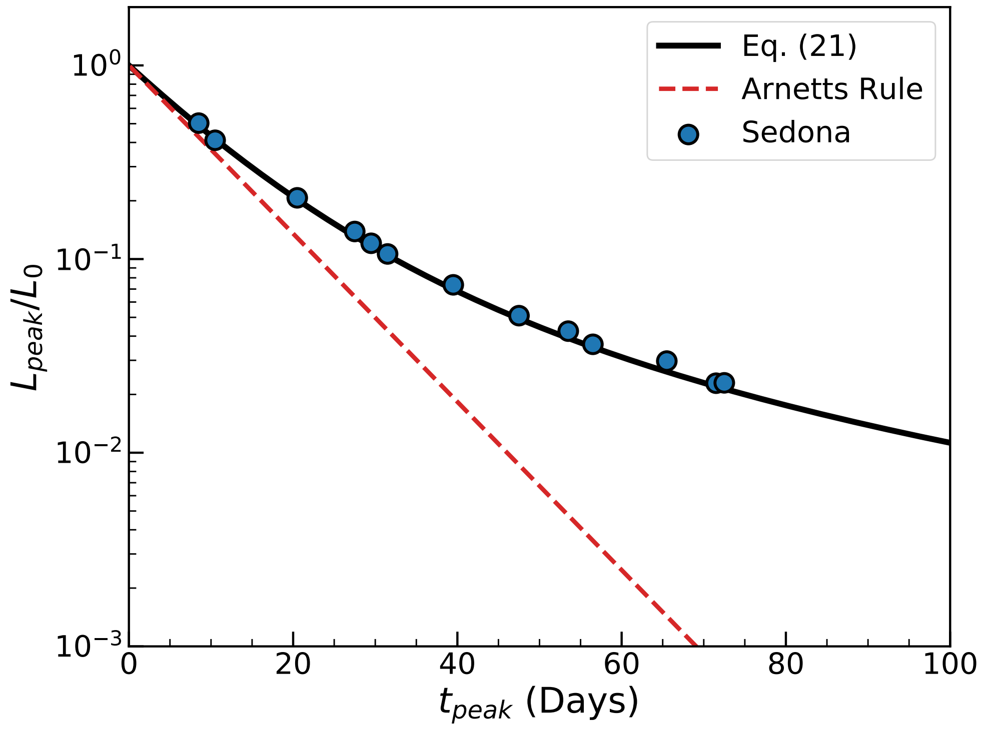

Figure 2.4: Relation between peak time and peak luminosity for a central exponential source with timescale $t_s = 10$ days. Numerical radiation transport simulations with various peak times are shown (circles) compared to Arnett's rule (black dashed line) and the new relation Eq.(2.19) with $\beta = 4/3$ (solid red line).

2.5 Relation Between Peak Time and Diffusion Time

Analyses of observed light curves often attempt to constrain the ejecta mass and velocity by setting the observed time of peak, t_{peak}, equal to the diffusion timescale τ_d [e.g., 63, 78]. Here we study that relation for constant opacity models, and show that t_{peak} depends not only on t_d, but also on the heating timescale t_s.

In Fig.(2.6), we show the dependence of t_{peak} on the ratio t_s/t_d, for a large number of numerical models with uniform density ejecta and two different central heating sources. The models have a range of masses, velocities, and constant opacities, although only the combination t_d is relevant for the light curve behavior. For $t_s/t_d \ll 1$, the peak time asymptotes to $t_{peak} \approx 0.4t_d$ independent of t_s. In this limit, the source can thus be approximated as an instantaneous "pulse" of energy deposited at t_s. The energy from such a pulse diffuses out

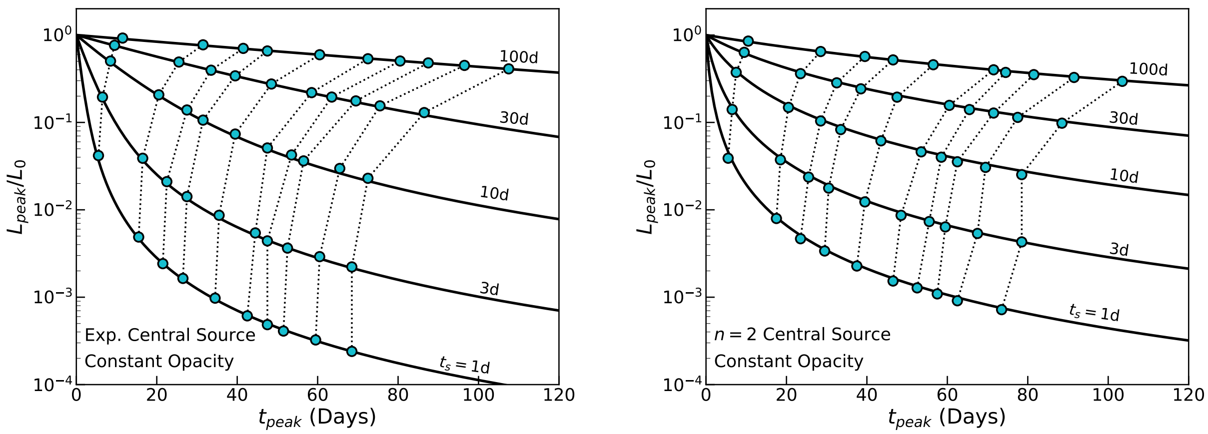

Figure 2.5: Same as Fig.(2.4), but for different values of t_s, and for an exponential (top) and magnetar (bottom) source. Numerical simulations are shown as points. Lines of constant diffusion timescales t_d are indicated (dotted black lines). Eq.(2.19) with $\beta = 4/3$ is indicated by solid black lines, for a given t_s.

and peaks at around $\sim 0.4 t_d$. In comparison, the Arnett models predict $t_{peak} \approx 0.2 t_d$ (see Fig. (2.1)).

For $t_s/t_d \gtrsim 0.1$, the continuing source deposition begins to lengthen the peak time. The dependence is fairly weak – t_{peak} only increases by a factor of ~ 2 as t_s changes over three orders of magnitude, implying that for the sources considered the light curve peak is mostly powered by heating deposited at early times.

An equation that captures the peak time of numerical models with constant opacity and central heating is

$$\frac{t_{peak}}{t_d} = 0.11 \ln\left(1 + \frac{9 t_s}{t_d}\right) + 0.36 \tag{2.23}$$

In the limit that $t_s \ll t_d$, Eq.(2.23) goes to $t_{peak} \approx 0.4 t_d$, while for $t_s \gg t_d$ it grows logarithmically with t_s. The relation is relatively insensitive to the functional form of the heating source (e.g. exponential vs. power-law) as long as the function is smoothly and gradually declining.

2.6 Spatial Distribution of Heating

Another important effect in shaping the light curve is the spatial distribution of heating within the ejecta, e.g. different amounts of "mixing" of ^{56}Ni in Type I SNe or assumed

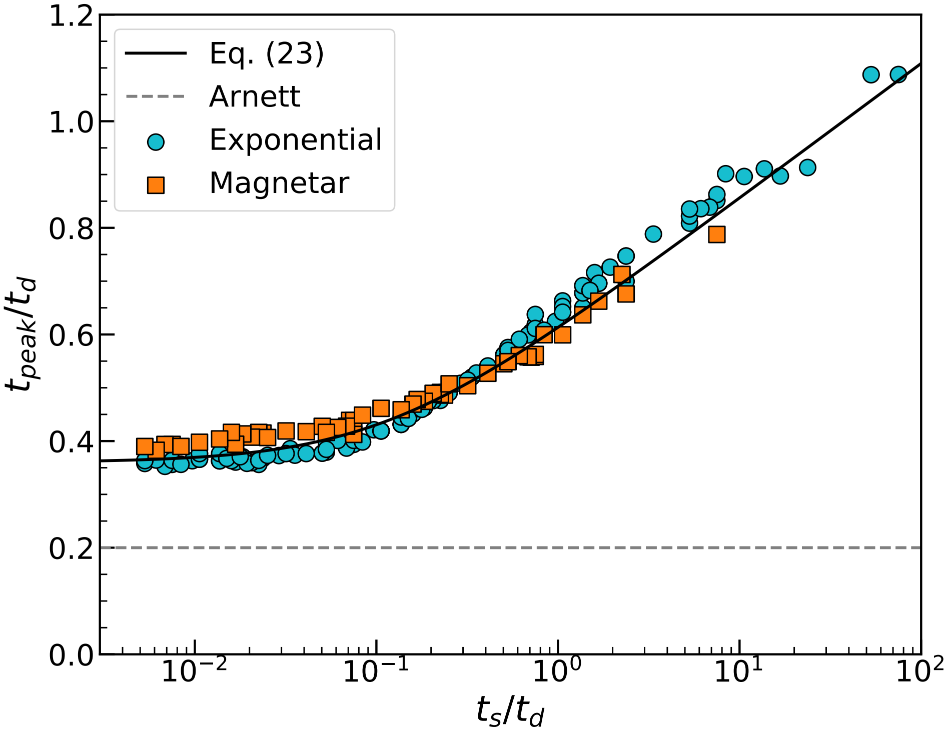

Figure 2.6: Relation between the source timescale t_s and the peak time t_{peak}, relative to the diffusion timescale t_d. Shown are an exponential (teal circles) and magnetar (orange squares) central heating source. The best-fit Eq.(2.19) is also shown (black dashed line). For comparison, the Arnett $t_{peak} = t_d$ relation is shown.

distribution of magnetar heating (see [79]). Indeed, In Fig. (2.2), we showed how the spatial distribution impacts both the peak time and luminosity of the light curve, and in particular found that the Arnett solution and Arnett's rule are most appropriate for less concentrated/more uniform heating.

To account for the spatial distribution of heating, we take the heating rate to be uniform out to a (scaled) radius x_s. Fig.(2.7) shows how the concentration affects the time of peak. The overall effect is to systematically drop the relation, i.e. for a given t_s and t_d, concentration causes the light curve to peak earlier. This was shown for the case of $t_s = 10$ days in Fig.(2.2). Interestingly, the peak time does not differ much unless the concentration radius is greater than $x_s > 1/3$.

In all cases, there is similar behavior of a "flattening" in the relation for $t_s \ll t_d$. For the most mixed case $x_s = 0.9$, the relation flattens as $t_{peak} \approx 0.1 t_d$. This lends further caution to

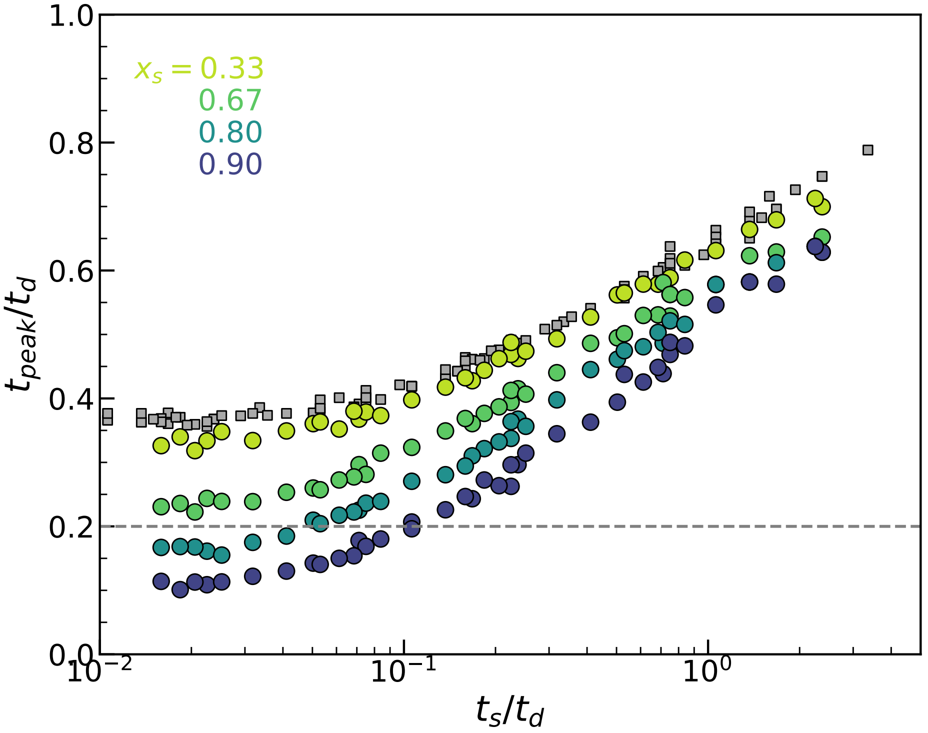

Figure 2.7: Relation between source timescale to the peak time, relative to the diffusion timescale. Different colors indicate different levels of concentration, parameterized by the concentration radius $x_s = 0.33, 0.67, 0.8$, and 0.90. For comparison, the case of a centrally concentrated source ($x_s = 0$) is shown (grey squares).

using t_d as a proxy for t_{peak}; in addition to depending on t_s, there is also another dependence on x_s.

In Fig.(2.8), we show the peak time-luminosity relation for the different spatial distributions of heating, for an exponential source with $t_s = 10$ days. Interestingly, for different concentrations, the relation Eq.(2.19) still holds. The only difference is in the value of β. For $x_s = 1/3$, the numerical simulations lie on the $\beta = 4/3$ relation, which was found to be appropriate for a central source. This is in agreement with the results shown in Figs. (2.2) and (2.7), where the $x_s = 1/3$ does not differ significantly from simply assuming a central source.

More centrally concentrated heating acts to increase the value of β. For the most uniform heating, $x_s = 0.9$, β increases by about a factor of 2 compared to a central source. For the central exponential source used in Fig.(2.7) and a constant opacity, we find that β depends

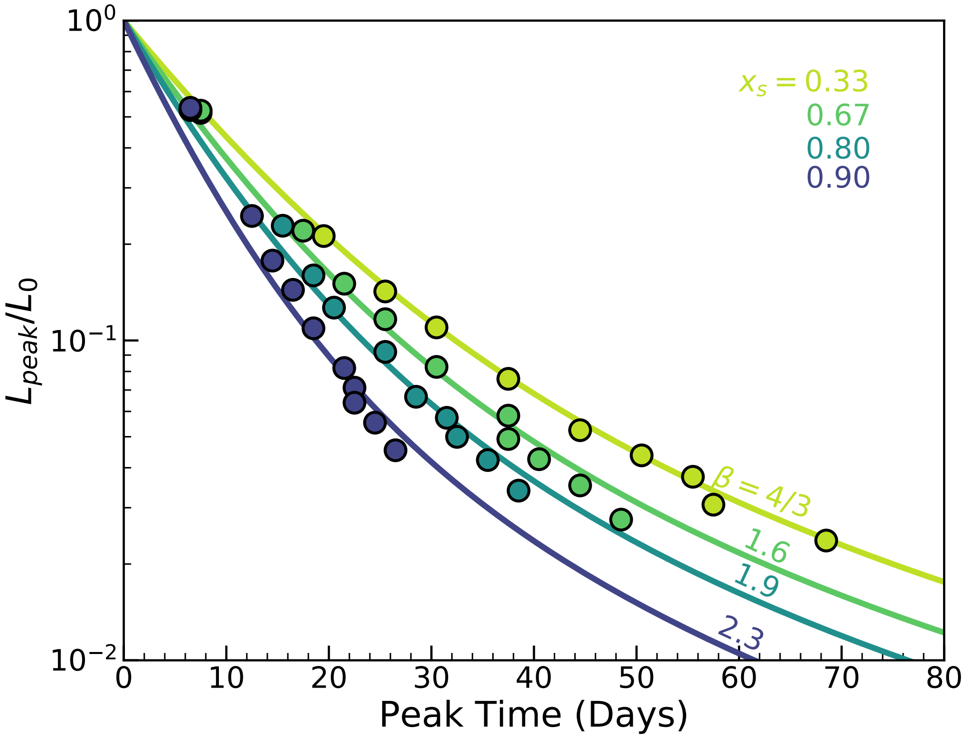

Figure 2.8: Peak time-luminosity relation for different spatial distributions of heating.

on x_s approximately as

$$\beta(x_s) \approx \frac{4}{3}\left(1 + x_s^4\right) \tag{2.24}$$

Note that we assume local deposition of the heating source. In reality, for the case of e.g. ^{56}Ni decay, there is the additional effect of gamma-ray deposition, which introduces a non-locality to the heating. In particular, gamma rays emitted closer to the center may deposit their energy farther out (or may escape entirely). Exploring this effect is outside the scope of this work (although see e.g. [70]).

2.7 Non-Constant Opacity and Recombination

While the previous results assumed a constant opacity, for certain compositions the opacity drops sharply when the ejecta cools and ions recombine. As the ejecta is typically hotter at the center, a cooling “recombination front” propagates from the surface inward [80–82].

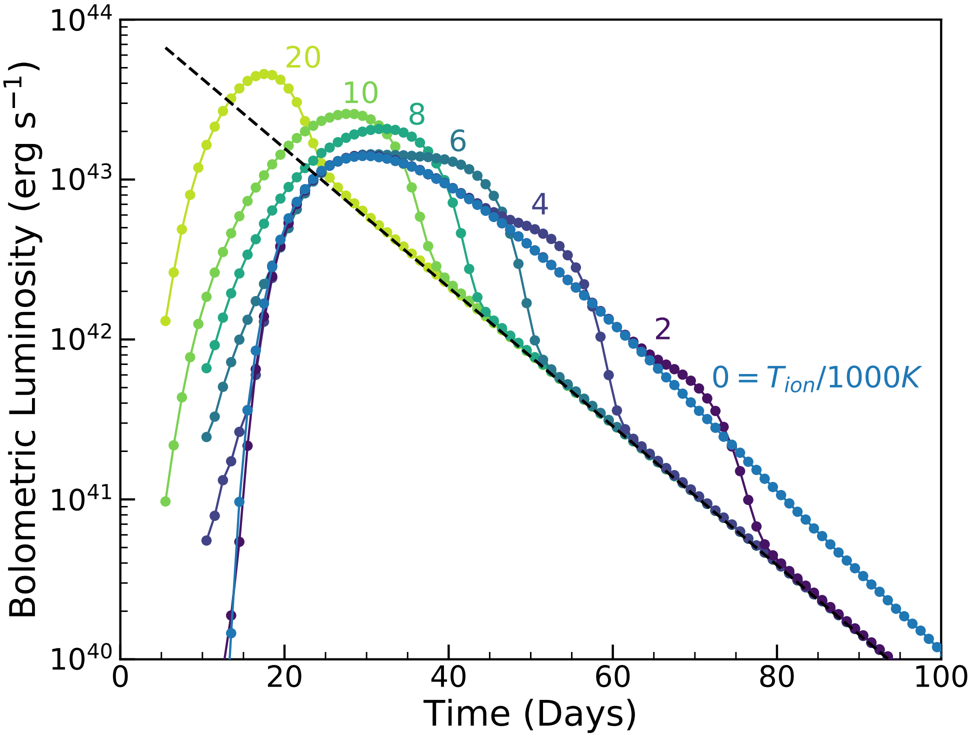

Figure 2.9: Light curves of a central exponential heating source with $t_s = 10$ days and fixed ejecta properties, but varying the recombination temperature T_{ion}. The input heating rate is shown (dashed black line). The case of $T_{ion} = 0$K is identical to assuming a constant grey opacity.

The photosphere is nearly coincident with the recombination front, with a temperature set by the ionization/recombination temperature T_{ion}.

To account for recombination effects in our numerical calculations, we prescribe a temperature dependence that mimics the behavior of the opacity in hydrogen and helium-rich compositions, for which electron scattering dominates for $T > T_{ion}$

$$\kappa(T) = \kappa_0 + \frac{\kappa_0 - \epsilon\kappa_0}{2}\left[1 + \tanh\left(\frac{T - T_{ion}}{\Delta T_{ion}}\right)\right]. \tag{2.25}$$

The opacity $\kappa = \kappa_0$ for temperatures $T > T_{ion}$ but drops to $\kappa = \epsilon\kappa_0$ for $T < T_{ion}$. The tanh function ensures a smooth transition over a temperature range ΔT_{ion}. We use $\epsilon = 10^{-3}$ and $\Delta T_{ion} = 0.1 T_{ion}$, although our results are not sensitive to the exact values. We take the temperature T to be equal to the radiation temperature $T_{rad} = (E/a)^{1/4}$, where E is the

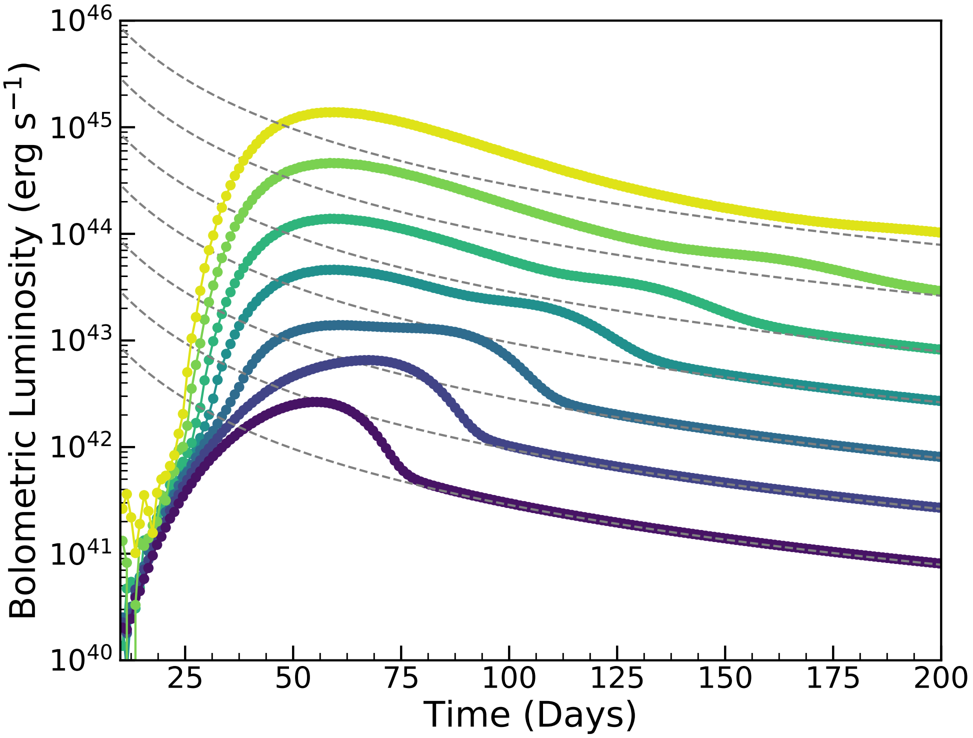

Figure 2.10: Light curves of a central magnetar heating source with $t_s = 10$ days and fixed ejecta properties and recombination temperature $T_{ion} = 6000$K, but varying the heating energy E_s. The input heating rate for each light curve is shown (dashed grey).

energy density and a the radiation constant. This is appropriate for a radiation-dominated ejecta and wavelength-independent opacity.

Fig.(2.7) shows the effect of changing the recombination temperature T_{ion}, while keeping the heating source and ejecta properties fixed. These runs use a central exponential source with timescale $t_s = 10$ days and energy $E_s = 10^{50}$ ergs, and uniform ejecta with mass $M_{ej} = 5M_\odot$, velocity $v_{ej} = 10^9$ cm s^{-1}, and opacity $\kappa_0 = 0.1$ cm^2 g^{-1}. For low T_{ion}, most of the ejecta remains ionized at and after peak and the light curve resembles the constant opacity case, with the exception of a late-time “bump” that occurs when recombination sets in and allows radiation to escape more easily. For higher T_{ion} recombination occurs earlier; for $T_{ion} \gtrsim 6000$ K recombination results in a brighter and earlier light curve peak.

When recombination is included, the total heating energy scale, E_s, impacts the light curve morphology. This is in contrast to constant opacity models, where E_s simply sets the normalization of the light curve but leaves the shape the same. Fig. (2.7) shows a set of

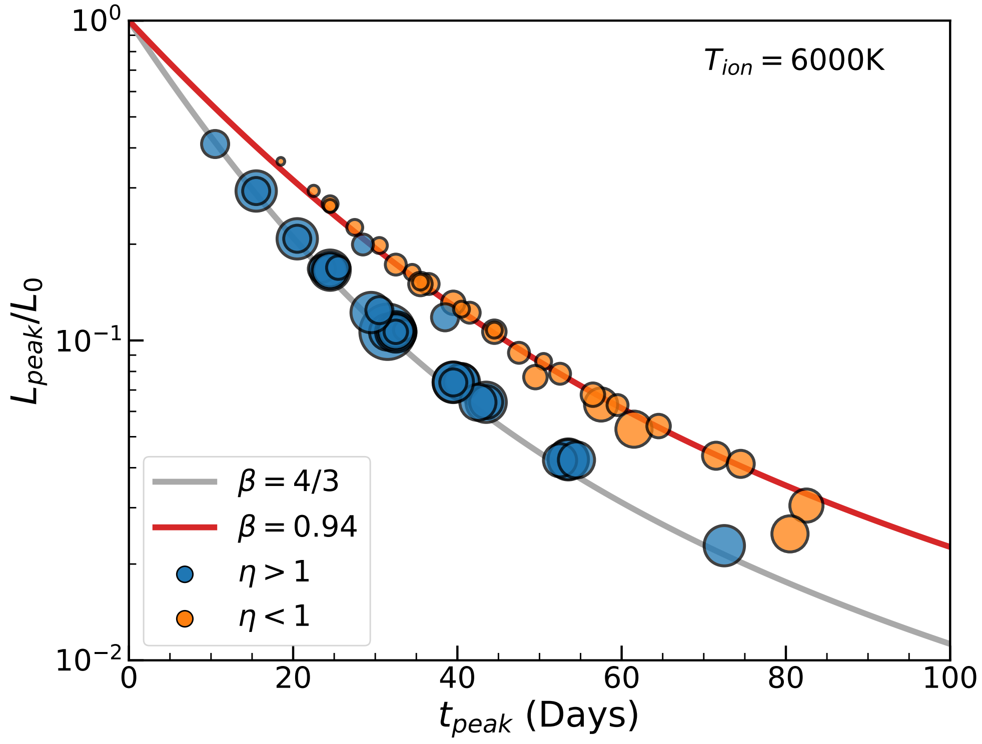

Figure 2.11: Peak time-luminosity relation with recombination effects, for a central exponential heating source with $t_s = 10$ days. Points correspond to numerical simulations with $T_{ion} = 6000$K and varying ejecta properties M_{ej}, v_{ej}, κ_{ej}, as well different values of E_s, whose relative value is indicated by the point size. Blue and orange circles correspond to Eq.(2.29) with $\eta > 1$ and $\eta < 1$, respectively. Also shown is Eq.(2.19) for different values of β (lines).

numerical light curves where only E_s is varied. At sufficiently large values of E_s, the heating source keeps the ejecta ionized until very late times, and the light curve shape resembles a constant opacity light curve. As E_s decreases, the ejecta recombines earlier, resulting in a "bump" at late times. For sufficiently low E_s, the heating source is unable to keep the ejecta temperature above T_{ion}, and so recombination impacts the light curve peak.

To determine whether recombination effects are important or not, we can compare the heating rate to the luminosity necessary to keep the ejecta ionized. The ionizing luminosity is set by the ejecta radius and the recombination temperature as

$$L_{ion} \approx 4\pi R_{ej}^2 \sigma_{sb} T_{ion}^4 \tag{2.26}$$

From Section 3, the luminosity will roughly scale as

$$L \sim \frac{E_s t_s}{t_d^2} \tag{2.27}$$

We define a ratio of the luminosity to the critical ionizing luminosity

$$\eta \equiv \frac{L}{L_{ion}} \propto \frac{c^2}{4\pi\sigma} \frac{E_s t_s}{\kappa^2 M_{ej}^2 T_{ion}^4} \tag{2.28}$$

We calibrate the proportionality based on numerical simulations of an exponential heating source to find

$$\eta \sim 0.2\, E_{s,51} t_{s,10} \kappa_{0.2}^{-2} M_{10}^{-2} T_4^{-4} \tag{2.29}$$

where $E_{s,51} = E_s/10^{51}$ erg, $t_{s,10} = t_s/10$ days, $\kappa_{0.2} = \kappa/0.2$ cm^2 g^{-1}, $M_{10} = M_{ej}/10M_\odot$, and $T_4 = T_{ion}/10^4$ K. For $\eta \lesssim 1$, the heating luminosity is too low to keep the ejecta sufficiently ionized and so recombination effects become important.

In Fig.(2.11), we show the results of a set of numerical simulations with $T_{ion} = 6000$K and various ejecta properties and E_s. Interestingly, the numerical simulations with recombination still fall on the relation Eq. (2.19). The only difference is that the value of β changes. Specifically, recombination tends to *decrease* the value of β. Also shown in Fig. (2.11) are the respective values of η for the numerical simulations. Points with $\eta > 1$ are not affected by recombination at peak, and so fall on the relation with $\beta = 4/3$, appropriate for a constant opacity. For $\eta < 1$, recombination is important and the points fall on a smaller $\beta = 0.94$ curve.

2.8 Discussion and Conclusions

We have shown how the light curve peak time and luminosity are related for luminous transients, and derived analytic relations that can be used to infer the physical properties of the heating mechanism. In particular, Eq.(2.19)

$$L_{peak} = \frac{2}{\beta^2 t_{peak}^2} \int_0^{\beta t_{peak}} t' L_{heat}(t')\, dt'$$

captures the relationship between t_{peak} and L_{peak} where the light curve physics (i.e. recombination and concentration) is contained in the β parameter. Furthermore, Eq.(2.24)

$$\beta(x_s) = \frac{4}{3}\left(1 + x_s^4\right)$$

gives the approximate dependence of β on the spatial distribution of heating. Another useful result is given in Eq.(2.23) for central sources,

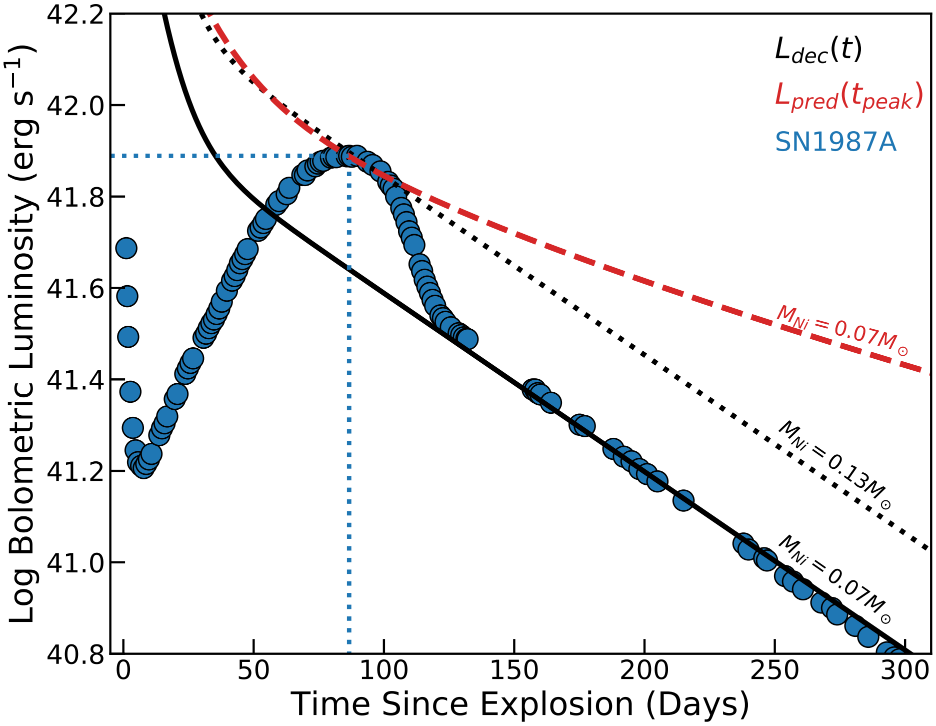

Figure 2.12: The light curve of SN1987A (blue points) from [83], compared to input Ni+Co decay of $M_{Ni} = 0.07M_\odot$ (solid black) and $0.13M_\odot$ (dashed black). Also shown is Eq.(2.19) for $0.07M_\odot$ of Ni and $\beta = 0.82$ (red dashed).

$$\frac{t_{peak}}{t_d} = 0.11 \ln\left(1 + \frac{9t_s}{t_d}\right) + 0.36$$

which shows how t_{peak} depends not only on the diffusion time t_d, but also the heating timescale t_s. In addition, recombination will change the value of β compared to a constant opacity. In Table 1, we give approximate values of β for a variety of transients. In Appendix A, we evaluate the peak time-luminosity relation for specific heating sources.

For example, one of the common sources of heating in luminous transients is the radioactive decay chain of ^{56}Ni [61, 62]. In particular, the decay chain of $^{56}\text{Ni} \rightarrow ^{56}\text{Co} \rightarrow ^{56}\text{Fe}$ dominates the heating at timescales of interest. Fig.(2.13) shows the peak time-luminosity parameter space of ^{56}Ni-powered transients, where the relation is given in Appendix A. For a given peak time and luminosity, one can thus infer an approximate value for the ^{56}Ni mass for an appropriate choice in β.

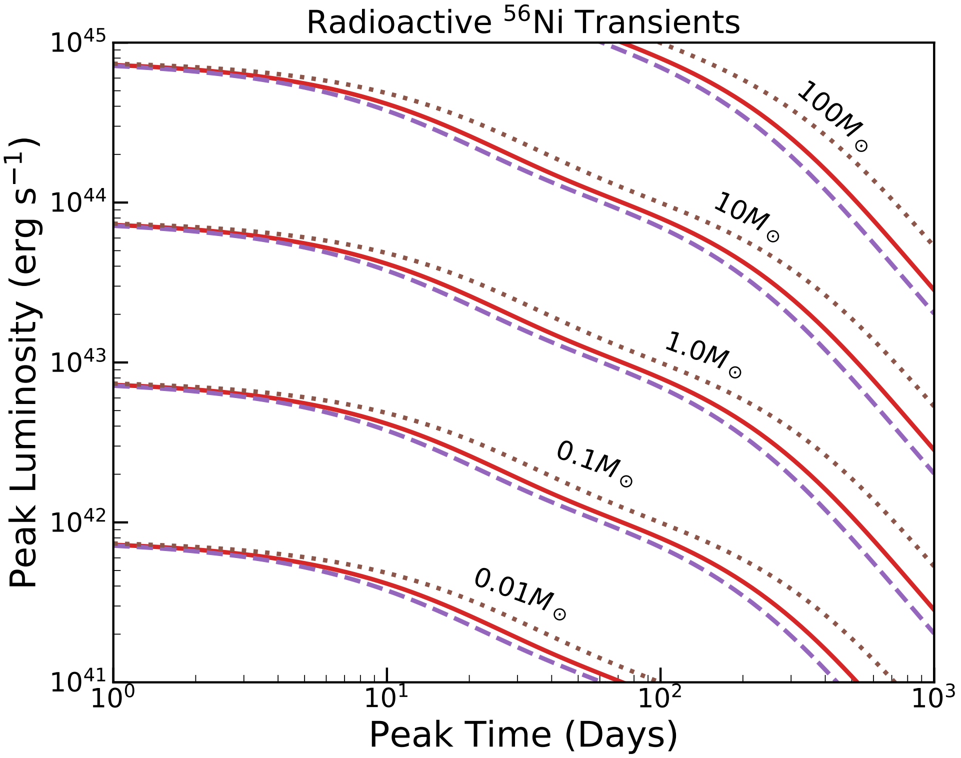

Figure 2.13: Peak time vs. peak luminosity for radioactive Ni-powered transients. Eq.(2.19) is shown for different values of $\beta = 0.82$ (dotted brown), $\beta = 9/8$ (solid red), and $\beta = 4/3$ (dashed purple).

We now consider the implications of our findings to analyzing observed SNe. In particular, Arnett's rule is often used to infer the nickel mass of Type Ia SNe. In Fig. (2.14) we show the effects of varying the nickel mass M_{Ni} in a set of toy Ia models with a total mass $M_{ej} = 1.4M_\odot$ and constant density and opacity. The inner layers of ejecta in these models are composed of pure ^{56}Ni, and so higher M_{Ni} corresponds to a larger nickel core and less centrally concentrated heating. As expected, Arnett's rule works better for larger M_{Ni} and becomes progressively worse for the more centrally concentrated low M_{Ni} models. This suggests that analyses of SNe Ia using Arnett's rule may be systematically biased, with the nickel mass of sub-luminous Ia's being overestimated.

As another case study, we show in Fig. (2.12) the observed bolometric light curve of SN1987A, a Type II supernova whose primary peak is powered by radioactive ^{56}Ni [71, 83]. The late-time light curve behavior gives a constraint on the ^{56}Ni mass to be $M_{Ni} \approx 0.07M_\odot$. Arnett's rule predicts a M_{Ni} a factor of 2 too large, whereas using the new relation Eq.(2.19)

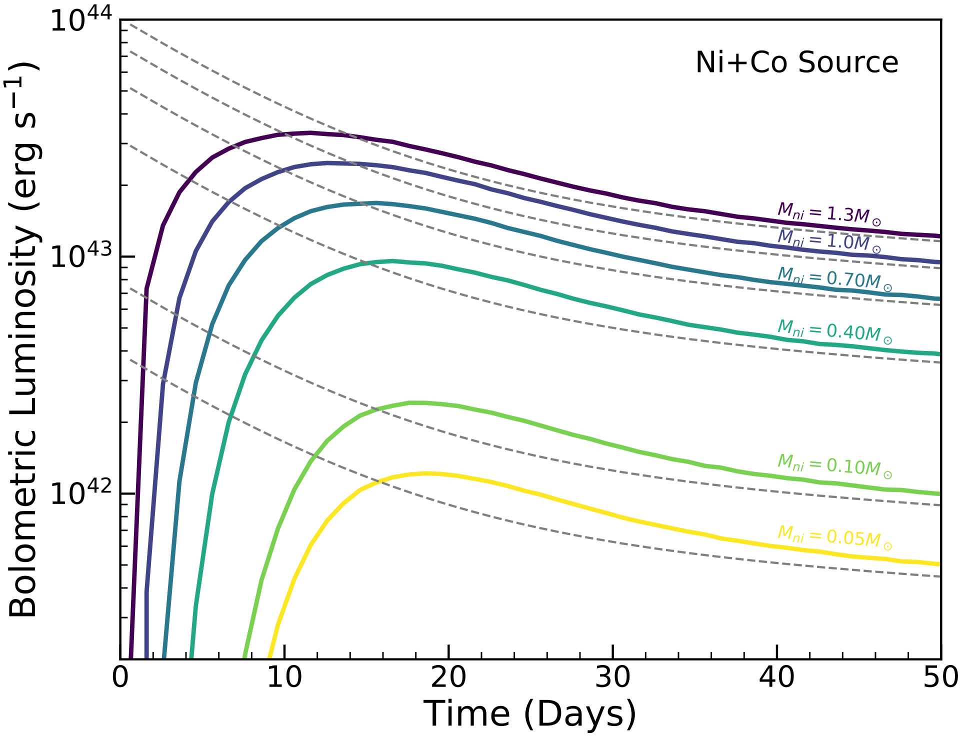

Figure 2.14: Bolometric light curves of toy Ia models, with $M_{ej} = 1.4M_\odot$, $v_{ej} = 10^9$ cm s^{-1}, $\kappa = 0.1$ cm^2 g^{-1} and assuming uniform density. Shown are light curves for different amounts of nickel masses M_{Ni} (heating rate shown as dashed grey lines) and, therefore, concentration.

with $\beta = 0.82$ (appropriate for hydrogen recombination $T_{ion} \approx 6000$K and a largely centrally-located Ni-Co heating source, as inferred from numerical simulations (see Fig.(2.11)), gives $M_{Ni} \approx 0.07M_\odot$, in agreement with the late-time determination.

As another example, we show in Fig.(2.15) the peak time-luminosity relation for the Type Ib/c SNe models presented in [70]. As noted in their work, Arnett's rule seems to overestimate the ^{56}Ni mass of their models. Using Eq.(2.19), we find that the models lie on a $\beta = 9/8$ relation. Given that the models do not have much mixing, we can assume centrally located heating and attribute any deviation from $\beta = 4/3$ to recombination effects. Interestingly, a $\beta = 9/8$ is in agreement with a recombination temperature of $T_{ion} = 4000$K, which is roughly that for a C- and O-rich composition. On the other hand, helium has a much higher recombination temperature and would imply a much smaller β; this indicates that the ^{56}Ni in the [70] models are primarily diffusing out from the much denser carbon/oxygen inner ejecta rather than the outer helium ejecta. This is in agreement with the results in

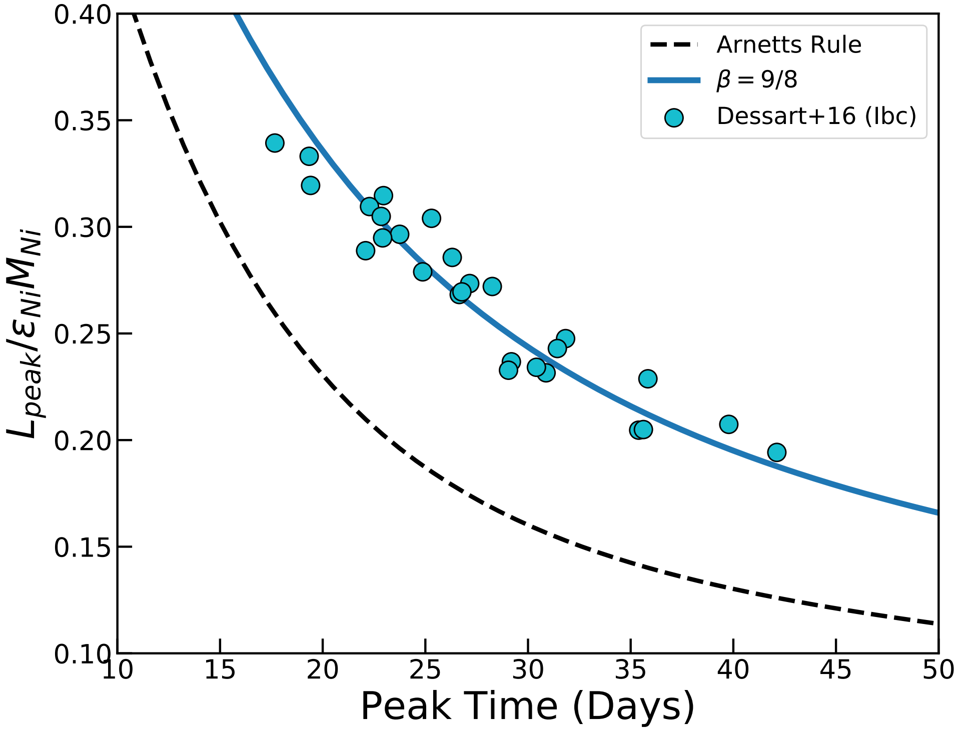

Figure 2.15: Peak time-luminosity relation of Eq.(2.19) compared to the Ibc models of [70].

[84], who similarly showed that light curve modeling is a better constraint on the C/O core rather than the helium.

The above examples demonstrate that, in principle, the peak time-luminosity relation may allow one to infer the composition of the ejecta *solely from photometric observations*. Suppose we know from observations of the radioactive tail of SN1987A that it is powered by $0.07M_\odot$ of ^{56}Ni, and we assume the nickel to be largely centrally concentrated. From the peak time and luminosity we can solve for $\beta \approx 0.94$. Since each recombination temperature has its own unique value of β, we can then infer $T_{ion} \sim 6000$K, suggesting a hydrogen-rich composition.

If the composition, and hence recombination temperature, of an observed supernova is constrained (e.g. from spectroscopic observations), then the derived value of β may indicate the spatial distribution of the heating source. For example, one can assume to good approximation a constant opacity for Type Ia SNe. Assuming central heating, this would point to a $\beta = 4/3$, yet SNe-Ia seem to obey Arnett's rule fairly well, which corresponds to a larger value of β if using Eq.(2.19). This is in agreement with the results presented in Fig.(2.8), since we expect Ia SNe to have a more uniform distribution of heating and hence fall on a larger β.

The main result, Eq.(2.19), is general enough to be applied to an arbitrary heating source, e.g. central-engine accretion, a magnetar, kilonovae, etc. Thus, for an observed transient peak time/luminosity that might be powered by other means than ^{56}Ni, one must simply choose a different $L_{in}(t)$ (which need not be analytic). Next, by choosing an appropriate β (e.g. 4/3 for constant opacity and a central source), one can constrain the heating source parameters. Note that there still remains a degeneracy in the heating source timescale t_s and energy E_s. One is not able to break this degeneracy from the peak time and luminosity alone. Such constraints require additional information/observations or by putting physical limits on allowed values.

Several physical effects were neglected in our analysis here so as to isolate the basic behavior of supernova light curves. The models presented assume spherical symmetry and adopt a grey opacity. Asymmetries in the ejecta/heating as well as non-grey effects likely play a role in the overall shape of the light curve, and on the inferred β in the new relation. [85] show that clumping affects the recombination rate, which would impact the inferred β. We also used a simple parameterization for the spatial distribution of heating, which was taken to be uniform out to some radius; more complicated distributions (e.g. from accounting for gamma-ray deposition throughout the ejecta) warrant further investigation. We further made the assumption of homologous expansion, which may be violated for supernovae interacting with a circumstellar material. Because our relations apply to the bolometric peak, errors can also arise from observational effects, such as uncertainties in the distance, reddening, or bolometric correction.

Conclusions drawn from the relation presented here are of course conditional on the specific form of the heating source assumed (e.g. radioactive decay vs. magnetar spindown). It is thus important to perform consistency checks on the nature of the heating source using additional information aside from the properties at peak, such as examining the slope of the late-time light curve tail.

While our comparisons here have demonstrated the limitations of the Arnett-like models, there exist other analytic models of transient light curves that attempt to account for the time-dependent diffusion effects that are important for setting the luminosity before and around peak (e.g. [76, 86, 87]). In future work, we will investigate a broader range of analytic models, and look for improved methods for calculating analytic light curves. Additionally, there exist other analytic techniques in estimating properties of the light curve, in particular the integral relation of [77]. This requires knowing the full shape of the light curve out to times well after peak, rather than the properties at peak. The Katz integral approach and the new relation presented here are thus complementary in inferring the physical properties of the light curve.

There is still much work to be done to understand how/why the peak time-luminosity relation as well as it does, and in particular to better calibrate its value for specific heating mechanisms and ejecta properties. Nonetheless, the framework presented here will be useful for more detailed modeling, as well as providing a fast way to characterize the large number of transients to be discovered in current and upcoming surveys.

Chapter 3

Supernova Light Curves Powered by Circumstellar Interaction

3.1 Abstract

The interaction of supernova ejecta with a surrounding circumstellar medium (CSM) generates a strong shock which can convert the ejecta kinetic energy into observable radiation. Given the diversity of potential CSM structures (arising from diverse mass loss processes such as late-stage stellar outbursts, binary interaction, and winds), the resulting transients can display a wide range of light curve morphologies. We provide a framework for classifying the transients arising from interaction with a spherical CSM shell. The light curves are decomposed into five consecutive phases, starting from the onset of interaction and extending through shock breakout and subsequent shock cooling. The relative prominence of each phase in the light curve is determined by two dimensionless quantities representing the CSM-to-ejecta mass ratio η, and a breakout parameter ξ. These two parameters define four light curve morphology classes, where each class is characterized by the location of shock breakout and the degree of deceleration as the shock sweeps up the CSM. We compile analytic scaling relations connecting the luminosity and duration of each light curve phase to the physical parameters. We then run a grid of radiation hydrodynamics simulations for a wide range of ejecta and CSM parameters to numerically explore the landscape of interaction light curves, and to calibrate and confirm the analytic scalings. We connect our theoretical framework to several case studies of observed transients, highlighting the relevance in explaining slow-rising and superluminous supernovae, fast blue optical transients, and double-peaked light curves.

3.2 Introduction

The light curves of typical supernovae are generally understood to be radiation diffusing from the hot stellar debris produced in the explosion blastwave and often further heated by the radioactive decay of ^{56}Ni [6, 88–90]. Diversity in the ejecta/nickel masses and explosion energies can produce a wide range of light curve durations and luminosities [20, 91]. Recent all-sky observations have enlarged the domain of transient types (e.g. [92–94]), uncovering highly luminous events outside of the realm of "typical" supernovae. These events occur on timescales as short as a day [22, 95, 96], to as long as several months [97, 98]. Their extreme brightness and gamut of timescales pose a challenge to usual explanations of luminous transients [99].

In typical core-collapse supernovae, roughly half of the explosion energy is converted into thermal energy from the passage of a strong neutrino-driven shock [100, 101]. Due to the high optical depths of stellar interiors, most of this energy is lost to adiabatic expansion of the ejecta [89, 102]. The bulk of the explosion energy is then stored in a reservoir of kinetic energy of order $\sim 10^{51}$ ergs [103]. If this prodigious store of energy can be tapped into and converted into observable electromagnetic radiation, it can power some of the most energetic events in the transient sky.

Interaction of the expanding supernova ejecta with a surrounding medium results in shocks that convert kinetic energy into internal energy of the gas [104] which can be radiated in a light curve; If the shock is optically thin, a *collisionless shock* forms and most of the kinetic energy remains as internal gas energy [105]. This is typically the case for supernova remnants [106, 107]. While such sites are expected to be efficient sources of energetic cosmic rays [108–110] and non-thermal radio/X-ray emission [111], they are incapable of powering the luminous *optical* transients that are being discovered (e.g. [95]). Instead, these events require the formation of a *radiative* shock [112, 113].

The formation of radiative shocks requires the presence of a dense circumstellar medium (CSM) that is optically thick and moving slowly relative to the ejecta velocity. Supernova progenitor stars typically lose significant mass to stellar winds over their lifetime [3, 12, 114, 115]. Gradual mass loss in winds will disperse into the interstellar medium. To produce a dense, local CSM, requires episodes of extreme mass loss that occur shortly before the supernova explosion. Such mass loss events are often referred to as stellar outbursts, and numerous explanations have been proposed regarding their origin, such as binary interaction [10, 13, 16] and wave-driven mass loss from e.g. unstable nuclear burning [15, 18, 116].

Observations of late-stage stellar outbursts [117–119] and the presence of narrow lines in supernova spectra [9] lend credence to the CSM interaction model as a viable explanation for at least some of the transients [20, 120–122]. Given the diversity of mass loss rates, they are an appealing mechanism for atypical supernovae, including superluminous events [49, 97, 99, 123, 124] and the recently emerging class of so-called fast blue optical transients, or FBOTs [22, 95, 96, 125–127].

The physics of CSM interaction has been extensively researched in the literature [e.g., 23, 49, 111, 128–130] including both numerical and analytical works that predict the light curve and spectra of CSM interaction [122, 131–134], as well as models to explain specific events [130, 135–137]. Different theoretical models, however, may make different physical assumptions and derive divergent expressions for how the light curve luminosity and duration depend upon physical parameters. The regions of applicability of such models is not always clear, and the degeneracy in parameter estimation when fitting observations with numerical models is often unconstrained. The same observed light curve, for example, may be fit with "shock breakout" [135] or "shock cooling" models [138, 139], leading to different inferences as to the nature of the event.

In this work, we outline a theoretical framework to help clarify the categorization of interaction light curves. We discuss how the physical parameters describing the configuration of supernova ejecta plus CSM shell can be reduced to two dimensionless parameters that primarily determine the light curve morphology. The values of these two quantities naturally partition the parameter space of interaction light curves into four classes. We compile analytic relations that express how the luminosity and duration of the light curve scale with physical parameters, and clarify their regimes of applicability. We then run a comprehensive set of spherically symmetric radiation-hydrodynamical simulations of interacting supernovae and explore the landscape of optical light curves. The numerical models are used to confirm the analytic relations and highlight the break in scaling relations that occurs when transitioning from one light curve class to the next.

The numerical models presented here aim to provide an expansive library of bolometric light curves for interacting supernova that can aid in the interpretation of observed events. Follow-up work will explore spectroscopic properties of the models and possible non-thermal emission mechanisms. In Section 3.3 we give a qualitative overview of CSM interaction, and the basic physics that controls each phase of the light curve. We give a more quantitative analysis in Section 3.4, including useful scaling relations for each phase, which we compare with numerical simulations in Section 3.5. Finally, in Section 3.6 we show how the results can be used to infer properties of the CSM mass and radius, and discuss the relevance of different interaction classes to observed classes of transient phenomena. For clarity of presentation, we provide a more complete description of the numerics and supplementary equations in the Appendix.

3.3 Qualitative Picture

We provide in this section a qualitative picture of the dynamics of interacting supernovae and the context of radiation emission. This is used to define the possible morphologies of the resulting light curves.

System Configuration

We consider supernovae interacting with a single CSM shell of mass M_{csm}. Such a configuration roughly approximates the structure of material ejected in a presupernova outburst. The key dimensional parameters of the system are

- M_{ej}: ejecta mass
- E_{sn}: ejecta kinetic energy

- M_{csm}: circumstellar mass
- R_{csm}: outer radius of circumstellar material
- κ: opacity

The density profile within the CSM shell is taken to be a power-law $\rho(r) \propto r^{-s}$ which transitions to a steep power law cutoff at the outer edge at R_{csm}. Usually, we take $s = 2$ (i.e. a wind-like CSM) but select models explore different density profiles. The CSM velocity is assumed to be much less than that of the ejecta and so set to zero.

The ejecta is assumed to be in homologous expansion with a broken power-law density profile, $\rho_{ej} \propto r^{-n}$ (where typically $n \approx 7-10$ in the outer layers of ejecta [140]). The ejecta is taken to be cold (thermal energy $\ll E_{sn}$) with a characteristic velocity $v_{ej} \equiv \sqrt{2E_{sn}/M_{ej}}$. These assumptions apply when the radius of the progenitor star is much less than R_{csm}, such that the ejecta are able to expand, cool and reach homology before interaction begins. Inclusion of initial thermal energy or heating due to radioactivity are unlikely to influence the interaction dynamics, but could contribute additional luminosity to the light curve. Finally, we assume that the inner CSM edge is much less than the outer CSM radius, $R_* \ll R_{csm}$.

It is helpful to combine the above five physical quantities into three dimensionless parameters which determine the morphology of the light curve; and two dimensional parameters which set the overall luminosity and time scale. The dimensionless parameters are

- $\eta \equiv M_{csm}/M_{ej}$: ratio of CSM to ejecta mass
- $\beta_0 \equiv v_{ej}/c$: ejecta velocity relative to the speed of light
- $\tau_0 \equiv \kappa M_{csm}/4\pi R_{csm}^2$: characteristic CSM optical depth

The dimensional scale parameters of the light curve are

- $L_0 \equiv M_{csm} v_{ej}^3/R_{csm}$: luminosity scale
- $t_0 \equiv R_{csm}/v_{ej}$: temporal scale

A combination of the dimensionless parameters that will be critical to understanding the light curve behavior is the **breakout parameter**

$$\boxed{\xi \equiv \tau_0 \beta_0 \eta^{-\alpha}}, \tag{3.1}$$

where the factor $\eta^{-\alpha}$ accounts for how shock propagation through the CSM modifies the velocity scale β_0 of the shock. Here α is an order-unity exponent that depends on the mass ratio η and the power-law exponent, n, of the ejecta density profile in the outer layers, whose expression is given by Eq. (3.12) and derived in Appendix B. In terms of the physical quantities, the breakout parameter is

$$\xi \approx 10\ \kappa\, M_{csm,\odot} v_9 R_4^{-2} \eta^{-\alpha} \tag{3.2}$$

where $\kappa \approx 0.34$ cm^2 g^{-1} for solar electron scattering, $M_{csm,\odot} = M_{csm}/M_\odot$, $v_9 = v_{ej}/10^9$ cm s^{-1}, and $R_4 = R_{csm}/10^4 R_\odot$.

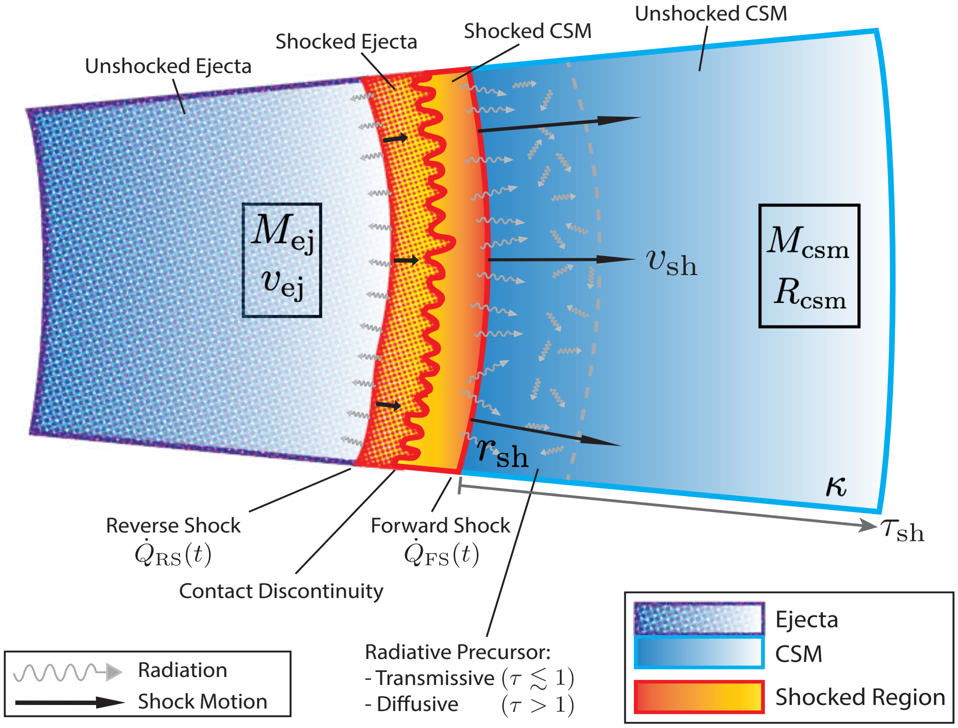

Figure 3.1: Illustration of the radiative shock structure during ejecta-CSM interaction, with the different shock features labeled.

Interaction Dynamics

Fig. 3.1 illustrates the structure of a generic interaction shock, with a forward shock propagating into the CSM and a reverse shock decelerating the ejecta. The properties of interaction light curves depend critically on the forward shock velocity, v_{sh}, which initially is characteristic of the fast outermost ejecta layers, $v_{sh} \gtrsim v_{ej}$, but decelerates as the shock progressively sweeps up the CSM. The degree to which the shock decelerates depends on the relative masses of the ejecta and CSM, η. If the shock evolves as a power-law in time $r_{sh} \propto t^{\lambda}$, then we can derive the shock velocity in terms of radius as [141]

$$v_{sh}(r_{sh}) \approx v_{ej}\eta^{-\alpha}\left(\frac{r_{sh}}{R_{csm}}\right)^{(\lambda-1)/\lambda} \tag{3.3}$$

where the factor $\eta^{-\alpha}$ accounts for the shock deceleration, and the order-unity shock exponent α depends on the density structure of the ejecta and CSM (see Appendix B.2). For $M_{csm} < M_{ej}$, the shock may decelerate only the outermost layers of ejecta and $v_{sh} \approx v_{ej}$. However, for $M_{csm} \gtrsim M_{ej}$ the shock velocity will be substantially lower than v_{ej}. The shock decelerates only so long as the density profile is shallower than $s < 3$. Acceleration of the shock for $s > 3$ [142] must be accounted for shocks that reach the outer edge of the CSM, above which the density drops off steeply.

The properties of the shock can be influenced by radiative diffusion. From Fig. 3.1, the shock front is located a distance $\Delta r = R_{csm} - r_{sh}$ from the outer edge of the CSM. The timescale for photons to diffuse out ahead of the shock and escape is $t_{esc} \sim \tau_{sh} \Delta r / c$, where $\tau_{sh} \sim \kappa \rho \Delta r$ is the radial optical depth from the shock to the CSM surface. We can compare this timescale to the dynamical timescale of the shock, $t_{sh} \sim \Delta r / v_{sh}$ for the shock of speed v_{sh} to traverse the same distance Δr. The ratio of these two timescales is

$$\frac{t_{esc}}{t_{sh}} \approx \tau_{sh} \frac{v_{sh}}{c} \tag{3.4}$$

When $\tau_{sh} \gtrsim c/v_{sh}$, radiation is trapped at the shock front and advected with the flow. Radiation pressure mediates the shock, and assuming gas and radiation are in equilibrium the shock temperature is found by setting the ram pressure $\frac{1}{2}\rho v_{sh}^2$ equal to the radiation pressure $\frac{1}{3} a T_{eq}^4$, giving

$$T_{sh} = T_{eq} \approx 10^5 \ \rho_{-12}^{1/4} v_9^{1/2} \ K \quad (\tau_{sh} \gtrsim c/v_{sh}) \tag{3.5}$$

where $\rho_{-12} = \rho / 10^{-12}$ g cm^{-3}, and $v_9 = v_{sh}/10^9$ cm s^{-1}. The trapped radiation collects into a reservoir behind the shock front until it is able to escape at a later time, either due to the shock reaching the edge of the CSM or due to the shock decelerating sufficiently that the photon diffusion speed $\sim c/\tau_{sh}$ exceeds v_{sh}. When radiation remains trapped in the expanding medium, photons adiabatically degrade, converting the internal shock energy back into kinetic energy and decreasing the radiative throughput of the interaction.

When $\tau_{sh} < c/v_{sh}$, photons are able to escape ahead of the shock and power the light curve. If gas and radiation are not in equilibrium, the immediate post-shock temperature is determined by equating the ram pressure with the gas pressure $P_g = \rho k_b T / \mu m_p$, giving

$$T_{sh} \approx 10^9 \ v_9^2 \ K \qquad (\tau_{sh} < c/v_{sh}) \tag{3.6}$$

which is much hotter than T_{eq} by several orders of magnitude. As photons are not trapped in the $\tau_{sh} < c/v_{sh}$ regime, we also need to determine how efficiently the shock can cool. The thermal radiative cooling timescale is given by

$$t_{cool} = \frac{1}{\epsilon c \kappa \rho} \frac{n k_b T / (\gamma - 1)}{a T^4} \approx 10^{-4} \ s \ \epsilon^{-1} T_5^{-3} \tag{3.7}$$

where $\epsilon = \chi_{abs} / (\chi_{abs} + \chi_{sc})$ is the ratio of absorptive to total (absoprtive plus scattering) extinction and we take the primary opacity source as electron scattering $\kappa \rho \approx \chi_{sc} = n_e \sigma_T$, n_e is the electron number density, and σ_T is the Thomson cross-section. Thermal free-free emission [143] is important in cooling the radiative shocks discussed here, where

$$\epsilon_{ff} \approx \frac{\chi_{ff}}{n_e \sigma_T} \approx 10^{-6} \ T_5^{-7/2} \rho_{-12} \tag{3.8}$$

The free-free cooling time will therefore increase with shock temperature and density as $t_{cool,ff} \propto T_{sh}^{1/2}\rho^{-1}$. For high enough shock temperatures (or low enough densities), the gas will not be able to radiatively cool faster than the shock dynamical timescale. More specifically, free-free cooling will be efficient so long as $t_{cool} < t_{sh}$, which holds for shock optical depths greater than [23]

$$\tau_{sh} \gtrsim 0.3v_9 \tag{3.9}$$

For an optical depth less than $0.3v_9$, the shock inefficiently cools and is adiabatic. In this regime, non-thermal emission will become important. Here, we limit our focus to CSM optical depths where $\tau_0 \gtrsim 1$, and additionally assume non-relativistic shock velocities $v_{ej} \lesssim 0.1c$ such that Eq. 3.9 more readily holds across the shock's evolution. Note that other processes which may aid in radiative cooling of the shock include lines and bound-free absorption, increasing the effective ϵ in Eq. 3.7. In particular, from Eq. 3.8 we see that free-free thermalization becomes less efficient at high temperatures (i.e. faster shocks). [23] show that at these higher shock temperatures, inverse Compton scattering becomes the dominant thermalization process, which expands the (τ_{sh}, v_{sh}) parameter space in which the shock can efficiently radiate.

The kinetic luminosity of the forward shock (in the strong shock limit) is approximately the kinetic energy density $\rho v_{sh}^2/2$ times the flux $4\pi r_{sh}^2 v_{sh}$ through the shock front,

$$L_{sh} \approx 2\pi r_{sh}^2 \rho(r_{sh}) v_{sh}^3. \tag{3.10}$$

A detailed analysis of how the shock heating evolves and eventually escapes to power the light curve is given in §3.4.

Light Curve Phases and Morphology

We can conceptually decompose the light curve arising from interaction into five phases, as illustrated in Figure 2.

(0) **Dark Phase:** The shock is propagating through the CSM, but photons are unable to escape ($\tau_{sh} \gg c/v_s$) and remain trapped at the shock front. The interaction therefore produces no observable signal.

(1) **Shock Breakout:** The forward shock front reaches a low enough optical depth ($\tau_{sh} \sim c/v_s$) that photons can diffuse ahead of the shock front, and the light curve rises to a peak.

(2) **Continued Interaction:** The forward shock continues propagating through the CSM and photons efficiently escape, such that the luminosity tracks the instantaneous energy deposition rate of the shock. Additionally, the reverse shock propagates inwards (in mass), generating additional heating of the ejecta.

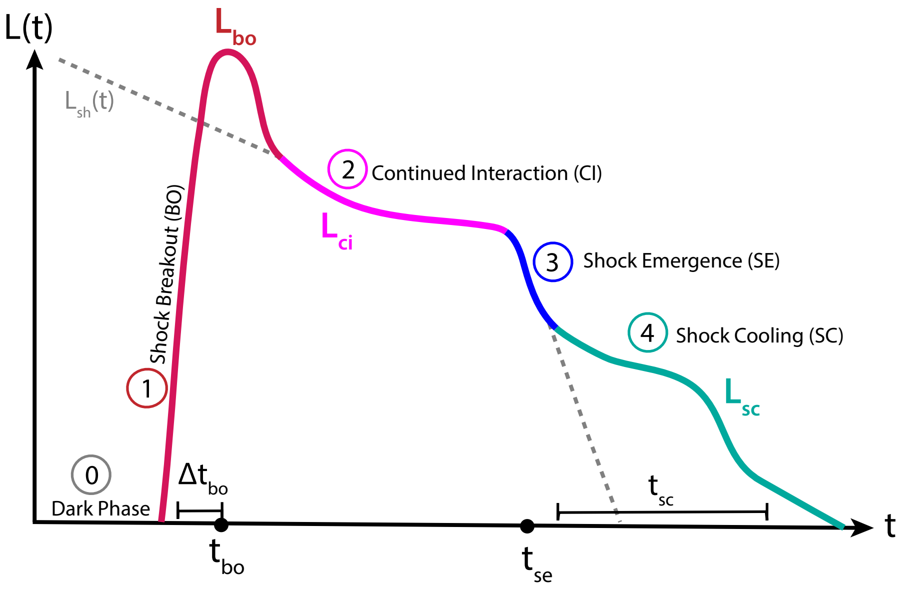

Figure 3.2: Schematic diagram (not to scale) of a CSM interaction light curve and the distinct phases that appear as the shock evolves in time. Also indicated are the characteristic luminosity and timescale of each phase, appearing in §3.4 as the boxed equations.

(3) **Shock Emergence:** The forward shock reaches the outer edge of the CSM resulting in a sharp drop in luminosity as the shock heating abates.

(4) **Shock Cooling:** Photons produced at earlier times in deeper shock-heated regions continue to escape and power the light curve. Continued heating from the reverse shock or other sources (e.g. radioactivity) may also contribute.

We emphasize that in this terminology ”shock breakout” refers to the escape of photons from the shock and not the exiting of shock from the system (which we instead label ”shock emergence”). In some scenarios, ”breakout” and ”emergence” occur almost simultaneously at the CSM edge and this distinction is not be significant, but in extended CSM it is essential to consider the case where breakout occurs interior to the CSM edge well before emergence [131].

The relative prominence of each of the above phases will depend on the parameters of the CSM/ejecta configuration. As a result, interaction is capable of producing a diversity of light curve behaviors. By taking $\tau_{sh} \sim \tau_0$ and $v_{sh} \sim v_{ej}\eta^{-\alpha}$ in Eq. (3.4), we get $t_{esc}/t_{sh} \sim \xi$, the breakout parameter defined in Eq. 3.1. If $\xi > 1$, shock breakout occurs at the CSM edge; if $\xi < 1$, breakout will instead occur within the CSM. We can then define four light curve classes (see Fig. 3.4) based on whether the CSM significantly decelerates the shock ($\eta > 1$, ”heavy CSM”) or not ($\eta < 1$, ”light CSM”) and whether breakout occurs at the CSM edge ($\xi > 1$) or in its interior ($\xi < 1$).

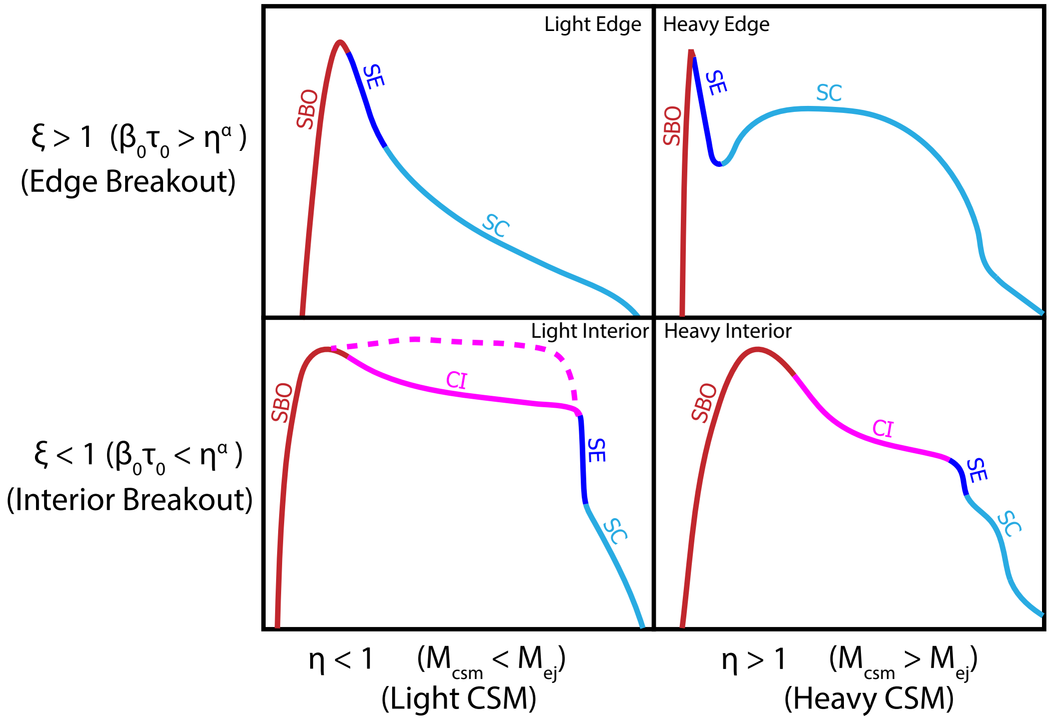

Figure 3.3: The four general classes of CSM interaction light curves, and the color-coded phases observable in each class. (*SBO* = shock breakout (Phase 1); *CI* = continued interaction (Phase 2); *SE* = shock emergence (Phase 3); *SC* = shock cooling (Phase 4)).

Edge-breakout; Light CSM ($\xi \gg 1$, $\eta \ll 1$): In this scenario, the CSM is so optically thick that shock breakout (phase 2) occurs in the steep density profile just outside the CSM edge at R_{csm} [113, 135]. The breakout of radiation is almost immediately followed by shock emergence (phase 4), with essentially no phase of continued interaction (phase 3). This leads to a relatively sharply rising and falling light curve. Shock cooling (phase 5) after the shock has emerged results in an extended light curve tail after breakout [138, 139].

Edge-breakout; Heavy CSM ($\xi \gg 1$, $\eta \gtrsim 1$): As with the previous scenario, breakout and emergence happen at the edge of the CSM, producing a shapr breakout peak in the light curve. The subsequent shock cooling phase, however, is more prominent, as the high CSM mass leads to a deceleration and thermalization of the bulk of the ejecta kinetic energy. Given the higher mass and lower velocity of the shocked gas, the cooling emission diffuses out on a longer timescale, leading to a distinct second ”shock-cooling” bump in the emergent light curve.

Interior-breakout; Light CSM ($\xi \lesssim 1; \eta \ll 1$): In this scenario, shock breakout occurs well before the forward shock has reached the CSM edge (see e.g., [131, 144]). The peak in the light curve associated with breakout is followed by an extended continued interaction phase, where the luminosity tracks the shock kinetic luminosity Eq. 3.10. The slope of the light curve in the continued interaction phase thus depends directly on the density profile of the CSM. Once the shock reaches the outer edge of the CSM shell and emerges, the shock luminosity drops rapidly, leading to a sharp decline in the light curve followed by a shock cooling tail.

Interior-breakout; Heavy CSM ($\xi \lesssim 1; \eta \gtrsim 1$): As with the previous scenario, shock breakout occurs before the forward shock has reached the CSM edge (see [49, 132]). Given the large CSM mass, the shock velocity is significantly decelerated as it sweeps up the CSM, such that the breakout condition $\tau_{sh} \sim c/v_{sh}$ is reached within the CSM, resulting in a more gradual rise to a breakout peak. Following a phase of continued interaction, shock emergence leads to a modest drop in luminosity as the light curve transitions to shock cooling emission.

3.4 Analytic Scalings

Numerous previous works have considered analytical models and scaling relations for interaction light curves (see e.g. [113, 131, 132, 135, 138, 144, 145]). These various results often contradict each other, usually due to different assumptions made in the derivation which renders particular results valid only in specific regions of parameter space. Here we present scaling relations for the light curve luminosity and duration, clarifying the regimes of applicability within the (ξ, η) parameter space. §3.5 validates these relations with numerical radiation-hydrodynamics simulations. Equations that correspond to quantities that appear in Fig. 3.2 are boxed for clarity. Correction factors for the scaling relations, calibrated to the numerical simulations, are provided in Appendix B.1.

Consider a shell of shocked material at radius r and of thickness Δr. After a shock has passed through the shell, the post-shock thermal energy is roughly

$$E_{sh} = 4\pi r^2 \Delta r \rho_s \frac{v_{sh}^2}{2} \tag{3.11}$$

Initially the shock velocity will be of order the ejecta velocity scale, $v_{ej} = (2E_{sn}/M_{ej})^{1/2}$. However, as the shock sweeps up material in the CSM, it is decelerated. From Eq. 3.3, by assuming the shock radius evolves as a power-law $r_{sh} \propto t^{\lambda}$, we have that the shock velocity evolves as

$$v_{sh}(r_{sh}) \approx v_{ej} \eta^{-\alpha} \left(\frac{r_{sh}}{R_{csm}} \right)^{(\lambda-1)/\lambda}$$

where the factor of $\eta^{-\alpha}$ accounts for the slowing down of the shock, and $\eta = M_{csm}/M_{ej}$. A full derivation of v_{sh}, as well as the shock exponents α and λ, is provided in Appendix B.2.

If $\eta \gtrsim 1$, then the bulk of the ejecta kinetic energy is tapped by the interaction, and $\alpha = 1/2$ from energy conservation. On the other hand, if $\eta \ll 1$, then only a fraction of E_{sn}

will be thermalized. The amount of deceleration that occurs will therefore depend on the outer density profile of the ejecta in the $\eta < 1$ case, and so

$$\alpha = \begin{cases} 1/2, & (\eta \gtrsim 1) \\ 1/(n-3), & (\eta \ll 1) \end{cases} \tag{3.12}$$

where n is the power-law exponent of the outer ejecta, $\rho_{ej} \propto r^{-n}$ with $n \approx 7 - 10$ [146]. The mass ratio between the inner and outer ejecta is equal to $(3-\delta)/(n-3)$ [140]. For $\delta = 1$ and $n = 10$, the shock will transition between the inner and outer portions of the ejecta for $\eta \gtrsim 0.3$.

The time it takes for the shock to reach the outermost shell at $r = R_{csm}$, accounting for the shock deceleration, is the *shock emergence* timescale,

$$\boxed{t_{se} \approx \eta^{\alpha} t_0}, \tag{3.13}$$

where $t_0 = R_{csm}/v_{ej}$. Depending on the optical depth of the CSM and how fast the shock is moving, shock breakout may occur at a deeper shell than the one located at R_{csm}, and must be accounted for. In this case, the light curve begins rising at a time $t < t_{se}$. We now separate our analysis into these two breakout regimes.

Scenario 1: Shock Breakout at CSM Edge ($\xi \gg 1$):

In this regime, the CSM is sufficiently optically thick that the condition $\tau_{sh} \approx c/v_{sh}$ is not reached until the shock has traversed the entire CSM and begun accelerating down the steep outer edge. This scenario resembles stellar surface shock breakout in several ways [142, 147], and so we proceed along a similar analysis.

Breakout happens at a radius r_{bo}, where the photons contained in a shell of width Δr_{bo} escape. The post-shock energy in the shell is

$$\Delta E_{bo} \approx 4\pi r_{bo}^2 \Delta r_{bo} \left(\frac{1}{2}\rho_{bo} v_{bo}^2\right) \tag{3.14}$$

where v_{bo} and ρ_{bo} are the shock velocity and CSM density at the breakout location. At breakout, $t_{bo} \approx t_{se} \approx \eta^{\alpha} t_0$, radiation escapes from the shell on a timescale comparable to the dynamical timescale, $\Delta t_{bo} \sim \Delta r/v$, giving a luminosity of

$$L_{bo} \approx \frac{\Delta E_{bo}}{\Delta t_{bo}} \approx 2\pi r_{bo}^2 \rho_{bo} v_{bo}^3 \tag{3.15}$$

When the shock just reaches the CSM edge its velocity is $v \sim v_{ej}\eta^{-\alpha}$, where the factor $\eta^{-\alpha}$ accounts for interaction with the bulk of the CSM (see Appendix B.2). Once the shock passes R_{csm} it begins accelerating down the steeply dropping outer density profile, which we take to be a power law

$$\rho(r) \approx \rho_0 x^{-p} \tag{3.16}$$

where $x = r/R_{csm}$ and the exact value of p will not matter in the limit $p \gg 1$. We account for shock acceleration using Sakurai's law $v \propto \rho^{-\hat{\delta}}$, [148], where $\hat{\delta} \approx 0.2$ for a strong shock [113]. The shock velocity in the steep outer region is then

$$v_{sh} \approx v_{ej}\eta^{-\alpha}x^{p\hat{\delta}} \tag{3.17}$$

To find the point x_{bo} where the shock reaches optical depth $\tau \sim c/v_s$ we integrate the density profile

$$\tau = \int_x^\infty \rho(r)\kappa dr \approx \tau_0 x^{-p} \tag{3.18}$$

where $\tau_0 = \kappa M_{csm}/4\pi R_{csm}^2$ and we have assumed $p \gg 1$. Setting this τ equal to c/v_{sh} where v_{sh} is given by Eq. 3.17, we can solve for the radius where breakout occurs

$$x_{bo} = \left[\tau_0\beta_0\eta^{-\alpha}\right]^{1/p(1-\hat{\delta})} = \xi^{1/p(1-\hat{\delta})} \tag{3.19}$$

where $\beta_0 = v_{ej}/c$ and $\xi = \beta_0\tau_0\eta^{-\alpha}$. For $p \gg 1$ we have $x_{bo} \approx 1$, but it is important to use Eq. 3.19 to evaluate the breakout velocity, v_{bo} (from Eq. 3.17) and the breakout density (from Eq. 3.16). Using these in the expression for the breakout luminosity Eq. 3.15 and choosing $\hat{\delta} = 0.2$ gives

$$\boxed{L_{bo} \approx \eta^{-3\alpha}\xi^{-1/2}L_0} \tag{3.20}$$

where $L_0 = M_{csm}v_{ej}^3/R_{csm}$ is the characteristic luminosity scale defined in §3.3.

The duration of this breakout emission is $\Delta r_{bo}/v_{bo}$. Given that the optical depth through the breakout layer $\tau \approx \kappa\rho_{bo}\Delta r_{bo}$ is roughly equal to c/v_{bo}, we have $\Delta r_{bo} = c/\kappa\rho_{bo}v_{bo}$ so the timescale is [113]

$$\Delta t_{bo} \approx \frac{\Delta r_{bo}}{v_{bo}} \approx \frac{c}{\rho_{bo}\kappa v_{bo}^2} \approx \frac{R}{c}\frac{1}{\tau_0\beta_0^2}\eta^{2\alpha}x_{bo}^{p(1-2\hat{\delta})} \tag{3.21}$$

Plugging in x_{bo} from Eq. 3.19 and taking $\delta = 0.2$ gives

$$\boxed{\Delta t_{bo} \approx \eta^{\alpha}\xi^{-1/4}t_0} \tag{3.22}$$

Post-Breakout Cooling Emission:

Following shock breakout, energy deposited by the shock at earlier times will begin to diffuse out from deeper layers. The total energy deposited will be

$$\Delta E \approx \frac{1}{2}M_{csm}(v_{ej}\eta^{-\alpha})^2 \tag{3.23}$$

To derive scaling relations we treat the system in a one zone approximation [138, 149]. Assuming that the remnant expands on a ballistic trajectory after shock breakout with speed $v_{ej}\eta^{-\alpha}$, the radius increases in time as $r(t) \approx R_{csm} + v_{ej}\eta^{-\alpha}t$. We can consider two limits. When the diffusion time is much faster than the expansion time $t_e = R_{csm}/v_{ej}\eta^{-\alpha}$,

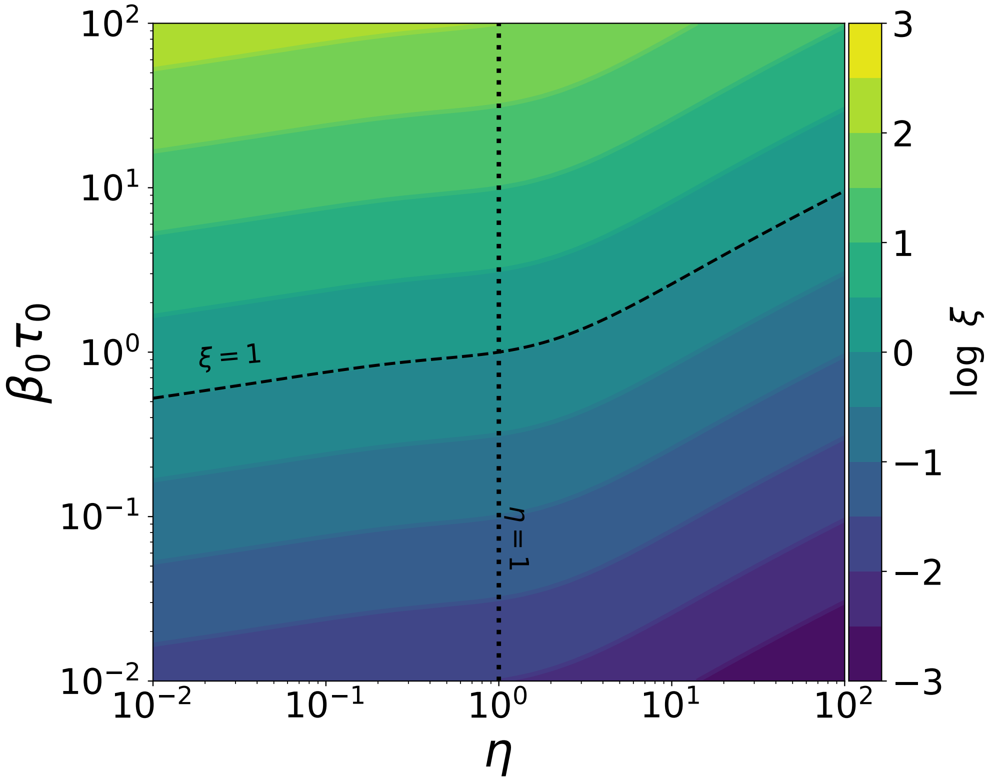

Figure 3.4: The breakout parameter ξ in the $\eta, \beta_0\tau_0$ space. Dashed and dotted lines denote $\xi = 1$ and $\eta = 1$, respectively, separating the four classes in Fig. 3.3.

the remnant can be considered quasi-static with fixed radius R_{csm}. The diffusion time is then $\Delta t = \tau_0 R_{csm}/c$, and the shock cooling luminosity $L_{sc} \sim \Delta E/\Delta t$ scales as

$$\boxed{L_{sc} \approx \eta^{-3\alpha}\xi^{-1}L_0} \tag{3.24}$$

In the other limit where the diffusion time is much longer than the expansion time, the remnant will expand by a significant factor before radiating and we approximate the radius as $r(t) \approx v_{ej}\eta^{-\alpha}t$. Radiation will escape when the remnant has expanded to the point that $\tau \sim c/v_{ej}\eta^{-\alpha}$ which occurs at a time

$$\boxed{t_{sc} \approx \eta^{\alpha}\xi^{1/2}t_0} \tag{3.25}$$

The shock deposited energy will be reduced due to expansion, such that the thermal energy remaining when radiation can diffuse out is

$$\Delta E \approx \frac{1}{2}M_{csm}(v_{ej}\eta^{-\alpha})^2\left(\frac{R_{csm}}{v_{ej}\eta^{-\alpha}t_{sc}}\right) \tag{3.26}$$

where the factor in parentheses accounts for the losses due to adiabatic expansion of a radiation dominated gas from an initial radius R_{csm} to a final one at $v_{ej}\eta^{-\alpha}t_{sc}$. The peak luminosity in this shock cooling phase will then scale as $L_{sc} \sim \Delta E/t_{sc}$ which results in a similar expression for the luminosity as Eq. 3.24.

Note that Eqs. 3.24 and 3.25 are identical to the expressions found in [138] for the case of $\alpha = 0.15$. A more detailed analysis of the shock cooling emission is presented in [149].

Scenario 2: Shock Breakout in CSM Interior ($\xi \lesssim 1$):

If the breakout shell is located within the CSM, then we need to account for the time-dependent evolution of the shock. In this case, the shock will propagate and be continuously decelerated within the CSM.

We assume the shock evolves in time as a power law, $r_{sh} \propto t^{\lambda}$, and so at $x_{bo} = r_{bo}/R < 1$

$$v_{bo} \approx v_{ej}\eta^{-\alpha}x_{bo}^{1-1/\lambda} \tag{3.27}$$

The shock exponent λ will depend on the CSM density profile for $\eta \gtrsim 1$ and, for $\eta \ll 1$, the ejecta density profile as well ([128, 141, 150]; see also Appendix B.2),

$$\lambda = \begin{cases} 2/(5-s) & (\eta \gtrsim 1) \\ (n-3)/(n-s) & (\eta \ll 1) \end{cases} \tag{3.28}$$

The breakout luminosity will be roughly equal to the shock luminosity at breakout (Eq. 3.10),

$$L_{bo} \approx L_0\eta^{-3\alpha}x_{bo}^{5-s-3/\lambda} \tag{3.29}$$

where we have assumed a power-law CSM density profile $\rho_{csm} \propto r^{-s}$.

In order to calculate the breakout time, we must integrate the CSM density profile to the breakout optical depth $\tau_{bo} = c/v_{bo}$ and set v_{bo} equal to Eq. 3.27, which results in a nonlinear equation that must be solved numerically (see Appendix B.2). Instead, we here approximate the breakout radius with the expression

$$x_{bo} \approx \left[\tau_0\beta_0\eta^{-\alpha}\right]^{\lambda k_0} = \xi^{\lambda k_0} \tag{3.30}$$

where $0 \leq k_0 \leq 1$. For $k_0 \approx 0$, $x_{bo} \approx 1$ i.e. breakout occurs at the CSM edge; this is the case discussed in the previous section. Interior breakout $x_{bo} < 1$ thus requires $k_0 > 0$ and $\xi < 1$. Note that $k_0 = 1$ gives $t_{bo} \approx \kappa M_{csm}/4\pi R_{csm}c$, which is simply the static diffusion timescale. This corresponds to the breakout time used in [131] and [132] up to a constant prefactor.

In general, k_0 will depend on the configuration of the ejecta and CSM parameters, which can be viewed as a weighted average of the shock emergence and static diffusion timescales. If radiation is able to immediately escape the CSM at the onset of interaction, then a choice of $k_0 = 1$ is more appropriate. On the other hand, if radiation escapes only once the shock nears the edge, then $k_0 \approx 0$. Here we adopt an intermediate value of $k_0 \approx 0.6$ based on fits to numerical simulations presented in §3.5, which is appropriate in the regime where the shock sweeps up a fraction of the CSM before being able to radiate ahead of the shock.

Using this approximation for x_{bo}, the breakout time is then given by

$$\boxed{t_{bo} \approx \eta^{\alpha} \xi^{k_0} t_0} \tag{3.31}$$

The breakout duration Δt_{bo} is proportional to the breakout time; comparison with numerical simulations of §3.5 show that $\Delta t_{bo} \approx t_{bo}/2$. Finally, to find the breakout luminosity, we use Eq.3.30 for x_{bo} to get

$$\boxed{L_{bo} \approx \eta^{-3\alpha} \xi^{\sigma_s} L_0} \tag{3.32}$$

where $\sigma_s = [(5-s)\,\lambda - 3]\,k_0$; the shock exponent λ is given by Eq. 3.28 ; and k_0 is the same as in Eq. 3.30. For the case of $n = 10$ and $s = 2$, this gives $\sigma_s \approx -0.23$ for $\eta < 1$ and $k_0 \approx 0.6$. For $\eta > 1$, $\sigma_s = -k_0$, independent of the density profiles. Note that Eqs. 3.31 and 3.32 are equivalent to that derived in [131] for the choice of $k_0 = 1$, $\lambda = 4/5$, and $\alpha = 1/4$ (corresponding to an outer ejecta density profile $\rho_{ej} \propto r^{-7}$ and CSM profile $\rho_{csm} \propto r^{-2}$), where they implicitly work in the $\eta < 1$ regime.

Post-Breakout Continued Interaction:

After shock breakout within the CSM, the light curve will continue to be powered by an additional supply of unshocked CSM, in addition to the reverse shock propagating inwards through the ejecta [131, 144, 145]. As the shock photons are able to efficiently radiate after breakout, the light curve tracks the instantaneous shock energy deposition rate Eq. 3.10. Using the power-law forms of the shock evolution Eq. 3.3 and assuming the forward shock dominates, the continued interaction luminosity becomes

$$\boxed{L_{ci}(t) \approx L_0 \eta^{-3\alpha} \left[\frac{t}{\eta^{\alpha} t_0}\right]^{(5-s)\lambda - 3}} \tag{3.33}$$

For $\eta \ll 1$ the exponents α and λ are identical to those provided in Eqs. 3.12 and 3.28, respectively, as these exponents hold for both energy and momentum-conserving shocks [128]. However, for $\eta \gtrsim 1$, the [151] exponents no longer hold, as the blastwave transitions to a momentum-conserving snowplow whose exponents are given by [141]

$$\alpha = 1,\ \lambda = \frac{1}{(4-s)} \quad (\eta > 1) \tag{3.34}$$

One interesting property of continued interaction emission is its direct dependence on the CSM density structure. In particular, if $s < 5 - 3/\lambda$ then the continued interaction phase will *rise* in time. For $\eta \ll 1$ and ejecta density $n \approx 10$, this requires a CSM shallower than

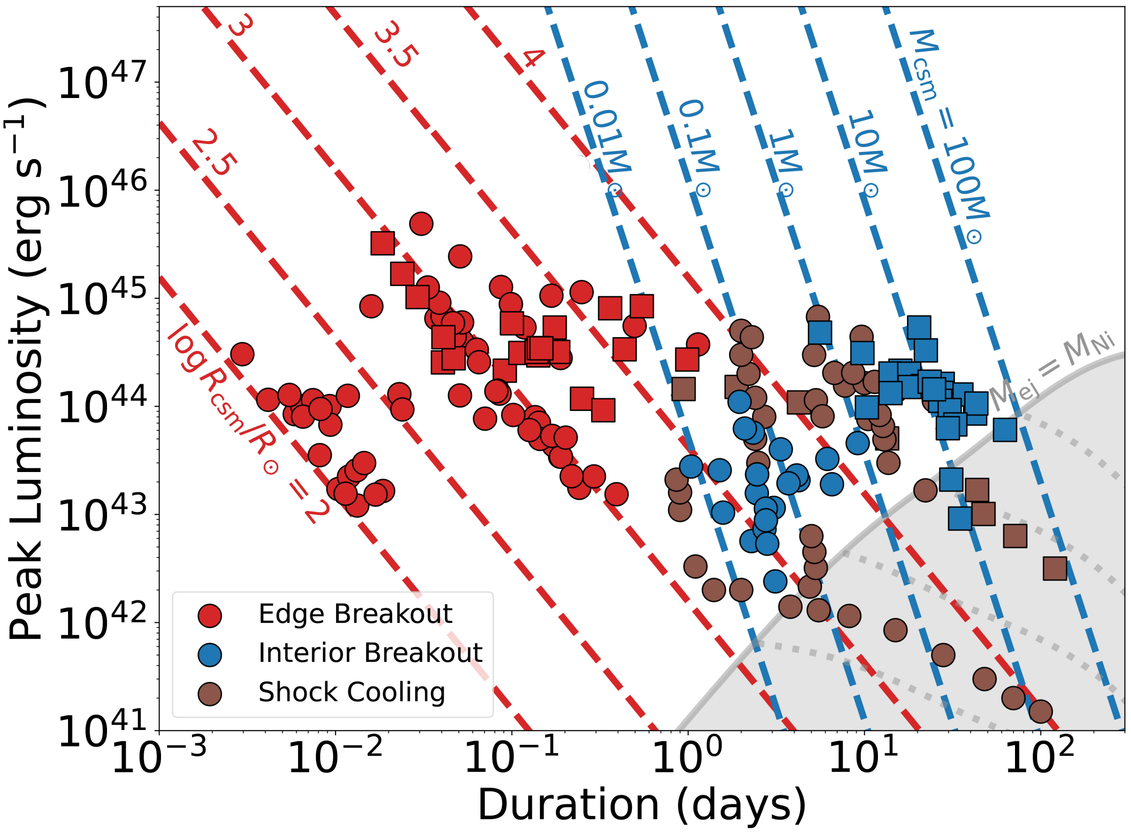

Figure 3.5: Numerical model results in terms of their breakout duration and luminosity for edge (red) and interior (blue) breakout events separated by light CSM (circles) and heavy CSM (squares). We also show the shock cooling emission for a subset of edge breakout events (brown points). Dashed blue and red lines denote M_{csm} and R_{csm} contours from Eqs. 3.52 and 3.54, respectively. The space of radioactive-powered transients is shown as a shaded grey region. Here, the models cover ejecta mass/energy in the range $0.1M_\odot \leq M_{ej} \leq 10M_\odot$ and $10^{49} \leq E_{sn} \leq 10^{52}$ ergs, respectively.

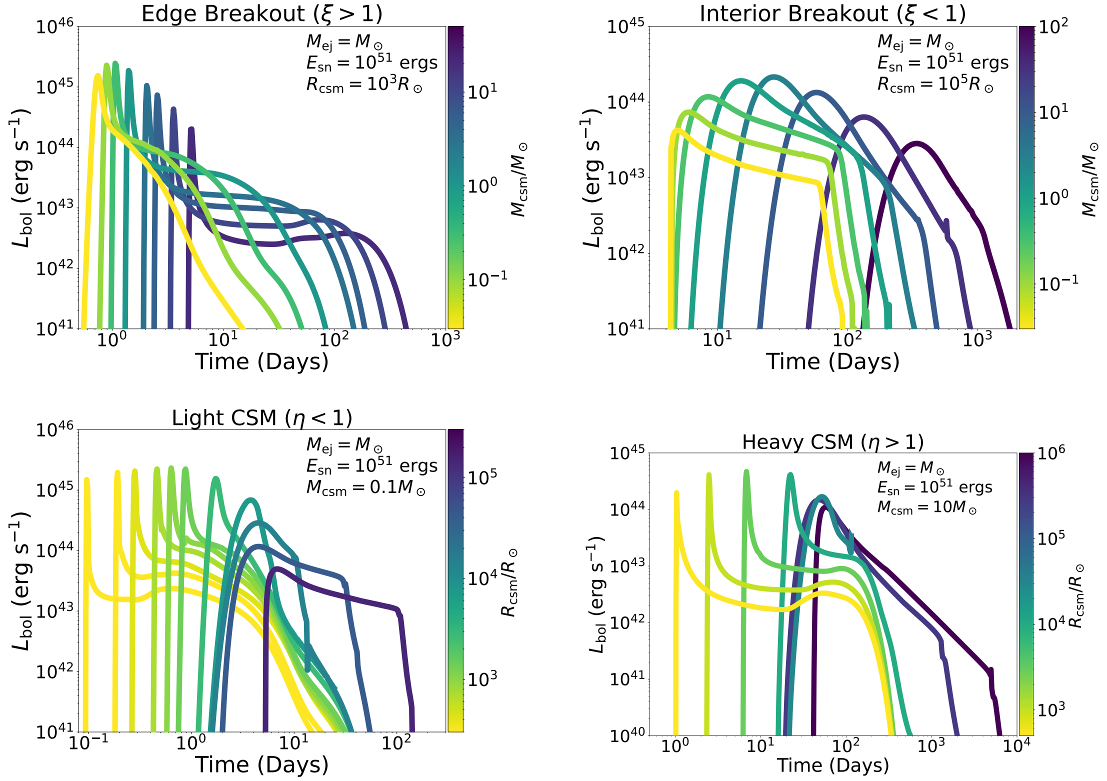

Figure 3.6: Numerical light curves of CSM interaction for different CSM parameters, assuming fixed ejecta properties $M_{ej} = M_\odot$ and $E_{sn} = 10^{51}$ ergs. *Top row*: varying M_{csm} for two fiducial choices of R_{csm} in the edge (*left*) and interior (*right*) regimes. *Bottom row*: varying R_{csm} for two fiducial choices of M_{csm} in the light (*left*) and heavy (*right*) CSM regimes.

$s < 5/4$.Note also that for a steady wind-like CSM profile $s = 2$, the light curve will decrease in time irrespective of the ejecta denisty profile.

The CSM density power-law index, s, does not significantly affect the time of shock breakout or shock emergence, but it does affect the overall luminosity (see Fig. 3.10). Breakout luminosity is more luminous for steeper CSM, while the luminosity at shock emergence $L_{ci}(t_{se})$ will be more luminous for shallower CSM profiles. Accounting for the density profile effects in the CSM, the characteristic shock luminosity scales with s as

$$L_{sh,0} = \frac{3-s}{4\pi}\left[1 - \left(\frac{R_*}{R_{csm}}\right)^{3-s}\right]^{-1} L_0 \qquad (3.35)$$

where R_* is the inner edge of the CSM and we have assumed $s < 3$.

Once the shock reaches the outer edge, the light curve will drop with only a residual amount of shock cooling emission, as nearly all of the shock energy had already been radiated

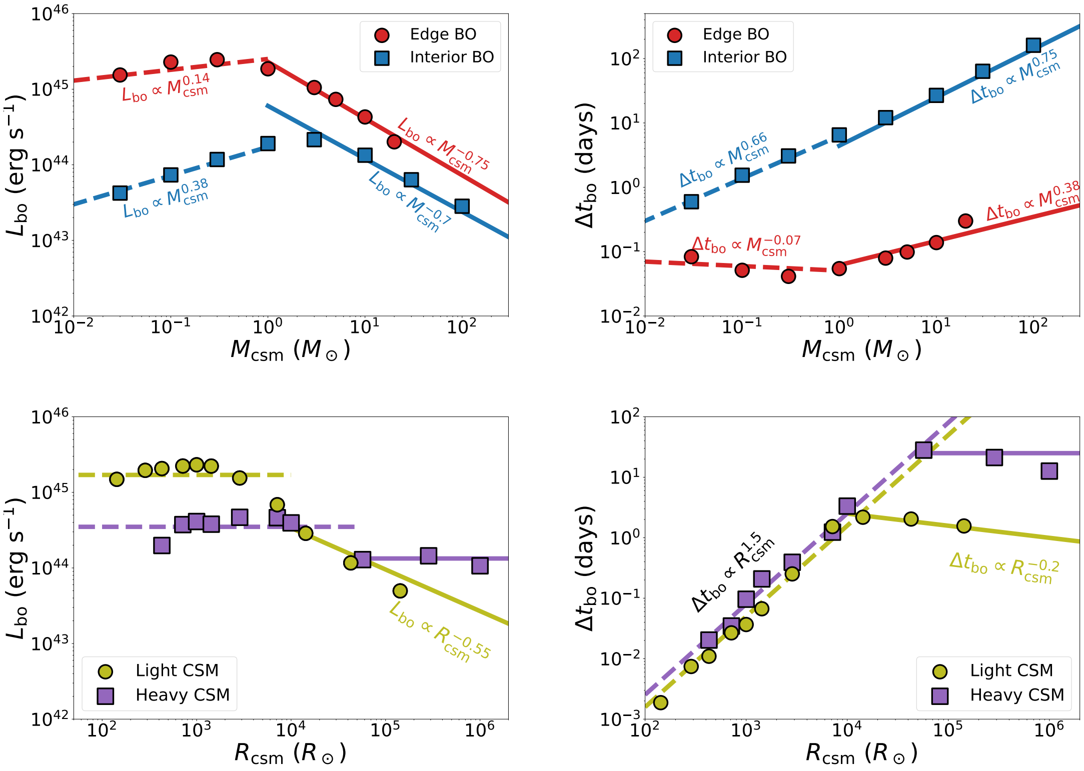

Figure 3.7: Correlation of the CSM properties with the breakout luminosity L_{bo} (*left column*) and duration Δt_{bo} (*right column*). Points correspond to model light curves in Fig. 3.6, while lines give the analytic scalings of §3.4 with specific formulae provided in Appendix A. *Top row*: dependence of L_{bo} and Δt_{bo} on M_{csm}, in the edge $\xi > 1$ *(red)* and interior $\xi < 1$ *(blue)* breakout regimes. The break in behavior around $M_{csm} = M_\odot$ corresponds to the transition from light ($\eta \ll 1$) to heavy ($\eta \gtrsim 1$) mass regimes. *Bottom row*: dependence of L_{bo} and Δt_{bo} on R_{csm}, in the light *(yellow)* and heavy *(purple)* CSM regimes. The break in the scaling behavior denotes the transition from edge to interior breakout.

away through continued interaction.

3.5 Numerical Simulations

We perform one-dimensional radiation hydrodynamics simulations of CSM interaction. We couple the finite-volume moving mesh method of [152] to a gray flux-limited diffusion solver based on [38] and [153].

We have implemented 1D spherically-symmetric radiation hydrodynamics in Sedona [75, 154], using the finite-volume moving-mesh method described in [152]. We modify the hydrodynamics to include radiation using a comoving-frame grey flux-limited diffusion treatment based on [153, 155] and [38]. We use an operator split approach where the hydrodynamics and radiation advection is solved explicitly with a second-order Runge Kutta timestepping with Courant condition $C_{CFL} = 0.1$; the nonlinear diffusion and matter-radiation coupling is solved implicitly using a Newton-Raphson method with relative error threshold of $\epsilon = 10^{-10}$. The resulting linear system for the radiation energy density is directly solved using Thomas' tridiagonal matrix algorithm [156]. We use an absorbing outer boundary condition for the radiation.

We use a uniform gray opacity κ for the ejecta and CSM that is constant in time, with a fiducial value of solar electron scattering, $\kappa = 0.34$ cm^2 g^{-1}. We take a fraction of the scattering opacity to be absorptive, i.e. $\kappa_{abs} = \epsilon_{abs}\kappa$, where $\epsilon_{abs} = 10^{-3}$ [157]. Note that we ignore recombination, which may be important in certain cases during lower-temperature shock interaction (see e.g. [122]).

We initially evolve the simulations with a fixed Eulerian grid of 1024 and 2048 cells for the ejecta and CSM, respectively. Note that this resolution may be insufficient to completely resolve the shock structure for cases where the shock radiation efficiently escapes. However, completely resolving the shock structure is not necessary as we are concerned primarily with the bulk conversion of kinetic energy into escaping radiation. We have confirmed with additional simulations that increasing the resolution to resolve the shock structure does not impact the resulting light curve.

Once the shock nears the breakout layer, we turn on Lagrangian mesh motion to follow the shock breakout and subsequent expansion, and evolve the system out to late times to capture shock cooling. We extract bolometric light curves by taking the comoving radiative flux at the outermost boundary of the domain.

Problem Setup

We assume a spherically symmetric ejecta of mass M_{ej} and energy E_{sn} with initial density profile given by a broken power law [140, 146]

$$\rho_{ej}(r) = f_\rho \frac{M_{ej}}{r_t^3} \left[\frac{r}{r_t}\right]^{-(\delta,n)} \tag{3.36}$$

where the inner and outer density profiles are δ and n, respectively. The normalization factor is given by

$$f_\rho = \frac{1}{4\pi}\frac{(n-3)(3-\delta)}{(n-\delta)} \tag{3.37}$$

The transition radius of the broken power law is given by

$$r_t = v_t t_0 \tag{3.38}$$

where

$$v_t = \sqrt{\frac{f_v E_{sn}}{M_{ej}}} \tag{3.39}$$

and

$$f_v = \frac{2(5-\delta)(n-5)}{(n-3)(3-\delta)} \tag{3.40}$$

We choose an initial time t_0 such that $r_t \ll R_{csm}$, the outer CSM radius, with a fiducial value of $t_0 = 10^3$ seconds.

The ejecta velocity is assumed to be homologous,

$$v_{ej}(r) = v_t \left[\frac{r}{r_t}\right] \tag{3.41}$$

Finally, we initialize the ejecta to be initially cold, with a uniform temperature $T_{ej} = 10^2$ K.

CSM Setup

We assume a shell of CSM of mass M_{csm} and radius R_{csm}. The CSM density profile is described by a power-law

$$\rho_{csm}(r) = f_{csm}\frac{M_{csm}}{R_{csm}^3}\left[\frac{r}{R_{csm}}\right]^{-s} \qquad (R_* < r < R_{csm}) \tag{3.42}$$

where

$$f_{csm} = \frac{(3-s)}{4\pi}\left[1-\left(\frac{R_*}{R_{csm}}\right)^{3-s}\right]^{-1} \tag{3.43}$$

Here, R_* is the inner radius of the CSM, and set to a fixed value of $10^{-2}R_{csm}$ (i.e. $R_* \ll R_{csm}$).

At the outer CSM edge $r = R_{csm}$, we stitch on a steep cutoff layer with density profile

$$\rho(r) = f_{csm}\frac{M_{csm}}{R_{csm}^3}\left[\frac{r}{R_{csm}}\right]^{-p} \qquad (R_{csm} < r < (1+f_{bo})R_{csm}) \tag{3.44}$$

where $p \gg 1$, and $(1+f_{bo})R_{csm}$ is the outer radius of the breakout layer. We adopt a fiducial width for the breakout layer of $f_{bo} = 1/3$, and a density profile $p = 30$. The exact numerical choice of p does not affect the solution (see §3.4), as long as $p \gg 1$. Finally, the CSM is initially stationary (i.e. $v = 0$) and cold, $T_{csm} = 10^2$ K.

A full description of the numerical method is given in Appendix (?). We adopt the same assumptions and parameters described in §3.4. Namely, the ejecta is described by a mass M_{ej} and kinetic energy E_{sn} undergoing homologous expansion, whose density structure is given by the broken power-law form of [140]. We assume fiducial values of $\delta = 1$ and $n = 10$ for the inner and outer ejecta density profiles, respectively.

The CSM extends from an inner edge R_* to an outer radius R_{csm} with mass M_{csm}, with a power-law density profile s. We adopt a fiducial wind-like $s = 2$ for most runs, unless otherwise stated, and take $R_* = 10^{-2}R_{csm}$ (i.e. $R_* \ll R_{csm}$). Additionally, we attach a steep cutoff layer at the outer edge of the CSM described by a power-law r^{-p}, which we take $p = 30$ as fiducial. As discussed in Sec. §3.4, the exact numerical choice does not matter so long as $p \gg 1$. The CSM and ejecta are both initially cold, with $T_0 = 10^2$ K, and described by the same uniform gray opacity $\kappa = 0.34$ cm^2 g^{-1}. We use a thermalization fraction of $\epsilon = 10^{-3}$. Finally, we initialize the setup at a time $t = 10^3$ seconds after explosion. For a more detailed description of the problem setup and relevant equations, see Appendix **??**.

We consider a range of ejecta and CSM properties to cover the diversity of light curves expected from the different regimes outlined in §3.3. Specifically, we use ejecta masses and energies between $0.1M_\odot \leq M_{ej} \leq 100M_\odot$ and $10^{49} \leq E_{sn} \leq 10^{52}$ ergs. For the CSM, we consider mass and radii in the range $0.01M_\odot \leq M_{csm} \leq 100M_\odot$ and $10^2R_\odot \leq R_{csm} \leq 10^6R_\odot$, respectively. In total, we ran approximately 100 different ejecta-CSM interaction scenarios within the numerical parameter space.

For each run, we measure the breakout peak luminosity L_{bo} and time t_{bo}, as well as the duration Δt_{bo} which we take to be the time to rise to peak by one order of magnitude. For the edge breakout events which feature two light curve peaks, we measure the secondary peak to determine L_{sc} and Δt_{sc}. We also fit a power-law to the continued interaction tail of interior breakout events to compare with Eq.3.33.

We use the grid to also construct numerical scalings for each phase of each interaction type. In particular, we adopt fitting formulae for luminosity and time of the i-th phase as

$$L_i = a_i\eta^{-3\alpha_i}\xi^{k_i}L_0 \tag{3.45}$$

$$t_i = b_i\eta^{\alpha_i}\xi^{c_i}t_0 \tag{3.46}$$

where (α_i, k_i, c_i) are fitting exponents, and (a_i, b_i) are normalization factors to account for numerical differences compared to the analytic scalings. The results of the numerical fits for the different phases and classes, as well as correction factors for the analytic scalings of §3.4, are given in Appendix B.1.

Overall Properties of Model Grid

In Fig. 3.5 we show the duration-luminosity phase space of the model grid breakout properties. We additionally show the secondary shock-cooling peak for the subset of edge breakout events that have a clear double-peaked light curve. The resulting light curves will have timescales ranging from very rapid ($\sim$ minutes) to long-lasting ($\sim$ months); and peak luminosities spanning the sub-luminous 10^{41} erg s^{-1} all the way to highly superluminous $\sim 10^{45}$ erg s^{-1} events. The peak luminosities correlate inversely with duration, with a spread in the trend due to the diversity of CSM and ejecta parameters. Note that more extreme events in terms of peak properties may be possible for an expanded parameter space broader than the range considered here.

The flashes from edge breakout events ($\xi \gg 1$) tend to occupy the high-luminosity and short-duration portion of phase space. For CSM radii of $R_{csm} \sim 10^2 - 10^3 R_{\odot}$, the edge breakout flash resembles expected stellar surface shock breakout luminosities and durations, lasting on the order of a few minutes to hours. Larger CSM radii tend to produce longer-lasting edge breakouts, as seen in Fig. 3.5. Typical edge breakout luminosities range from a few times 10^{43} erg s^{-1} on the lower end, reaching up to highly superluminous events $\gtrsim 10^{45}$ erg s^{-1} for the most energetic interactions.

The flashes from interior breakouts ($\xi \lesssim 1$) bifurcate into different regions of phase space depending on the value of $\eta = M_{CSM}/M_{ej}$. Heavy CSMs ($\eta \gtrsim 1$) occupy the brighter and longer-duration of the interior breakouts, spanning days to months in duration and peaks of $\sim 10^{44}$ erg s^{-1}. Interior breakouts from light CSMs ($\eta \ll 1$) are comparatively shorter (days to weeks) and dimmer, with a wider range in peak luminosities from $\sim 10^{42}$ to 10^{44} erg s^{-1}.

Compared to shock breakout, the post-breakout shock cooling emission generally produces lower peak luminosities and longer durations, comparable to those observed in typical radioactive nickel-powered transients. If the breakout flash from these events is missed due to its rapid timescale, it may in practice be hard to distinguish between interaction and radioactive decay light curves using photometry alone.

Dependence on Circumstellar Mass

To numerically examine the effect of M_{csm} on the light curve, we hold constant the ejecta properties ($M_{ej} = M_{\odot}$, $E_{sn} = 10^{51}$ erg) and vary the CSM mass in the range $10^{-2} M_{\odot} < M_{csm} < 10^2 M_{\odot}$. This covers the CSM regime from light ($\eta \ll 1$) to heavy ($\eta \gtrsim 1$). Additionally, we adopt two fiducial values of $R_{csm} = 10^3 R_{\odot}$ and $10^5 R_{\odot}$, which result in an edge and interior breakout, respectively.

The top row of Fig. 3.6 shows the resulting light curves as a function of M_{csm} while Figure 3.7 plots the dependence of L_{peak} and Δt on M_{csm}. The dependencies are non-monotonic and – as expected from the analytic relations of §3.3 – scale differently in the regimes of edge breakout ($\xi > 1$) and interior breakout ($\xi < 1$) and for $\eta \ll 1$ and $\eta \gtrsim 1$.

In Fig. 3.7, the breakout scalings of L_{bo} and Δt_{bo} with R_{csm} and M_{csm} are shown compared to the analytic scalings derived in Sec. 3.4. Overall, the analytics agree well with the numerical results, correctly predicting different scalings depending on a light/heavy and edge/interior breakout scenario. In particular, the turnover in the dependence of L_{bo} on M_{csm} around $\eta \sim 1$ is reproduced for both edge and interior breakouts. The numerical results show a turnover in the edge breakout case at a lower CSM mass than the analytics predict, as the shock reaches the shallow inner portion of the ejecta and the self-similar scalings break down. Specifically, the ratio of outer to inner ejecta mass is equal to $(3-\delta)/(n-3) \approx 0.3$ for $\delta = 1$ and $n = 10$ [140], and so for $\eta \gtrsim 0.3$ the shock behavior changes. Note that the exact behavior of the transition in the $\eta \approx 1$ range is not well-sampled in our numerical simulations, which limits the applicability of our analysis for interaction events in this parameter space.

Consider first the case of light CSM ($\eta \ll 1$). If we are in the regime of edge breakout ($\xi \gtrsim 1$) the luminosity of the light curve peak depends only weakly on M_{csm}, since breakout happens at effectively the same radius $r_{bo} \sim R_{csm}$ and velocity $v_{bo} \sim v_{ej}$ (since there is not much deceleration for $\eta \ll 1$). If breakout occurs in the CSM interior ($\xi \lesssim 1$), the light curve is slightly brighter for higher values of M_{csm}, since the breakout location $\tau \sim c/v_{bo}$ is reached later during the shock evolution (i.e. at a larger breakout radius r_{bo}).

The breakout duration also scales differently depending on whether we are in the interior or edge breakout regime. For interior breakouts ($\xi \lesssim 1$), the duration is set primarily by shock crossing and radiative diffusion, giving a longer duration for larger M_{csm}. However, for edge breakouts ($\xi \gtrsim 1$) from light CSM, the duration actually *decreases* with increasing M_{csm}. This can be understood by examining Eq. 3.22, where the edge breakout duration depends on the shock crossing of the breakout layer. For a light CSM, the width of the breakout layer decreases with increasing M_{csm} while the ejecta is not much decelerated $v_{bo} \sim v_{ej}$, and so the shock crossing time $\delta r_{bo}/v_{bo}$ (i.e. breakout duration) decreases.

As we continue increasing M_{csm}, we enter the heavy CSM regime, $\eta > 1$. For this regime, the entirety of the ejecta is decelerated, and the maximum shock energy of $\sim E_{sn}$ is reached at $\eta = 1$. Any additional CSM mass beyond M_{ej} only acts to decrease the shock velocity $\sim v_{ej}\eta^{-\alpha}$, resulting in a dimmer light curve. As a result, the heavy CSM $\eta \gtrsim 1$ breakout luminosity *decreases* with M_{csm}, with similar scalings for both edge and interior breakouts, as shown in Fig. 3.7. Furthermore, the breakout duration increases with M_{csm}, with a steeper dependence for interior breakouts.

In addition to the breakout properties, M_{csm} will also impact the the post-breakout emission, i.e. shock cooling and continued interaction for edge and interior breakouts, respectively. For the edge breakout case in Fig. 3.6, the shock cooling emission becomes dimmer and longer-lasting with M_{csm}. A larger M_{csm} results in a longer diffusion timescale, which keeps the radiation trapped for longer and exacerbates adiabatic losses in the cooling phase. This effect is most pronounced for the heavy CSM, which have a longer-lasting "plateau" of shock cooling emission, seen in the upper left panel of Fig. 3.6. For light CSM, the shock cooling appears more as a tail immediately following the breakout emission, while for heavy CSMs the shock cooling is more distinctly separated from breakout, appearing as a secondary feature in the light curve well after the breakout has subsided.

The post-breakout emission in interior breakout events is produced through continued interaction, which powers a tail in the light curve before a sharp drop in luminosity at shock

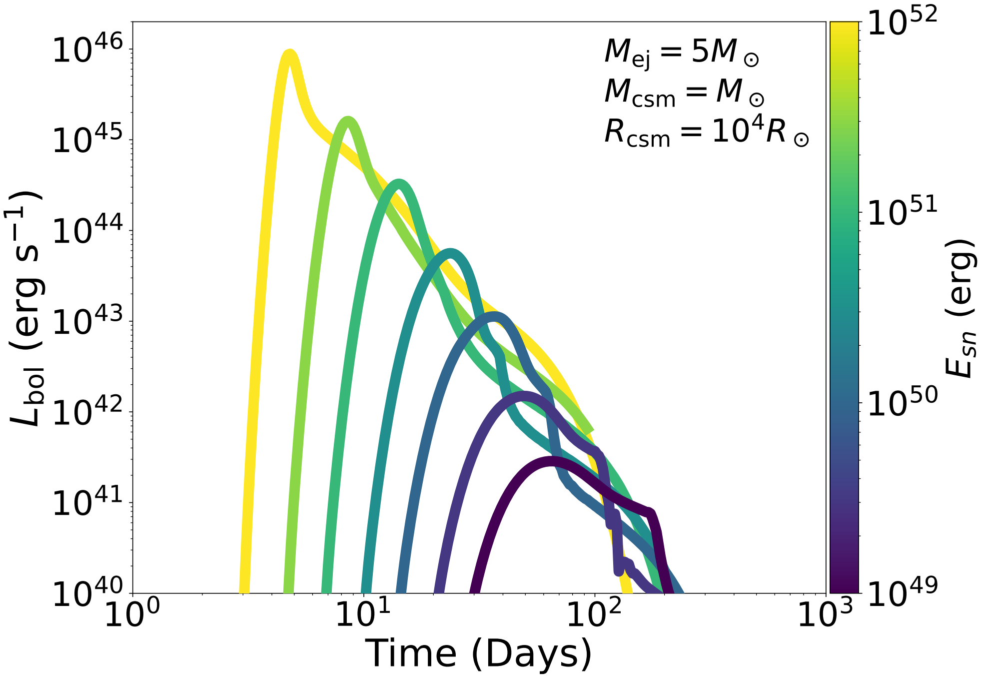

Figure 3.8: Numerical light curves for fixed CSM properties and ejecta mass $M_{ej} = 5M_\odot$, varying the kinetic energy E_{sn}.

emergence. The continued interaction luminosity is more luminous with increasing M_{csm} in the light CSM regime $\eta \ll 1$, since v_{sh} is only minimally decelerated while the CSM density increases with M_{csm}. For $\eta \gtrsim 1$, due to the significant shock deceleration, the continued interaction luminosity instead decreases with M_{csm}. This also leads to a much later shock emergence time once we reach heavy CSM masses.

The continued interaction tail reaches a maximum luminosity for masses $\eta = 1$, whereby any additional $M_{csm} > M_{ej}$ instead results in a less luminous light curve. Furthermore, the light curve slope becomes steeper as we enter the heavy CSM $\eta \gtrsim 1$ regime, as the shock begins to behave more as a snowplow blastwave whose exponents are given by Eq. 3.34 instead of the $\eta \ll 1$ exponents in Eq. 3.28.

Dependence on Circumstellar Radius

Here we use the same ejecta properties as in the previous section ($M_{ej} = M_\odot$ and $E_{sn} = 10^{51}$ ergs), but instead vary R_{csm} while keeping M_{csm} fixed. We consider CSM radii in the range $10^2 R_\odot < R_{csm} < 10^6 R_\odot$ for two fiducial masses corresponding to a light $M_{csm} = 0.1M_\odot$ and

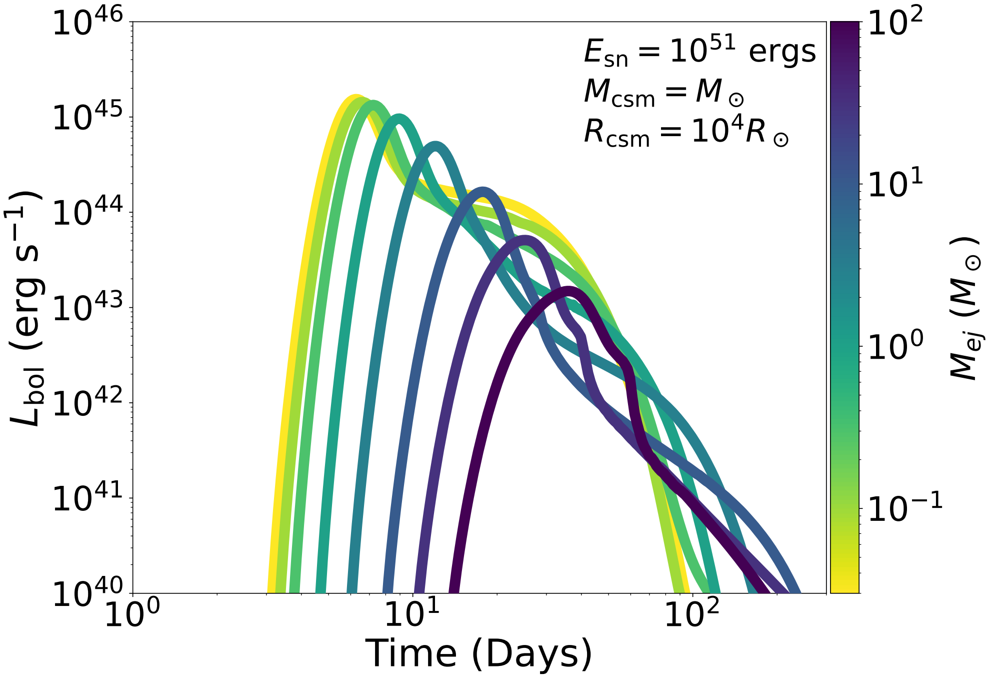

Figure 3.9: Same as Fig. 3.8, but varying the ejecta mass with a fixed $E_{sn} = 10^{51}$ ergs.

heavy $M_{csm} = 10 M_\odot$ CSM.

As the models in the bottom row of Fig. 3.6 have fixed M_{csm} and ejecta properties, the criteria $\xi > 1$ (i.e. breakout occuring at the CSM edge) is reached for $R_{csm} \lesssim 10^4 R_\odot$. The light curves display a qualitative change in behavior in the two regimes of edge and interior breakout, transitioning from a double-peaked breakout with shock cooling for $R_{csm} \lesssim 10^4 R_\odot$ ($\xi \gtrsim 1$) to a single peak with a continued interaction tail for $R_{csm} \gtrsim 10^4 R_\odot$ ($\xi \lesssim 1$).

In Fig. 3.7 the analytic scalings of L_{bo} and Δt_{bo} on R_{csm} are compared with the numerical results. In the limit of an edge or interior breakout, the analytic scalings match reasonably well with the numerical simulations. In the intermediate regime around $10^4 R_\odot$, the scalings are less robust, given the assumption of a fixed k_0 as introduced in §3.4 for interior breakouts. Note also that the analytics presented predict an independence of L_{bo} on R_{csm} for the edge breakout scenario. The numerical simulations qualitatively agree with this prediction, albeit with a slight positive correlation with R_{csm}.

In general, larger CSM radii produce later and longer-lasting light curves, as the shock takes more time to reach the outer edge of the CSM. Furthermore, with increasing R_{csm} and fixed M_{csm}, we are spreading the mass out over a larger volume, which decreases τ_{sh} during interaction. Eventually, R_{csm} becomes large enough that we enter the interior breakout regime $\xi \lesssim 1$, whose light curve is marked by continued interaction rather than a shock cooling tail. This behavior holds for both a light and heavy CSM, with the primary difference of the two CSM mass regimes being the relative prominence of the post-breakout emission.

For small CSM radii such that we are in the edge breakout regime, increasing R_{csm} results in a longer-lasting dark phase, brighter breakout peaks, and a slower breakout rise. This behavior holds for both light $\eta \ll 1$ and heavy $\eta \gtrsim 1$ CSM masses which also have similar scalings, shown in Figs. 3.7. The post-breakout shock cooling luminosity increases strongly as $L_{sc} \propto R_{csm}$, although the cooling timescale appears nearly independent of the radius.

As we continue to increase the CSM radius we eventually enter the interior breakout regime $\xi \lesssim 1$. In this case, the breakout duration and luminosity turn over and begin decreasing slightly with increasing R_{csm}. This break is more pronounced for light CSM masses, shown in the bottom-left panel of Fig. 3.6. Furthermore, the post-breakout emission changes from shock cooling to continued interaction at these larger radii. While the shock cooling luminosity increases with R_{csm}, the continued interaction tail becomes less luminous for larger R_{csm}; the decrease is more pronounced for light CSM masses. Finally, while the shock cooling duration is independent of R_{csm}, the continued interaction tail scales directly with the shock emergence timescale $t_{se} \propto R_{csm}$.

Dependence on Ejecta Mass and Energy

Next, we consider the case of a fixed CSM, $M_{csm} = M_\odot$ and $R_{csm} = 10^{14}$ cm (i.e. fixed $\tau_0 \sim 10^3$), while holding $M_{ej} = 5M_\odot$ constant ($\eta = 0.2$). We vary the ejecta kinetic energy across the range $10^{49} \leq E_{sn} \leq 10^{52}$ ergs, which is equivalent to a characteristic velocities between $10^{-3} \leq \beta_0 \leq 0.05$.

We show the resulting light curves for the different E_{sn} in Fig. 3.8. We find higher-energy explosions produce earlier, faster, and brighter light curves, with $L_{bo} \propto E_{sn}^{5/2}$; this is due to higher kinetic energies producing faster and stronger shocks. The scale of E_{sn} does not just affect the characteristic timescale and luminosity of the light curve; it can also affect the type of interaction. As we go to lower energies in Fig. 3.8, eventually we enter the $\xi \lesssim 1$ regime and the shock breaks out within the CSM rather than at the edge. In this case, the post-breakout emission will change from a shock cooling to a continued interaction phase.

We also examine the effect of a fixed ejecta kinetic energy $E_{sn} = 10^{51}$ ergs with the same CSM properties as above, but vary the ejecta mass across $0.03M_\odot \leq M_{ej} \leq 100M_\odot$. We show the resulting light curves of the M_{ej} range in Fig. 3.9. As we increase $M_{ej} > M_\odot$, which corresponds to the $\eta > 1$ case, the light curves become longer and dimmer since $v_{sh} \approx v_{ej} \propto M_{ej}^{-1/2}$ for fixed E_{sn}. Furthermore, as the amount of energy tapped in the $\eta < 1$ case is $\sim M_{csm} v_{sh}^2$, we are also *fractionally* converting less kinetic energy as we increase M_{ej}. For large enough M_{ej}, the shock velocity drops low enough that the post-breakout emission transitions from shock cooling to continued interaction, similar to the case of the lower-energy explosions.

On the other hand, as we decrease M_{ej} below $M_\odot$, we enter the $\eta \gtrsim 1$ regime where the light curve becomes nearly independent of M_{ej}. This corresponds to the limit of a point

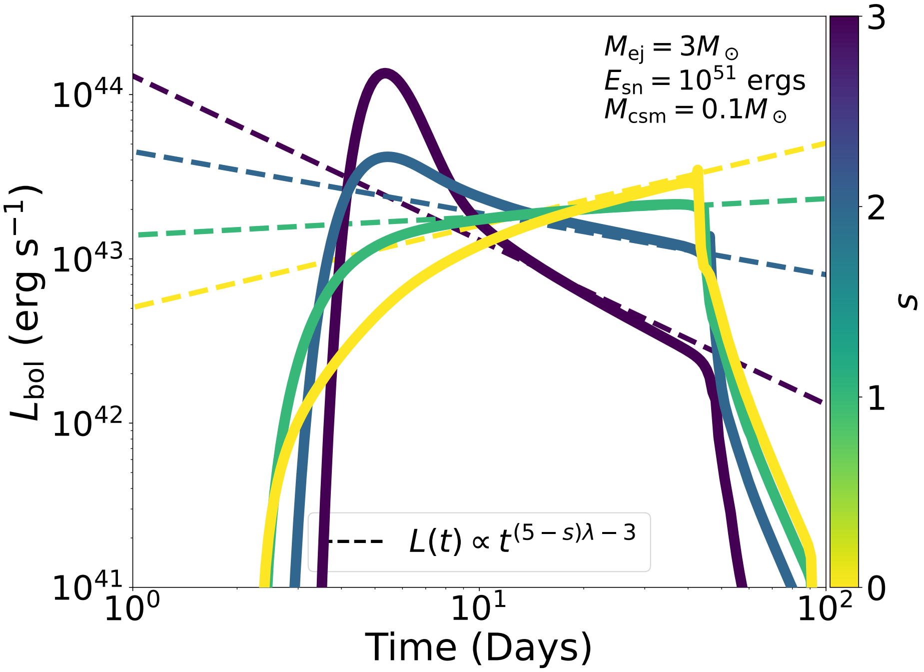

Figure 3.10: Numerical light curves for a light interior breakout ($\eta \ll 1$, $\xi < 1$), with different assumed CSM density profile $\rho \propto r^{-s}$. Dashed lines correspond to the power-law expression for the continued interaction phase Eq. 3.33.

explosion inside the CSM, and the only ejecta parameter that sets the light curve behavior will be E_{sn}. Furthermore, the exact density structure of the ejecta is irrelevant, unlike the $\eta \ll 1$ case where the continued interaction tail is set directly by the outer density profile. In practice, this can make constraining the ejecta mass challenging in this limit due to the M_{ej} degeneracy.

Radiated Efficiency

The efficiency with which interaction converts kinetic energy into observable radiation is an important consideration when physically interpreting transients. In particular, for interaction to explain long-lasting luminous supernovae with integrated radiated energy reaching 10^{51} erg likely requires efficiencies not far below unity. Here we quantify the achievable efficiency throughout the parameter space.

We can determine the radiated efficiency of our numerical models by integrating the light

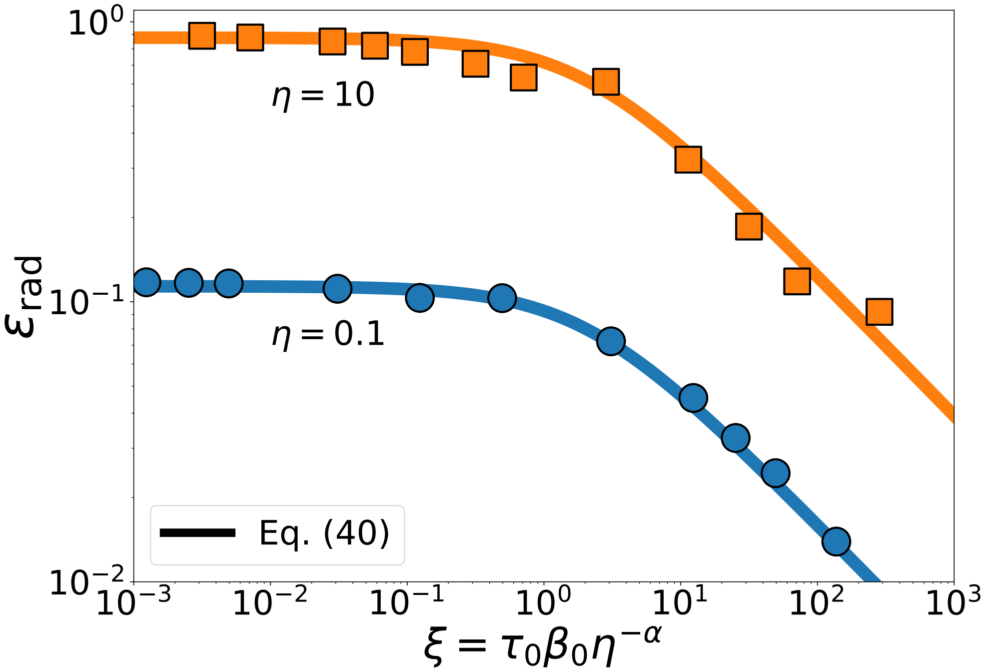

Figure 3.11: Radiated efficiency ε_{rad} as a function of the breakout parameter ξ. Points correspond to numerical simulations for the case of $\eta = 0.1$ (blue circles) and $\eta = 10$ (orange squares). Solid lines give the analytic expression in Eq. 3.48 for each choice of η.

curve and comparing it to the initial ejecta kinetic energy,

$$\varepsilon_{rad} = \frac{1}{E_{sn}} \int L(t)\, dt \tag{3.47}$$

For $\eta \ll 1$, from energy conservation, the interaction will convert a fraction $E_{sh} \sim E_{sn}\left(v_{sh}/v_{ej}\right)^{5-n}$ of the amount of kinetic energy contained in the steep outermost layer of the ejecta into internal gas/radiation energy, where $v_{sh} \sim v_{ej}\eta^{-\alpha}$ and $\alpha = 1/(n-3)$ (see Appendix B.2 for a full derivation). Thus, the radiated efficiency for $\eta \ll 1$, assuming no adiabatic losses and efficient conversion of shock energy into radiation, is roughly $\varepsilon_{rad} \sim \eta^{a_0}$, where $a_0 = (n-5)/(n-3)$. For $\eta \gtrsim 1$, this reaches a potential maximum of unity, as the shock will tap into the entirety of the ejecta kinetic energy.

While the radiation remains trapped in the shocked region, it will suffer adiabatic losses that acts to degrade the efficiency by converting the radiation back into kinetic energy. For $\xi < 1$, adiabatic losses are minimal as the shock radiation is able to efficiently escape. For $\xi > 1$, the radiation will be adiabatically degraded by a factor proportional to $(t_d/t_0) \sim \left(\kappa M_{csm} v/R_{csm}^2 c\right)^{1/2} \sim \xi^{-1/2}$, where $t_d = \sqrt{\kappa M_{csm}/v_{ej} c}$ and $t_0 = R_{csm}/v_{ej}$.

We can interpolate between the regimes of light/heavy CSM and the effect of adiabatic losses with the analytic expression

$$\varepsilon_{rad} \approx \frac{1}{(1+2/\eta)^{a_0}} \left(1+\frac{\xi}{2}\right)^{-1/2} \tag{3.48}$$

where $a_0 = (n-5)/(n-3) = 5/7$ for $n = 10$. In Fig. 3.11 we show the efficiency compared to Eq. 3.48 for a series of light ($\eta = 0.1$) and heavy ($\eta = 10$) CSM interactions, where we vary R_{csm} to produce a range of breakout parameters ξ. The numerical simulations agree well with Eq. (3.48) across the different interaciton regimes. We see that the efficiency reaches a maximum in the regime of $\xi < 1$, i.e the interior breakout regime. In this case, the photons from the breakout and continued interaction tail are able to escape before incurring much adiabatic losses, and hence are the more efficient class of interaction. The *most* efficient case corresponds to $\eta = 1$ and $\xi < 1$, where we tap almost all of the kinetic energy and quickly radiate away the shock photons.

In contrast, once we enter the regime of $\xi > 1$, the photons can no longer quickly escape, coming out during the shock cooling phase after being adiabatically degraded. This corresponds to the edge breakout case, and $\varepsilon_{rad} \propto \xi^{-1/2}$. Thus, although edge breakouts produce some of the more luminous transients expected from interaction, they are also reduced in their net radiative throughput due to the large optical depths of the CSM. In Fig. 3.12 we show the radiated efficiency for the case of interaction of a solar mass ejecta with kinetic energy $E_{sn} = 10^{51}$ ergs, in terms of the M_{csm}-R_{csm} space. We see that massive, extended CSMs are the most efficient interactions, while a compact low-mass CSM only converts a small fraction of E_{sn}.

There is one other effect that will reduce the radiated efficiency of the interaction, which occurs when the shock is unable to cool efficiently, as described in §3.3. Specifically, if the CSM is so optically thin $\tau_0 \lesssim 0.3 v_9$, then we enter the adiabatic shock regime, and few photons are produced. Thus, although low CSM optical depths improve efficiency by reducing adiabatic losses, it cannot be too low such that the shock is unable to cool. At the $\tau_0 \lesssim 0.3 v_9$ limit, we therefore expect the efficiency to turn over again.

3.6 Discussion

When invoking circumstellar interaction to interpret an observed transient, care must be taken to ensure that the analysis is self-consistent. That is, we must first decompose the light curve and identify the separate phases outlined in §3.3, as each phase has a different dependence on the underlying physical parameters (§3.4). The relative prominence of each phase and the corresponding scaling are determined by the dimensionless parameters η and ξ. For example, as shown in Fig. 3.7, the light curve duration and luminosity depend on M_{csm} and R_{csm} in a non-monotonic way as we transition from an edge ($\xi > 1$) to an interior breakout ($\xi < 1$), or from a light ($\eta \ll 1$) to heavy CSM ($\eta \gtrsim 1$). Applying an edge breakout

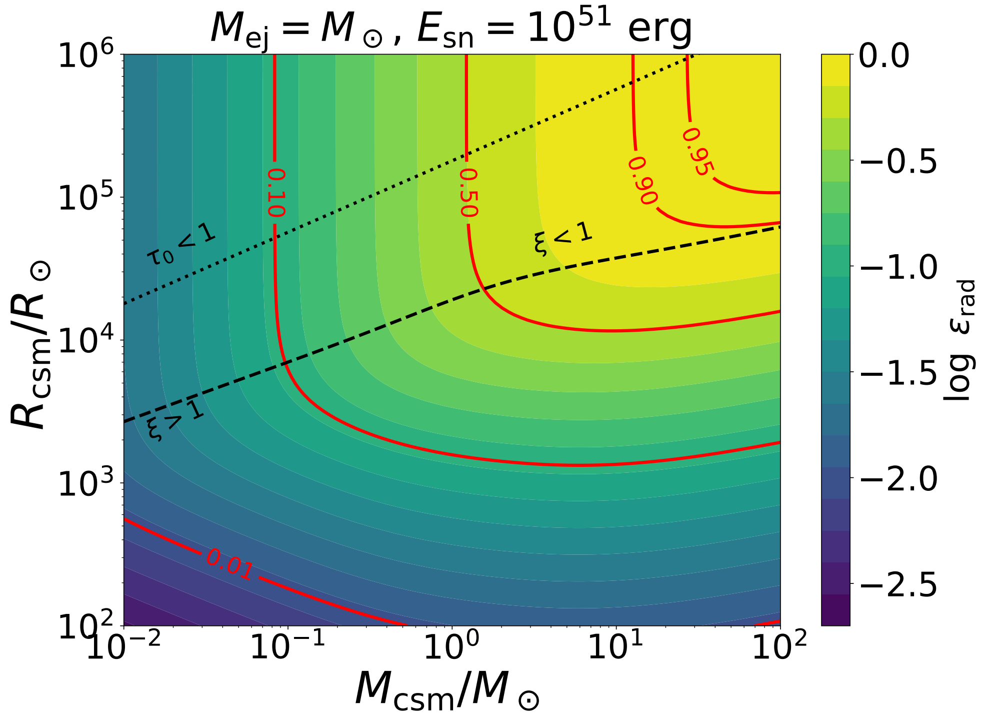

Figure 3.12: Radiated efficiencies from the interaction of a solar mass ejecta with $E_{sn} = 10^{51}$ ergs of kinetic energy, for a range of CSM masses and radii. Lighter regions denote higher efficiencies.

scaling relation to e.g. an interior breakout would result in an incorrect estimate of the physical parameters of the system.

It may be challenging to observe a light curve at a high enough cadence to see all of the interaction phases. The flash originating from an edge breakout is a particularly hard phase to capture, given its fast rise and immediate decline. If we are unable to catch the transient early enough, only the post-breakout shock cooling emission may be observed. In contrast, an interior breakout from a heavy CSM will be much easier to observe given its gradual rise and fairly luminous peak, but the light curve may need to be followed up for a fairly long time to capture the continued interaction tail and shock emergence drop, which can take more than a year in certain cases. When all phases of the interaction are not observed, there are typically degenerate solutions that fit the same light curve photometry with very different CSM masses and radii (see Figure 3.5). Invoking significant heating by radioactive nickel or a central engine further increases this degeneracy. In such cases, spectral information can be valuable for refining the interpretation.

Another issue that can arise when interpreting observed light curve concerns the dark phase which is by definition unobservable. This phase obfuscates the exact time of progenitor explosion. In certain cases, the interaction may completely overshadow the stellar breakout burst and radioactive heating. In other cases, the transient light curve will be explained by a combination of early interaction emission followed by heating from additional sources e.g. radioactive decay [11, 96].

In what follows, we give four case studies of observed transients which apply the theoretical framework introduced in this work. We suggest a connection between each observed transient class and one of the four theoretical interaction classes delineated in §3.3. While the true mapping may be more multi-faceted than this, we intend only to illustrate how the general framework can be useful in organizing data samples, as well as to point out the degeneracies that may arise when trying to fit observed events with interaction models. Due to these degeneracies, the model parameters may contain significant uncertainty when fitting to specific events, such as is shown in Fig. (3.14).

Light Interior Interaction as Type Ibcn/IIn Supernovae

CSM interaction has historically been used to explain narrow emission features in supernova spectra [9, 160, 161], where the narrow lines reflect the slow-moving velocity of the unshocked CSM. Such transients (i.e. type Ibn, Icn, IIn, and related events) may be associated with the continued interaction phase that occurs in interior breakout events. Given the typical luminosity range and inferred velocities, they are likely the result of an $\eta \ll 1$ ”light” CSM interaction which converts only a fraction of the ejecta kinetic energy into radiation (i.e. $\varepsilon_{rad} \ll 1$).

Once the breakout radiation has subsided, the light curve will enter the continued interaction phase and track the instantaneous shock luminosity $L(t) = L_{sh}$, where L_{sh} is given by Eq. (3.10). If we assume power-law ejecta and CSM density profiles $\rho_{ej} \propto r^{-n}$ and $\rho_{csm} \propto r^{-s}$, then the numerically-calibrated continued interaction phase can be analytically expressed from Eq. (3.33) as

$$L(t) \approx 0.2 L_0 \eta^{-3\alpha} \left[\frac{t}{t_{se}} \right]^{(5-s)\lambda - 3} \tag{3.49}$$

where $L_0 = M_{csm} v_{ej}^3 / R_{csm}$; $t_{se} = \eta^{\alpha} R_{csm}/v_{ej}$ is the shock emergence time Eq. 3.13; and the exponents for the $\eta < 1$ regime are given by Eqs. 3.12 and 3.28 as

$$\lambda = \frac{(n-3)}{(n-s)}, \ \alpha = \frac{1}{(n-3)}$$

For the specific case of a constant wind mass loss $\dot{M}$, the CSM density profile is $\rho_{csm}(r) = \dot{M}/4\pi r^2 v_w$ where v_w is the wind velocity. The continued interaction phase of a wind will therefore evolve as

$$L(t) \approx \frac{\dot{M}}{v_w} v_{sh}^{3(n-3)/(n-2)} R_w^{3/(n-2)} t^{-3/(n-2)} \tag{3.50}$$

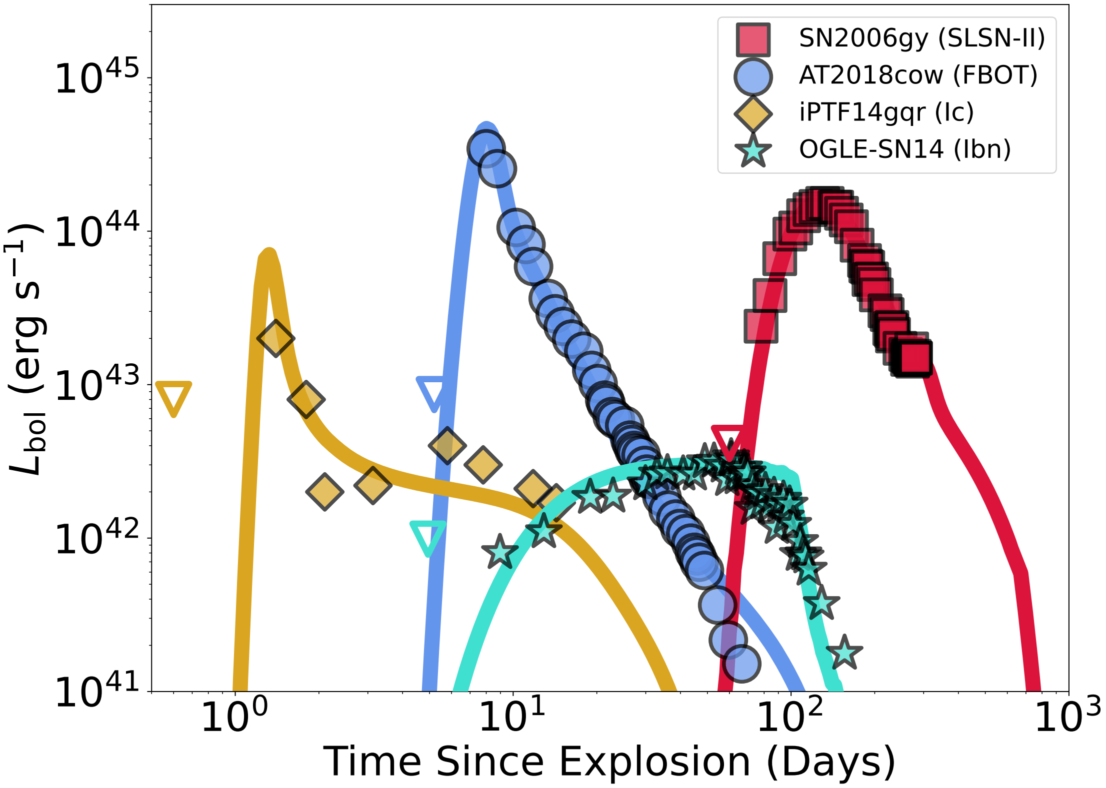

Figure 3.13: Fits of numerical simulations of each interaction type to several observed transients spanning a range of durations and luminosities. Open triangles denote upper limits on the light curve during the dark phase. Data taken from [158] for OGLE-2014-SN-131; [97] for SN2006gy; [159] for AT2018cow; and [11] for iPTF14gqr.

where $R_w \approx v_w t_w$ is the outer radius of a wind moving at a constant velocity v_w for a duration t_w. For our fiducial case of $n = 10$ and scaled to physical units, this becomes

$$L(t) \approx 8.8 \cdot 10^{43}\ \dot{M}_{yr} v_{w,5}^{-5/8} t_{w,yr}^{3/8} v_{sh,8}^{21/8}\ t_{1d}^{-3/8}\ \ erg\ \ s^{-1} \tag{3.51}$$

where M_{yr} is the wind mass loss in units of $M_{\odot}/$ yr; $v_{w,5} = v_w/10^5$ cm s^{-1}; $t_{w,yr} = t_w/1$ yr; $v_{sh,8} = v_{sh}/10^8$ cm s^{-1}; and t_{1d} is the time in days. From this we see that continued interaction with a steady wind will always produce a declining light curve. Thus, a flat or rising continued interaction phase requires a flatter wind density profile created by a non-constant mass loss episode $\dot{M}_w(t)$.

This class of interaction will display a fairly wide diversity of light curve morphologies due to its sensitive dependence on the CSM density profile. In Fig. 3.10, we show how such continued interaction-dominated light curves vary with the density profile. For steeper CSM profiles, the breakout becomes more luminous and prominent, even though the time of breakout as well as shock emergence does not change. For $\eta > 1$, the shape is not affected as drastically by the CSM density profile. Given that these events track the instantaneous shock luminosity, any minute variation in the CSM density profile will show up in the light curve as a "bump" during the continued interaction phase [162].

Fig. 3.13 shows an example of an observed interacting SN, OGLE-2014-SN-131, a type Ibn event whose light curve rose gradually then abruptly fell off [158]. In our framework, this can be interpreted as an $\eta < 1$ and $\xi < 1$ interaction event with a sustained continued interaction phase. To get a rising light curve in this phase requires a shallow CSM density profile exponent $s < 5 - 3/\lambda$, where λ is given above and in Eq. 3.28. For an ejecta density profile of $n = 10$, this gives $\lambda = 7/(10 - s)$ i.e. requiring a CSM density profile shallower than $s < 5/4$.

The best-fitting model for OGLE-2014-SN-131 estimates $s \approx 1$ to get the correct rise and peak luminosity, which would indicate an episode of unsteady mass loss compared to the wind-like $s = 2$. In this model, the sharp decline in the light curve after peak is associated with shock emergence from the outer edge of the CSM layer, which leads to a sudden halt to the interaction power.

Heavy Interior Interaction as Superluminous Supernovae

Some superluminous supernovae have total radiated energies in excess of $\sim 10^{51}$ ergs [99]. To achieve this in an interaction model requires efficient conversion of the ejecta kinetic energy to radiation (i.e. $\epsilon_{rad} \sim 1$). From Figure 3.12, this can occur for heavy CSM ($\eta \gtrsim 1$) and an interior breakout scenario $\xi < 1$ for which adiabatic expansion losses are minimized.

For heavy interior interactions, we can combine the light curve expressions Eqs. 3.31 and 3.32 using the Sedov exponents $\alpha = 1/2$ and $\lambda = 2/(5 - s)$ (from Eqs. 3.12 and 3.28) to get a constraint on the CSM mass as

$$M_{csm} \approx 5\, \kappa^{-2/3} L_{bo,44}^{1/3} \Delta t_{bo,30d}^{5/3}\ M_{\odot} \tag{3.52}$$

where $\Delta t_{bo,30d} = \Delta t_{bo}/30$ days. This equation only remains valid if the inferred CSM mass M_{csm} is indeed greater than the supernova ejecta mass M_{sn}.

For SN2006gy [97], the observed breakout properties were $L_{bo} \approx 1.8 \cdot 10^{44}$ erg s^{-1} and $\Delta t_{bo} \approx 60$ days. Thus, assuming a solar composition $\kappa = 0.34$ cm^2 g^{-1}, we get $M_{csm} \approx 40 M_\odot$.

Additionally, for $\eta > 1$, the shock emergence timescale Eq. 3.13 can be rewritten using $\alpha = 1/2$ to get $t_{se} \approx R_{csm} M_{csm}^{1/2} E_{sn}^{-1/2}$. For heavy interior breakouts we can then approximate $E_{sn} \approx \int L(t) dt = E_{rad}$ by assuming large radiated efficiencies $\varepsilon_{rad} \approx 1$ from Eq. 3.47. Thus, our additional CSM constraint based on light curve measurements becomes

$$R_{csm} \approx 10^3 \, E_{rad,51}^{1/2} M_{csm,\odot}^{-1/2} t_{se,d} \; R_\odot \tag{3.53}$$

For SN2006gy, the observed measurements were $E_{rad} \approx 1.2 \cdot 10^{51}$ ergs and $t_{se} \gtrsim 300$ days, giving $R_{csm} \approx 5 \cdot 10^4 R_\odot$ using $M_{csm} \approx 40 M_\odot$ from above.

In Fig. 3.13 we show the best-fit model based on the parameters given in Table **??**, showing that our estimate is fairly close to the above analysis compared to a full numerical simulation. Note that the model kinetic energy is $E_{sn} = 2.5 \cdot 10^{51}$ ergs, implying a radiated efficiency closer to $\varepsilon_{rad} \approx 0.5$. We have also found that a CSM density profile of $r^{-2.5}$ rather than the fiducial wind-like r^{-2} better fits the late-time light curve evolution, which would be indicative of a non-constant mass-loss episode in producing SN2006gy's circumstellar environment.

Finally, note that the continued interaction phase is still present in this case, although it may be less pronounced as that for Ibn/IIn due to the longer duration and much more luminous breakout peak, since it takes longer to subside and reveal the underlying instantaneous shock luminosity Eq. 3.33 with the snowplow exponents Eq.3.34. Similar to the previous case, any variations in the CSM density profile will be imprinted on the light curve, resulting in light curve bumps. Such behavior has been seen in superluminous supernovae [163].

Light Edge Interaction as Fast Blue Optical Transients

Interaction may be relevant in explaining the light curves of so-called fast blue optical transients, or FBOTs [94, 125, 159, 164]. These events generally rise in less than a day to reach peak luminosities in excess of 10^{44} erg s^{-1}. Perhaps the most well-studied example is AT2018cow, also referred to as "The Cow" [159].

The fast rise and decline of the light curve favors a breakout flash as the theoretical interpretation, followed by a shock cooling tail. In order to get a rapid breakout flash, we must be in the edge breakout regime, $\xi > 1$. Furthermore, the rapid timescale of the shock cooling implies lowish diffusion times, i.e. $\eta < 1$.

To constrain the properties of the CSM in this regime, we can combine the edge breakout expressions Eqs. 3.20 and 3.22 to get an expression for the CSM radius as

$$R_{csm} \approx 2 \cdot 10^3 \; \kappa^{1/3} L_{bo,44}^{1/3} \Delta t_{bo,d}^{2/3} \; R_\odot \tag{3.54}$$

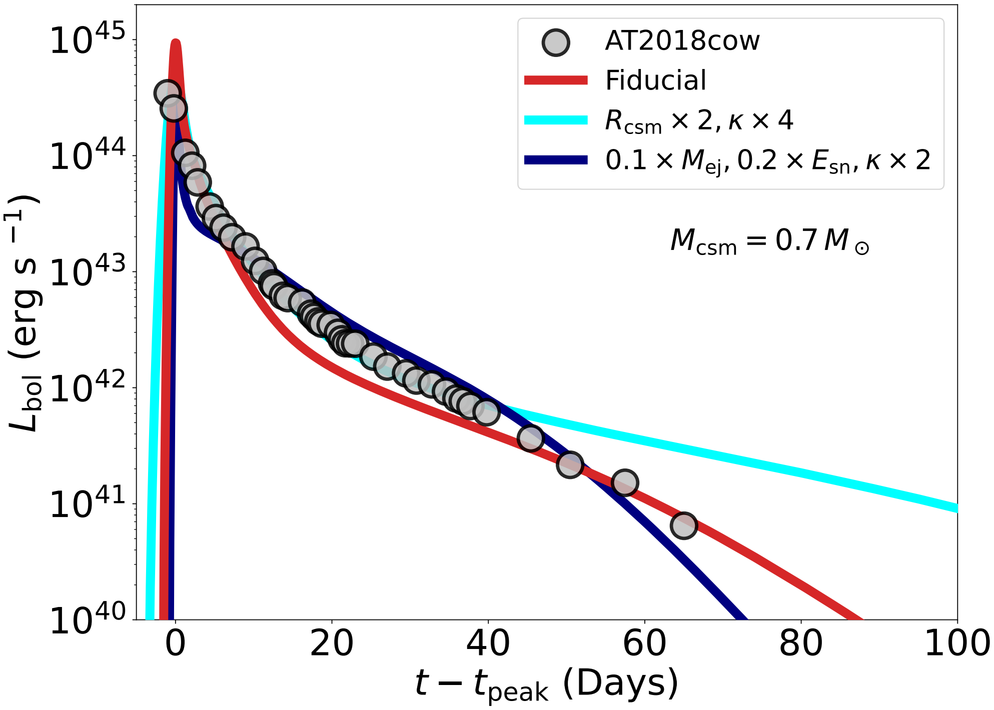

Figure 3.14: Numerical model fits to the light curve of AT2018cow [159], using slightly different ejecta and CSM parameters. The fiducial model corresponds to the one shown in Fig. 3.13.

For The Cow which had $L_{peak} \approx 3 \cdot 10^{44}$ erg s^{-1} and a rise to peak time of ~ 1.5 days, this gives a radius $R_{csm} \approx 3 \cdot 10^{3} R_\odot$ (assuming $\kappa = 0.34$ cm^2 g^{-1}), in rough agreement with the numerical best fit model shown in Fig. 3.13.

In the $\eta < 1$ case, it may be difficult to distinguish between the breakout flash and subsequent shock cooling tail. In Fig. 3.14 we show how the early part of The Cow can be fit with a variety of ejecta and CSM parameters, using a slightly different CSM mass than in Fig. 3.13. All three models give a reasonably good fit to the rise and peak luminosity of the light curve, i.e. the breakout. Their primary difference around peak is how much of the early emission comes from the breakout flash vs. shock cooling, each of which is described by different expressions Eqs. 3.20 and 3.24. It is only until much later that the models begin to reveal differences during the shock cooling phase, which may be harder to observe due to its lower luminosity and contamination from other effects such as recombination [122, 137] or radioactive decay [96].

Heavy Edge Interaction as Double-peaked Transients

The observed Type Ic SN iPTF14gqr had a fast-rising (~ 1 day) early luminosity excess, followed by a more extended primary light curve [11]. This light curve can be explained in multiple ways. In the original interpretation of [11], shock cooling powered the early bump while radioactive decay powered the primary light curve. In Fig. 3.15 we use the same parameters as described in [11], showing that the early excess can indeed be fit by a shock cooling tail. However, this model also predicts a breakout flash that is two orders of magnitude more luminous than the brightest measurement. That such an observed breakout flash was unseen in iPTF14gqr may be a result of the cadence of the observations and the fact that this flash is primarily in very blue bands that might not have been easily captured by optical observations.

Alternatively, the double-peaked light curve can be explained entirely by interaction, *without invoking multiple heating sources.* Namely, shock breakout produces the initial brief and luminous peak, while shock cooling produces the secondary longer-duration peak. The CSM mass must be sufficiently high, otherwise the shock cooling emission blends into the breakout emission, rather than forming a distinct double-peaked morphology (see Figure 3.6). This can be quantified using Eqs. 3.20 and 3.24, to write the ratio of the shock cooling peak to the breakout peak

$$\frac{L_{sc}}{L_{bo}} \sim \xi^{-1/2} \tag{3.55}$$

Similarly, the two timescales are, using Eqs. 3.22 and 3.25,

$$\frac{\Delta t_{bo}}{t_{sc}} \sim \xi^{-3/4} \tag{3.56}$$

For scenarios in the regime $\xi \gg 1$ these equations imply $L_{sc} < L_{bo}$ and $\Delta t_{bo} < t_{sc}$, and hence distinct double peaks.

In Fig. 3.15, we additionally fit a numerical model to the entirety of iPTF14gqr's light curve assuming only interaction (i.e. no radioactive heating), where the first peak is produced by shock breakout rather than shock cooling. Although the CSM radius and ejecta mass are comparable in both interpretations, the simultaneous fit of both peaks requires an interaction consisting of ejecta an order of magnitude less energetic, and a larger CSM mass by a factor of about 30. In summary, both scenarios are plausible explanations for double-peaked events, depending on whether one invokes additional heating for the second peak, and whether the much bluer breakout flash is covered by the bands used.

Caveats and Additional Physics

Several physical processes were neglected in constructing our analysis in order to provide a broadly applicable yet tractable theoretical framework. In §3.3 we briefly discussed the issue of inefficient radiative cooling of the shock. This will arise most likely in the $\eta \ll 1$ and

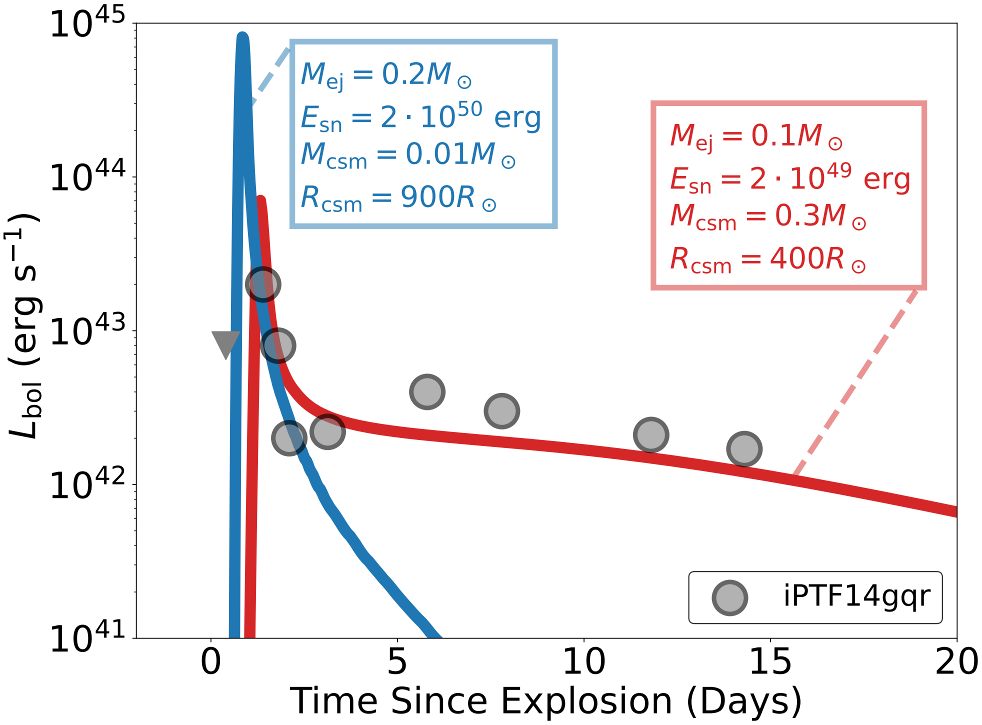

Figure 3.15: Numerical fits to the light curve of the Type Ic SN iPTF14gqr, with inset model parameters. The leftmost blue light curve fits only the first peak with a shock cooling tail, while the broader red light curve fits both the primary peak (shock breakout) and secondary bump (shock cooling). Light curve measurements taken from [11].

$\xi < 1$ regime, where the CSM is optically thin and the shock velocity is still sufficiently fast. The net effect of this is to reduce the radiative throughput and efficiency of the light curve (see §3.5), and we must account for non-thermal emission processes of collisionless shocks that are typically encountered in the context of supernova remnants.

[23] have delineated the regimes in which circumstellar shocks behave, where the addition of inverse Compton scattering expands the space in which the shocks are radiative. They found that fast-moving (e.g. relativistic) shocks in an optically thin CSM are radiatively inefficient. Thus, our analysis is applicable only to non-relativistic shock velocities, particularly where the shock is moving slow enough and the CSM optically thick enough that free-free cooling is effective.

We have also neglected predictions of the color/spectra of the resulting interaction, which requires a careful treatment of all the relevant physical processes (e.g. photoionization, inverse Comptonization, and lines). Thus, our results are only applicable in a bolometric sense, which limits the predictive power if we do not have accurate bolometric corrections of observed events. Of particular interest is the photospheric behavior of the interaction as the shock progresses, and any reprocessing effects the CSM will have on the shock, such as "thermalizing" hot X-ray shock photons into optical wavelengths via large bound-free opacities [23, 49].

While our models and analysis have used a simple constant opacity, the opacity may change significantly when temperatures become cool enough for atoms to recombine [122]. This is of particular importance for interior breakouts from a heavy CSM, which substantially decelerates the ejecta velocity resulting in a lower-temperature shock. Additionally, for edge breakout events, the decreasing temperature of the expanding shock cooling region will drop low enough that the ejecta also recombines, which will affect the late-time light curves from these events. Our scalings and models only remain reliable when the temperatures remain greater than the recombination temperature of the matter.

The configuration of all of our models consists of single a spherical CSM shell with a sharp outer edge, reminiscent of the CSM produced by an eruptive mass loss episode. When considering more general CSM configurations our expectations may need to be revised. If, for example, a long-duration wind produces a gradually declining CSM density profile without a sharp edge, then the situation will resemble one of our shell models with R_{csm} taken to be very large, such that breakout happens in the CSM interior and the phase of continued interaction persists indefinitely. If on the other hand repeated episodes of eruptive mass occur, as for example in pulsational pair-instability supernovae [165], the CSM may consist of numerous spherical shells. If these CSM shells are well separated, iterative application of the formalism presented here may be used to analyze each shell interaction individually. It is also possible that the CSM is non-spherical, with perhaps a disk-like configuration (see for example [166, 167]). In that case, the physical behavior of the escaping radiation differs from the spherically symmetric case, as only a sliver of the ejecta will participate in the interaction.

We have assumed in the analytic scalings and numerical simulations that $R_* \ll R_{csm}$, i.e. the inner edge of the CSM is much smaller than the outer CSM radius. However, it is possible to expect geometrically "thin" CSM shells due to e.g. brief episodes of mass loss, where $R_* \sim R_{csm}$. This introduces an additional physical parameter to the dynamics that must be explicitly accounted for. In the case of an edge breakout, where radiation is only able to escape once the shock reaches R_{csm}, the value of R_* does not influence the resulting light curve or breakout duration, although it can alter the time of shock emergence relative to the supernova epxlosion, $t_{se} \sim \eta^{\alpha}(R_{csm} - R_*)/v_{ej}$. The effect of a thin CSM shell will be most prominent for an interior breakout and resulting continued interaction phase, shown by the explicit dependence of R_* in Eq. (3.35).

Finally, we have also assumed in our analytical treatment that the forward shock dominates the light curve at all phases, and the shock luminosity terminates at shock emergence. In reality, a reverse shock will form at the interface of the shocked ejecta region, illustrated in Fig. 3.1, which will provide an additional luminosity source for the light curve [111, 145]. The strength of the reverse shock depends on the CSM mass, where a larger contribution is expected in the $\eta > 1$ heavy CSM regime. [144] have shown that the reverse shock can be an important source of emission during the continued interaction phase. The reverse shock will also persist for some time after shock emergence, i.e. during the shock cooling phase. We have confirmed the existence of a luminous reverse shock in our numerical simulations, which is especially prominent for the $\eta > 1$ models. Further analytic study and numerical investigation is necessary to fully characterize its behavior.

3.7 Conclusions

CSM interaction significantly expands the light curve duration and luminosity phase space that normal supernovae may otherwise occupy. This is due to the efficient conversion of the large store of ejecta kinetic energy from the preceding supernova, into radiation at the shock front. Here, we articulated a conceptual framework to interpret interaction light curves. We decompose the interaction light curve into five distinct phases, each of which may produce distinct features in the light curve morphology. We separate interaction light curves into four distinct classes, which depend on a combination of (1) where shock breakout occurs; and (2) the relative masses of the ejecta and CSM.

In §3.4 we derived quantitative relations for the qualitative picture given in §3.3. We provide scaling relations for each of the light curve phases, using a simplified model for the shock evolution. We then confirmed in §3.5 the analytical model by running a grid of one-dimensional radiation hydrodynamics simulations across a broad parameter space. Finally, we provided four case studies of observed transients in §3.6 to demonstrate how the framework can be used in practice.

Our results should be useful to study stellar mass loss through observations of supernova light curves. In particular, different physical mass loss mechanisms will have distinct predictions regarding the progenitor and structure of the CSM [15, 18]. While light interior breakouts can be explained by interaction with a typical stellar wind, heavy interior breakouts will require prodigious mass loss from a supermassive progenitor [116]. In other cases, the small radii necessary to produce edge breakouts will require episodes of significant mass loss near the end of the star's life [96].

We have limited our analysis to the bolometric properties of the interaction light curve. The broadband spectra and observed colors also likely provide important information pertaining to the interaction, particularly given the wide range in shock temperatures that can result depending on how efficiently the shock can cool. We might therefore find that each light curve phase has a distinct color evolution and photospheric behavior. An accurate bolometric correction of the light curve may require detailed coverage from X-ray to optical wavelengths [23], although these capabilities are recently becoming attainable (see for example [21, 22]). This poses a unique observational challenge in several ways, particularly for the edge breakout flash due to its brief timescale and likely rapid color evolution. We have also neglected any non-thermal emission that may be produced by the shock, which is of particular importance in understanding radio observations of interacting supernovae.

In addition to the broadband colors, it would be interesting to connect the spectral evolution of the interaction to the different light curve phases and classes. Narrow emission lines have been the hallmark signature of interaction as it implies slow-moving material above the heating at the shock front. While the presence of narrow lines favors interaction, the absence of such features does not preclude CSM interaction as the mechanism behind the light curve. Interior breakouts are the natural interaction type to expect such features, while edge breakouts may have little to no narrow lines in their spectra as the bulk of the CSM has already been swept up. An accurate investigation of interaction spectra requires running expensive non-LTE radiation hydrodynamics simulations, such as is done in [49] for the case of a heavy interior breakout.

In constructing a broadly applicable light curve framework, we have neglected several important physical effects that will influence the results presented in this paper. Potentially important effects are briefly discussed in §3.6 and warrant further investigation. Of particular interest include how asymmetric CSM configurations affect the observed phase properties, since the shock will only occupy a fraction of the full 4π solid angle of the ejecta. Indeed, several mass loss mechanisms such as binary interaction may produce a more disk-like geometry. The shock region is also prone to hydrodynamical instabilities which require high-resolution multidimensional radiation hydrodynamics simulations to fully investigate. It is unclear how such effects impact the resulting phases and classes discussed in this work.

Chapter 4

Computational Methods in Supernova Light Curve Modeling

4.1 Introduction

In Chapter 2, I considered the case where the hydrodynamics was described simply by homologous expansion, and used a frequency-independent (grey) opacity. In Chapter 3, I then extend for the effect of radiation hydrodynamics by using a grey flux-limited diffusion approach. While both approaches provide reasonable results when discussing bolometric light curves, they fail to accurately capture the complex physics behind frequency-resolved emission. We therefore require a multigroup radiative transfer approach coupled to a hydrodynamics scheme. Furthermore, since non-equilibrium radiation fields can drive the excitation and ionization state of the plasma, we furthermore require an inline NLTE approach during each numerical substep. Finally, we must also account for potential non-thermal contributions from relativistic electrons, which is important when studying radio emission from circumstellar interaction [105].

In this chapter, I present extensive developmental efforts in the Sedona code [75] that implement efficient multigroup radiation hydrodynamics capabilities and self-consistently account for all of the necessary physical processes. I give a brief overview of the implicit Monte Carlo implementation [45, 154, 168], highlighting NLTE modifications in the original approach. Next, I give a numerical description of our finite-volume hydrodynamics scheme [152], including a novel implementation of arbitrary Lagrangian-Eulerian (ALE) mesh motion that is particularly well-suited to problems with strong compression around shocks.

I then discuss the implementation of inline non-LTE atomic kinetics to get physically accurate ionization and excitation states of the plasma, and various acceleration techniques to speed up the inline computational cost. I explore the various opacity contributions, including an approximate method of handling unresolved line emission. I introduce an explicit Compton scattering approach, which includes temperature coupling with the plasma. Finally, I discuss a non-thermal electron particle transport method to evolve relativistic electrons due to collisionless shock injection. Details of the atomic data that goes into the kinetics and opacities are described in Appendix E.

4.2 Implicit Monte Carlo Radiation Transport

The lab-frame equation of radiative transfer is given by [46, 75, 154]

$$\frac{1}{c}\frac{\partial I_\nu}{\partial t} + \hat{\mathbf{n}} \cdot \nabla I_\nu = -\chi_\nu I_\nu + \eta_\nu \tag{4.1}$$

$$\tag{4.2}$$

Here η_ν is the emissivity, which is related to the extinction coefficient χ_ν through the source function $S_\nu \equiv \eta_\nu/\chi_\nu$.

It is more intuitive to move into the comoving frame, where we make the following assumptions: (1) all absorption and emission processes, including scattering, are isotropic; and (2) scattering in the comoving frame is elastic/coherent [154].

The extinction coefficient and emissivity can be decomposed into an absorptive and scattering component:

$$\chi_{0\nu} = \alpha_{0\nu} + \sigma_{0\nu} \tag{4.3}$$

$$\eta_{0\nu} = j_{0\nu} + \eta^{\mathrm{s}}_{0\nu} \tag{4.4}$$

Here $j_{0\nu}$ is the thermal emissivity of the gas.

We can define an absorptive fraction of the opacity as

$$\epsilon_\nu = \frac{\alpha_{0\nu}}{\chi_{0\nu}} \tag{4.5}$$

where $\epsilon_\nu = 0$ corresponds to the case of pure scattering, while $\epsilon_\nu = 1$ is the case of pure absorption.

Now in LTE, the thermal emissivity is related to the opacity through Kirchoff's law:

$$j_{0\nu} = \alpha_{0\nu} B_{0\nu}(T) = \epsilon_\nu \chi_{0\nu} B_{0\nu}(T) \tag{4.6}$$

where $B_{0\nu}(T)$ is the Planck function at the local gas temperature T.

Next, we define a quantity $U = aT^4$ and rewrite the comoving-frame thermal emissivity as

$$j_{0\nu} = \epsilon_\nu \chi_{0\nu} b_{0\nu} \frac{cU}{4\pi} \tag{4.7}$$

where we have also introduced the dimensionless Planck function

$$b_{0\nu} = \frac{B_{0\nu}}{\int B_{0\nu'} d\nu'} = \frac{B_{0\nu}}{acT^4/4\pi} = \frac{4\pi}{cU} B_{0\nu} \tag{4.8}$$

In order to convert back into the lab frame, we perform a Lorentz transformation to get the expression

$$j_\nu = \epsilon_\nu \chi_\nu b_\nu \frac{cU}{4\pi} P_\eta \tag{4.9}$$

where

$$P_\eta(\nu, \hat{\mathbf{n}}) = \left(\frac{\nu}{\nu_0}\right) \frac{b_{0\nu}}{b_\nu} \tag{4.10}$$

captures the effects of doppler shifting on the frequency and angle distribution of the emissivity.

Our recast lab-frame transfer equation then becomes

$$\frac{1}{c}\frac{\partial I_\nu}{\partial t} + \hat{\mathbf{n}} \cdot \nabla I_\nu = -\chi_\nu I_\nu + \epsilon_\nu \chi_\nu b_\nu \frac{cU}{4\pi} P_\eta + (1-\epsilon_\nu)\chi_\nu J_\nu \tag{4.11}$$

The goal of the implicit Monte Carlo method is to handle the nonlinearity of U in a numerically stable manner, due to potentially stiff coupling with the gas temperature from both absorption and emission [45]. To proceed further, we now turn our attention to the time evolution of the gas internal energy/temperature. The gas temperature equation, accounting for heating and cooling processes, is

$$c_V \frac{dT}{dt} = \int \epsilon_\nu \chi_{0\nu} \left(cE_{0\nu} - 4\pi B_{0\nu}\right) d\nu \tag{4.12}$$

where $c_v = nk_b/(\gamma - 1)$ is the volumetric heat capacity, and

$$E_{0\nu} = \frac{4\pi}{c} J_{0\nu} = \frac{1}{c} \oint I_\nu d\Omega \tag{4.13}$$

is the comoving-frame radiation energy density.

At this point we introduce the energy and Planck mean opacities:

$$\chi_{0E} = \frac{\int \epsilon_\nu \chi_{0\nu} E_{0\nu} d\nu}{\int E_{0\nu} d\nu} \tag{4.14}$$

$$\chi_{0P} = \frac{\int \epsilon_\nu \chi_{0\nu} B_{0\nu} d\nu}{\int B_{0\nu} d\nu} \tag{4.15}$$

and so the temperature equation becomes

$$c_V \frac{dT}{dt} = c\chi_{0E} E_0 - c\chi_{0P} a_r T^4 \tag{4.16}$$

where $E_0 = \int E_{0\nu} d\nu$. Using the definition of $U = aT^4$, we can rewrite this as

$$\frac{1}{\beta}\frac{dU}{dt} = c\chi_{0E} E_0 - c\chi_{0P} U \tag{4.17}$$

where

$$\beta \equiv \frac{4aT^3}{c_V} \tag{4.18}$$

Our aim is to formulate a stable time-stepping method. Discretizing in time, we have

$$\frac{U^{n+1} - U^n}{\Delta t} = c\chi_{0E}^n \beta^n E_0^n - c\chi_{0P}^n \beta^n \bar{U} \tag{4.19}$$

where $\Delta t = t_{n+1} - t_n$ is the timestep size, and the n superscript for the quantities indicates that we are holding the begining-of-timestep values fixed for the absorbed radiation energy density and coupling coefficient β. The overbar denotes an appropriately time-averaged quantity, which we can write as a Crank-Nicholson type linear combination of the beginning and end-of-step values:

$$\bar{U} = (1 - \alpha)U^n + \alpha U^{n+1} \tag{4.20}$$

where α is a free parameter between 0 and 1, with 0 being fully explicit and 1 being "implicit". In practice, α must be greater than 0.5 (or 0.75 according to others) to guarantee an unconditionally stable method, which usually refers to preventing the occurrence of spurious oscillations and potentially negative values for the temperature [45].

"Solving" for the time-averaged quantity we get

$$\bar{U} = f_n U^n + (1 - f_n) \frac{\chi_{0E}^n}{\chi_{0P}^n} E_0^n \tag{4.21}$$

where we have introducted the Fleck factor [168]

$$f_n = \frac{1}{1 + \alpha c \beta^n \chi_0^n \Delta t} \tag{4.22}$$

The gas temperature is then updated as

$$\begin{aligned} c_V \frac{T^{n+1} - T^n}{\Delta t} &= c\chi_{0E}^n E_0^n - c\chi_{0P}^n \bar{U} && (4.23) \\ &= f_n c\chi_{0E} E_0^n - f_n c\chi_{0P} U^n && (4.24) \end{aligned}$$

Thus, we see that both the absorption and emission are suprressed by an amount equal to the Fleck factor f_n.

Returning back to the radiative transfer equation, we replace the U appearing in the thermal emissivity with $\bar{U}$:

$$\begin{gathered} \frac{1}{c}\frac{\partial I_\nu}{\partial t} + \hat{\mathbf{n}} \cdot \nabla I_\nu = -\chi_\nu I_\nu + \epsilon_\nu \chi_\nu b_\nu f_n \frac{cU^n}{4\pi} P_\eta \\ +(1 - f_n) P_\eta \left[\int \oint \mathcal{R}_\nu^n \epsilon_\nu \chi_\nu I_\nu \, d\Omega d\nu \right] + (1 - \epsilon_\nu)\, \chi_\nu J_\nu \end{gathered} \tag{4.25}$$

where $\mathcal{R}_\nu^n$ is the *effective scattering redistribution kernel*:

$$\mathcal{R}_\nu^n = \frac{\epsilon_\nu \chi_\nu B_\nu(T^n)}{\int \epsilon_\nu \chi_\nu B_\nu(T^n) d\nu} \tag{4.26}$$

From this, what we see is that the thermal emission is reduced by a factor of f_n, the second term on the right hand side. Furthermore, what the implicit Monte Carlo method introduces is a term that appears like a scattering term, the third term on the right hand side. A fraction of the true absorptive opacity equal to $(1 - f_n)$ instead acts to scatter the photon. This process is inelastic, described by the redistribution kernel that depends on the thermal emissivity through $\mathcal{R}_\nu^n$.

NLTE Modifications to the IMC Method

One of the assumptions made in the original derivation of the Fleck factor is that the thermal emissivity is described in LTE conditions:

$$j_\nu = \epsilon_\nu \chi_\nu B_\nu(T) \tag{4.27}$$

This assumption is what causes the T^4 factor to pop out from the integrating the Planck function over frequency. However, under NLTE conditions, the source function may no longer be a blackbody. We therefore attempt to account for NLTE effects while still using the machinery of the fleck factor by retaining the T^4 dependence in the derivation, but replacing the Planck mean opacity that appears in the fleck factor with a "generalized" Planck mean:

$$\tilde{\chi}_{0P} = \left(\frac{\int \frac{j_\nu}{\epsilon_\nu \chi_\nu} d\nu}{\int j_\nu \, d\nu} \right)^{-1} \tag{4.28}$$

where j_ν here is the NLTE emissivity calculated from the atomic kinetics. In LTE where we can use Kirchoff's law, this reduces back to the Planck mean opacity.

Finally we also modify the effective scattering kernel to use the NLTE emissivity:

$$\mathcal{R}_\nu^n = \frac{j_\nu^n}{\int j_\nu^n \, d\nu} \tag{4.29}$$

This is only a crude attempt at attempting to include NLTE effects in the original IMC method, which was designed around the assumption of LTE emissivities. A more thorough investigation is needed to find a more robust method, which is outside of the scope of this thesis. That said, our approach is better than nothing.

Numerical Procedure

At the beginning of each timestep, we isotropically emit N_{emit} equal-energy packets per zone (which is done in the comoving frame), where

$$\mathcal{E}_{0p} = \frac{f_{imc} L_{th} \Delta V \Delta t}{N} \tag{4.30}$$

where $L_{th} = 4\pi \int j_{0\nu} d\nu_0$ is the total thermal emissivity of zone i. The frequency of each packet is sampled from a CDF constructed from the emissivity.

The packets are evolved from the start of timestep t to the end $t + \Delta t$ using a history-based Monte Carlo approach. Namely, for each particle, we calculate the distance to the next interaction event as

$$l_k = \frac{1}{\chi_\nu} \left[-\ln(\mathcal{R}) \right] \tag{4.31}$$

where $\mathcal{R}$ is a uniform number between 0 and 1. This distance is compared to the distance to the boundary of the cell or domain, as well as the distance to the end of the timestep $c\delta t_k$.

If the interaction distance is the shortest, we then determine what type of interaction occurred. We draw another random number $\mathcal{R}'$ between 0 and 1. If $\mathcal{R}' > \epsilon_\nu$, then the packet undergoes a scattering (e.g. Compton). If $\mathcal{R}' < \epsilon_\nu$, we then draw a third random number $\mathcal{R}''$ in the range of 0 and 1. If $\mathcal{R}'' > f_{imc}$, the fleck factor, then the packet undergoes an "effective scatter', which samples a new isotropic direction, and changes its frequency by sampling the local emissivity CDF. If $\mathcal{R}'' < f_{imc}$, the packet is absorbed and we cease tracking the history of the particle.

Particles are tracked until they either reach the end of the timestep, are absorbed, or escape at one of the boundaries. If the particle escapes from the outer boundary, then we tally its contribution to the emergent specific luminosity as

$$L_\nu = \frac{4\pi}{\Delta t \Delta \nu_g \Delta \Omega} \sum \mathcal{E}_p \tag{4.32}$$

where $\Delta\Omega$ is the solid angle bin. At the start of a new timestep, we emit new particles as well as continue tracking the packets that remain from the last timestep.

Construction of Estimators

The comoving frame radiation field is constructed by the pathlength estimator approach [154], which sums over the paths of all particles during a timestep

$$J_{0\nu} = \frac{1}{4\pi} \frac{1}{\Delta V \Delta t \Delta \nu_g} \sum_p \mathcal{E}_p l_p \left(\frac{\nu_0}{\nu} \right)^2 \tag{4.33}$$

where $\Delta\nu_g$ is the width of the frequency group that contains particle p. The radiation four-force vector is constructed as

$$cG_0^0 = c \int \epsilon_\nu \chi_{0\nu} E_{0\nu} d\nu - 4\pi \int j_{0\nu} \, d\nu \tag{4.34}$$

where $E_{0\nu} = 4\pi J_{0\nu}/c$, and $j_{0\nu}$ is the thermal emissivity in the comoving frame.

The radiation fource contribution is constructed as

$$\mathbf{G}_0 = \frac{1}{c} \int \chi_{0\nu} \mathbf{F}_{0\nu} \, d\nu \tag{4.35}$$

where

$$\mathbf{F}_{0\nu} = \frac{1}{c\Delta V \Delta t \Delta \nu_g} \sum_p \mathcal{E}_p l_p \left(\frac{\nu_0}{\nu}\right)^2 \hat{\mathbf{n}}_0 \tag{4.36}$$

where $\hat{\mathbf{n}}_0$ is the direction of the photon packet in the comoving frame.

4.3 Finite-Volume Arbitrary Lagrangian-Eulerian Hydrodynamics

The equations of radiation hydrodynamics to $\mathcal{O}(v/c)$ are [31, 154]

$$\frac{\partial \rho}{\partial t} + \nabla \cdot (\rho \mathbf{v}) = 0 \tag{4.37}$$

$$\frac{\partial (\rho \mathbf{v})}{\partial t} + \nabla \cdot (\rho \mathbf{v}\mathbf{v}) + \nabla P = \mathbf{G}_0 \tag{4.38}$$

$$\frac{\partial \left(\rho \left[\frac{v^2}{2} + e\right]\right)}{\partial t} + \nabla \cdot \left[\left(\rho \frac{v^2}{2} + \rho e + P\right) \mathbf{v}\right] = cG_0^0 + \mathbf{v} \cdot \mathbf{G}_0 \tag{4.39}$$

We can write the hydrodynamics equations as a system of conservation laws as [169]

$$\frac{\partial \mathbf{U}}{\partial t} + \nabla \cdot \mathbf{F} = \mathbf{S} \tag{4.40}$$

where

$$\mathbf{U} = \begin{bmatrix} \rho \\ \rho \mathbf{v} \\ \rho \left(\frac{v^2}{2} + e\right) \end{bmatrix} \tag{4.41}$$

$$\mathbf{F} = \begin{bmatrix} \rho \mathbf{v} \\ \rho \mathbf{v}\mathbf{v} + P \\ \left[\rho \left(\frac{v^2}{2} + e\right) + P\right] \mathbf{v} \end{bmatrix} \tag{4.42}$$

and

$$\mathbf{S} = \begin{bmatrix} 0 \\ \mathbf{G}_0 \\ cG_0^0 + \mathbf{v} \cdot \mathbf{G}_0 \end{bmatrix} \tag{4.43}$$

In 1D spherical symmetry, the conservation equations become

$$\frac{\partial \mathbf{U}}{\partial t} + \frac{1}{r^2} \frac{\partial}{\partial r} \left(r^2 \mathbf{F}\right) = \mathbf{S} + \mathbf{S}_{geom} \tag{4.44}$$

where

$$\mathbf{S}_{geom} = \begin{bmatrix} 0 \\ 2P/r \\ 0 \end{bmatrix} \tag{4.45}$$

is a “geometric” source term due to the flux divergence in spherical coordinates [152, 169].

Finite-Volume Method

In a finite-volume discretization, the domain is divided into control volumes, or cells, with cell-centered coordinates $\mathbf{r}_i$. In 1D spherical symmetry, the cells have an inner and outer face with radial coordinates $\mathbf{r}_{i-1/2}$ and $\mathbf{r}_{i+1/2}$, respectively. Cell volumes are therefore calculated as

$$\Delta\mathbf{V}_i = \frac{4\pi}{3}\left(\mathbf{r}^3_{i+1/2} - \mathbf{r}^3_{i-1/2}\right) \tag{4.46}$$

Cell faces are defined as

$$\Delta\mathbf{A}_{i\pm1/2} = 4\pi\mathbf{r}^2_{i\pm1/2} \tag{4.47}$$

By integrating quantities over the control volume and applying the divergence theorem, the conserved system becomes

$$\frac{d\tilde{\mathbf{U}}_i}{dt} + \oint_{\partial\mathbf{V}_i} \mathbf{F}\cdot d\mathbf{A} = \tilde{\mathbf{S}}_i \tag{4.48}$$

where the over-tilde denotes quantities integrated over the control volume, e.g. $\tilde{\mathbf{U}}_i = \mathbf{U}_i\Delta\mathbf{V}_i$. For the equations of hydrodynamics, these quantities evaluate to the total cell mass, total momentum, and total (internal + kinetic) energy.

For an explicit time discretization between times t_n and t_{n+1}, we therefore get

$$\tilde{\mathbf{U}}^{n+1}_i = \tilde{\mathbf{U}}^n_i - \Delta t\sum_k \mathbf{F}\cdot\Delta A_k + \tilde{\mathbf{S}}_i\Delta t \tag{4.49}$$

where $\Delta t = t_{n+1} - t_n$, and the sum k runs over the faces of cell i. In 1D spherical symmetry, there are two sums: the inner $d\mathbf{A}_{i-1/2}$ and outer $d\mathbf{A}_{i+1/2}$ faces, respectively.

The critical ingredient in a finite-volume method is an accurate estimate of the numerical flux at the faces $\mathbf{F}_{i\pm1/2}$. This is done by solving a Riemann problem at the cell face [169], given the state quantities at the left and right sides $\mathbf{U}_\mathrm{L}$ and $\mathbf{U}_\mathrm{R}$, respectively.

What we are given in the finite-volume method are *cell-averaged* quantities, i.e. $\mathbf{U}_i = \tilde{\mathbf{U}}_i/\Delta\mathbf{V}_i$ for $\mathbf{r} \in \left\{\mathbf{r}_{i-1/2}, \mathbf{r}_{i+1/2}\right\}$. What we require for the Riemann problem are quantities at the cell faces. A simple approach would be to simply take the cell-centered value to be the face-centered quantity, which reduces the method to a first-order approach.

Instead, we can take a more accurate approach (although potentially prone to numerical instabiltiies) by performing a left/right piecewise linear reconstruction [35, 152]. For a cell face located at $\mathbf{r}_{i-1/2}$, the left/right reconstructed states are

$$\mathbf{U}_{\mathrm{L}} = \mathbf{U}_{i-1} + (\nabla\mathbf{U})_{i-1} \cdot \big(\mathbf{r}_{i-1/2} - \mathbf{r}_{i-1}\big) \tag{4.50}$$

$$\mathbf{U}_{\mathrm{R}} = \mathbf{U}_{i} + (\nabla\mathbf{U})_{i} \cdot \big(\mathbf{r}_{i-1/2} - \mathbf{r}_{i}\big) \tag{4.51}$$

Our next step is to calculate the cell gradients in a manner that is both accurate and numerically stable. This is particularly important in the presence of large gradients, i.e. shocks. This is the essence of slope limiters, which forms an enormous body of previous and ongoing work.

The limited slopes are written as

$$(\nabla\mathbf{U})_i^{lim} = \xi_i\,(\nabla\mathbf{U})_i' \tag{4.52}$$

where

$$(\nabla\mathbf{U})_i' = \frac{1}{2}\,(1+\omega)\,\nabla\mathbf{U}_{i-1/2} + \frac{1}{2}\,(1-\omega)\,\nabla\mathbf{U}_{i+1/2} \tag{4.53}$$

$$\nabla\mathbf{U}_{i-1/2} = \frac{\mathbf{U}_i - \mathbf{U}_{i-1}}{\mathbf{r}_i - \mathbf{r}_{i-1}} \tag{4.54}$$

$$\nabla\mathbf{U}_{i+1/2} = \frac{\mathbf{U}_{i+1} - \mathbf{U}_{i}}{\mathbf{r}_{i+1} - \mathbf{r}_{i}} \tag{4.55}$$

and $\omega \in \{-1, 1\}$ is a free parameter with $\omega = 0$ corresponding to a cell-centered scheme which is what we take here.

There are multiple expressions for the slope limiter ξ_i which depend on the ratio of the up- and downwind gradients,

$$r = \frac{\nabla\mathbf{U}_{i-1/2}}{\nabla\mathbf{U}_{i+1/2}} \tag{4.56}$$

We use the SUPERBEE-type limiter [169, 170], given by

$$\xi(r) = \begin{cases} 0 & r \le 0, \\ 2r & 0 < r \le 1/2, \\ 1 & 1/2 < r \le 1, \\ \min\left[r, \xi_R(r), 2\right] & r > 1. \end{cases} \tag{4.57}$$

where

$$\xi_R(r) = \frac{2\beta}{1-\omega+(1+\omega)r} \tag{4.58}$$

with β another free parameter which we take to be 1.

With the left $\mathbf{U}_L$ and right $\mathbf{U}_R$ reconstructed states appropriately calculated and limited, we next need to actually solve the Riemann problem in order to determine the fluxes. We use an HLLC Riemann solver [171] to calculate the numerical flux at each face as

$$\mathbf{F}_{\mathrm{HLLC}} = \begin{cases} \mathbf{F}_L & 0 \leq S_L, \\ \mathbf{F}_L^* & S_L \leq 0 \leq S_*, \\ \mathbf{F}_R^* & S_* \leq 0 \leq S_R, \\ \mathbf{F}_R & 0 \geq S_R. \end{cases} \tag{4.59}$$

here, the left-right fluxes are found by evaluating the flux for the left/right reconstructed quantities, $\mathbf{F}_L = \mathbf{F}(\mathbf{U}_L)$ and $\mathbf{F}_R = \mathbf{F}(\mathbf{U}_R)$. The wavespeeds are (in the absence of any mesh motion) given by

$$S_L = \min\left\{v_L - c_{s,L}, v_R - c_{s,R}\right\} \tag{4.60}$$

$$S_R = \max\left\{v_L + c_{s,L}, v_R + c_{s,R}\right\} \tag{4.61}$$

where $v_{L,R}$ and $c_{s,L/R}$ are the fluid velocities and sound speeds using the reconstructed quantities. The wavespeed estimate in the *Star* region is

$$S_* = \frac{P_R - P_L + \rho_L v_L \left(S_L - v_L\right) - \rho_R v_r \left(S_R - v_R\right)}{\rho_L \left(S_L - v_L\right) - \rho_R \left(S_R - v_R\right)} \tag{4.62}$$

where $\rho_{L,R}$ $P_{L,R}$ are the left/right reconstructed gas density and pressure, respectively.

The left/right star fluxes are given by

$$\mathbf{F}_K^* = \frac{S_*(S_K \mathbf{U}_K - \mathbf{F}_K) + S_K(P_K + \rho_L(S_K - v_K)(S_* - v_K))D_*}{S_K - S_*} \tag{4.63}$$

where $K = L, R$ and

$$D_* = \begin{bmatrix} 0 \\ 1 \\ S_* \end{bmatrix} \tag{4.64}$$

for the density, momentum, and energy fluxes.

The last thing needed is an appropriate time-stepping method. We use a three-step Runge Kutte algorithm [172] to advance the conserved quantities from $\mathbf{U}^(n) = \mathbf{U}(t_n)$ to $\mathbf{U}^{(n+1)} = \mathbf{U}(t_{n+1})$:

$$\mathbf{U}^{(1)} = \mathbf{U}^{(n)} + \Delta t \mathcal{L}\left(\mathbf{U}^{(n)}\right) \tag{4.65}$$

$$\mathbf{U}^{(2)} = \frac{3}{4}\mathbf{U}^{(n)} + \frac{1}{4}\left[\mathbf{U}^{(1)} + \Delta t \mathcal{L}\left(\mathbf{U}^{(1)}\right)\right] \tag{4.66}$$

$$\mathbf{U}^{(n+1)} = \frac{1}{3}\mathbf{U}^{(n)} + \frac{2}{3}\left[\mathbf{U}^{(1)} + \Delta t \mathcal{L}\left(\mathbf{U}^{(2)}\right)\right] \tag{4.67}$$

where $\Delta t = t_{n+1} - t_n$ and $\mathcal{L}\left(\cdot\right)$ is the hydro substep.

ALE Mesh Motion

Interacting supernovae provide several unique challenges to numerically model. Eulerian methods are favored for problems with strong shocks and have been used in previous studies of CSM interaction [49, 173]; however, they must rely on either a large of number of cells to resolve the shock; or more advanced numerical techniques, such as adaptive mesh refinement [174]. This problem is especially pronounced for radiative shocks where the shock width will be of order the radiation mean free path [31], and becomes exceedingly small once the shock becomes optically thin. In addition, in order to follow the shock breakout and shock cooling phases, an ambient medium is required for the material to expand into, which adds another layer of difficulty in evolving the light curves out to late times post breakout.

Due to these difficulties, a Lagrangian approach seems more favorable, as the grid will naturally move with the interaction. This comes at the drawback of poorly resolving the shock compared to an Eulerian approach. Furthermore, Lagrangian methods will suffer from severe mesh distortion at the shock front [175], as material is swept up into a shell and compressed to a great degree, leading to an exceedingly small timestep constraint. In order to overcome this issue, one must rely on similar techniques as in Eulerian methods, such as coarsening regions where the mesh is too distorted.

Moving mesh methods have been used previously in various astrophysical contexts [34]; in particular [152] and [166] have demonstrated their utility in modeling interacting supernovae. Moving mesh methods belong to a wider class of numerical techniques known as direct ALE methods [176], where the mesh is moved during the timestep by setting the new mesh node locations (in contrast to indirect ALE methods, which evolve a timestep assuming a fixed mesh, followed by a remapping phase to the new mesh positions; see e.g.). One approach is to solve a Poisson equation on the domain based on a user-defined mesh potential [177]. The mesh potential acts to steer cells to be of equal mass and/or volume, using the same numerical method as done for the self-gravity solver. Other methods rely on solving a set of moving mesh partial differential equations (so-called MMPDE methods), where the system itself depends on time, to prevent artificially large jumps in mesh location for time-independent systems [178].

Our primary objective is to move the domain in a mostly Lagrangian manner while providing a higher degree of resolution around the shock front. In addition, we would also like to prevent severe mesh distortion that occurs in Lagrangian methods around shocks. In the shock region, we would like the mesh to behave in a more Eulerian fashion.

To accomplish this, we add fictitious mesh “springs” that couple the mesh nodes to each other. In 1D, the net force acting on the i-th node is

$$F_i = k_{i+1/2}\left(\Delta r_{i+1/2} - \delta x_{i+1/2}\right) - k_{i-1/2}\left(\Delta r_{i-1/2} - \delta x_{i-1/2}\right) \tag{4.68}$$

where $\Delta r_{i+1/2} = r_{i+1} - r_i$ is the cell width, $k_{i\pm1/2}$ are the fictitious spring constants, and $\delta x_{i\pm1/2}$ are the fictitious spring rest lengths. We solve the coupled spring system across the entire mesh such that the net force acting on each node is zero:

$$\sum_{i=0}^{N} F_i = 0 \tag{4.69}$$

We then set the mesh velocities in a timestep such that the mesh positions at the end of that timestep correspond to the solutions r_i^s of the mesh spring:

$$\left(\frac{dr}{dt}\right)_i^{n+1/2} = \frac{r_i^s - r_i^n}{\Delta t^n} \tag{4.70}$$

There is a freedom of choice in defining both the spring constants $k_{i\pm 1/2}$ and the spring rest lengths $\delta x_{i\pm 1/2}$. To achieve our desired Lagrangian behavior, we set the spring rest lengths based on the fluid velocity

$$\delta x_{i+1/2} = r_{i+1}^n - r_i^n + (v_{i+1}^n - v_i^n)\Delta t^n \tag{4.71}$$

where $v_i = \left(v_{i+1/2} + v_{i-1/2}\right)/2$ is the face average of the cell-centered velocities $v_{i\pm 1/2}$. Next, we prevent mesh distortion by enforcing a minimum δx_{min} and maximum δx_{max} for the spring rest lengths, i.e.

$$\delta x_{i+1/2} = \min\left\{\delta x_{max}, \max\left[\delta x_{min}, r_{i+1}^n - r_i^n + \left(v_{i+1}^n - v_i^n\right)\Delta t^n\right]\right\} \tag{4.72}$$

The mesh spring length therefore acts to prevent the cell from being compressed below δx_{min}, or from becoming too large above δx_{max}. This spring resistance then affects the rest of the mesh nodes in the domain to account for the nonzero force resulting from non-Lagrangian mesh motion. In practice, we set $\delta x_{max} = L/N_{cell}$ and $\delta x_{min} = f_{spring} L$, where L is the domain size and $f_{spring} = 10^{-5}$ for this work. Note that for $\delta x_{max} \to \infty$ and $\delta x_{min} \to 0$, the mesh springs will give purely Lagrangian motion.

The mesh spring constants determine the degree to which cells will adjust to compensate for any non-Lagrangian motion in the grid (i.e. around the shock front). Stiffer springs (i.e. larger spring constants) will tend to resist deviations from Lagrangian cell motion as well as the cell minimum/maximum size thresholds. We set the spring constants to be inversely proportional to the cell sizes at the begining of the timestep,

$$k_{i+1/2} = \left(r_{i+1}^n - r_i^n\right)^{-1} \tag{4.73}$$

Our numerical tests show that this choice of spring constant provides the desired behavior of concentrating the mesh resolution around the shock region. At each timestep, the coupled system of linear equations is solved for the mesh spring positions to get the mesh velocity during the timestep In 1D, this forms a tridiagonal system of equations which we solve using Thomas' algorithm [179], incurring negligible cost compared to the hydrodynamics and radiation substeps.

4.4 Non-LTE Atomic Kinetics

The atomic state of the gas is given by the number densities (or atomic populations) of level j for each charge state/ion i for all species. Let n_{ij} denote the number density of level j of charge state i, normalized such that

$$\sum_i \sum_j n_{ij} = n \tag{4.74}$$

where n is the total species number density. Additionally, let Q_i denote the charge state/ionization fraction for charge state i, normalized such that

$$\sum_i Q_i = 1 \tag{4.75}$$

Furthermore, let f_{ij} denote the *relative* level population for a level *within* charge state i, normalized such that

$$\sum_j f_{ij} = 1 \tag{4.76}$$

Thus, we can write the individual level number density as

$$n_{ij} = Q_i f_{ij} n \tag{4.77}$$

Local Thermodynamic Equilibrium (LTE)

In local thermodynamic equilibrium (LTE), the relative level population is given by a Boltzmann distribution at the local electron temperature T_e, i.e.

$$f_{ij} = \frac{g_{ij}}{\mathcal{Z}_i} e^{-\beta E_{ij}} \tag{4.78}$$

where $\beta = 1/k_b T_e$ is the inverse temperature; g_{ij} is the level statistical weight/degeneracy; and

$$\mathcal{Z}_i(T_e) = \sum_j g_{ij} e^{-\beta E_{ij}} \tag{4.79}$$

is the ion partition function.

The charge state distribution Q_i is given in LTE by the Saha equation, where the relative population of two successive ionization states is [50, 75]

$$\frac{Q_{i+1}}{Q_i} = \frac{1}{n_e \lambda^3} \frac{2\mathcal{Z}_{i+1}}{\mathcal{Z}_i} e^{-\beta \chi_i} \tag{4.80}$$

where χ_i is the ground ionization energy of charge state i, and the thermal electron de-Broglie wavelength is given by

$$\lambda = \left(\frac{h^2}{2\pi m_e k_b T_e} \right)^{1/2} \tag{4.81}$$

As the Saha equation only gives *relative* charge populations for successive ionization states, we need to normalize to get the actual charge distribution. Care must be taken when doing this numerically, as the partition function ratio can become enormous and so a direct normalization may run into machine-precision errors.

What one can instead do is first search for the iso-sequence peak. This is done as follows: starting with the neutral charge state, we iterate until we find the first ratio such that $Q_{i+1}/Q_i < 1$, which is identified as the isosequence peak i_{pk}. We then arbitrarily set the charge population $Q_{i_{pk}} = 1$. We then work left and right of the isosequence peak by setting the neighboring charge states using the ion ratios calculated using Eq. (?). Finally, we then renormalize all charge states so that $\sum_i Q_i = 1$.

Finally, note that the charge state distribution (CSD) depends on the electron number density n_e, which itself depends on knowledge of the CSD,

$$n_e = n \sum_{i>0} (i \times Q_i) \tag{4.82}$$

where we skip the neutral state $i = 0$ since it contributes no free electrons. Thus, we must iterate the equation for charge conservation along with the Saha-Boltzmann distribution (although note that the ion partition functions and relative level populations only need to be calculated once). We use a Brent-Dekker root-finding algorithm to accomplish this numerically, and set a fractional electron number density convergence threshold of 10^{-3}. This method is easily generalized to an arbitrary mixture of multiple atomic species.

Once the charge state distribution Q_i and relative level populations f_{ij} are known, then we can evaluate individual atomic opacities and other quantities of interest, such as the mean molecular weight for the equation of state (EOS).

Non-Local Thermodynamic Equilibrium (NLTE)

When LTE no longer holds, we must instead solve a system of rate equations for the level populations and charge state distribution [50, 180].

The rate equations are given by

$$\frac{dn_{ij}}{dt} = -n_{ij} \left(\mathcal{I}_{ij} + \sum_{k \neq j} \mathcal{E}_{i,j \to k} \right) + \sum_{k \neq j} n_{ik} \mathcal{E}_{i,k \to j} + \sum_l n_{i+1,l} \mathcal{R}_{i+1,l \to j} + \sum_l n_{i-1,l} \mathcal{I}_{i-1,l \to j} \tag{4.83}$$

The first term in parentheses gives the loss rate due to ionizations and recombinations $\mathcal{I}_{ij}$ out of the charge state i, as well as (de)-excitations $\mathcal{E}_{i,j \to k}$ within the charge state. These include

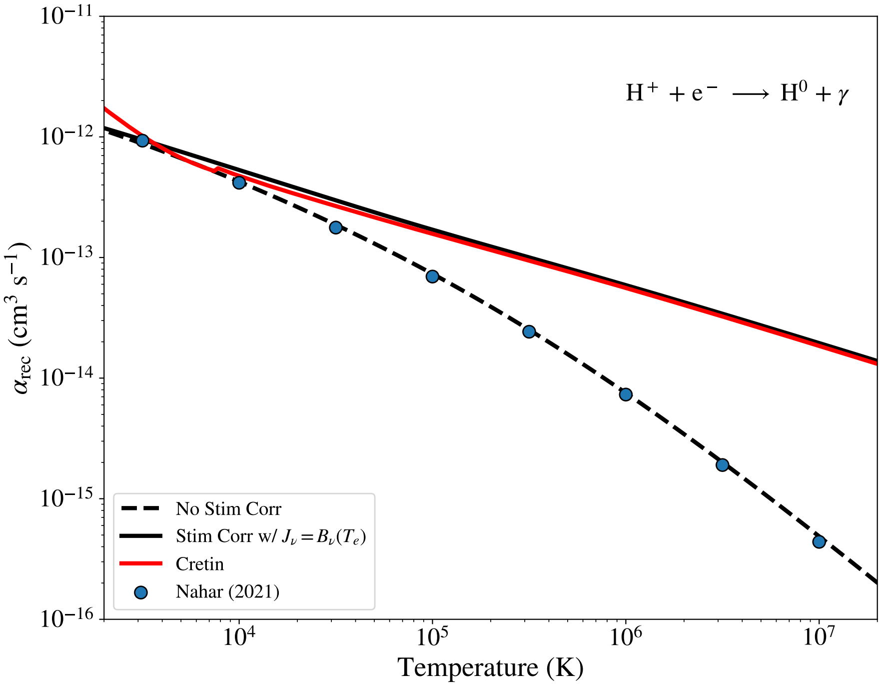

Figure 4.1: Radiative recombination rate coefficient of hydrogen. Black lines show Sedona for the case of spontaneous (dashed) and spontaneous+stimulated recombination (solid). For comparison, we show the recombination rate calculated with Cretin [181](red line) as well as the results of Nahar [182].

both radiative and collisional contributions. The second term accounts for (de)-excitations into the (i, j) state from within the charge state i; the third and fourth terms gives potential contributions from ionization and recombinations of a different charge state into the (i, j) state (three-body, radiative, and dielectronic). These are typically only non-zero if j is either a ground state or $K-$ or $L-$ shell state [181](i.e. inner hole state).

The ionization/recombination rate from the (i, j) state is given by a combination from collisional and photoionization processes:

$$\mathcal{I}_{ij} = \mathcal{P}_{ij}(J_\nu) + n_e\mathcal{C}_{ij}(T_e) + n_e \sum_l \left[\mathcal{R}_{i,j\to l}(J_\nu, T_e) + n_e\mathcal{C}_{i,j\to l}(T_e)\right] \tag{4.84}$$

The first and second terms account for photoionization and collisional ionizations, respsectively. The third term in brackets gives the radiative (spontaneous+stimulated) and three-body recombination rates into a level of charge state $i-1$, if (i, j) is a ground or inner-shell state. Note that we do not include excitation/ionization from non-thermal electrons, which could be additional terms in the rate equation.

The (de)-excitation rates are given by

$$\sum_{k\neq j}\mathcal{E}_{i,j\to k} = \sum_{l<j}\left[\mathcal{A}_{i,j\to l} + \mathcal{B}_{i,j\to l}\bar{J} + n_e\mathcal{C}_{i,j\to l}(T_e)\right] + \sum_{u>j}\left[\mathcal{B}_{i,j\to u}\bar{J} + n_e\mathcal{C}_{i,j\to u}(T_e)\right] \tag{4.85}$$

The first term in brackets gives the de-excitation rate of state (i,j) into a lower state (i,l) with $l<j$, where $\bar{J}$ is the mean intensity averaged over the transition line profile (and assuming complete redistribution within the line). $\mathcal{A}_{i,j\to l}$ and $\mathcal{B}_{i,j\to l}\bar{J}$ give the spontaneous and stimulated radiative emission contributions, respectively; and $n_e\mathcal{C}_{i,j\to l}(T_e)$ gives the collisional de-excitation rate. Similarly, $\mathcal{B}_{i,j\to u}\bar{J}$ and $n_e\mathcal{C}_{i,j\to u}(T_e)$ give the radiative (photoabsorptive) and collisional excitation rates.

Note that the electron number density n_e appears in the collisional and recombination terms. As such, the rate equations must be iterated along with the equation of charge conservation, just as in the LTE case. We use the Brent-Dekker root-finding algorithm for this as well, the major difference in the NLTE case being the need to re-evaluate the rates for each iteration. Note that we hold the radiation field J_ν fixed throughout the iterations.

Autoionizing Resonances and Dielectronic Recombination

At this point it is worth discussing how autoionization and dielectronic recombination are handled. Some codes such as CMFGEN [52] treat autoionizing transitions as resonances in the bound-free cross-section. Indeed, the process looks fairly similar to a photoionization and radiative recombination if the energy carrier is a photon (versus say a collisional transition)

$$X_i + h\nu \Longleftrightarrow X_i^* \Longleftrightarrow X_{i+1} + e^- \tag{4.86}$$

Here, X_i^* denotes an autoionizing state within charge state i, which is a metastable atomic state whose energy lies above the ionization threshold. As this is a metastable state, it will either decay (via a radiative or collisional transition) into a lower energy level of charge state i, or undergo an autoionization resulting in the ejection of a free electron and an ion in charge state $i+1$. The inverse process, known as dielectronic recombination, occurs when a free electron comes into resonance with a nucleus in charge state $i+1$, a process known as resonant capture. If this metastable configuration then decays to a non-autoionizing bound state, then the net outcome is a recombination.

Our approach is to explicitly include such autoionizing states, which act as an intermediary between two successive charge states. As such, the process of autoionization is accounted for due to radiative and collisional excitations of a bound state (i,j) into an autoionizing state (i,a), which appears as a normal excitation term in $\mathcal{E}_{i,j\to a}$. These autoionizing states are distinct from a bound state since, in addition to normal radiative decay into a lower bound state (i,j) they also have a "spontaneous autoionization" rate $\mathcal{A}_{i,a}$ into the $i+1$ charge state that acts as an additional term in $\mathcal{I}_{ij}$. The inverse process of resonant capture and can be obtained from detailed balance [181, 183].

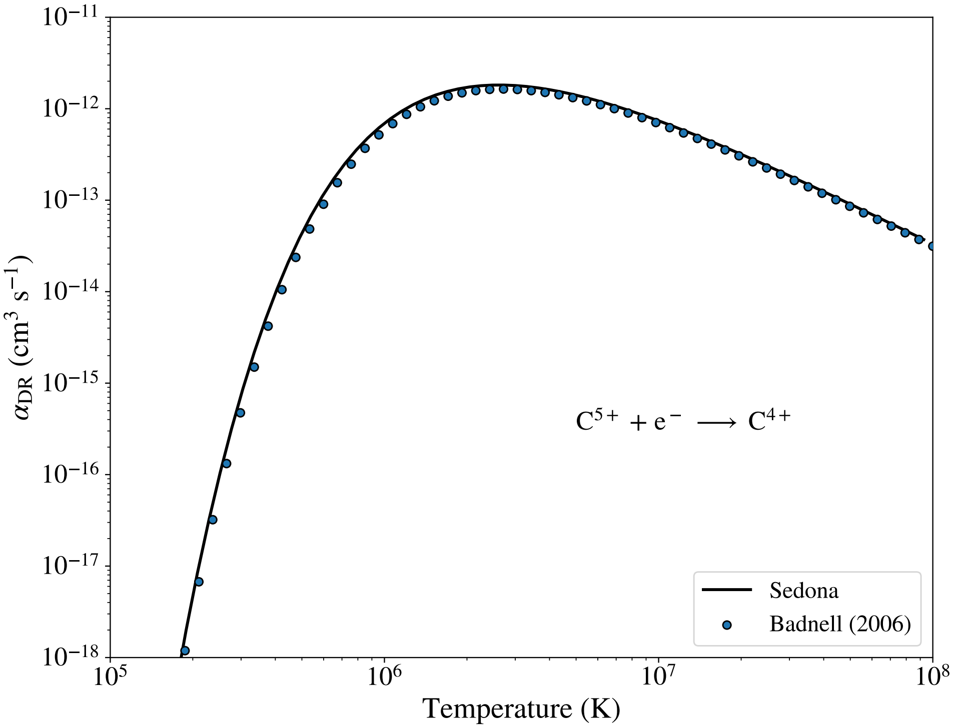

Figure 4.2: Dielectronic recombination rate coefficient of C V. For comparison, we show the AUTOSTRUCTURE results [183], showing excellent agreement.

Numerical Methods

We assume statistical equilibrum [50], also referred to as steady-state, in evaluating the level populations and charge state distribution, i.e.

$$\frac{dn_{ij}}{dt} = 0 \tag{4.87}$$

Due to the large dynamic range of the level populations, we prefer instead to work with the *departure coefficients* [184]

$$b_{ij} = \frac{n_{ij}}{n^\star_{ij}} \tag{4.88}$$

where $n^\star_{ij}$ denotes the level population under LTE conditions. Namely, in LTE, all departure coefficients evaluate to $b_{ij} = 1$. Given the radiation field J_ν, local electron temperature T_e, and the current iteration value of n_e, we evaluate all collisional and radiative rates for each zone. We then solve the linear system of equations

$$\mathbf{M}\mathbf{b} = \mathbf{c} \tag{4.89}$$

where $\mathbf{M}$ is the rate matrix consisting of all the levels of all charge states of each species; and $\mathbf{b} = b_{ij}$. Note that we close the system using the statement of number conservation

$$\sum_{ij} n_{ij} = n \tag{4.90}$$

where

$$n = \frac{\rho x}{A m_p} \tag{4.91}$$

is the total species number density, x the mass fraction, and A the atomic weight. In practice, this is accomplished by replacing one of the rows r of the rate matrix with entries equal to $n^{\star}_{ij}/n$, and the right hand side to

$$\mathbf{c} = \begin{bmatrix} 0 \\ 0 \\ \vdots \\ 1 \\ 0 \\ \vdots \\ 0 \end{bmatrix} \tag{4.92}$$

where the nonzero entry corresponds to the r-th row.

The rate matrix can be ill-conditioned and cause numerically unstable results for the level populations, such as negative or NaN values [180]. We therefore multiply the number conservation row (and right hand side) by a constant factor equal to $|\mathrm{tr}(\mathbf{M})|$, which denotes the absolute value of the trace of the rate matrix.

The linear system is solved using the Eigen numerical linear algebra library [185]. As the number conservation row results in a non-block-diagonal structure, we are forced to use a dense solver routine. However, given that we are using reduced atomic models that consist of at most several hundred levels per species [181], the performance cost is usually modest. We solve the system by performing an LU decomposition with full pivoting [186]. We have found that partial pivoting is numerically unstable for elements heavier than helium.

4.5 NLTE Solver Acceleration Techniques

Including an NLTE solution inline for every zone in the mesh, at each timestep, can quickly dominate the computational expense relative to the other physics including transport, the latter of which is typically what we want to keep as the most expensive physics substep [181]. Without appropriate acceleration, this added expense can bog down the simulations to the point of being unable to fully run simulations long enough for the desired science results. This is no good. As such, we have implemented several user-configurable acceleration methods for speeding up the NLTE kinetics step, which we describe below.

Near-LTE Switch

The easiest NLTE acceleration technique is to simply do an LTE solution when certain criteria are met. At extremely high temperatures and low densities, all species will be near or completely ionized, and so an LTE solution will typically suffice (especially since the dominant opacity will come from free-free rather than bound transitions, and so we can get away with less accurate level and charge state information). We set a maximum temperature T_{max} above which we perform a simple LTE solution. For the elements used in our simulations we typically set $T_{max} = 3 \cdot 10^8$ K. This forces the shocked circumstellar gas, which can contain a pileup of zones due to the Lagrangian/ALE compression of the mesh at shock fronts, to use the approximate LTE solution.

We have also implemented another more sophisticated LTE switch that compares the gas and radiation temperatures. Given the radiation field J_ν, we can define a radiation temperature

$$T_r = \left(\frac{E_0}{a}\right)^{1/4} \tag{4.93}$$

where $E_0 = (4\pi/c)\int J_\nu d\nu$. We then compare the fractional difference of T_r with the local electron temperature, relative to a user-defined threshold ϵ. If

$$\frac{|T_r - T_e|}{T_e} < \epsilon \tag{4.94}$$

then the local conditions are likely close to LTE, and we activate the switch. We use $\epsilon = 0.1$ as a fiducial value for our simulations. Note that it is possible for T_r and T_e to still be close and not in LTE conditions; in these cases, other indicators might be better suited, e.g. the color temperature or deviation from B_ν.

Isosequence Windows

In most plasmas of interest, there are usually only a handful of charge states that contain non-negligible populations. For example, it is unnecessary (and potentially even more numerically unstable) to solve the full linear system of e.g. Fe containing all levels of all 27 charge states.

What we can instead do is retain only the levels from the relevant charge states, which is accomplished by defining an isosequence window around the peak charge state. Let i_{pk}

denote the isosequence peak. We define an isosequence width Δi_{iso}, i.e. our isosequence window consists of charge states in the range $[i_{min}, i_{max}]$, where

$$i_{min} = \max\{0, i_{pk} - \Delta i_{iso}\} \tag{4.95}$$

$$i_{max} = \min\{i_{pk} + \Delta i_{iso}, Z\} \tag{4.96}$$

The total number of charge states we keep is therefore at most $N_{max} = 2\Delta i_{iso} + 1$. For species with $Z \leq N_{max}$, we therefore retain all charge states. We find $\Delta i_{iso} = 3$ to provide identical results compared to a full isosequence window, and so all charge states are retained for all species up to nitrogen.

The major challenge is identifying what the isosequence peak i_{iso} is in the first place, which itself depends on the NLTE solution. As such, we iteratively solve the NLTE solution using a "sliding window". At first iteration, we set the isosequence peak peak to be the LTE value, $i_{pk} = i^{\star}_{iso}$. We then calculate the rates and solve the linear system consisting of the subsystem of the levels that belong to one of the retained window charge states. From this solution, we then calculate what the new peak is, i'_{pk}. For the next iteration, we then "slide" the isosequence peak as

$$i_{pk}^{(k+1)} = i_{pk}^{(k)} + \text{sign}\left\{i'_{pk} - i_{pk}^{(k)}\right\} \tag{4.97}$$

Namely, we either increment or decrement the next iteration's isosequence peak by one, depending on if the returned NLTE peak is to the left or right of the most recent iterations value. We then repeat this procedure until the k and $k+1$-th isosequence peaks are equal. We find this sliding method to be more stable than simply setting the next iteration of the NLTE solve equal to i'_{pk}, and usually converges in fewer than 2 or 3 iterations (or 0 if in LTE conditions).

Selective Charge Conservation

One of the major slowdowns in evaluating the NLTE solution is due to the fact that the free electron number density n_e appears in several of the rate quantities (collisonal and recombination). As such, the NLTE solution must be iterated with the statement of charge conservation, thus requiring a new NLTE solution at every iteration. However, it is often the case that only one or two elements will dominate the contribution to n_e, such as hydrogen and helium in solar-composition plasmas.

We can accelerate the solve by *excluding* the NLTE solution from all elements other than e.g. hydrogen and helium within the charge conservation iterations. Once n_e has been appropriately converged with the retained NLTE species solutions, we then follow up and perform a single NLTE solve for the skipped species using the n_e returned by the iterated solution. We then correct for n_e by adding on the contribution from the skipped species. If warranted, we re-solve the NLTE solution using the corrected n_e for all species if larger than the uncorrected value by a specified amount (e.g. 10%).

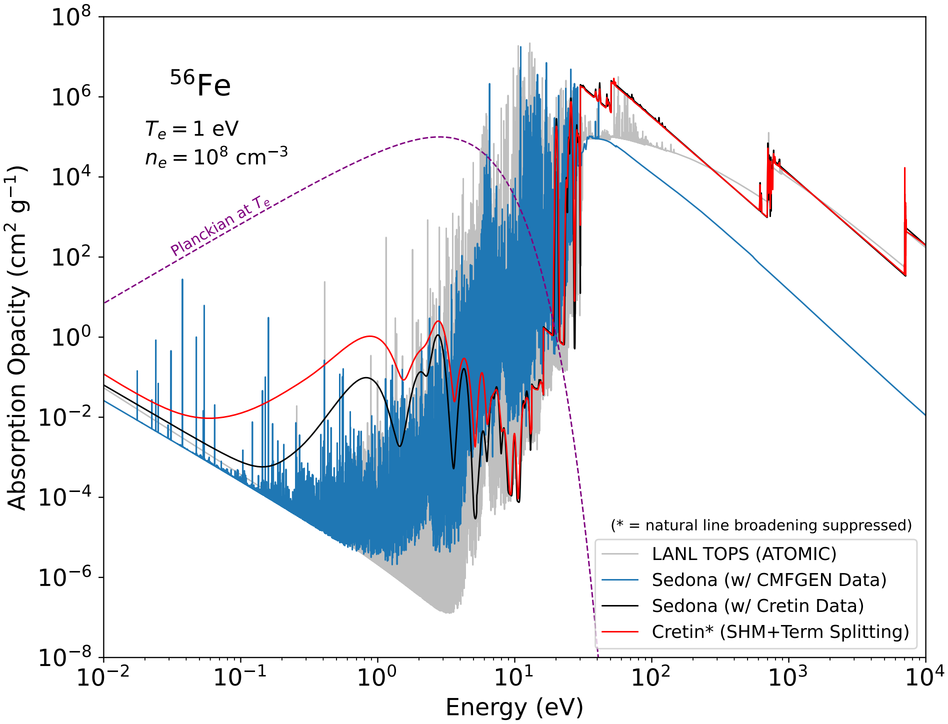

Figure 4.3: Iron absorption opacity at supernova-relevant conditions. The DCA opacities [181] used in this work are shown as a solid black line, giving overall good agreement compared to when run with the Cretin code (red line). The blue line shows the iron opacity when using the CMFGEN atomic data [52], which itself uses the Kurucz linelist [75, 187]. The iron opacity provided by LANL TOPS [48] is also shown for copmarison (grey line).

Hydrogen and helium only have 1 and 2 bound charge states and therefore have much fewer levels than metals. Given that the electron number density can be slow to converge (which from experience typically requires 10-30 Brent iterations for optically thin regions in CSM interaction problems), bypassing the heavier elements can result in enormous computational savings up to an order of magnitude or more.

4.6 Radiative Opacity and Emissivity

Once the kinetic state state of the plasma is known, we can then calculate the radiative opacities and emissivities used by the transport package. While the opacities are defined as continuous in frequency, we assume that we have a discretized frequency grid with bin centers $\{\nu_g\}$ consisting of G groups, which we take to be logarithmically spaced. Opacities and emissivities for that bin are then taken to be constant at the value computed at bin center.

Bound-Free

The bound-free opacity from level j of charge state i of each species is [184]

$$\alpha^{\mathrm{bf}}_{i,j} = n_{ij}\sigma_{ij}(\nu) - n_{i+1,c}\sigma_{ij}(\nu)\left[\frac{n_{ij}}{n_{i+1,c}}\right]_{\star} e^{-h\nu/k_b T_e} \tag{4.98}$$

The first term is the direct extinction from photo-absorption, while the second term accounts for stimulated emission from the continuum state $(i+1, c)$ that the (i, j) state photoionizes to. The star denotes quantities in LTE and is given by a Saha-Boltzmann distribution as

$$\left[\frac{n_{ij}}{n_{i+1,c}}\right]_{\star} = \lambda^3 n_e \frac{g_{ij}}{2g_{i+1,c}} e^{\tilde{\chi}_{ij}/k_b T_e} \tag{4.99}$$

where $\tilde{\chi}_{ij} = \chi_{ij} + \epsilon_{i+1,c}$ with χ_{ij} the ionization energy of the (i, j) ionizing state, and $\epsilon_{i+1,c}$ is the excitation energy above ground of the continuum state being ionized into ($\epsilon_{i+1,c} = 0$ if the continuum state is the ground state of $i+1$). The thermal electron de-Broglie wavelength is given by

$$\lambda = \left(\frac{h^2}{2\pi m_e k_b T_e}\right)^{1/2} \tag{4.100}$$

As such, we can write the opacity as

$$\alpha^{\mathrm{bf}}_{ij}(\nu) = n_{ij}\sigma_{ij}(\nu) - n_{i+1,c} n_e \sigma_{ij}(\nu)\Phi_{ij}(\nu, T_e) \tag{4.101}$$

where

$$\Phi_{ij}(\nu, T_e) = \lambda^3 \frac{g_{ij}}{2g_{i+1,c}} \exp\left[-\left(h\nu - \tilde{\chi}_{ij}\right)/k_b T_e\right] \tag{4.102}$$

The total bound-free opacity from each species is then summed over all levels of all ionizing states

$$\alpha^{\mathrm{bf}}_{\nu} = \sum_{i,j} \alpha^{\mathrm{bf}}_{ij}(\nu) \tag{4.103}$$

We can alternatively use the total species number density n, the charge state distribution Q_i, and relative level populations f_{ij}, such that the level number density is given by $n_{ij} = nQ_i f_{ij}$, and so

$$\frac{\alpha^{\mathrm{bf}}_{\nu}}{n} = \sum_i \sum_j Q_i f_{ij}\sigma_{ij}(\nu) - n_e \sum_i \sum_j Q_{i+1} f_{i+1,c}\Phi_{ij}(\nu, T_e)\sigma_{ij}(\nu) \tag{4.104}$$

Similarly, the bound-free emissivity is given by

$$j_{ij}^{\rm bf}(\nu) = n_{i+1,c}\sigma_{ij}(\nu)\left[\frac{n_{ij}}{n_{i+1,c}}\right]_\star \left(1 - e^{-h\nu/k_b T_e}\right) B_\nu(T_e) \tag{4.105}$$

$$= \frac{2h\nu^3}{c^2} n_{i+1,c}\sigma_{ij}(\nu)\left[\frac{n_{ij}}{n_{i+1,c}}\right]_\star e^{-h\nu/k_b T_e} \tag{4.106}$$

We can rewrite this expression as

$$j_{ij}^{\rm bf}(\nu) = \frac{2h\nu^3}{c^2} n_{i+1,c} n_e \sigma_{ij}(\nu)\Phi_{ij}(\nu, T_e) \tag{4.107}$$

The total bound-free emissivity from each species is then

$$j_\nu^{\rm bf} = \frac{2h\nu^3}{c^2} n_e \sum_i \sum_j n_{i+1,c}\Phi_{ij}(\nu, T_e)\sigma_{ij}(\nu) \tag{4.108}$$

Again using the total species number density and the charge+level state distributions, we have

$$\frac{j_\nu^{\rm bf}}{n} = \frac{2h\nu^3}{c^2} n_e \sum_i \sum_j Q_{i+1} f_{i+1,c}\Phi_{ij}(\nu, T_e)\sigma_{ij}(\nu) \tag{4.109}$$

Free-free

The thermal free-free, or Bremsstrahlug, absorption coefficient for each species is given by [188]

$$\frac{\alpha_{ff}(\nu)}{n} = \frac{4e^6}{3m_e hc}\left(\frac{2\pi}{3k_b m_e}\right)^{1/2} T^{-1/2}\nu^{-3}\left(1 - e^{-h\nu/k_b T}\right) n_e \bar{g}_{ff} \sum_{i>0} i^2 \cdot Q_i \tag{4.110}$$

where $\bar{g}_{ff}$ is the thermally-averaged free-free Gaunt factor. The free-free emissivity is given through Kirchoff's law

$$j_{ff}(\nu) = \alpha_{ff}(\nu) B_\nu(T) \tag{4.111}$$

We set the Gaunt factor to unity, although there exist accurate tables across a range of densities and temperatures [189]

Bound-bound

The bound-bound opacity from a transition from lower level l to upper level u, assuming complete redistribution in the line, is [184]

$$\chi_\nu^l = \frac{h\nu}{4\pi} n_l B_{lu}\phi_{lu}(\nu)\left[1 - \frac{n_u g_l}{n_l g_u}\right] \tag{4.112}$$

where B_{lu} is the Einstein B coefficient, $\phi_{lu}(\nu)$ is the line profile of the transition, and the term in brackets corrects for stimulated emission. We can write this in terms of the total line cross section as

$$\chi^l_\nu = n_l \sigma_{lu} \phi(\nu) \left[1 - \frac{n_u g_l}{g_l n_u} \right] \tag{4.113}$$

where

$$\sigma_{lu} = \frac{\pi e^2}{m_e c} f_{lu} \tag{4.114}$$

and the oscillator strength is given in terms of the spontaneous emission coefficient as

$$f_{lu} = \frac{m_e c^3}{8\pi^2 e^2 \nu_0^2} \frac{g_u}{g_l} A_{ul} \tag{4.115}$$

where $h\nu_0 = E_u - E_l$ is the frequency of the transition.

The total bound-bound emissivity is given in terms of its source function as

$$j^l_\nu = \alpha^l_\nu S^l_\nu \tag{4.116}$$

where

$$S^l_\nu = \frac{2h\nu^3}{c^2} \frac{1}{\frac{g_u n_l}{g_l n_u} - 1} \tag{4.117}$$

Total bound-bound opacities and emissivities are then taken as the sum of all included transitions between levels of all charge states.

If the line profile is dominated by thermal Doppler broadening (which is usually a good approximation at high temperatures and low densities), then it is given as a Gaussian with

$$\phi(\nu) = \frac{1}{\sqrt{\pi}\Delta\nu_d} e^{-(\nu-\nu_0)^2/\Delta\nu_d^2} \tag{4.118}$$

where

$$\Delta\nu_d = \frac{\nu_0}{c} v_{th} \tag{4.119}$$

and $v_{th} = \sqrt{2k_b T/m_i}$ is the thermal ion velocity.

As our atomic levels are in reality superconfigurations that consist of an averaging over levels with the same principal quantum number [181, 190, 191], transitions are instead given as unresolved transition arrays (UTAs) with a UTA energy width ΔE [180, 192]. The UTA contribution is added to the Doppler broadening as $\Delta\nu = \Delta\nu_d + \Delta E/h$.

Approximate Unresolved Line Treatment

For the radiation hydrodynamics simulations, it will often be the case that the frequency mesh is too coarse to resolve individual line profiles. As such, we require an approximate treatment of line absorption and emission without needing to perform full spectral line transport. We therefore average photo-excitations over the frequency group in which they fall in. I.e.

$$\phi(\nu) = \begin{cases} 1/\Delta\nu_g, & \nu_{g-1/2} \leq \nu \leq \nu_{g+1/2} \\ 0, & \text{otherwise.} \end{cases} \tag{4.120}$$

Next, we need to make sure that, in LTE, the source function correctly reduces to the Planck function. We start with the expression from the equivalent two-level atom approach [50], which approximates the source function as

$$S_\nu = \epsilon_\nu B_\nu + (1-\epsilon_\nu)\bar{J} \tag{4.121}$$

We rewrite this to get an expression for $\epsilon_n u$ as

$$\epsilon_\nu = \frac{S_\nu - \bar{J}}{B_\nu - \bar{J}} \tag{4.122}$$

Clearly when $S_\nu = B_\nu$ for LTE, $\epsilon_\nu = 1$.

The thermal contribution to the opacity and emissivity is given by

$$\epsilon_\nu = \frac{S_\nu}{B_\nu} \tag{4.123}$$

The thermal line emissivity is then written as

$$j_\nu^l = \epsilon_\nu \chi_\nu^l B_\nu \tag{4.124}$$

While this may seem like a pointless rewriting of the same thing, it is numerically advantageous for unresolved line profiles. The reason for this is that the source function is defined in terms of the atomic level populations, therefore:

$$\epsilon_\nu = \frac{S_\nu}{B_\nu} = \frac{\exp\left[h\nu_0/k_b T - 1\right]}{\dfrac{g_u n_l}{g_l n_u} - 1} \tag{4.125}$$

However, our frequency grid is defined in terms of bin center frequencies $\nu_g \neq \nu_0$, i.e. the frequency at which opacities and emisisvites are defined is not the same as the transition frequency. By writing the line epsilon in this way, we ensure that LTE is correctly recovered for the radiation field and therefore level populations.

Next, we account for potential trapipng and destruction of lines through the use of escape factors [193, 194]. Our net line emissivity equation therefore becomes

$$j_\nu^l = \epsilon_\nu \chi_\nu^l B_\nu P^l \tag{4.126}$$

where $P^l \in \{0,1\}$ are the escape factors. If lines are either trapped in resonance at the excitation, or destroyed by some other means such as collisional de-excitation, then $P^l \to 0$. On the other hand, if line radiation is able to freely escape from the emitting region, then $P^l \to 1$.

We write the escape factors consisting of both a resonant line scattering escape in the wings contribution, as well as line destruction probability, as

$$P^l = P_{esc} \times (1 - P_{th}) \tag{4.127}$$

The static escape probabilities are taken from [193] using the Holstein factors

$$P_{static} = \left\{ \begin{array}{ll} \tau_0^{-1} \left(\pi \ln \tau_0\right)^{-1/2}, & \tau_0 \geq 2.5 \\ \exp\left[-\tau_0/1.73\right], & \tau_0 < 2.5 \end{array} \right\} \tag{4.128}$$

where

$$\tau_0 \approx \frac{n_l \sigma_{lu}}{\Delta\nu_d} L \tag{4.129}$$

and L is a characteristic length scale of the problem, which we take to be the zone size.

In addition to the static escape factors, we also account for line escape due to velocity gradients using the Sobolev approximation [194]:

$$P_{sob} = \frac{1 - \exp\left[-\tau_s\right]}{\tau_s} \tag{4.130}$$

where the Sobolev optical depth is given by

$$\tau_s = \frac{n_l \sigma_{lu}}{\Delta\nu_d} \frac{v_{th}}{|dv/ds|} \tag{4.131}$$

To interpolate between static and Sobolev limits, we use the approximation in [194]

$$P^l = P_{static}(1 - P_{sob}) + P_{sob} \tag{4.132}$$

For strongly scattering lines, it is possible for the line to be "destroyed" by collisional de-excitation [50]. The probability that the line is collisionally de-excited is

$$P_{th} = \frac{1}{1 + \dfrac{A_{ul}}{n_e \mathcal{C}_{ul} \Delta\tau_l}} \tag{4.133}$$

where we use van Regemorter's approximation [195] for the collisional rate coefficient:

$$\mathcal{C}_{ul} \approx 3.9 \frac{k_b T}{h\nu_0} T^{-3/2} \frac{g_l}{g_u} f_{lu} \tag{4.134}$$

Note that the rate of collisional de-excitation is increased by a factor equal to the line optical depth $\Delta\tau_l$, as each line scatter provides another opportunity for the line to be collisionally de-excited.

The final form for our net line emissivity, accounting for potential line trapping and collisional line destruction, is

$$j^l_\nu = \epsilon_\nu \chi^l_\nu B_\nu P_{esc}(1 - P_{th}) \tag{4.135}$$

In order to correctly recover LTE conditions and radiative equilibrium, we therefore add an absorptive opacity contribution equal to

$$\alpha^l_\nu = \frac{j^l_\nu}{B_\nu} \tag{4.136}$$

The net effect of this approximation is that line emission is suppressed in highly optically thick or collisionally dominated regions, effectively assuming they are destroyed. In optically thin regions, we get a reasonable approximation for the emissivity for e.g. line cooling. Note that the inclusion of a non-zero opacity is a strictly numerical kluge, as the use of escape factors presumes the opacity to be zero once the line escapes. As mentioned earlier, the kluge is necessary to get correct temperature behavior in optically thick regions by forcing the source function to B_ν [180].

Non-thermal Synchrotron

We allow for the possibility of synchrotron absorption and emission due to a population of non-thermal electrons. The synchrotron emissivity emitted by a non-thermal electron with energy $\varepsilon = \gamma m_e c^2$ and Lorentz factor γ, averaged over pitch angle, is [143]

$$P(\nu, \gamma) = \frac{\sqrt{3}}{2} \frac{e^3 B}{m_e c^2} \mathcal{F}\left(\frac{\nu}{\nu_c}\right) \tag{4.137}$$

where B is the magnetic field strength,

$$\nu_c(\gamma) = \gamma^2 \frac{eB}{2\pi m_e c} \tag{4.138}$$

and the dimensionless function $\mathcal{F}(x)$ is given by

$$\mathcal{F}(x) = x \int_x^\infty K_{5/3}(\xi) d\xi \tag{4.139}$$

where $K_{5/3}(\xi)$ is the modified Bessel function of the second kind with order 5/3. The asymptotic limits are

$$\mathcal{F}(x) \approx \begin{cases} \frac{4\pi}{\sqrt{3}\Gamma(\frac{1}{3})} \left(\frac{x}{2}\right)^{1/3} & x \ll 1 \\ \sqrt{\frac{\pi}{2}} e^{-x} x^{1/2} & x \gg 1 \end{cases} \tag{4.140}$$

We find a good functional fit to better than 1% with the piecewise approximation

$$\mathcal{F}(x) \approx \begin{cases} 1.32x^{1/3} & x \leq 10^{-3} \\ 0.84x^{0.27} & 10^{-3} < x \leq 0.2 \\ 0.57e^{-0.3x^2} & 0.2 < x \leq 2 \\ 0.96x^{1/2}e^{-x} & x > 2 \end{cases} \tag{4.141}$$

Let $N(\gamma)d\gamma$ denote the number density of non-thermal electrons with Lorentz factor between γ and $\gamma + d\gamma$. The total synchrotron emissivity is therefore given by

$$j_\nu^{synch} = \int P(\nu, \gamma) N(\gamma)\, d\gamma \tag{4.142}$$

In addition to emissivity, synchrotron can also act as an absorption source, commonly referred to as synchrotron self-absorption when referring to absorption of the synchrotron emissivity from the same non-thermal electrons.

The synchrotron absorption coefficient is given by [188]

$$\alpha_\nu^{synch} = \frac{c^2}{8\pi h\nu^3} \int \varepsilon^2 P(\nu, \varepsilon) \left[\frac{N(\varepsilon - h\nu)}{(\varepsilon - h\nu)^2} - \frac{N(\varepsilon)}{\varepsilon^2}\right] d\varepsilon \tag{4.143}$$

where again $\varepsilon = \gamma m_e c^2$. Several textbooks [188, 196] then expand to first order in $h\nu$ to get

$$\alpha_\nu^{synch} = -\frac{c^2}{8\pi\nu^2} \int \varepsilon^2 P(\nu, \varepsilon) \frac{\partial}{\partial\varepsilon}\left[\frac{N(\varepsilon)}{\varepsilon^2}\right] d\varepsilon \tag{4.144}$$

Here we instead take a different approach, as the derivative of the number density can be subject to numerical noise and may be a poor approximation. We assume that $h\nu \ll \varepsilon$, and so we can rewrite the term in brackets as

$$\frac{N(\varepsilon - h\nu)}{(\varepsilon - h\nu)^2} - \frac{N(\varepsilon)}{\varepsilon^2} \approx -\frac{2h\nu}{\varepsilon^3} N(\varepsilon) \tag{4.145}$$

Thus, the final expression for synchrotron absorption is given by

$$\alpha_\nu^{synch} = -\frac{c^2}{4\pi\nu^2} \int \frac{P(\nu, \varepsilon)}{\varepsilon} N(\varepsilon) d\varepsilon \tag{4.146}$$

Note that this is identical to the expression derived in [188] for the case of a power-law distribution of electrons, up to a constant factor equal to $(p + 2)/2$.

4.7 Compton Scattering

The electron scattering coefficient is given by

$$\chi_{es}(\nu) = n_e \sigma_T F_{KN}(\nu) \tag{4.147}$$

where n_e is the free electron number density, $\sigma_T = 8\pi e^4/3m_e^2c^4$ the Thomson cross section, and

$$F_{KN}(\nu) = \frac{3}{4}\left(\frac{1+x}{x^2}\left[\frac{2(1+x)}{1+2x} - \frac{\ln(1+2x)}{x}\right] + \frac{\ln(1+2x)}{2x} - \frac{1+3x}{(1+2x)^2}\right) \tag{4.148}$$

is the Klein-Nishina correction where $x = h\nu/m_ec^2$. In the limit that $x \ll 1$ ($h\nu \ll m_ec^2$), $F_{KN} = 1$ [188].

We take the approach done in [197], which takes its implementation from [198] while accounting for relativistic effects by using a Maxwell-Juttner distribution for the thermal electrons, which is important in the high shock temperatures reached during CSM interaction. After being transformed into the comoving frame of the plasma, the photon is additionally transformed into the electron rest frame by using a rejection sampling technique to get the electron velocity vector in the comoving frame, $\mathbf{v}_e$. This is due to the fact that it is more likely for the photon to be scattered by electrons moving towards the photon. Once an acceptable electron velocity has been found and the photon moved into the electron rest frame, a new direction is selected by sampling from the differential cross-section of Compton scatering

$$P(\theta, x) = \frac{3}{8}\frac{1}{(1+x-x\cos\theta)^2}\left[x - x\cos\theta + \cos^2\theta + \frac{1}{1+x-\cos\theta}\right] \tag{4.149}$$

Once the direction has been selected, the new packet frequency and energy, in the electron rest frame, are

$$\frac{\nu'}{\nu} = \frac{E'}{E} = \frac{1}{1+x(1-\cos\theta)} \tag{4.150}$$

The photon is then Lorentz transformed out of the electron rest frame, and then again from the comoving to the lab frame. The difference in energy before and after the scatter is tallied in a Compton absorption quantity E_{comp}, which is negative if there is a net gain of energy of the photons from the electrons (i.e. inverse Compton cooling).

Test Problem

We follow the problem description and setup as in [197]. Photons with number density n_γ are initialized at a single frequency ν_0 in a uniform static region of fully ionized gas with initial electron temperature T_i and number density n_e, with electrons constituting a fraction f_e of the total number density of particles. Gas and radiation exchange energy via Compton scattering until they come into equilibrium at a temperature T_c, with the radiation forming a Wien spectrum with chemical potential μ_c.

The mean intensity of the Wien equilibrium distribution is

$$J_\nu = \frac{2h\nu^3}{c^2}\exp\left[-\left(\frac{h\nu}{kT_c} + \mu_c\right)\right] \tag{4.151}$$

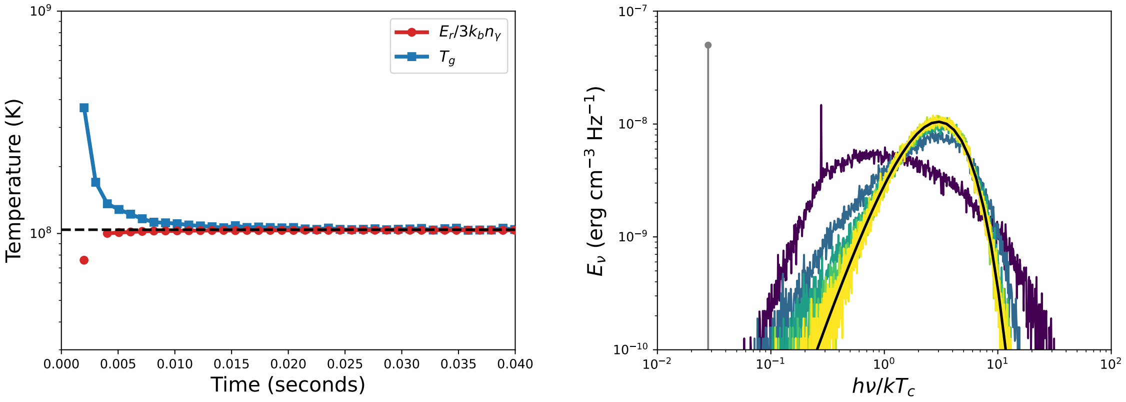

Figure 4.4: Numerical test of Compton scattering. Shown is the evolution of the gas and radiation temperatures to the equilibrium $T_c = 1.04 \times 10^8$ K (left) and the spectrum (right) with photons initially at $h\nu/kT_c \approx 0.028$ (grey) evolving towards the equilbriium Wien distribution Eq. (4.151), indicated by a solid black line.

with a corresponding photon number density of

$$n_\gamma = 16\pi \left(\frac{k_bT_c}{hc}\right)^3 e^{-\mu_c} \tag{4.152}$$

and equilibrium radiation energy density $E_r = 3k_bT_cn_\gamma$. The equilibrium temperature and potential can be solved in terms of the initial conditions to get

$$T_c = \frac{h\nu_0}{k_b} \frac{\frac{k_bT_i}{h\nu_0} + \frac{n_\gamma}{n_e} f_e \left(\gamma_{ad} - 1\right)}{1 + 3\frac{n_\gamma}{n_e} f_e \left(\gamma_{ad} - 1\right)} \tag{4.153}$$

$$\mu_c = -\ln\left[\left(\frac{hc}{k_bT_c}\right)^3 \frac{n_\gamma}{16\pi}\right] \tag{4.154}$$

For our test, we set $T_i = 10^9$ K, $n_e = 2.5\times10^{17}$ cm^{-3}, $n_\gamma = 2.38\times10^{18}$ cm^{-3}, $\nu_0 = 6\times10^{17}$ Hz, $f_e = 0.5$, and $\gamma_{ad} = 5/3$. The equilibrium values are then $T_c = 1.04\times10^8$ K and $\mu_c = 15.9$. The test uses 5×10^4 particles and is run for $t = 0.04$ seconds, with constant timesteps of size $\Delta t = 10^{-6}$ seconds. The results are shown in Fig. 4.4.

4.8 Relativistic Electrons

When the optical depth of the circumstellar shock drops below of order c/v_{sh}, the shock can enter the *collisionless* regime [199], where the shock transition layer is mediated by long-range collective plasma processes rather than coulomb collisions [200]. One interesting aspect of collisionless physics is that it opens up the possibility for efficient shock particle acceleration [200]. This phenomena is responsible for energetic cosmic rays that appear in various contexts, particularly in the field of supernova remnant shocks with the interstellar medium, and their impact on galaxy evolution [201].

In circumstellar shocks, we are interested in possible signatures of this non-thermal electromagnetic emission in supernova light curves. While the bulk of the energy is carried by the ions, the electrons are primarily responsible for any observable emission, particularly at radio and x-ray wavelengths due to synchrotron radiation (although hadronic emission can contribute additional gamma-ray emission, [202]).

A fully self-consistent calculation would require a kinetic approach, such as is done in hybrid PIC codes [200]. Unfortunately, the numerical resolution needed to capture the collisionless transition layer, which is of order the plasma skin depth, can be many orders of magnitude of order $\mathcal{O}(10^3 - 10^6)$ smaller than the dynamical scale of the evolving circumstellar shock. As such, we require a subgrid treatment of the non-thermal electron population that captures the essential physics of injection at the shock front due to particle acceleration, and the energy losses in the plasma as the simulation evolves.

Shock Injection

We base our method on that persented in [203]. Our first step is to identify the phase-space distribution of non-thermal electrons that are injected by a collisionless shock. Let $\varepsilon = \gamma m_e c^2$ be the energy of a non-thermal electron, where γ is the Lorentz factor. Furthermore, let $N(\gamma)d\gamma$ denote the number density of non-thermal electrons with Lorentz factors between γ and $\gamma + d\gamma$.

Suppose a given zone/cell is flagged as containing a shock, with volumetric shock heating rate $\dot{Q}_{sh}$ which we estimate using the method in [166] by comparing the end-of-step internal energy to the isentropic case. We assume that a fraction ϵ_e of the shock heating goes into a population of non-thermal electrons. The change in the non-thermal electron population from shock injection is therefore

$$\left[\frac{dE(\gamma)}{dt}\right]_{sh} = \epsilon_e \dot{Q}_{sh} \mathcal{J}(\gamma) \tag{4.155}$$

where

$$E(\gamma)d\gamma = \gamma m_e c^2 N(\gamma) d\gamma \tag{4.156}$$

is the energy contained in non-thermal electrons, and $\mathcal{J}(\gamma)$ is the shock injection spectrum, normalized such that

$$\int \mathcal{J}(\gamma) d\gamma = 1 \tag{4.157}$$

We assume that the shock injection spectrum is a power-law distribution from γ_{min} to γ_{max},

$$\mathcal{J}(\gamma)d\gamma = C_{\mathcal{J}}\gamma^{-p}d\gamma \tag{4.158}$$

where

$$C_{\mathcal{J}} = (1-p)\gamma_{min}^{p-1}\left[\left(\frac{\gamma_{max}}{\gamma_{min}}\right)^{1-p}\right]^{-1} \tag{4.159}$$

Energy Losses

After the shock injects a population of non-thermal electrons, they will continuously lose energy to several physical processes. One mechanism is through adiabatic expansion of the shocked region:

$$\left[\frac{dE(\gamma)}{dt}\right]_{ad} = -E(\gamma)\nabla\cdot\mathbf{v} \tag{4.160}$$

In spherical symmetry, the divergence evaluates to

$$\nabla\cdot\mathbf{v} = \frac{\partial v}{\partial r} + \frac{2v}{r} \tag{4.161}$$

A special case is homologous expansion $v = r/t$, which gives $\nabla\cdot\mathbf{v} = 3/t$ and so an initial electron population subject purely to adiabatic losses evolves as $E(\gamma) = E_0\,(t/t_0)^{-3}$.

In addition to adiabatic losses, the non-thermal electrons may lose their energy due to Coulomb collisions with thermal electrons. Technically, they can also collide with other non-thermal electrons, but because of the much larger energy $\gamma m_e c^2 \gg k_b T_e$ assumed, they will occur much less frequently.

In the test particle approximation for an electron with energy ε, the rate of plasma energy losses from collisions with a population of thermal electrons with number density n_e and temperature T_e is [203, 204]

$$\left[\frac{d\tilde{\varepsilon}}{dt}\right]_{coll} = -7.7\cdot 10^{-5} n_e \lambda_{ee}\tilde{\varepsilon}^{-1/2}\left(1 - \frac{3.9}{7.7}\frac{T_e}{\tilde{\varepsilon}}\right) \tag{4.162}$$

where $\tilde{\varepsilon} = \varepsilon/1$ MeV is the electron energy measured in MeV, and $\lambda_{ee} \sim 10$ is the Coulomb logarithm for electron-electron collisions. From this, we see that less-energetic electrons will lose energy from Coulomb collisions more quickly compared to more energetic ones. Generally, Coulomb losses will be sub-dominant relative to other loss mechanisms discussed in this section.

Another important process that modifies the non-thermal electron population is from inverse Compton scattering off of “cold” photons, where by cold we mean $h\nu \ll \gamma m_e c^2$. During CSM interaction, the photon population will come primarily from photospheric emission of the supernova at early times, followed by post-shock free-free emission form the forward and reverse shocks. The rate of energy losses due to inverse Compton scattering is [188]

$$\left[\frac{d\varepsilon}{dt}\right]_{IC} = -\frac{4}{3}c\sigma_T\gamma^2 U_{rad} \tag{4.163}$$

where σ_T is the Thomson cross-section, and

$$U_{rad} = \frac{4\pi}{c}\int J_\nu d\nu \tag{4.164}$$

is the radiation energy density at the non-thermal electron location from a radiation field with mean intensity J_ν. Inverse Compton will more strongly impact electrons with large Lorentz factors.

The final process we include comes from synchrotron losses. In order to account for synchrotron emission, we need to furthermore know the magnetic energy density

$$U_B = \frac{B^2}{8\pi} \tag{4.165}$$

where B is the magnetic field. There are several ways in which the magnetic field can be sourced. One example comes from the ambient magnetic field B_0 from the pre-supernova environment, which can be further compressed in the shocked region to increase the energy density. Another possibility is from magnetic field amplification that is expected to occur in collisionless shocks [205]. It has been argued that in this case, the magentic field may reach equipartition with the non-thermal energy [200, 206]. If possible, this can result in a much stronger magnetic field (and therefore much greater synchrotron emission) compared to the case of shock compression of a pre-existing field.

We assume efficient field amplification such that the magnetic energy density is proportional to the non-thermal electron energy

$$U_B = \epsilon_B \int E(\gamma)d\gamma \tag{4.166}$$

Note that this is different from the usual definition of ϵ_B used in the literature [105]. Energy equipartition with the non-thermal electrons will therefore correspond to the case of $\epsilon_B = 1$. Since the non-thermal electron population evolves in time (due to continued injection at the shock, as well as the various loss mechanisms), the magnetic field will as well.

Once the magnetic field is known, the loss rate due to synchrotron radiation is approximated as [188]

$$\left[\frac{d\varepsilon}{dt}\right]_{synch} = -\frac{1}{6\pi}c\sigma_T\gamma^2 B^2 \tag{4.167}$$

Numerical Implementation

The equation that we need to evolve is given by

$$\frac{\partial E(\gamma)}{\partial t} + \mathbf{v} \cdot \nabla E(\gamma) = \epsilon_e \dot{Q}_{sh} \mathcal{J}(\gamma) - E(\gamma) \nabla \cdot \mathbf{v} - N(\gamma) \left\{ \left[\frac{d\varepsilon}{dt}\right]_{coll} + \left[\frac{d\varepsilon}{dt}\right]_{IC} + \left[\frac{d\varepsilon}{dt}\right]_{synch} \right\} \tag{4.168}$$

The second term on the left-hand side accounts for advection of the non-thermal electrons by the bulk flow. On the right are the sum of the shock injection source term, as well as the various loss processes discussed in the preceding sections. Note that by creating an entirely local (zone-by-zone) subgrid model, we are assuming the Larmor radius is sufficiently small such that the non-thermal electrons are trapped by the magnetic fields.

We use a particle transport approach to evolve the nonthermal electron distribution [203]. At the start of each timestep, we inject N equal energy nonthermal electron packets in zones where $\dot{Q}_{sh} > 0$. We calculate $\dot{Q}_{sh}$ during the hydro substep as described using the method in [166]. The energy of each packet emitted in the zone is set to be

$$\Delta E = \frac{\epsilon_e \dot{Q}_{sh} \Delta V \Delta t}{N} \tag{4.169}$$

where ΔV is the zone volume and Δt the timestep size. Each packet's Lorentz factor is sampled by constructing a CDF of the injection spectrum $\mathcal{J}(\gamma)$.

We then substep each particle from time t to time $t + \Delta t$ using N_t substeps of the hydro-limited step,

$$\Delta t_{sub} = \frac{\Delta t}{N_t} \tag{4.170}$$

where we typically choose $N_t = 1000$.

During each subcycle, we decrease the packet energy by the corresponding amount for each loss process. Once the end of timestep has been reached, if the packet energy falls below a threshold $\Delta E/E_0 < 10^{-3}$ of its initial energy, we kill the particle and cease tracking of it. We then census the remaining particles on the grid to construct the numerical estimate for $N(\gamma)$.

Once the electron distribution $N(\gamma)$ at the end of the timestep is constructed, we then calculate the magnetic field. Next, we construct the synchrotron emissivity. In the transport step, during the thermal emission, we additionally emit synchrotron radiation packets using the constructed non-thermal emissivity CDF.

4.9 Discussion and Conclusions

Due to the novelty of these simulation capabilities, more thorough code testing and benchmarking is needed to ensure the validity of the simulation output. While we have carried out the standard radiation hydrodynamics tests as performed in the literature, as well as 0D tests of the other physics such as Compton equilibration [197], there is a notable lack of available multi-group radiation hydrodynamics benchmarks due to its inherent complexity. More complete testing, in addition to comparisons with the non-LTE radiative transfer code Cretin [181], is ongoing to ensure the robustness of the Sedona implementation.

We have provided extensive modifications to the original Sedona code to do fully self-consistent multi-group non-LTE radiation hydrodynamics. In particular, the new physics provides the capability to fruitfully investigate multi-frequency emission from circumstellar interaction, which we discuss in the following chapter. Other astrophysical problems of interest include magnetar-powered supernovae [207]; wind-reprocessed emission from tidal disruption events [208, 209]; common envelope evolution and recombination-powered light curves [14, 210]; and other high energy astrophysical environments with non-thermal radio and/or x-ray emission (e.g. AGN and accretion disk reflection spectral modeling [211]). Additionally, while our hydrodynamics scheme is currently only limited to 1D, the transport, atomic kinetics package, and non-thermal electrons work in 2D and 3D, which opens the realm to investigate many interesting phenomena with asymmetries.

Chapter 5

Panchromatic Emission from an Interacting Supernova

5.1 Introduction

In Chapter 3, I provided a broad framework with which to interpret the diversity of interacting supernova light curves. Due to the simplifying assumptions of a frequency-independent and constant opacity, the framework only provides insight into the bolometric properties of the shock emission. However, interacting supernovae are observed to be panchromatic events, detectable not just in the optical but also radio and x-ray wavelengths [212–214].

Most works rely on analytic estimates of the radio and x-ray emission in order to extract physical quantities such as the CSM mass and radius [105, 215]. Given that the analytic models are independently constructed, they can at times give inferred parameters that disagree [216]. It is therefore essential to determine which, if any, of these analytic estimates is valid through the use of detailed numerical simulations.

Fortunately, the extensive improvements made to Sedona as discussed in 4 now puts such a task within reach. In this chapter, I perform time-dependent non-equilibrium multi-frequency radiation hydrodynamics simulations of an interacting supernova. Inspired by the recent event SN2023ixf [217, 218], I focus on the specific case of a Type IIP supernova with an extended CSM surrounding the ejecta.

5.2 Numerical Setup

Included Physics

At each timestep, we solve inline the non-LTE atomic kinetics of the atomic mixture using the Cretin DCA atomic models (described in Appendix E), accounting for all relevant collisional and radiative rates. The atomic level populations are used to calculate the frequency-dependent opacity, with lines included by using the approximate treatment discussed in Chapter 4.

Along with the NLTE radiation hydrodynamics, we also evolve non-thermal electron populations created in shocked regions. We assume that the shock injects a fraction ϵ_e of the numerically estimated zone shock-heating rate, with the injection spectrum assumed to be a power-law with $N(\gamma) \propto \gamma^{-3}$ between Lorentz factors $\gamma_{min} = 1$ and $\gamma_{max} = 10^6$. The non-thermal electrons are evolved in time using a substepping procedure, accounting for the combined effects of coulomb, adiabatic, synchrotron, and inverse Compton losses. We then use the evolved non-thermal electron distribution to emit synchrotron radiation, which is tracked during the radiation transport step. We estimate the magnetic field needed in the expression for synchrotron by assuming equipartition with the non-thermal electrons, i.e. $U_{mag} = B^2/8\pi = \int E(\gamma) d\gamma$. We also assume electron-ion equilibrium of the thermal plasma, i.e. both electrons and ions are characterized by the same temperature $T_e = T_i$.

Finally, in order to account for late-time optical emission, we include a time-dependent energy source term for the radioactive decay of Nickel-56 and Cobalt-56 for a nickel mass M_{ni}. We spread the source term out to an ejecta velocity coordinate of 2000 km/s.

Ejecta-CSM Setup

We assume that the supernova ejecta is expanding homologously with a broken power-law density profile [140, 219]

$$\rho_{ej}(r) = f_\rho \frac{M_{ej}}{r_t^3} \left[\frac{r}{r_t}\right]^{-(\delta,n)} \tag{5.1}$$

where $r_t = v_t t_0$ and

$$v_t = \sqrt{\frac{f_v E_{sn}}{M_{ej}}} \tag{5.2}$$

The numerical coefficients are given by

$$f_\rho = \frac{1}{4\pi} \frac{(n-3)(3-\delta)}{(n-\delta)} \tag{5.3}$$

$$f_v = \frac{2(5-\delta)(n-5)}{(n-3)(3-\delta)} \tag{5.4}$$

where we adopt fiducial values of $\delta = 0, n = 10$. We assume an initial radiation energy density profile in the ejecta of [59]

$$E_{rad}(r) = a_r T_0^4 \frac{\sin(\pi x)}{\pi x} \tag{5.5}$$

where $x = r/R_*$, with R_* the outer edge of the ejecta. The CSM is given similarly by a power-law

$$\rho_{csm}(r) = f_{csm} \frac{M_{csm}}{R_{csm}^3} \left[\frac{r}{R_{csm}}\right]^{-s} \tag{5.6}$$

where

$$f_{csm} = \frac{(3-s)}{4\pi}\left[1-\left(\frac{R_*}{R_{csm}}\right)^{3-s}\right]^{-1} \tag{5.7}$$

and R_{csm} are the inner/outer radius of the CSM, respectively. We assume a stationary wind-like CSM with $s = 2$ and $v_{csm} = 0$, and an initial temperature $T_{csm} = 10^4$ K.

Fiducial Model

We use an ejecta mass of $M_{ej} = 10M_\odot$, outer CSM radius $R_{csm} = 2 \cdot 10^{16}$ cm, and CSM mass corresponding to a mass-loss rate of $10^{-4}M_\odot$ yr^{-1} and wind velocity of 50 km s^{-1}. The simulation is initialized at a time $t_0 = 10$ days with initial ejecta temperature $5 \cdot 10^4$ K. We assume the ejecta contains a radioactive mass $M_{Ni} = 0.05M_\odot$ whose heating is locally thermalized by the ejecta. We account for atomic opacities of hydrogen, helium, and oxygen as a representative metal. We use mass fractions of $x_H = 0.75$, $x_{He} = 0.25$, and $x_C = 0.005$. Both the ejecta and CSM are assumed to have identical chemical compositions. We set the non-thermal shock energy injection parameter to $\epsilon_e = 0.01$ and energy equipartition of the magnetic field $\epsilon_B = 1$ with the non-thermal electrons. Note that the ϵ_B definition used here is not identical to that previously used in the literature (such as e.g. [105]).

Numerical Parameters

The opacities and output spectra are defined frequency grid between 10^7 and 10^{21} Hz. We use approximately 1000 logarithmically spaced frequency groups spanning this frequency range. The ejecta and CSM are divided into 400 and 600 uniformly-spaced zones, respectively. The ALE mesh spring is used with CFL of 0.2, a constant spring constant and minimum zone size of 10^{12} cm. At each timestep, we emit 32 thermal particles per zone, along with $2 \cdot 10^4$ non-thermal synchrotron particles. We include Compton scattering in zones with electron scattering optical depths less than $\Delta\tau_{es} = 5$. For zones with optical depths larger than this, we instead add a fraction of the electron scattering opacity $\epsilon = 10^{-4}$ to be absorptive to mimic the effects of Compton thermalization. In order to minimize spurious temperature fluctuations, we limit the fraction change in gas temperature between timesteps to be at most 20%. For the non-thermal electrons, we inject 100 tracer particles at each zone with a non-zero shock heating rate, sampling an energy CDF corresponding to a γ^{-3} injection spectrum. We track the non-thermal electrons until their energy falls below 10^{-4} their initial energy. We evolve all of the aforementioned processes and their coupling out to a time of 300 days since explosion. We then tally the escaping emission ton construct frequency-dependent light curves, with time bin sizes of 1 day.

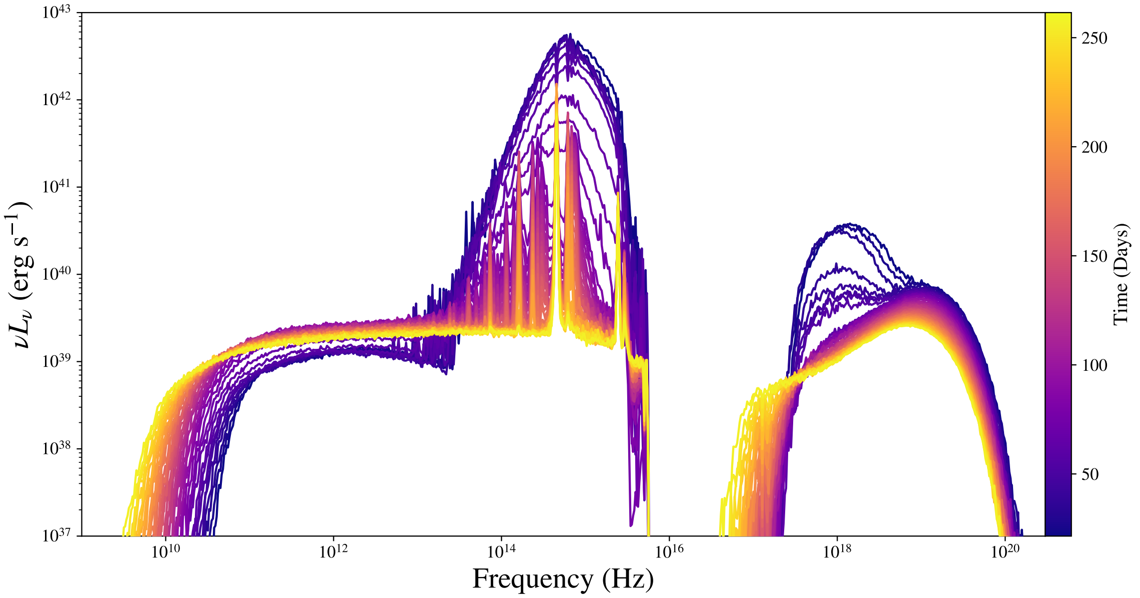

Figure 5.1: Time evolution of the panchromatic spectral energy distribution (SED) for the interacting type II supernova, from photospheric (20 days) to nebular times ($\sim$ 300 days).

5.3 Panchromatic Spectral Energy Distribution

In Fig. 5.1, we show the resulting spectral energy distribution (SED) of the circumstellar interaction, covering the early photospheric to later nebular phases. The SED contains contributions both from the cooling supernova ejecta, as well as thermal and non-thermal emission from the shocked region. The interaction produces observable and luminous emission across the electromagnetic spectrum, owing to the multitude of radiative processes.

At early times, up to roughly 100 days, the bulk of the radiation comes from photospheric emission generated by the supernova ejecta, resulting in a near-Planckian distribution that peaks in the optical and near-UV range. [220] At these frequencies, the shock interaction emission contributes very little. Once the the supernova ejecta has completely recombined (at times $\gtrsim$ 100 days), the optical continuum is replaced by strong nebular lines, primarily Hα [221]. These lines are superimposed on the optically thin synchrotron spectrum. One notable effect of shock interaction is the electron scattering of emission features, broadening the wings of the lines [220].

There is a notable lack of observable emission in the FUV and EUV frequency range of $\sim 10^{16}$ to 10^{17} Hz. In the absence of any absorptive processes, the radiation in this region would come from free-free emission from primarily the reverse shock and to a lesser extent the forward shock and optically thin synchrotron. However, the reverse shock is obscured not only by the unshocked CSM, but also by the formation of a cold dense shell

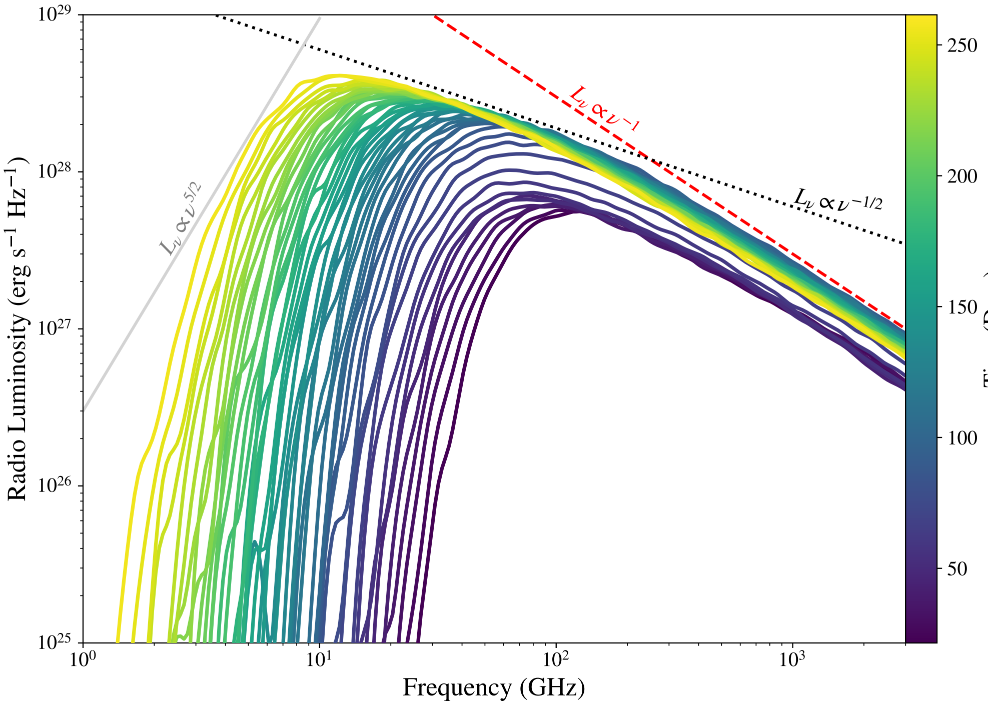

Figure 5.2: Time evolution of the radio to submm spectrum. Red dashed line gives a power-law fit to the high-frequency end of $L_\nu \propto \nu^{-1}$. Dotted black line gives the expected power-law slope for an optically thin synchrotron spectrum $L_\nu \propto \nu^{(1-p)/2}$ with $p = 3$. Solid grey line is the expected power-law slope for self-absorbed synchrotron.

overlying the shock region [20]. These components will obfuscate the shock radiation through bound-free absorption, particularly from helium and oxygen. For these model parameters, the absorption comes primarily from He II and O VI. However, as the shock propagates outwards, the amount of absorbing material decreases (due to expansion and decreasing line-of-sight optical depth) and the reverse shock begins shining through, starting at higher frequencies and progressively filling in the UV region.

Radio Emission

The radio through submm emission comes entirely from non-thermal synchrotron emission of relativistic shock-accelerated electrons. Fig 5.2 shows the spectral evolution between 1 GHz and 3000 GHz. The spectrum is characterized by a steep low-frequency rise to a

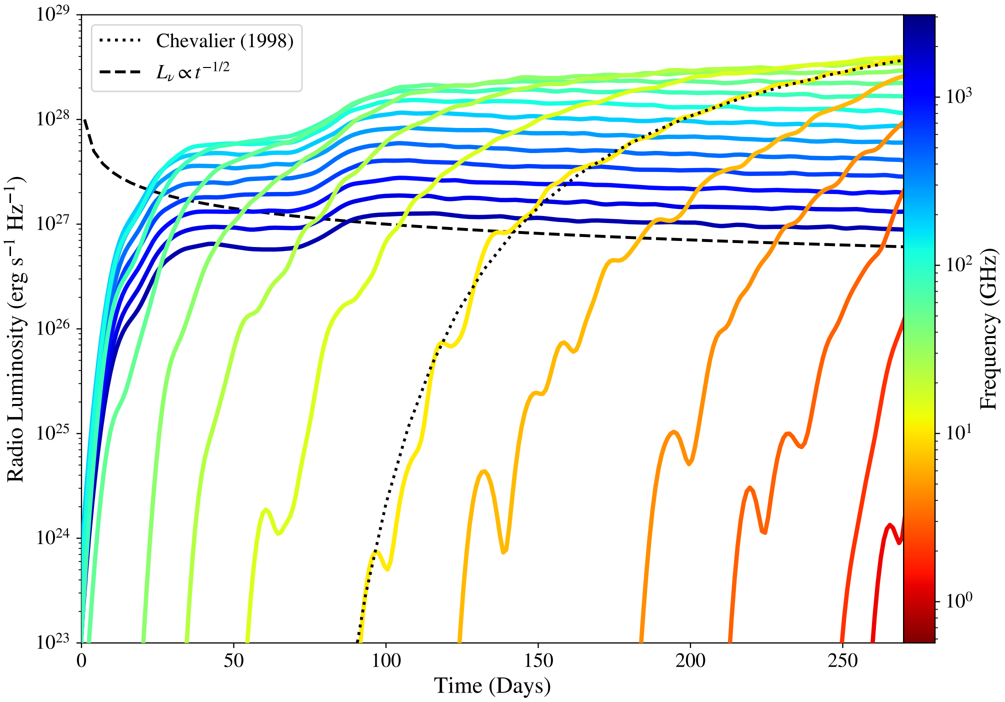

Figure 5.3: Radio to Submilimeter light curves for the frequency range 500 MHz to 3000 GHz. Dashed line shows an approximate fit to optically thin synchrotron, while the dotted line is the synchrotron self-absorption+free-free model [215].

peak, followed by a more gradual power-law tail to the submm range. As the interaction evolves in time, the spectral peak progressively shifts to lower frequencies and higher specific luminosities, peaking at around 300 GHz at 250 days.

The steep lower-frequency rise is caused by external free-free absorption by the overlying unshocked CSM, As the shock propagates outwards, the amount of free-free absorbing material decreases, and so the frequency cutoff at which the radio emission becomes optically thin to free-free moves to progressively longer wavelengths. There is a slight softening in the spectral rise near the peak frequency, implying that synchrotron self-absorption is starting to impact the observable emission.

At frequencies higher than the peak frequency, the spectral slope follows the usual optically thin synchrotron emission expected from a power-law distribution of non-thermal electrons [188]. However, as we start going to frequencies greater than $\gtrsim$ 200 GHz, the spectrum appears to steepen, from $\nu^{-1/2}$ to ν^{-1}. This is due to the combined effects of inverse Compton and synchrotron losses of the non-thermal electrons. As both loss processes scale with the Lorentz factor as γ^2, the more energetic electrons will be more susceptible to energy losses, thus steepening the non-thermal electron distribution compared to the shock injection spectrum.

The impact of inverse Compton is more readily seen in Fig. 5.3, which shows the light curves for radio through submm wavelengths. In particular, during the plateau phase of the type II supernova, there is a copious amount of soft photospheric photons streaming through the shocked region. This results in inverse Compton cooling of the non-thermal electrons, decreasing the total synchrotron throughput they are able to produce.

However, at around $\sim$ 80 days, the supply of soft photons drops precipitously as the ejecta recombines and the photospheric emission fades. As a result, at submm frequencies, a sudden rise in the radio luminosity occurs that is coincident with the end of the plateau phase, indicating a direct connection of the impact of inverse Compton cooling.

The optically thin synchrotron radiation seems to decline more gradually than analytic expectations, following a $t^{-1/2}$ compared to t^{-1} expected in [222]. This is due to the fact that synchrotron is being radiated at not just the forward, but also the reverse shock. The combined effect of these two shocks results in a flattening in the time evolution, which is something also seen in the x-ray emission discussed in the next section. Interestingly, the analytic expression of [215] appears to provide a remarkably good fit to the numerical light curves, albeit with slightly modified numerical values.

X-ray Emission

The x-ray emission from interacting supernova comes from the free-free emission of $T \gtrsim 10^7$ K shock-heated plasma. In Fig. 5.4, we show the x-ray spectral evolution in the range of 0.1 to 300 keV. The x-ray emission will come from both the forward and reverse shock, each with different density and temperature conditions. As such, the x-ray spectra shows a notable reverse shock excess at early times around a few keV, superimposed on the forward shock free-free continuum. The reverse shock bump also appears to drop off steeply around 800 eV due to oxygen bound-free absorption.

Interestingly, the large reverse shock excess seems to rapidly fade early on during the interaction. This is due to the delayed formation of a cold dense shell between the forward and reverse shock regions. As the reverse shock is obfuscated by the overlying cold dense shell, much of it will be photo-absorbed. Note that this absorption doesn't occur for the forward shock emission, as it lies above the cold dense shell relative to our observing line of sight. Nonetheless, there still appears to be an excess emission between 1 and 10 keV, as a single-component free-free continuum would be flat, while the spectra appear to show a slight slope. Thus, some of the reverse shock emission may still be able to escape through the cold dense shell.

Similar to the radio emission, as the shock moves outwards, the amount of external *bound-free* photoabsorption from the unshocked CSM decreases. Thus, at later times, there is a gradual increase in the amount of soft (0.1-1 keV) emission that is observable. Finally, as

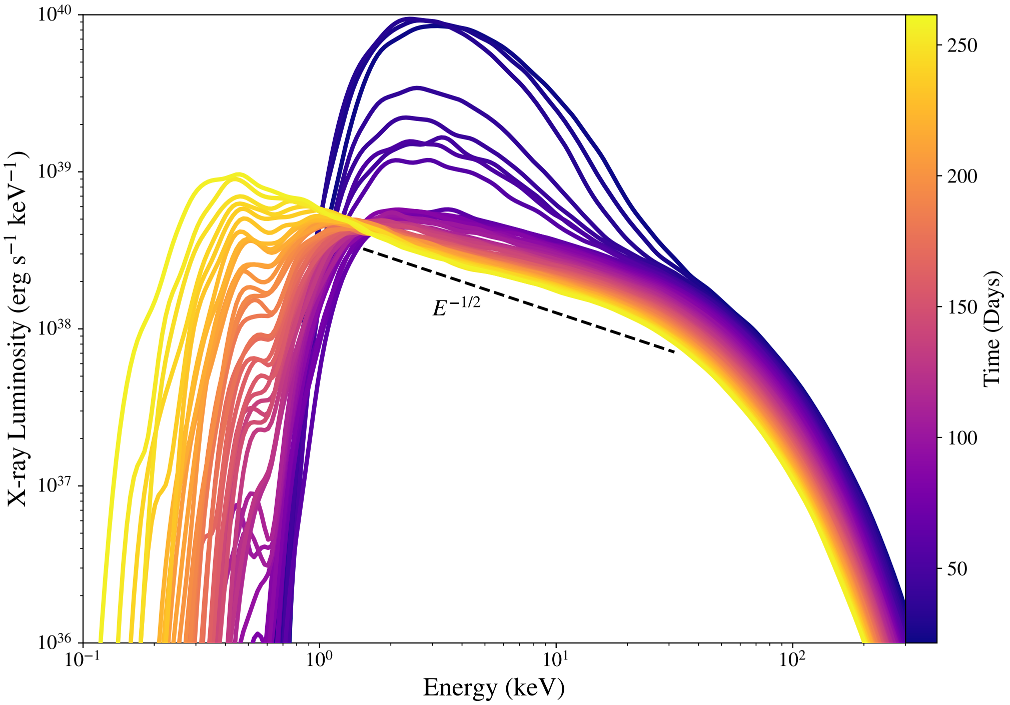

Figure 5.4: Time evolution of the soft to hard X-ray spectrum. Dashed black line gives a power-law fit to the 1-10 keV component of $E^{-1/2}$.

the ejecta decelerates and the shocked region cools and adiabatically expands, the decreased temperature causes the free-free turnover of both the forward and reverse shocks to move to progressively lower energies.

5.4 Discussion and Future Work

This simulation of the panchromatic emission from an interacting supernovae demonstrates how one can self-consistently model the full electromagnetic spectrum using a single model. While the numerical results seem give qualitatively good agreement with analytic estimates, there are notable differences that are not usually accounted for in simplified modeling. In particular, these preliminary results have shown the significant impact the reverse shock can have on both the radio and x-ray emission. One further novelty of these simulations is the ability to naturally form a cold dense shell, something which has been previously invoked but rarely included in modeling interacting light curves.

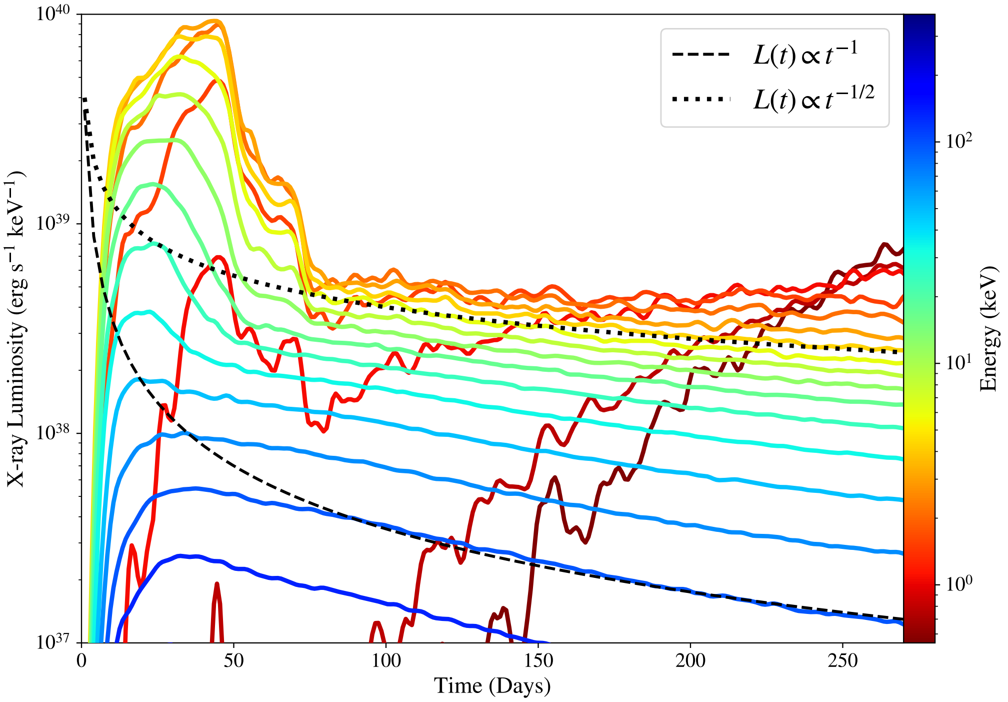

Figure 5.5: X-ray light curves for the energy range 0.5-300 keV. Dashed line gives a fit to the hard x-ray emission of t^{-1}, as expected from optically thin free-free emission from the shocked region [223]. Dotted line gives a fit to the soft component of $t^{-1/2}$.

The other important finding is that inverse Compton scattering plays an important role in shaping the radio emission due to its effect on the non-thermal electron distribution. Namely, inverse Compton cooling of the fast electrons leads to a steeper spectral index in both the electron distribution and, as a consequence, the synchrotron emission.

There is still much work to be done to fully investigate how the panchromatic SED changes for different ejecta and CSM properties. In particular, for a dense enough CSM, the shocks can become collisional [104], and so the non-thermal component will disappear. It would be interesting to determine what the criteria is in order for radio emission to appear during CSM interaction, and what its presence or absence tells us about the event. Additionally, the dense CSM interaction should begin contributing significantly to optical and UV wavelengths, thereby altering the overall morphology of the SED.

Another aspect not explored here is how different supernova progenitors impact the resultant SED. In particular, stripped-envelope supernovae will have a much different photospheric evolution compared to the plateau of Type II supernovae [115]. Combined with their differing chemical composition, ejecta mass, and shock velocity, it remains to be seen what the panchromatic SEDs of e.g. Type Ibn and Icn supernovae look like, which we leave for future work.

One simplification we have made is our approximate treatment of the opacities. In particular, we have used a single representative metal, oxygen, to qualitatively capture the effects of metal line cooling and photo-absorption. Recent observations of SN2023ixf indicate the presence of K-shell emission from neutral Fe [218]. The exact structure of this feature, along with the nebular lines, is something that can be obtained through spectral post-processing of these radiation hydrodynamics simulations, using a resolved line treatment.

Bibliography

[1] A. A. Vidotto, “The evolution of the solar wind”, Living Reviews in Solar Physics **18**, 3, 3 (2021).

[2] S. R. Cranmer, “Mass-loss Rates from Coronal Mass Ejections: A Predictive Theoretical Model for Solar-type Stars”, **840**, 114, 114 (2017).

[3] J. S. Vink, A. de Koter, and H. J. G. L. M. Lamers, “Mass-loss predictions for O and B stars as a function of metallicity”, **369**, 574–588 (2001).

[4] J. H. Groh, G. Meynet, and S. Ekström, “Massive star evolution: luminous blue variables as unexpected supernova progenitors”, **550**, L7, L7 (2013).

[5] S. Jones et al., “Advanced Burning Stages and Fate of 8-10 M $_\odot$ Stars”, **772**, 150, 150 (2013).

[6] S. E. Woosley, A. Heger, and T. A. Weaver, “The evolution and explosion of massive stars”, Reviews of Modern Physics **74**, 1015–1071 (2002).

[7] E. R. Beasor, B. Davies, and N. Smith, “The Impact of Realistic Red Supergiant Mass Loss on Stellar Evolution”, **922**, 55, 55 (2021).

[8] T. Ertl et al., “The Explosion of Helium Stars Evolved with Mass Loss”, **890**, 51, 51 (2020).

[9] A. V. Filippenko, “Optical Spectra of Supernovae”, **35**, 309–355 (1997).

[10] T. M. Tauris, N. Langer, and P. Podsiadlowski, “Ultra-stripped supernovae: progenitors and fate”, **451**, 2123–2144 (2015).

[11] K. De et al., “A hot and fast ultra-stripped supernova that likely formed a compact neutron star binary”, Science **362**, 201–206 (2018).

[12] N. Langer, “Presupernova Evolution of Massive Single and Binary Stars”, **50**, 107–164 (2012).

[13] H. Sana et al., “Binary Interaction Dominates the Evolution of Massive Stars”, Science **337**, 444 (2012).

[14] N. Ivanova et al., “Common envelope evolution: where we stand and how we can move forward”, **21**, 59, 59 (2013).

[15] S. Wu and J. Fuller, “A Diversity of Wave-driven Presupernova Outbursts”, **906**, 3, 3 (2021).

[16] S. C. Wu and J. Fuller, “Extreme Mass Loss in Low-mass Type Ib/c Supernova Progenitors”, **940**, L27, L27 (2022).

[17] A. Cristini et al., “3D hydrodynamic simulations of carbon burning in massive stars”, **471**, 279–300 (2017).

[18] J. Fuller, “Pre-supernova outbursts via wave heating in massive stars - I. Red supergiants”, **470**, 1642–1656 (2017).

[19] J. Fuller and S. Ro, “Pre-supernova outbursts via wave heating in massive stars - II. Hydrogen-poor stars”, **476**, 1853–1868 (2018).

[20] N. Smith, “Interacting Supernovae: Types IIn and Ibn”, in *Handbook of supernovae, isbn 978-3-319-21845-8. springer international publishing ag, 2017, p. 403*, edited by A. W. Alsabti and P. Murdin (2017), p. 403.

[21] R. Margutti et al., “Ejection of the Massive Hydrogen-rich Envelope Timed with the Collapse of the Stripped SN 2014C”, **835**, 140, 140 (2017).

[22] R. Margutti et al., “An Embedded X-Ray Source Shines through the Aspherical AT 2018cow: Revealing the Inner Workings of the Most Luminous Fast-evolving Optical Transients”, **872**, 18, 18 (2019).

[23] B. Margalit, E. Quataert, and A. Y. Q. Ho, “Optical to X-Ray Signatures of Dense Circumstellar Interaction in Core-collapse Supernovae”, **928**, 122, 122 (2022).

[24] Y.-F. Jiang et al., “Local Radiation Hydrodynamic Simulations of Massive Star Envelopes at the Iron Opacity Peak”, **813**, 74, 74 (2015).

[25] H. Fukushima and H. Yajima, “Radiation hydrodynamics simulations of massive star cluster formation in giant molecular clouds”, **506**, 5512–5539 (2021).

[26] J. Rosdahl et al., “Galaxies that shine: radiation-hydrodynamical simulations of disc galaxies”, **451**, 34–58 (2015).

[27] P. Ocvirk et al., “Cosmic Dawn (CoDa): the First Radiation-Hydrodynamics Simulation of Reionization and Galaxy Formation in the Local Universe”, **463**, 1462–1485 (2016).

[28] D. S. Clark et al., “Radiation hydrodynamics modeling of the highest compression inertial confinement fusion ignition experiment from the National Ignition Campaign”, Physics of Plasmas **22**, 022703, 022703 (2015).

[29] G. Duffa and R. Turpault, “Multigroup model for radiating flows during atmospheric hypersonic re-entry”, in Radiation of high temperature gases in atmospheric entry, Vol. 533 (2003), pp. 103–110.

[30] M. T. Burkey et al., “X-Ray Energy Deposition Model for Simulating Asteroid Response to a Nuclear Planetary Defense Mitigation Mission”, **4**, 243, 243 (2023).

[31] D. Mihalas and B. W. Mihalas, *Foundations of radiation hydrodynamics* (1984).

[32] J. I. Castor, *Radiation Hydrodynamics* (2004).

[33] L. A. Elliott, "Similarity Methods in Radiation Hydrodynamics", Proceedings of the Royal Society of London Series A **258**, 287–301 (1960).

[34] R. Kannan et al., "AREPO-RT: radiation hydrodynamics on a moving mesh", **485**, 117–149 (2019).

[35] P. C. Duffell and A. I. MacFadyen, "TESS: A Relativistic Hydrodynamics Code on a Moving Voronoi Mesh", **197**, 15, 15 (2011).

[36] A. Robinson et al., "Alegra: an arbitrary lagrangian-eulerian multimaterial, multiphysics code", in 46th aiaa aerospace sciences meeting and exhibit (2008), p. 1235.

[37] S. Chandrasekhar, *Radiative transfer.* (1950).

[38] L. H. Howell and J. A. Greenough, "Radiation diffusion for multi-fluid Eulerian hydrodynamics with adaptive mesh refinement", Journal of Computational Physics **184**, 53–78 (2003).

[39] J. E. Morel, "Diffusion-limit asymptotics of the transport equation, the P1/3 equations, and two flux-limited diffusion theories", **65**, 769–778 (2000).

[40] Z. Guo and S. Kumar, "Three-dimensional discrete ordinates method in transient radiative transfer", Journal of thermophysics and heat transfer **16**, 289–296 (2002).

[41] U. M. Noebauer and S. A. Sim, "Monte Carlo radiative transfer", Living Reviews in Computational Astrophysics **5**, 1, 1 (2019).

[42] J. D. Densmore, K. G. Thompson, and T. J. Urbatsch, "A hybrid transport-diffusion Monte Carlo method for frequency-dependent radiative-transfer simulations", Journal of Computational Physics **231**, 6924–6934 (2012).

[43] N. A. Gentile, "Implicit Monte Carlo Diffusion—An Acceleration Method for Monte Carlo Time-Dependent Radiative Transfer Simulations", Journal of Computational Physics **172**, 543–571 (2001).

[44] K. P. Keady and M. A. Cleveland, "An improved random walk algorithm for the implicit Monte Carlo method", Journal of Computational Physics **328**, 160–176 (2017).

[45] A. B. Wollaber, "Four decades of implicit monte carlo", Journal of Computational and Theoretical Transport **45**, 1–70 (2016).

[46] D. Mihalas and L. Auer, "On laboratory-frame radiation hydrodynamics", Journal of Quantitative Spectroscopy and Radiative Transfer **71**, 61–97 (2001).

[47] C. A. Iglesias and F. J. Rogers, "Updated opal opacities", Astrophysical Journal v. 464, p. 943 **464**, 943 (1996).

[48] J. Colgan et al., "A New Generation of Los Alamos Opacity Tables", **817**, 116, 116 (2016).

[49] L. Dessart, E. Audit, and D. J. Hillier, "Numerical simulations of superluminous supernovae of type IIn", **449**, 4304–4325 (2015).

[50]D. Mihalas, *Stellar atmospheres* (1978).

[51]M. Busquet, “Radiation-dependent ionization model for laser-created plasmas”, Physics of Fluids B **5**, 4191–4206 (1993).

[52]D. J. Hillier and D. L. Miller, “The Treatment of Non-LTE Line Blanketing in Spherically Expanding Outflows”, **496**, 407–427 (1998).

[53]L.-X. Li and B. Paczyński, “Transient Events from Neutron Star Mergers”, The Astrophysical Journal **507**, L59–L62 (1998).

[54]E. Chatzopoulos, J. Craig Wheeler, and J. Vinko, “Generalized semi-analytical models of supernova light curves”, Astrophysical Journal **746**, 121 (2012).

[55]C. Inserra et al., “SUPER-LUMINOUS TYPE Ic SUPERNOVAE: CATCHING A MAGNETAR BY THE TAIL”, The Astrophysical Journal **770**, 128 (2013).

[56]V. A. Villar et al., “The Combined Ultraviolet, Optical, and Near-infrared Light Curves of the Kilonova Associated with the Binary Neutron Star Merger GW170817: Unified Data Set, Analytic Models, and Physical Implications”, The Astrophysical Journal **851**, L21 (2017).

[57]M. Nicholl, J. Guillochon, and E. Berger, “The Magnetar Model for Type I Superluminous Supernovae. I. Bayesian Analysis of the Full Multicolor Light-curve Sample with MOSFiT”, The Astrophysical Journal **850**, 55 (2017).

[58]J. Guillochon et al., “MOSFiT: Modular Open Source Fitter for Transients”, The Astrophysical Journal Supplement Series **236**, 6 (2018).

[59]W. D. Arnett, “Analytic solutions for light curves of supernovae of Type II”, The Astrophysical Journal **237**, 541 (1980).

[60]W. D. Arnett, “Type I supernovae. I - Analytic solutions for the early part of the light curve”, The Astrophysical Journal **253**, 785 (1982).

[61]M. Stritzinger et al., “Consistent estimates of $\mathsf{
{56}}$Ni yields for type Ia supernovae”, Astronomy & Astrophysics **460**, 793–798 (2006).

[62]S. Valenti et al., “The broad-lined Type Ic supernova 2003jd”, Monthly Notices of the Royal Astronomical Society **383**, 1485–1500 (2007).

[63]M. R. Drout et al., “THE FIRST SYSTEMATIC STUDY OF TYPE Ibc SUPERNOVA MULTI-BAND LIGHT CURVES”, The Astrophysical Journal **741**, 97 (2011).

[64]R. Scalzo et al., “Type Ia supernova bolometric light curves and ejected mass estimates from the Nearby Supernova Factory”, Monthly Notices of the Royal Astronomical Society **440**, 1498–1518 (2014).

[65]S. J. Prentice et al., “The bolometric light curves and physical parameters of stripped-envelope supernovae”, Monthly Notices of the Royal Astronomical Society **458**, 2973–3002 (2016).

[66] S. Blondin et al., “One-dimensional delayed-detonation models of type ia supernovae: Confrontation to observations at bolometric maximum”, Monthly Notices of the Royal Astronomical Society **429**, 2127–2142 (2013).

[67] P. Hoeflich et al., “Light and Color Curve Properties of Type Ia Supernovae: Theory Versus Observations”, The Astrophysical Journal **846**, 58 (2017).

[68] a. Khokhlov, E. Mueller, and P. Hoeflich, “Light curves of Type Ia supernova models with different explosion mechanisms”, Astronomy and Astrophysics (1993).

[69] L. Dessart et al., “Radiative-transfer models for supernovae IIb/Ib/Ic from binary-star progenitors”, Monthly Notices of the Royal Astronomical Society **453**, 2189–2213 (2015).

[70] L. Dessart et al., “Inferring supernova IIb/Ib/Ic ejecta properties from light curves and spectra: Correlations from radiative-transfer models”, Monthly Notices of the Royal Astronomical Society, `10.1093/mnras/stw418` (2016).

[71] S. E. Woosley, “SN 1987A - After the peak”, The Astrophysical Journal **330**, 218 (1988).

[72] W. D. Arnett, “On the theory of Type I supernovae”, The Astrophysical Journal **230**, L37 (1979).

[73] D. Kasen and L. Bildsten, “SUPERNOVA LIGHT CURVES POWERED BY YOUNG MAGNETARS”, The Astrophysical Journal **717**, 245–249 (2010).

[74] P. A. Pinto and R. G. Eastman, “The Physics of Type Ia Supernova Light Curves. I. Analytic Results and Time Dependence”, The Astrophysical Journal **530**, 744–756 (2000).

[75] D. Kasen, R. C. Thomas, and P. Nugent, “Time-dependent Monte Carlo Radiative Transfer Calculations for Three-dimensional Supernova Spectra, Light Curves, and Polarization”, **651**, 366–380 (2006).

[76] A. L. Piro and E. Nakar, “WHAT CAN WE LEARN FROM THE RISING LIGHT CURVES OF RADIOACTIVELY POWERED SUPERNOVAE?”, The Astrophysical Journal **769**, 67 (2013).

[77] B. Katz, D. Kushnir, and S. Dong, “An exact integral relation between the Ni56 mass and the bolometric light curve of a type Ia supernova”, (2013).

[78] S. J. Prentice et al., “The Cow: Discovery of a Luminous, Hot, and Rapidly Evolving Transient”, The Astrophysical Journal **865**, L3 (2018).

[79] L. Dessart, “A magnetar model for the hydrogen-rich super-luminous supernova iPTF14hls”, Astronomy & Astrophysics **610**, L10 (2018).

[80] E. K. Grassberg, V. S. Imshennik, and D. K. Nadyozhin, “On the theory of the light curves of supernovae”, Astrophysics and Space Science **10**, 28–51 (1971).

[81] E. K. Grassberg and D. K. Nadyozhin, “The cooling wave in supernova shells”, Astrophysics and Space Science **44**, 409–428 (1976).

[82] D. V. Popov, “An analytical model for the plateau stage of Type II supernovae”, The Astrophysical Journal **414**, 712 (1993).

[83] N. B. Suntzeff and P. Bouchet, “The bolometric light curve of SN 1987A. I - Results from ESO and CTIO U to Q0 photometry”, The Astronomical Journal **99**, 650 (1990).

[84] A. L. Piro and V. S. Morozova, “TRANSPARENT HELIUM IN STRIPPED ENVELOPE SUPERNOVAE”, The Astrophysical Journal **792**, L11 (2014).

[85] L. Dessart, D. J. Hillier, and K. D. Wilk, “Impact of clumping on core-collapse supernova radiation”, Astronomy & Astrophysics **619**, A30 (2018).

[86] A. L. Piro and E. Nakar, “CONSTRAINTS ON SHALLOW 56 Ni FROM THE EARLY LIGHT CURVES OF TYPE Ia SUPERNOVAE”, The Astrophysical Journal **784**, 85 (2014).

[87] E. Waxman et al., “Constraints on the ejecta of the GW170817 neutron star merger from its electromagnetic emission”, Monthly Notices of the Royal Astronomical Society **481**, 3423–3441 (2018).

[88] S. A. Colgate and R. H. White, “The Hydrodynamic Behavior of Supernovae Explosions”, **143**, 626 (1966).

[89] W. D. Arnett, “Type I supernovae. I - Analytic solutions for the early part of the light curve”, **253**, 785–797 (1982).

[90] H. .-. Janka et al., “Theory of core-collapse supernovae”, **442**, 38–74 (2007).

[91] D. Branch and J. C. Wheeler, *Supernova Explosions* (2017).

[92] A. Rau et al., “Exploring the Optical Transient Sky with the Palomar Transient Factory”, **121**, 1334 (2009).

[93] M. J. Graham et al., “The Zwicky Transient Facility: Science Objectives”, **131**, 078001 (2019).

[94] A. Y. Q. Ho et al., “The Photometric and Spectroscopic Evolution of Rapidly Evolving Extragalactic Transients in ZTF”, arXiv e-prints, arXiv:2105.08811, arXiv:2105.08811 (2021).

[95] M. R. Drout et al., “Rapidly Evolving and Luminous Transients from Pan-STARRS1”, **794**, 23, 23 (2014).

[96] A. Y. Q. Ho et al., “Evidence for Late-stage Eruptive Mass Loss in the Progenitor to SN2018gep, a Broad-lined Ic Supernova: Pre-explosion Emission and a Rapidly Rising Luminous Transient”, **887**, 169, 169 (2019).

[97] N. Smith et al., “SN 2006gy: Discovery of the Most Luminous Supernova Ever Recorded, Powered by the Death of an Extremely Massive Star like η Carinae”, **666**, 1116–1128 (2007).

[98] C. Inserra et al., “Super-luminous Type Ic Supernovae: Catching a Magnetar by the Tail”, **770**, 128, 128 (2013).

[99] A. Gal-Yam, “Luminous Supernovae”, Science **337**, 927 (2012).

[100] S. E. Woosley and T. A. Weaver, “The physics of supernova explosions.”, **24**, 205–253 (1986).

[101] H.-T. Janka, “Neutrino-Driven Explosions”, in *Handbook of supernovae*, edited by A. W. Alsabti and P. Murdin (2017), p. 1095.

[102] W. D. Arnett, “Analytic solutions for light curves of supernovae of Type II”, **237**, 541–549 (1980).

[103] T. Sukhbold et al., “Core-collapse Supernovae from 9 to 120 Solar Masses Based on Neutrino-powered Explosions”, **821**, 38, 38 (2016).

[104] Y. B. Zel’dovich and Y. P. Raizer, *Physics of shock waves and high-temperature hydrodynamic phenomena* (1967).

[105] R. A. Chevalier, “The radio and X-ray emission from type II supernovae.”, **259**, 302–310 (1982).

[106] K. W. Weiler et al., “Radio Supernovae”, **301**, 790 (1986).

[107] K. W. Weiler and R. A. Sramek, “Supernovae and supernova remnants.”, **26**, 295–341 (1988).

[108] A. R. Bell, “The acceleration of cosmic rays in shock fronts - I.”, **182**, 147–156 (1978).

[109] R. Blandford and D. Eichler, “Particle acceleration at astrophysical shocks: A theory of cosmic ray origin”, **154**, 1–75 (1987).

[110] K. Koyama et al., “Evidence for shock acceleration of high-energy electrons in the supernova remnant SN1006”, **378**, 255–258 (1995).

[111] R. A. Chevalier and C. Fransson, “Thermal and Non-thermal Emission from Circumstellar Interaction”, in *Handbook of supernovae, isbn 978-3-319-21845-8. springer international publishing ag, 2017, p. 875*, edited by A. W. Alsabti and P. Murdin (2017), p. 875.

[112] R. P. Drake, “Radiative Shocks in Astrophysics and the Laboratory”, **298**, 49–59 (2005).

[113] E. Waxman and B. Katz, “Shock Breakout Theory”, in *Handbook of supernovae, isbn 978-3-319-21845-8. springer international publishing ag, 2017, p. 967*, edited by A. W. Alsabti and P. Murdin (2017), p. 967.

[114] N. Smith, “Mass Loss: Its Effect on the Evolution and Fate of High-Mass Stars”, **52**, 487–528 (2014).

[115] S. E. Woosley, T. Sukhbold, and D. N. Kasen, “Model Light Curves for Type Ib and Ic Supernovae”, **913**, 145, 145 (2021).

[116] E. Quataert and J. Shiode, “Wave-driven mass loss in the last year of stellar evolution: setting the stage for the most luminous core-collapse supernovae”, **423**, L92–L96 (2012).

[117] R. M. Humphreys and K. Davidson, “The Luminous Blue Variables: Astrophysical Geysers”, **106**, 1025 (1994).

[118] K. Davidson and R. M. Humphreys, “Eta Carinae and Its Environment”, **35**, 1–32 (1997).

[119]P. A. Crowther, “Physical Properties of Wolf-Rayet Stars”, **45**, 177–219 (2007).

[120]V. A. Villar et al., “Theoretical Models of Optical Transients. I. A Broad Exploration of the Duration-Luminosity Phase Space”, **849**, 70, 70 (2017).

[121]A. Nyholm et al., “Type IIn supernova light-curve properties measured from an untargeted survey sample”, **637**, A73, A73 (2020).

[122]A. Suzuki, T. J. Moriya, and T. Takiwaki, “A Systematic Study on the Rise Time-Peak Luminosity Relation for Bright Optical Transients Powered by Wind Shock Breakout”, **899**, 56, 56 (2020).

[123]E. Chatzopoulos et al., “Analytical Light Curve Models of Superluminous Supernovae: χ^2-minimization of Parameter Fits”, **773**, 76, 76 (2013).

[124]C. Inserra et al., “On the nature of hydrogen-rich superluminous supernovae”, **475**, 1046–1072 (2018).

[125]A. Rest et al., “A fast-evolving luminous transient discovered by K2/Kepler”, Nature Astronomy **2**, 307–311 (2018).

[126]S. J. Prentice et al., “The Cow: Discovery of a Luminous, Hot, and Rapidly Evolving Transient”, **865**, L3, L3 (2018).

[127]C. Pellegrino et al., “Circumstellar Interaction Powers the Light Curves of Luminous Rapidly Evolving Optical Transients”, **926**, 125, 125 (2022).

[128]R. A. Chevalier, “Self-similar solutions for the interaction of stellar ejecta with an external medium.”, **258**, 790–797 (1982).

[129]R. A. Chevalier and C. Fransson, “Emission from Circumstellar Interaction in Normal Type II Supernovae”, **420**, 268 (1994).

[130]T. J. Moriya et al., “Light-curve modelling of superluminous supernova 2006gy: collision between supernova ejecta and a dense circumstellar medium”, **428**, 1020–1035 (2013).

[131]R. A. Chevalier and C. M. Irwin, “Shock Breakout in Dense Mass Loss: Luminous Supernovae”, **729**, L6, L6 (2011).

[132]S. Ginzburg and S. Balberg, “Superluminous Light Curves from Supernovae Exploding in a Dense Wind”, **757**, 178, 178 (2012).

[133]V. Morozova, A. L. Piro, and S. Valenti, “Unifying Type II Supernova Light Curves with Dense Circumstellar Material”, **838**, 28, 28 (2017).

[134]B. D. Metzger, “Luminous Fast Blue Optical Transients and Type Ibn/Icn SNe from Wolf-Rayet/Black Hole Mergers”, **932**, 84, 84 (2022).

[135]E. O. Ofek et al., “Supernova PTF 09UJ: A Possible Shock Breakout from a Dense Circumstellar Wind”, **724**, 1396–1401 (2010).

[136]S.-C. Leung et al., “A Model for the Fast Blue Optical Transient AT2018cow: Circumstellar Interaction of a Pulsational Pair-instability Supernova”, **903**, 66, 66 (2020).

[137] S.-C. Leung, J. Fuller, and K. Nomoto, “Fast Blue Optical Transients Due to Circumstellar Interaction and the Mysterious Supernova SN 2018gep”, **915**, 80, 80 (2021).

[138] A. L. Piro, “Using Double-peaked Supernova Light Curves to Study Extended Material”, **808**, L51, L51 (2015).

[139] A. L. Piro, A. Haynie, and Y. Yao, “Shock Cooling Emission from Extended Material Revisited”, **909**, 209, 209 (2021).

[140] R. A. Chevalier and N. Soker, “Asymmetric Envelope Expansion of Supernova 1987A”, **341**, 867 (1989).

[141] J. P. Ostriker and C. F. McKee, “Astrophysical blastwaves”, Reviews of Modern Physics **60**, 1–68 (1988).

[142] C. D. Matzner and C. F. McKee, “The Expulsion of Stellar Envelopes in Core-Collapse Supernovae”, **510**, 379–403 (1999).

[143] G. B. Rybicki and A. P. Lightman, *Radiative processes in astrophysics* (1979).

[144] D. Tsuna, K. Kashiyama, and T. Shigeyama, “Type IIn Supernova Light Curves Powered by Forward and Reverse Shocks”, **884**, 87, 87 (2019).

[145] E. Chatzopoulos, J. C. Wheeler, and J. Vinko, “Generalized Semi-analytical Models of Supernova Light Curves”, **746**, 121, 121 (2012).

[146] D. Kasen, B. D. Metzger, and L. Bildsten, “Magnetar-driven Shock Breakout and Double-peaked Supernova Light Curves”, **821**, 36, 36 (2016).

[147] B. Katz, N. Sapir, and E. Waxman, “Non-relativistic Radiation Mediated Shock Breakouts. II. Bolometric Properties of Supernova Shock Breakout”, **747**, 147, 147 (2012).

[148] A. Sakurai, “On the problem of a shock wave arriving at the edge of a gas”, Communications on Pure and Applied Mathematics **13**, 353–370 (1960).

[149] B. Margalit, “Analytic Light Curves of Dense CSM Shock Breakout and Cooling”, **933**, 238, 238 (2022).

[150] E. N. Parker, *Interplanetary dynamical processes.* (1963).

[151] L. I. Sedov, *Similarity and Dimensional Methods in Mechanics* (1959).

[152] P. C. Duffell, “A One-Dimensional Model for Rayleigh-Taylor Instability in Supernova Remnants”, **821**, 76, 76 (2016).

[153] W. Zhang et al., “CASTRO: A New Compressible Astrophysical Solver. II. Gray Radiation Hydrodynamics”, **196**, 20, 20 (2011).

[154] N. Roth and D. Kasen, “Monte Carlo Radiation-Hydrodynamics With Implicit Methods”, **217**, 9, 9 (2015).

[155] W. Zhang et al., “CASTRO: A New Compressible Astrophysical Solver. III. Multigroup Radiation Hydrodynamics”, **204**, 7, 7 (2013).

[156] W. H. Press, B. P. Flannery, and S. A. Teukolsky, *Numerical recipes. The art of scientific computing* (1986).

[157] E. Lovegrove, S. E. Woosley, and W. Zhang, “Very Low-energy Supernovae: Light Curves and Spectra of Shock Breakout”, Astrophys. J. **845**, 103 (2017).

[158] E. Karamehmetoglu et al., “OGLE-2014-SN-131: A long-rising Type Ibn supernova from a massive progenitor”, **602**, A93, A93 (2017).

[159] D. A. Perley et al., “The fast, luminous ultraviolet transient AT2018cow: extreme supernova, or disruption of a star by an intermediate-mass black hole?”, **484**, 1031–1049 (2019).

[160] A. Gal-Yam, “Observational and Physical Classification of Supernovae”, in *Handbook of supernovae*, edited by A. W. Alsabti and P. Murdin (2017), p. 195.

[161] A. Gal-Yam et al., “A WC/WO star exploding within an expanding carbon-oxygen-neon nebula”, **601**, 201–204 (2022).

[162] A. Nyholm et al., “The bumpy light curve of Type IIn supernova iPTF13z over 3 years”, **605**, A6, A6 (2017).

[163] G. Hosseinzadeh et al., “Bumpy Declining Light Curves Are Common in Hydrogen-poor Superluminous Supernovae”, **933**, 14, 14 (2022).

[164] M. R. Drout et al., “The Fast and Furious Decay of the Peculiar Type Ic Supernova 2005ek”, **774**, 58, 58 (2013).

[165] S. E. Woosley, “Pulsational Pair-instability Supernovae”, **836**, 244, 244 (2017).

[166] A. T. McDowell, P. C. Duffell, and D. Kasen, “Interaction of a Supernova with a Circumstellar Disk”, **856**, 29, 29 (2018).

[167] A. Suzuki, T. J. Moriya, and T. Takiwaki, “Supernova Ejecta Interacting with a Circumstellar Disk. I. Two-dimensional Radiation-hydrodynamic Simulations”, **887**, 249, 249 (2019).

[168] J. Fleck J. A. and J. D. Cummings, “An implicit Monte Carlo scheme for calculating time and frequency dependent nonlinear radiation transport”, Journal of Computational Physics **8**, 313–342 (1971).

[169] E. F. Toro, *Riemann solvers and numerical methods for fluid dynamics: a practical introduction* (Springer Science & Business Media, 2013).

[170] M. Arora and P. L. Roe, “A well-behaved tvd limiter for high-resolution calculations of unsteady flow”, Journal of Computational Physics **132**, 3–11 (1997).

[171] E. F. Toro, “The hllc riemann solver”, Shock waves **29**, 1065–1082 (2019).

[172] J. C. Butcher, “A history of runge-kutta methods”, Applied numerical mathematics **20**, 247–260 (1996).

[173] A. Suzuki, T. J. Moriya, and T. Takiwaki, "Supernova ejecta interacting with a circumstellar disk. I. two-dimensional radiation-hydrodynamic simulations", arXiv e-prints, arXiv:1911.09261, arXiv:1911.09261 (2019).

[174] W. Zhang et al., "AMReX: a framework for block-structured adaptive mesh refinement", The Journal of Open Source Software **4**, 1370, 1370 (2019).

[175] V. A. Dobrev, T. V. Kolev, and R. N. Rieben, "High-order curvilinear finite element methods for lagrangian hydrodynamics", SIAM Journal on Scientific Computing **34**, B606–B641 (2012).

[176] C. W. Hirt, A. A. Amsden, and J. L. Cook, "An Arbitrary Lagrangian-Eulerian Computing Method for All Flow Speeds", Journal of Computational Physics **14**, 227–253 (1974).

[177] V. Springel, "E pur si muove: Galilean-invariant cosmological hydrodynamical simulations on a moving mesh", **401**, 791–851 (2010).

[178] W. Cao, W. Huang, and R. D. Russell, "Anr-adaptive finite element method based upon moving mesh pdes", Journal of Computational physics **149**, 221–244 (1999).

[179] W. Lee, "Tridiagonal matrices: thomas algorithm", MS6021, Scientific Computation, University of Limerick (2011).

[180] Y. Ralchenko, *Modern Methods in Collisional-Radiative Modeling of Plasmas* (2016).

[181] H. A. Scott and S. B. Hansen, "Advances in NLTE modeling for integrated simulations", High Energy Density Physics **6**, 39–47 (2010).

[182] S. N. Nahar, "Photoionization and Electron-Ion Recombination of n = 1 to Very High n-Values of Hydrogenic Ions", Atoms **9**, 73, 73 (2021).

[183] N. R. Badnell, "Radiative recombination data for modeling dynamic finite-density plasmas", The Astrophysical Journal Supplement Series **167**, 334 (2006).

[184] R. J. Rutten, "Radiative transfer in stellar atmospheres", (2000).

[185] G. Guennebaud, B. Jacob, et al., *Eigen v3*, http://eigen.tuxfamily.org, 2010.

[186] W. H. Press, *Numerical recipes 3rd edition: the art of scientific computing* (Cambridge university press, 2007).

[187] R. L. Kurucz, "Including all the lines", Canadian Journal of Physics **89**, 417–428 (2011).

[188] G. B. Rybicki and A. P. Lightman, *Radiative processes in astrophysics* (John Wiley & Sons, 1991).

[189] P. A. M. van Hoof et al., "Accurate determination of the free-free Gaunt factor - I. Non-relativistic Gaunt factors", **444**, 420–428 (2014).

[190] O. Peyrusse, "A superconfiguration model for broadband spectroscopy of non-lte plasmas", Journal of Physics B: Atomic, Molecular and Optical Physics **33**, 4303 (2000).

[191] P. D. Aberg et al., *The opus radiative opacity code, a new implementation of the super-transition array method*, tech. rep. (Lawrence Livermore National Lab.(LLNL), Livermore, CA (United States), 2020).

[192]J. Bauche, C. Bauche-Arnoult, and M. Klapisch, “Unresolved transition arrays”, **37**, 659–663 (1988).

[193]G. J. Phillips et al., “Escape factors in zero-dimensional radiation-transfer codes”, High Energy Density Physics **4**, 18–25 (2008).

[194]G. Rybicki and D. Hummer, “A generalization of the sobolev method for flows with nonlocal radiative coupling”, Astrophysical Journal, Part 1, vol. 219, Jan. 15, 1978, p. 654-675. **219**, 654–675 (1978).

[195]H. Van Regemorter, “Rate of collisional excitation in stellar atmospheres.”, Astrophysical Journal, vol. 136, p. 906 **136**, 906 (1962).

[196]M. S. Longair, *High energy astrophysics* (Cambridge university press, 2011).

[197]N. Roth et al., “General Relativistic Implicit Monte Carlo Radiation-hydrodynamics”, **933**, 226, 226 (2022).

[198]E. Canfield, W. Howard, and E. Liang, “Inverse comptonization by one-dimensional relativistic electrons”, Astrophysical Journal, Part 1 (ISSN 0004-637X), vol. 323, Dec. 15, 1987, p. 565-574. **323**, 565–574 (1987).

[199]E. Ofek et al., “X-ray emission from supernovae in dense circumstellar matter environments: a search for collisionless shocks”, The Astrophysical Journal **763**, 42 (2013).

[200]A. Spitkovsky, “Simulations of relativistic collisionless shocks: shock structure and particle acceleration”, in Aip conference proceedings, Vol. 801, 1 (American Institute of Physics, 2005), pp. 345–350.

[201]E. Berezhko, V. Elshin, and L. Ksenofontov, “Cosmic ray acceleration in supernova remnants”, Journal of Experimental and Theoretical Physics **82**, 1–21 (1996).

[202]K. Murase et al., “High-energy emission from interacting supernovae: new constraints on cosmic-ray acceleration in dense circumstellar environments”, The Astrophysical Journal **874**, 80 (2019).

[203]J. Barnes et al., “Radioactivity and thermalization in the ejecta of compact object mergers and their impact on kilonova light curves”, The Astrophysical Journal **829**, 110 (2016).

[204]J. D. Huba, *Nrl plasma formulary*, Vol. 6790, 98-358 (Naval Research Laboratory, 1998).

[205]B. Lembège et al., “Selected problems in collisionless-shock physics”, Space Science Reviews **110**, 161–226 (2004).

[206]R. Treumann, “Fundamentals of collisionless shocks for astrophysical application, 1. nonrelativistic shocks”, The Astronomy and Astrophysics Review **17**, 409–535 (2009).

[207]K.-J. Chen, S. Woosley, and T. Sukhbold, “Magnetar-powered supernovae in two dimensions. i. superluminous supernovae”, The Astrophysical Journal **832**, 73 (2016).

[208]K. Kremer et al., “Wind-reprocessed transients from stellar-mass black hole tidal disruption events”, Monthly Notices of the Royal Astronomical Society **524**, 6358–6373 (2023).

[209] A. L. Piro and W. Lu, "Wind-reprocessed transients", The Astrophysical Journal **894**, 2 (2020).

[210] N. Ivanova, S. Justham, and P. Podsiadlowski, "On the role of recombination in common-envelope ejections", Monthly Notices of the Royal Astronomical Society **447**, 2181–2197 (2015).

[211] J. Garcia and T. R. Kallman, "X-ray reflected spectra from accretion disk models. i. constant density atmospheres", The Astrophysical Journal **718**, 695 (2010).

[212] R. Margutti et al., "A panchromatic view of the restless sn 2009ip reveals the explosive ejection of a massive star envelope", The Astrophysical Journal **780**, 21 (2013).

[213] P. Chandra, "Circumstellar interaction in supernovae in dense environments—an observational perspective", Space Science Reviews **214**, 27 (2018).

[214] A. M. Soderberg et al., "Panchromatic observations of sn 2011dh point to a compact progenitor star", The Astrophysical Journal **752**, 78 (2012).

[215] R. A. Chevalier, "Synchrotron self-absorption in radio supernovae", The Astrophysical Journal **499**, 810 (1998).

[216] W. V. Jacobson-Galán et al., "Sn 2019ehk: a double-peaked ca-rich transient with luminous x-ray emission and shock-ionized spectral features", The Astrophysical Journal **898**, 166 (2020).

[217] A. Singh et al., "Unravelling the asphericities in the explosion and multi-faceted circumstellar matter of sn 2023ixf", arXiv preprint arXiv:2405.20989 (2024).

[218] S. Panjkov et al., "Probing the soft x-ray properties and multi-wavelength variability of sn2023ixf and its progenitor", arXiv preprint arXiv:2308.13101 (2023).

[219] D. Kasen, B. D. Metzger, and L. Bildsten, "MAGNETAR-DRIVEN SHOCK BREAKOUT AND DOUBLE-PEAKED SUPERNOVA LIGHT CURVES", The Astrophysical Journal **821**, 36 (2016).

[220] L. Dessart and W. Jacobson-Galán, "Using spectral modeling to break light-curve degeneracies of type ii supernovae interacting with circumstellar material", Astronomy & Astrophysics **677**, A105 (2023).

[221] L. Dessart and D. J. Hillier, "Radiative-transfer modeling of nebular-phase type ii supernovae-dependencies on progenitor and explosion properties", Astronomy & Astrophysics **642**, A33 (2020).

[222] R. A. Chevalier, "The radio and x-ray emission from type ii supernovae", Astrophysical Journal, Part 1, vol. 259, Aug. 1, 1982, p. 302-310. Research supported by the University of Virginia **259**, 302–310 (1982).

[223] C. Fransson, P. Lundqvist, and R. A. Chevalier, "Circumstellar interaction in sn 1993j", arXiv preprint astro-ph/9406054 (1994).

[224] P. Bodenheimer and J. P. Ostriker, “Do Pulsars Make Supernovae? 11. Calculations of Light Curves for Type 11 Events”, The Astrophysical Journal **191**, 465 (1974).

[225] B. Gaffet, “Pulsar theory of supernova light curves. II - The light curve and the continuous spectrum”, The Astrophysical Journal **216**, 852 (1977).

[226] S. E. Woosley, “BRIGHT SUPERNOVAE FROM MAGNETAR BIRTH”, The Astrophysical Journal **719**, L204–L207 (2010).

[227] J. Dexter and D. Kasen, “SUPERNOVA LIGHT CURVES POWERED BY FALLBACK ACCRETION”, The Astrophysical Journal **772**, 30 (2013).

[228] B. D. Metzger et al., “Electromagnetic counterparts of compact object mergers powered by the radioactive decay of r-process nuclei”, Monthly Notices of the Royal Astronomical Society **406**, 2650–2662 (2010).

[229] L. F. Roberts et al., “ELECTROMAGNETIC TRANSIENTS POWERED BY NUCLEAR DECAY IN THE TIDAL TAILS OF COALESCING COMPACT BINARIES”, The Astrophysical Journal **736**, L21 (2011).

[230] J. Lippuner and L. F. Roberts, “R-PROCESS LANTHANIDE PRODUCTION and HEATING RATES in KILONOVAE”, Astrophysical Journal **815**, 82 (2015).

[231] D. Kasen and J. Barnes, “Radioactive Heating and Late Time Kilonova Light Curves”, (2018).

[232] N. M. H. Vaytet et al., “A numerical model for multigroup radiation hydrodynamics”, **112**, 1323–1335 (2011).

[233] Y.-F. Jiang, “An Implicit Finite Volume Scheme to Solve the Time-dependent Radiation Transport Equation Based on Discrete Ordinates”, **253**, 49, 49 (2021).

[234] L. Ensman and A. Burrows, “Shock Breakout in SN 1987A”, **393**, 742 (1992).

Appendix A

Additional Expressions for the Peak Time-Luminosity Relation

A.1 Expressions for the Peak Time-Luminosity Relation

From Section 3, we found an expression for the peak time-luminosity relation as

$$L_{peak} = \frac{2}{\beta^2 t_{peak}^2} \int_0^{\beta t_{peak}} t' L_{heat}(t')\, dt' \tag{A.1}$$

where L_{peak} is the observed peak luminosity at the peak time t_{peak}, $L_{heat}(t)$ is the time-dependent heating rate, and β is a constant that depends on opacity/concentration effects. Eq.(A.1) can be evaluated analytically for several functional forms of $L_{heat}(t)$.

Suppose the heating source can be written most generally as

$$L_{heat}(t) = \frac{E_s}{t_s} \mathcal{H}(t, t_s) \tag{A.2}$$

where $\mathcal{H}(t, t_s)$ is the time-dependent component of $L_{heat}(t)$, t_s is the heating source timescale, and E_s the characteristic heating energy. Equivalently, the heating source can be expressed in terms of a characteristic luminosity by setting $L_0 = E_s/t_s$.

Let $\tau = t_{peak}/t_s$ be the ratio between the peak time and source timescale. Then the peak luminosity can be evaluated to get

$$L_{peak} = \frac{2E_s t_s}{\beta^2 t_{peak}^2} \times f(\tau, \beta) \tag{A.3}$$

where $f(\tau, \beta)$ depends on the exact functional form of $\mathcal{H}(t, t_s)$. For an exponential source,

$$\mathcal{H}(t, t_s) = \exp\left[-t/t_s\right] \tag{A.4}$$

the integral can be evaluated to get

$$f(\tau,\beta) = 1 - (1+\beta\tau)\, e^{-\beta\tau} \tag{A.5}$$

In Table 1, we give the analytic expressions of $f(\tau,\beta)$ for a variety of heating functions $\mathcal{H}(t,t_s)$. The choice of β again depends on opacity/recombination effects, as well as the spatial distribution of heating. In Table 2, we give approximate values of β based on numerical results.

Radioactive Two-Decay Chain

Numerous transients are powered by the radioactive decay of synthesized elements, e.g. ^{56}Ni in Type I and IIb/pec supernovae.

Consider a decay chain consisting of $0 \to 1 \to 2$ with decay timescales t_0 and t_1, respectively (ignoring the contribution to heating of species 2). The total number of the species at time t is expressed as

$$N_0(t) = N e^{-t/t_0} \tag{A.6}$$

$$N_1(t) = N \frac{t_1}{t_1 - t_0} \left(e^{-t/t_1} - e^{-t/t_0}\right) \tag{A.7}$$

where $N = N_0(0)$, and it is assumed that $N_1(0) = 0$. Let Q_0, m_0, Q_1, and m_1 be the decay energies and species mass. Define heating rates per unit mass as

$$\varepsilon_0 = \frac{Q_0}{m_0 t_0} \tag{A.8}$$

$$\varepsilon_1 = \frac{Q_1}{m_1(t_1 - t_0)} \tag{A.9}$$

Then the heating luminosity can be expressed as

$$L_{heat}(t) = M\left[(\varepsilon_0 - \varepsilon_1)e^{-t/t_0} + \varepsilon_1 e^{-t/t_1}\right] \tag{A.10}$$

where $M = N m_0$ is the total initial mass of species 0.

With this expression we can derive the peak time-luminosity relation as

$$\begin{aligned} L_{peak} = \frac{2\varepsilon_0 M t_0^2}{\beta^2 t_{peak}^2} \Bigg[& \left(1 - \frac{\varepsilon_1}{\varepsilon_0}\right)\left(1 - (1+\beta t_{peak}/t_0)e^{-\beta t_{peak}/t_0}\right) \\ & + \frac{\varepsilon_1 t_1^2}{\varepsilon_0 t_0^2}\left(1 - (1+\beta t_{peak}/t_1)e^{-\beta t_{peak}/t_1}\right)\Bigg] \end{aligned} \tag{A.11}$$

Radioactive Nickel Decay

Supernovae of Type I and IIb/pec are powered primarily by the radioactive decay of ^{56}Ni followed by ^{56}Co [61, 62]. The heating function can be written in terms of the nickel mass M_{Ni} as

$$L_{heat}(t) = M_{Ni}\left[\left(\varepsilon_{Ni} - \varepsilon_{Co}\right)e^{-t/t_{Ni}} + \varepsilon_{Co}e^{-t/t_{Co}}\right] \tag{A.12}$$

where $\varepsilon_{Ni} = 3.9 \cdot 10^{10}$ erg g^{-1} s^{-1} and $\varepsilon_{Co} = 6.8 \cdot 10^{9}$ erg g^{-1} s^{-1} are the specific heating rates of Ni- and Co-decay, and $t_{Ni} = 8.8$ days and $t_{Co} = 111.3$ days are the decay timescales.

We can evaluate the peak time-luminosity relation in terms of β as

$$\begin{aligned} L_{peak} = \frac{2\varepsilon_{Ni}M_{Ni}t_{Ni}^2}{\beta^2 t_{peak}^2}&\left[\left(1-\frac{\varepsilon_{Co}}{\varepsilon_{Ni}}\right)\left(1-(1+\beta t_{peak}/t_{Ni})e^{-\beta t_{peak}/t_{Ni}}\right)\right. \\ &\left. +\frac{\varepsilon_{Co}t_{Co}^2}{\varepsilon_{Ni}t_{Ni}^2}\left(1-(1+\beta t_p/t_{Co})e^{-\beta t_p/t_{Co}}\right)\right] \end{aligned} \tag{A.13}$$

Let $t_p = t_{peak}/\text{day}$ be the peak time in days. Using the numerical values of ε_{Ni}, ε_{Co}, t_{Ni}, and t_{Co} we get a more compact numerical expression (accurate to within $\sim 1\%$) as

$$\begin{aligned} L_{peak} = 10^{46}&\left(\frac{M_{Ni}}{M_\odot}\right)\frac{1}{\beta^2 t_p^2}\times \\ &[34.78 - (1+0.114\beta t_p)\exp\left(-0.114\beta t_p\right) \\ &-33.78\left(1+0.009\beta t_p\right)\exp\left(-0.009\beta t_p\right))]\ erg\ s^{-1} \end{aligned} \tag{A.14}$$

Magnetar-powered Supernovae

The spindown luminosity of a magnetar is generally described by [73, 224–226]

$$L_{mag}(t) = \frac{E_{mag}}{t_{mag}}\frac{l-1}{\left(1+t/t_{mag}\right)^l} \tag{A.15}$$

where $l = 2$ for magnetic dipole spin-down,

$$E_{mag} = \frac{I_{NS}\Omega^2}{2} = 2\times 10^{50}P_{10}^{-2}\ erg \tag{A.16}$$

is the magnetar energy with $P_{10} = P/10\text{ms}$ is the spindown period, and

$$t_{mag} = \frac{6I_{NS}c^3}{B^2R_{NS}^6\Omega^2} = 1.3B_{14}^{-2}P_{10}^2\ yr \tag{A.17}$$

is the spindown timescale with $B_{14} = B/10^{14}$G the magnetic field strength. For $l = 2$, we get

$$L_{peak} = \frac{2E_{mag}t_{mag}}{\beta^2 t_{peak}^2}\left[\ln(1+\beta\tau) - (1+1/(\beta\tau))^{-1}\right] \tag{A.18}$$

were $\tau = t_{peak}/t_{mag}$.

Accretion-Powered Transients

Another interesting heating source is that of an accreting compact object [227]. Let $\dot{M} \sim M_{acc}/t_{acc}$ be the accretion rate of mass M_{acc} and timescale t_{acc}. We here consider two functional forms of accretion luminosity. The first is of constant heating that "shuts off" after a time t_{acc},

$$L_{acc}(t) = \frac{\epsilon M_{acc} c^2}{t_{acc}} \Theta(t - t_{acc}) \tag{A.19}$$

where $\Theta(t - t_{acc})$ is the Heaviside step function, and ϵ is the radiative efficiency. Substituting this into Eq.(2.19) we get

$$L_{peak} = \frac{\epsilon M_{acc} t_{acc}}{\beta^2 t_{peak}^2} \tag{A.20}$$

Another functional form of interest is that of an $n = -5/3$ power law, appropriate for fallback accretion

$$L_{acc}(t) = \frac{\epsilon M_{acc} c^2}{t_{acc}} \left(\frac{t}{t_{acc}}\right)^{-5/3} \tag{A.21}$$

Again evaluating this source in Eq.(2.19) we get

$$L_{peak} = \frac{6\epsilon M_{acc} c^2 t_{acc}}{\beta^2 t_{peak}^2} \left[\left(\frac{\beta t_{peak}}{t_{acc}}\right)^{1/3} - 1\right] \tag{A.22}$$

Kilonovae

The kilonova heating rate from the radioactive decay of r-process elements can be parameterized as [53, 228–230].

$$L_{heat}(t) = \varepsilon_0 M_{ej} \left(\frac{t}{t_0}\right)^{-\eta} \times f(t) \tag{A.23}$$

where $\varepsilon_0 \approx 10^{11}$ erg g^{-1} s^{-1} is the specific heating rate, M_{ej} is the ejecta mass, $t_0 \approx 1$ day, and $\eta \approx 1.3$. The function $f(t)$ gives the thermalization efficiency with which the radioactive decay energy is able to deposit as heat in the ejecta.

[231] suggest an analytic approximation of the thermalization efficiency of electrons

$$f(t) = \left(1 + \frac{t}{t_e}\right)^{-1} \tag{A.24}$$

where

$$t_e \approx 12.9 M_{0.01}^{2/3} v_{0.2}^{-2} \ days \tag{A.25}$$

is the electron thermalization timescale, $M_{0.01} = M_{ej}/0.01M_{\odot}$, and $v_{0.2} = v_{ej}/0.2c$ the ejecta velocity.

Evaluating the integral for $\eta = 1.3$ and the above approximation for the thermalization efficiency, we get

$$L_{peak} = 2.86 \varepsilon_0 M_{ej} \left(\frac{t_0}{\beta t_{peak}} \right)^{1.3} {}_2F_1 \left(0.7, 1, 1.7, -\beta t_{peak}/t_e\right) \tag{A.26}$$

where ${}_2F_1(a, b, c, x)$ is the hypergeometric function which we approximate by a functional fit of

$${}_2F_1 \left(0.7, 1, 1.7, -\beta t_{peak}/t_e\right) \approx \left(1 + \beta t_{peak}/t_e\right)^{-1/2} \tag{A.27}$$

Thus, the peak time-luminosity relation for kilonova is approximately

$$L_{peak} = 2.86 \varepsilon_0 M_{ej} \left(\frac{t_0}{\beta t_{peak}} \right)^{1.3} \cdot \left(1 + \beta t_{peak}/t_e\right)^{-1/2} \tag{A.28}$$

Assuming the r-process heating is uniformly mixed throughout the ejecta, we choose an approximate $\beta \approx 2$ based on numerical simulations.

A.2 Derivation of the Peak Time-Luminosity Relation

In Section 3, we showed that a simple relation holds between the peak time and luminosity of a light curve

$$L_{peak} = \frac{2}{\beta^2 t_{peak}^2} \int_0^{\beta t_{peak}} t' L_{heat}(t') dt' \tag{A.29}$$

assuming there exists some time $t = \beta t_{peak}$ such that $\epsilon(t) = 0$, where we defined

$$\epsilon(t) = \left[\frac{t^2}{2} L_{peak} - \int_0^t t' L(t') \, dt' \right] - tE(t) \tag{A.30}$$

Our goal, then, is to motivate that such a time when $\epsilon(t) = 0$ exists. We define two quantities

$$\mathcal{F}(t) = \frac{t^2}{2} L_{peak} - \int_0^t t' L(t') \, dt' \tag{A.31}$$

and

$$\mathcal{E}(t) = tE(t) \tag{A.32}$$

Thus, the time when $\epsilon(t) = 0$ also implies

$$\mathcal{F}(t) = \mathcal{E}(t) \tag{A.33}$$

Initially, $\mathcal{E}(t)$ will rise as heat is deposited and trapped in the optically thick ejecta. Eventually, the expanding ejecta becomes optically thin, allowing radiation to freely escape. As a result, any heating goes directly into the light curve, $L(t) = L_{heat}(t)$. This implies that $\mathcal{E}(t) = 0$ at late times $t \gg t_{peak}$.

Since $\mathcal{E}(t)$ is continuous, if $\mathcal{F}(t)$ is a monotonically *increasing* function of time and $\mathcal{F}(t) < \mathcal{E}(t)$ for some t, then it follows that $\mathcal{F}(t)$ and $\mathcal{E}(t)$ must intersect.

Taking the derivative in time of $\mathcal{F}(t)$ we get

$$\mathcal{F}'(t) = t\left[L_{peak} - L(t)\right] \tag{A.34}$$

Since $L(t) \leq L_{peak}$ by definition, it follows that

$$\mathcal{F}'(t) \geq 0 \tag{A.35}$$

and so $\mathcal{F}(t)$ is indeed a monotonically increasing function of time.

Next, we need to show that there exists a time such that $\mathcal{F}(t) < \mathcal{E}(t)$. At $t = 0$ we have $\mathcal{F}(t) = \mathcal{E}(t) = 0$. For small t, we can expand the derivative of $\mathcal{E}(t)$ to get

$$\mathcal{E}'(t) \approx t\left[L_{heat}(0) + tL'_{heat}(0) - t^2 L'(0)\right] \tag{A.36}$$

$$\approx tL_{heat}(0) + \mathcal{O}(t^2) \tag{A.37}$$

where we make use of the fact that $L(0) = 0$. Similarly, for $\mathcal{F}(t)$, we get

$$\mathcal{F}'(t) \approx t\left[L_{peak} - t^2 L'(0)\right] \tag{A.38}$$

$$\approx tL_{peak} + \mathcal{O}(t^3) \tag{A.39}$$

If the condition $L_{heat}(0) > L_{peak}$ is satisfied, then

$$\mathcal{E}'(t) > \mathcal{F}'(t) \tag{A.40}$$

for small t. Since $\mathcal{F}(0) = \mathcal{E}(0) = 0$, we have that, at early times, $\mathcal{E}(t) > \mathcal{F}(t)$. Combined with the monotonicity of $\mathcal{F}(t)$ and the fact that $\mathcal{E}(t) \to 0$ at late times, it follows that $\mathcal{E}(t)$ and $\mathcal{F}(t)$ must intersect. In other words, there exists a time such that $\epsilon(t) = 0$ and the peak time-luminosity relation holds.

There is a-priori mathematical justification for $L_{heat}(0) > L_{peak}$, however in physical cases of interest (e.g. radioactive decay, magnetar spindown, etc.), this seems to be a valid assumption, whereby $L_{heat}(t)$ is monotonically decreasing in time. Furthermore, both diffusion and adiabatic degradation act to spread out and decrease the heating luminosity in time. This is confirmed in our numerical simulations for a wide variety of heating functions, wherein all the light curves seem to indicate $L_{heat}(0) > L_{peak}$ (see e.g. Figs. (2.1) and 2.2).

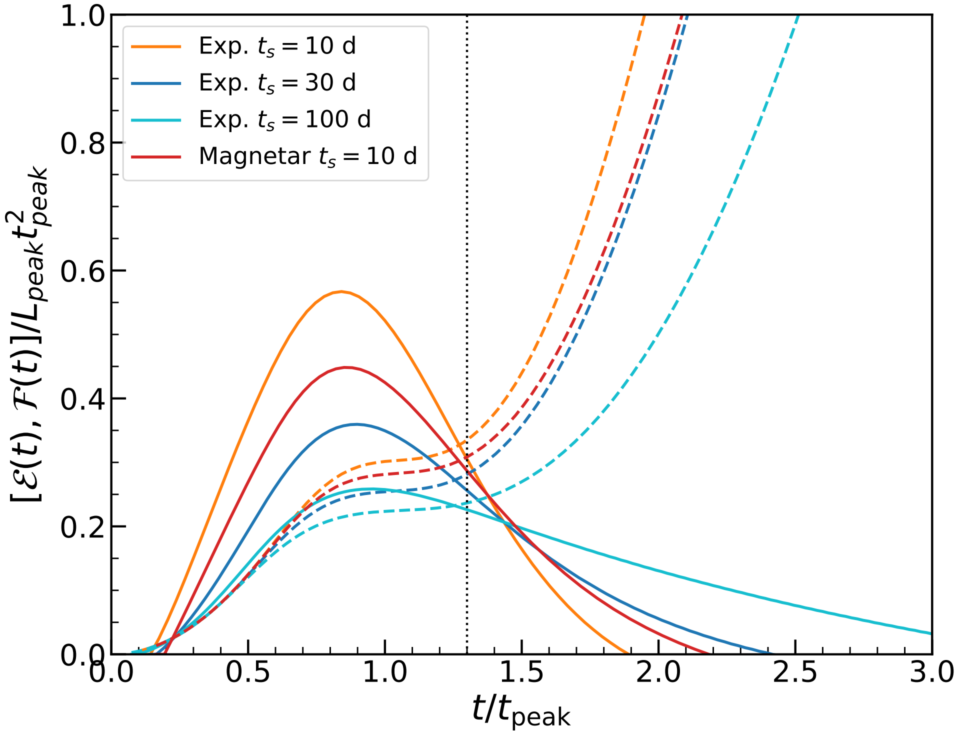

Figure A.1: Comparison of the quantities $\mathcal{E}(t)$ (solid lines) and $\mathcal{F}(t)$ (dashed lines) as a function of time, for a central heating source with different functional forms and source timescales. The time when $\mathcal{E}(t) = \mathcal{F}(t)$ gives the value of β.

Another mathematical possibility is that $\mathcal{F}(t)$ and $\mathcal{E}(t)$ intersect more than once. Assuming $L_{heat}(0) > L_{peak}$, since $\mathcal{F}(t)$ is monotonically increasing, such behavior requires $\mathcal{E}(t)$ to "oscillate", i.e. there exists more than one time that $d\mathcal{E}/dt = 0$. It is unclear whether such behavior is physical.

In summary, it is difficult to prove definitively that the peak time-luminosity relation holds for an arbitrary heating function. For a variety of monotonically decreasing heating functions, we have confirmed numerically that $L_{heat}(0) > L_{peak}$. Furthermore, this intersection appears to occur only once. In Fig.(A.1), we show the behavior of $\mathcal{E}(t)$ and $\mathcal{F}(t)$ for a subset of numerical simulations, assuming a central source and constant opacity. We pick different functional forms (exponential and magnetar-like) as well as different source timescales. In all cases, the time when $\epsilon(t) = 0$ is nearly identical, with $\beta \approx 1.3$.

Appendix B

Supplementary Equations and Derivations of Circumstellar Interaction

B.1 Numerical Scalings

In §3.5 we performed numerical simulations of CSM interaction to determine the scaling behavior of the different light curve phases, and compare against the analytics presented in §3.4. Namely, we proposed fitting formula of the i-th phase luminosity and timescale of

$$L_i = a_i \eta^{-3\alpha_i} \xi^{k_i} L_0 \tag{B.1}$$

$$t_i = b_i \eta^{\alpha_i} \xi^{c_i} t_0 \tag{B.2}$$

where $L_0 = M_{csm} v_{ej}^3 / R_{csm}$, $t_0 = R_{csm}/v_{ej}$, $\eta = M_{csm}/M_{ej}$, and the breakout parameter is

$$\xi = \beta_0 \tau_0 \eta^{-\alpha} \approx 10\, \kappa M_{csm,\odot} v_9 R_4^{-2} \eta^{-\alpha} \tag{B.3}$$

Here, $\beta_0 = v_{ej}/c$ (where $v_{ej} = \sqrt{2E_{sn}/M_{ej}}$), $\tau_0 = \kappa M_{csm}/4\pi R_{csm}^2$, $v_9 = v_{ej}/10^9$ cm s^{-1}, $M_{csm,\odot} = M_{csm}/M_\odot$, and $R_4 = R_{csm}/10^4 R_\odot$. The value of α in the breakout parameter can be estimated from analytic arguments (see Appendix B.2) as

$$\alpha = \begin{cases} 1/2, & (\eta \gtrsim 1) \\ 1/(n-3), & (\eta \ll 1) \end{cases} \tag{B.4}$$

where $\rho_{ej} \propto r^{-n}$ is the outer ejecta density profile, and $n \approx 7 - 10$ [140].Note that the scaling of $\alpha = 1/(n-3)$ for $\eta \ll 1$ breaks down when the shock reaches the flatter inner portion of the ejecta. This occurs when the amount of swept up CSM mass exceeds the mass contained in the steep outer ejecta. The ratio of outer to inner ejecta mass is equal to

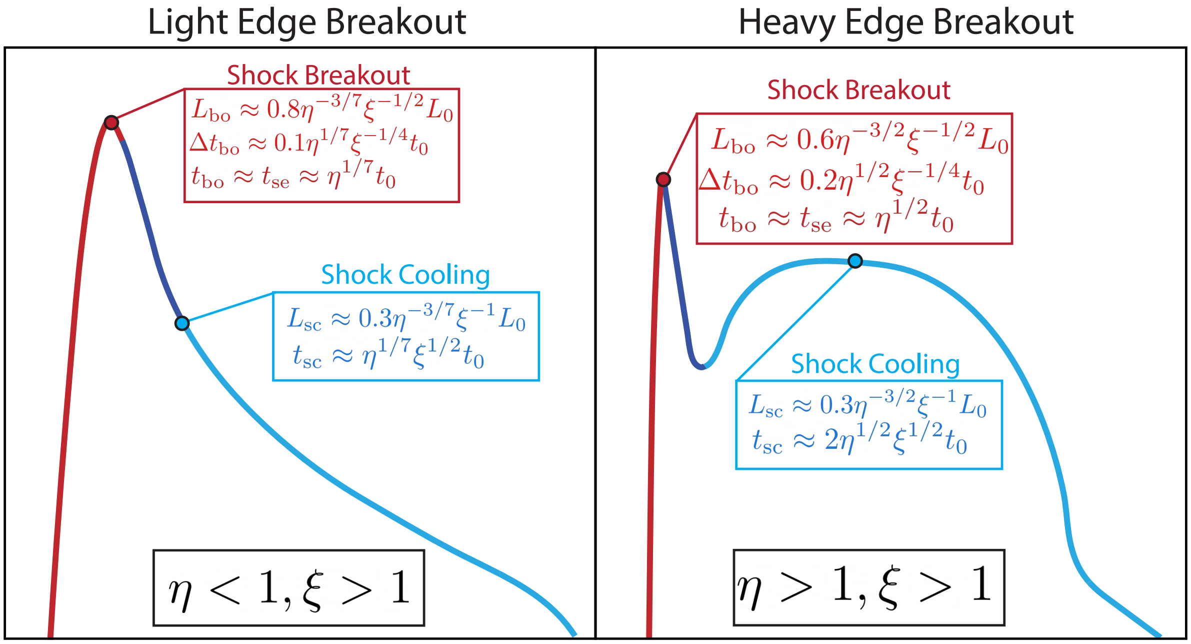

Figure B.1: Schematic diagram with numerically calibrated scalings for edge breakout light curves, in the light *(left)* and heavy *(right)* CSM regimes. Assumes ejecta density profile $\rho_{ej} \propto r^{-10}$ and CSM density profile $\rho_{csm} \propto r^{-2}$. More general scalings for other profiles given in §3.4.

$(3-\delta)/(n-3) = 2/7$ for the fiducial power-laws. Thus, for CSM masses $M_{csm} \gtrsim 0.3 M_{ej}$, the behavior of the shockwave will change.

The scaling exponents (a_i, k_i), (b_i, c_i), and α_i are fit to the numerical simulations described in §3.5. The numerical fits are given for each interaction class and phase in Figs. B.1 and B.2, which we then convert into physical scalings below. Note that the models assume an $n = 10$ ejecta density profile, and an $s = 2$ CSM density profile. For more general density profiles, refer to the analytical scalings in §3.4.

Light Edge Breakout ($\eta < 1, \xi > 1$)

$$L_{bo} \sim 7\, M_{csm}^{1/7} M_{ej}^{-25/28} E_{sn}^{5/4} \kappa^{-1/2} c^{1/2} \tag{B.5}$$

$$\Delta t_{bo} \sim 0.1\ M_{csm}^{-1/14} R_{csm}^{3/2} M_{ej}^{25/56} E_{sn}^{-5/8} \kappa^{-1/4} c^{1/4} \tag{B.6}$$

$$t_{bo} \approx t_{se} \sim 0.7\ M_{csm}^{1/7} R_{csm}^{1} M_{ej}^{5/14} E_{sn}^{-1/2} \tag{B.7}$$

$$L_{sc} \sim 8\, M_{csm}^{-2/7} R_{csm}^{1} M_{ej}^{-5/7} E_{sn}^{1} \kappa^{-1} c \tag{B.8}$$

$$t_{sc} \sim 0.2\, M_{csm}^{4/7} M_{ej}^{5/28} E_{sn}^{-1/4} \kappa^{1/2} c^{-1/2} \tag{B.9}$$

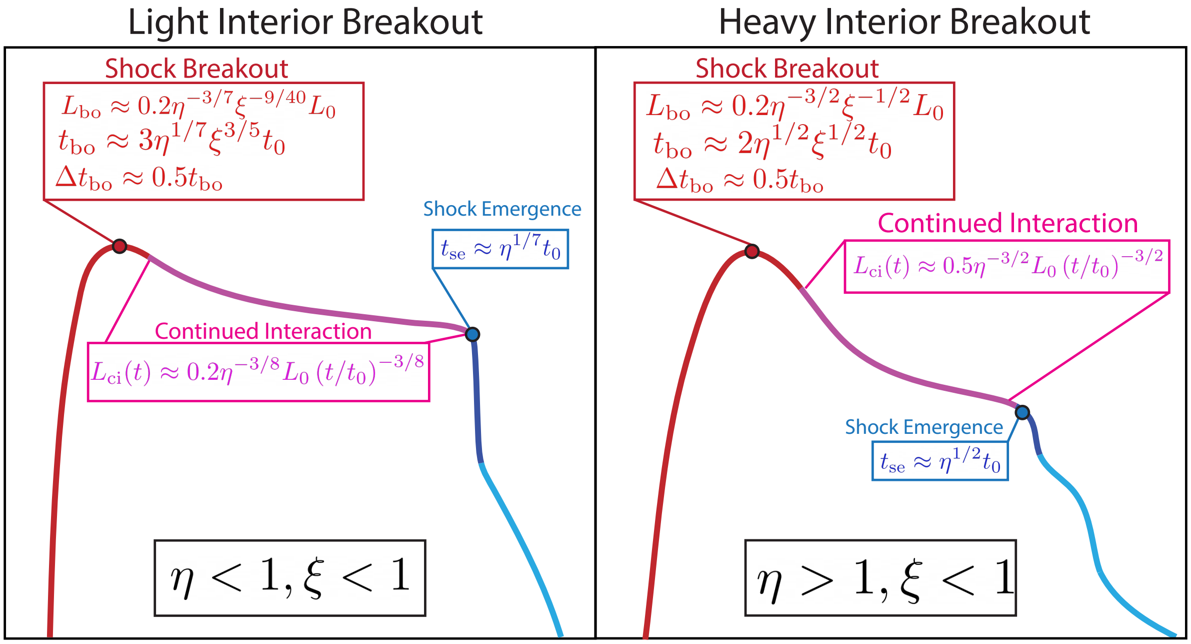

Figure B.2: Same as Fig. B.1 but for interior breakout events, for light (*left*) and heavy (*right*) CSM regimes. Assumes ejecta density profile $\rho_{ej} \propto r^{-10}$ and CSM density profile $\rho_{csm} \propto r^{-2}$. More general scalings for other profiles given in §3.4.

Heavy Edge Breakout $(\eta > 1, \xi > 1)$

$$L_{bo} \sim 5\, M_{csm}^{-3/4} E_{sn}^{5/4} \kappa^{-1/2} c^{1/2} \tag{B.10}$$

$$\Delta t_{bo} \sim 0.2\, M_{csm}^{3/8} R_{csm}^{3/2} E_{sn}^{-5/8} \kappa^{-1/4} c^{1/4} \tag{B.11}$$

$$t_{bo} \approx t_{se} \sim 0.7\, M_{csm}^{1/2} R_{csm}^{1} E_{sn}^{-1/2} \tag{B.12}$$

$$L_{sc} \sim 8\, M_{csm}^{-1} R_{csm}^{1} E_{sn}^{1} \kappa^{-1} c \tag{B.13}$$

$$t_{sc} \sim 0.5\, M_{csm}^{3/4} E_{sn}^{-1/4} \kappa^{1/2} c^{-1/2} \tag{B.14}$$

Light Interior Breakout $(\eta < 1, \xi < 1)$

$$L_{bo} \sim 0.9\, M_{csm}^{53/140} R_{csm}^{-11/20} M_{ej}^{-111/112} E_{sn}^{111/80} \kappa^{-9/40} c^{9/40} \tag{B.15}$$

$$t_{bo} \approx 2\Delta t_{bo} \sim 0.6\, M_{csm}^{23/35} R_{csm}^{-1/5} E_{sn}^{-1/5} M_{ej}^{1/7} \kappa^{3/5} c^{-3/5} \tag{B.16}$$

$$t_{se} \sim 0.7\, M_{csm}^{1/7} R_{csm}^{1} M_{ej}^{5/14} E_{sn}^{-1/2} \tag{B.17}$$

$$L_{ci}(t) \sim 0.5\, M_{csm}^{5/8} R_{csm}^{-5/8} M_{ej}^{-15/16} E_{sn}^{-21/16} t^{-3/8} \tag{B.18}$$

Heavy Interior Breakout ($\eta > 1, \xi < 1$)

$$L_{bo} \sim 2\, M_{csm}^{-3/4} E_{sn}^{5/4} \kappa^{-1/2} c^{1/2} \tag{B.19}$$

$$t_{bo} \approx 2\Delta t_{bo} \sim 0.5\, M_{csm}^{3/4} E_{sn}^{-1/4} \kappa^{1/2} c^{-1/2} \tag{B.20}$$

$$t_{se} \sim 0.7\, M_{csm}^{1/2} R_{csm}^{1} E_{sn}^{-1/2} \tag{B.21}$$

$$L_{ci}(t) \sim 0.8\, M_{csm}^{-1/2} R_{csm}^{1/2} M_{ej}^{3/4} E_{sn}^{3/4} t^{-3/2} \tag{B.22}$$

B.2 Derivation of Shock Similarity Exponents

In §3.4, we introduced power-law forms of the radius with time as

$$r_{sh}(t) \sim R_{csm} \left(\frac{t}{\eta^{\alpha} t_0} \right)^{\lambda} \tag{B.23}$$

where $t_0 = R_{csm}/v_{ej}$,and $\eta = M_{csm}/M_{ej}$. The shock velocity is similarly expressed as

$$v_{sh}(t) = \frac{dr_{sh}}{dt} \sim v_{ej} \eta^{-\alpha} \left(\frac{t}{\eta^{\alpha} t_0} \right)^{\lambda - 1} \tag{B.24}$$

These two expressions can be combined to get the shock velocity in terms of the shock radius as

$$v_{sh}(r_{sh}) = v_{ej} \eta^{-\alpha} \left(\frac{r_{sh}}{R_{csm}} \right)^{(\lambda-1)/\lambda} \tag{B.25}$$

For a power-law CSM density $\rho_{csm}(r) \propto r^{-s}$ with inner radius R_* and outer radius R_{csm}, the amount of mass swept up by the shock will go as

$$\delta M(r_{sh}) = \int_{R_*}^{r_{sh}} 4\pi r^2 \rho_{csm}(r)\, dr \tag{B.26}$$

$$\approx M_{csm} \left(\frac{r_{sh}}{R_{csm}} \right)^{3-s} \tag{B.27}$$

where we have assumed in the last step that $R_* \ll R_{csm}$.

The shock radius and velocity depends on the two similarity exponents (α, λ), which in turn will depend on η. We now derive the shock equations and exponents in the different regimes.

Light CSM Regime ($M_{csm} < M_{ej}$)

If $\eta < 1$, then the steep outermost layer of the ejecta will dominate the bulk of the shock evolution. Only a portion of the ejecta mass of order $\sim M_{csm}$ will participate in the interaction.

The amount of momentum contained in the ejecta above a radius r_0 is

$$\delta(Mv) = \int_{r_0}^{\infty} 4\pi r^2 \rho_{ej}(r) v(r)\, dr \tag{B.28}$$

If we assume the ejecta expands homologously, $v = r/t$, we can write the ejecta density profile as a power-law in velocity coordinates,

$$\rho_{ej}(v_0) = \frac{f_\rho M_{ej}}{v_{ej}^3 t^3} \left(\frac{v_0}{v_{ej}} \right)^{-n} \tag{B.29}$$

where $\rho_0(t) \sim M_{ej}/(v_{ej} t)^3$ and f_ρ is a constant of order unity (see Appendix **??**). The momentum above a velocity coordinate v_0 is therefore

$$\delta(Mv)(v_0) = \frac{4\pi}{(n-4)} f_\rho M_{ej} v_{ej} \left(\frac{v_0}{v_{ej}} \right)^{4-n} \tag{B.30}$$

As the shock runs through the CSM, it sweeps up as mass δM_{sh} at a velocity v_{sh}. From conservation of momentum,

$$2 \delta M_{sh} v_{sh} = \delta(Mv)(v_{sh}) \tag{B.31}$$

Using Eq. B.26 for the swept up mass and Eq. B.30 for the ejecta momentum, we get

$$M_{csm} \left(\frac{r_{sh}}{R_{csm}} \right)^{3-s} v_{sh} \approx M_{ej} v_{ej} \left(\frac{v_{sh}}{v_{ej}} \right)^{4-n} \tag{B.32}$$

where we have dropped order-unity constants. Using $v_{sh} = dr_{sh}/dt$ and rearranging to solve for r_{sh}, we get

$$r_{sh}(t) \sim R_{csm} \left(\frac{t}{\eta^{1/(n-3)} t_0} \right)^{(n-3)/(n-s)} \tag{B.33}$$

From this, we see that the similarity exponents in the light CSM regime $\eta < 1$ are

$$\lambda = \frac{(n-3)}{(n-s)}, \;\; \alpha = \frac{1}{(n-3)} \quad (\eta < 1) \tag{B.34}$$

These similarity exponents hold for both adiabatic and radiative shocks in this regime.

Heavy CSM Regime ($M_{csm} > M_{ej}$)

If the CSM mass exceeds the ejecta mass, $\eta > 1$, then the interaction will tap the entirety of the ejecta kinetic energy, and will obey a blastwave evolution. The behavior of the blastwave depends on whether it is adiabatic or radiative.

Adiabatic Blastwave (Sedov)

Once the shock sweeps up of order $\delta M_{sh} \sim M_{ej}$, the shock transitions into a blastwave. If the blastwave is adiabatic, then energy is conserved and so

$$M_{ej} v_{ej}^2 \approx \delta M_{sh} v_{sh}^2 \tag{B.35}$$

where we have assumed the bulk of the ejecta kinetic energy is located near the shock front.

Using Eq.B.26 for δM_{sh} and $v_{sh} = dr_{sh}/dt$, we get

$$r_{sh}(t) \sim R_{csm} \left(\frac{t}{\eta^{1/2} t_0} \right)^{2/(5-s)} \tag{B.36}$$

which is the usual Sedov-Taylor blastwave solution for a power-law medium $\rho \propto r^{-s}$. Thus, the similarity exponents for an energy-conserving blastwave are

$$\lambda = \frac{2}{(5-s)}, \;\; \alpha = \frac{1}{2} \quad (\eta > 1) \tag{B.37}$$

Radiative Blastwave (Snowplow)

If radiation is able to escape ahead of the shock, then energy is no longer conserved. Instead, from conservation of momentum, we have

$$M_{ej} v_{ej} \approx \delta M_{sh} v_{sh} \tag{B.38}$$

Using Eq.B.26 for δM_{sh} and $v_{sh} = dr_{sh}/dt$, we therefore get that a radiative blastwave will evolve in time as

$$r_{sh}(t) \sim R_{csm} \left(\frac{t}{\eta t_0} \right)^{1/(4-s)} \tag{B.39}$$

which gives the evolution for a momentum-conserving "snowplow" blastwave in a power-law medium. Thus, the similarity exponents for a radiative blastwave are

$$\lambda = \frac{1}{(4-s)}, \;\; \alpha = 1 \;\; (\eta > 1) \tag{B.40}$$

Shock Breakout Radius

Shock breakout occurs when the shock optical depth τ_{sh} equals c/v_{bo}, where v_{bo} is the breakout velocity that depends on time. To find this point, we integrate the shock optical depth to the breakout radius

$$\tau_{bo} = -\int_{R_{csm}}^{r_{bo}} \kappa \rho_{csm}(r)\, dr \approx -\frac{\tau_0}{(1-s)} \left[x_{bo}^{1-s} - 1 \right] \tag{B.41}$$

where $\tau_0 = \kappa M_{csm}/4\pi R_{csm}^2$ and $x_{bo} = r_{bo}/R_{csm}$. For a shock radius that evolves in time as a power-law $r_{sh} \propto t^{\lambda}$ and using the fact that $v_{sh} = dr_{sh}/dt$, the breakout velocity can be expressed in terms of x_{bo} as

$$v_{bo} \approx v_{ej}\eta^{-\alpha}x_{bo}^{1-1/\lambda} \tag{B.42}$$

Setting $\tau_{sh} = c/v_{bo}$ we get a non-linear equation for x_{bo}

$$(1-s)x_{bo}^{1/\lambda-1} = -\frac{\beta_0\tau_0}{\eta^{\alpha}}\left[x_{bo}^{1-s}-1\right] = -\xi\left[x_{bo}^{1-s}-1\right] \tag{B.43}$$

where $\beta_0 = v_{ej}/c$ and $\xi = \beta_0\tau_0\eta^{-\alpha}$. In general Eq. B.43 must be solved numerically for x_{bo}, given $\beta_0, \tau_0, \eta^{\alpha}$, and the density profile s. For the case of $s = 2$ we can write this as

$$x_{bo}^{1/\lambda} = (1-x_{bo})\,\xi \tag{B.44}$$

Note that in the limit of $x_{bo} \ll 1$, the breakout location becomes

$$x_{bo} \approx \xi^{\lambda} = \left[\beta_0\tau_0\eta^{-\alpha}\right]^{\lambda} \tag{B.45}$$

Furthermore, for the case of $\xi \gg 1$ ($\beta_0\tau_0 \gg \eta^{\alpha}$) Eq. B.43 is simply $x_{bo} \approx 1$. We can interpolate between these two regimes with a free parameter k_0 as

$$x_{bo} \approx \left(\frac{\beta_0\tau_0}{\eta^{\alpha}}\right)^{\lambda k_0} \approx \xi^{\lambda k_0} \tag{B.46}$$

where $0 \leq k_0 \leq 1$, which is our proposed interior breakout expression Eq. 3.19 used in Sec. 3.4. Note that Eq. B.46 is equivalent to Eq. B.45 for the choice of $k_0 = 1$. Using the fact that $x_{bo} = r_{bo}/R_{csm}$ from the earlier shock derivation, this corresponds to a breakout time of

$$t_{bo} \approx \frac{\kappa M_{csm}}{4\pi R_{csm}c} \tag{B.47}$$

which is the static diffusion time. For the case of $k_0 \approx 0$, we instead have $x_{bo} \approx 1$ and so $t_{bo} \approx t_{se} \approx \eta^{\alpha}t_0$, the shock emergence time. In general, k_0 will take on an intermediate value between these two regimes, and comparison with numerical simulations discussed in Sec. 3.5 and Appendix B.1 show that $k_0 \approx 0.6$ works reasonably well for a range of interior breakout interactions.

Appendix C

Numerical Implementation of Flux-limited Radiation Diffusion

Unlike a Monte-Carlo method discussed later, in very optically thick regions, the radiation field will be near-Planckian (i.e. in equilibrium) with the transport well-described by Fick's law of diffusion. In the following, we work in the comoving frame to $\mathcal{O}(v/c)$, and also limit ourselves to grey (frequency-integrated) equations.

The flux-limited diffusion method is essentially a "moments"-based method, which solves the radiative transfer equation by expanding the specific intensity I_ν in terms of its angular moments. The first and second freuqency-integrated moments of in the comoving frame are

$$\frac{\partial E_0}{\partial t} + \nabla \cdot (\mathbf{v} E_0) + \nabla \cdot \mathbf{F}_0 + \mathbf{P}_0 : \nabla \mathbf{v} = -cG_0^0 \tag{C.1}$$

and

$$\frac{\partial \mathbf{F}_0}{\partial t} + \nabla \cdot (\mathbf{v}\mathbf{F}_0) = c^2 \nabla \cdot \mathbf{P}_0 = \mathbf{F}_0 \cdot \nabla \mathbf{v} = -c^2 \mathbf{G}_0 \tag{C.2}$$

where $\mathbf{P}_0$ is the comoving radiation pressure tensor, and : denotes a tensor contraction. Here we have dropped acceleration terms which are $\mathcal{O}(v^2/c^2)$ (Lowrie & Morel 2001; Mihalas & Mihalas 1984). Furthermore, in what follows, we drop the term $\mathbf{F}_0 \cdot \nabla \mathbf{v}$, which is negligible in the streaming and diffusion limit (Mihalas & Mihalas 1984, although see Lowrie et al. 2001 for a discussion of this term in intermediate regimes).

In order to proceed, we need to adopt a closure that relates the radiation pressure tensor and flux to the energy density. In the flux-limited diffusion approximation, the comoving flux is proportional the the comoving energy density gradient

$$\mathbf{F}_0 = -\frac{c\lambda}{\chi_{0R}} \nabla E_0 \tag{C.3}$$

where χ_{0R} is the Rosseland mean opacity, and λ is the flux limiter such that $\lambda \to \chi_{0R} E_0 / |\nabla E_0|$ in the optically thin limit (and so $|\mathbf{F}_0| = cE_0$, while $\lambda = 1/3$ in the optically thick limit. We adopt the Levermore & Pomraning (1981) flux limiter

$$\lambda = \frac{2+R}{6+3R+R^2} \tag{C.4}$$

where

$$R = \frac{|\nabla E_0|}{\chi_{0R} E_0} \tag{C.5}$$

The corresponding radiation pressure tensor is

$$\mathbf{P}_0 = E_0 \left[\frac{1-f}{2}\mathbf{I} + \frac{3f-1}{2}\hat{\mathbf{n}}_0\hat{\mathbf{n}}_0 \right] \tag{C.6}$$

where $\hat{\mathbf{n}}_0 = \mathbf{F}_0/|\mathbf{F}_0|$, $\mathbf{I}$ is the identity tensor, and the Eddington scalar is given by

$$f = \lambda + (\lambda R)^2 \tag{C.7}$$

The comoving frame equation for the radiation energy density then becomes

$$\frac{\partial E_0}{\partial t} + \nabla \cdot (\mathbf{v} E_0) - \nabla \cdot \left(\frac{c\lambda}{\chi_{0R}} \nabla E_0 \right) + \frac{1-f}{2} E_0 \nabla \cdot \mathbf{v} + \frac{3f-1}{2} E_0 \hat{\mathbf{n}}_0\hat{\mathbf{n}}_0 : \nabla \mathbf{v} = -cG_0^0 \tag{C.8}$$

The corresponding four-force vector in FLD is

$$\mathbf{G}_0 = -\lambda \nabla E_0 \tag{C.9}$$

and

$$cG_0^0 = c\kappa_{0P}\left(E_0 - a_r T^4\right) \tag{C.10}$$

In the gas equations, conservation of mass remains unchanged, while we use the FLD forms of of the radiation four-force for the source terms given above. For example, the total gas energy (kinetic + internal) equation becomes

$$\frac{\partial \left[\rho\left(\frac{v^2}{2} + e\right)\right]}{\partial t} + \nabla \cdot \left[\left(\rho v^2 2 + \rho e + P\right)\mathbf{v}\right] + \lambda \mathbf{v} \cdot \nabla E_0 = c\kappa_{0P}\left(E_0 - a_r T^4\right) \tag{C.11}$$

Using the fact that

$$\nabla \cdot \left[\frac{1-f}{2} \mathbf{v} E_0 \right] = \frac{1-f}{2} \mathbf{v} \cdot \nabla E_0 + \frac{1-f}{2} E_0 \nabla \cdot \mathbf{v} \tag{C.12}$$

we can rewrite the radiation energy density equation as

$$\begin{gathered} \frac{\partial E_0}{\partial t} + \nabla \cdot \left[\left(\frac{3-f}{2} \right) \mathbf{v} E_0 \right] - \nabla \cdot \left(\frac{c\lambda}{\chi_{0R}} \nabla E_0 \right) = \\ \frac{1-f}{2} \mathbf{v} \cdot \nabla E_0 - \frac{3f-1}{2} E_0 \hat{\mathbf{n}}_0\hat{\mathbf{n}}_0 : \nabla \mathbf{v} - c\kappa_{0P}\left(E_0 - a_r T^4\right) \end{gathered} \tag{C.13}$$

Finally, if we work with the *total* (gas kinetic + internal + radiation) energy density equation we have

$$\begin{aligned}\frac{\partial E_T}{\partial t} + \nabla \cdot \left[\left(E_T + P + \frac{1-f}{2}E_0\right)\mathbf{v}\right] - \nabla \cdot \left(\frac{c\lambda}{\chi_{0R}}\nabla E_0\right) \\ = \left(\frac{1-f}{2} - \lambda\right)\mathbf{v} \cdot \nabla E_0 - \frac{3f-1}{2}E_0\hat{\mathbf{n}}_0\hat{\mathbf{n}}_0 : \nabla \mathbf{v}\end{aligned} \tag{C.14}$$

where $E_T = \rho v^2/2 + \rho e + E_0$ is the total energy.

To see the behavior of the equations, consider the optically thick limit where $\lambda = f = 1/3$ and $\mathbf{P}_0 = E_0/3\mathbf{I}$. Then the radiation energy equation becomes

$$\frac{\partial E_0}{\partial t} + \nabla \cdot \left(\frac{4}{3}\mathbf{v}E_0\right) - \nabla \cdot \left(\frac{c}{3\chi_{0R}}\nabla E_0\right) = \frac{1}{3}\mathbf{v} \cdot \nabla E_0 - c\kappa_{0P}\left(E_0 - a_r T^4\right) \tag{C.15}$$

The total energy equation becomes

$$\frac{\partial E_T}{\partial t} + \nabla \cdot \left[\left(E_T + P_T\right)\mathbf{v}\right] - \nabla \cdot \left(\frac{c}{3\chi_{0R}}\nabla E_0\right) = 0 \tag{C.16}$$

where $P_T = P + E_0/3$ is the total (gas + radiation) pressure.

When solving the coupled equations of radiation hydrodynamics, we require a time-stepping method that handles the potentially stiff radiation source/sink terms. Furthermore, an explicit treatment of the radiation diffusion will be limited by a much stricter timestep

$$\Delta t < \frac{\chi_{0R}\Delta x^2}{c} \tag{C.17}$$

As a result, it is usually more advantageous to treat the diffusion and source/sink terms with an implicit scheme. On the other hand, the radiation advection and work terms can generally be stably treated explicitly since they operate on a fluid flow timescale. The splitting of the radiation terms into two different time-stepping treatments is known as an implicit-explicit (IMEX) scheme, which we now discuss separately below.

Implicit Subsystem

We treat the gas-radiation coupling and diffusion terms explicitly as these terms can become stiff and require unacceptably small timesteps with an explicit method. The subsystem we solve is

$$\frac{d\left(\rho e\right)}{dt} = +c\kappa_{0P}\left(E_0 - a_r T^4\right) \tag{C.18}$$

$$\frac{\partial E_0}{\partial t} - \nabla \cdot \left(\frac{c\lambda}{\chi_{0R}}\nabla E_0\right) = -c\kappa_{0P}\left(E_0 - aT^4\right) \tag{C.19}$$

Using a Backward Euler method in time:

$$\frac{(\rho e)^{n+1} - (\rho e)^{n}}{\Delta t} = c\kappa_{0P}^{n}\left[E_0^{n+1} - \left(aT^4\right)^{n+1}\right] \tag{C.20}$$

$$\frac{E_0^{n+1} - E_0^{n}}{\Delta t} - \nabla\cdot\left(\frac{c\lambda^n}{\chi_{0R}^{n}}\nabla E_0^{n+1}\right) = -c\kappa_{0P}^{n}\left[E_0^{n+1} - \left(aT^4\right)^{n+1}\right] \tag{C.21}$$

Note that here we take a semi-implicit approach where the flux limiter and opacities are constant over the update, set to the beginning-of-timestep value. The implicit subsystem is solved iterately using Newton's method. Specifically, define two values

$$F_e = (\rho e)^{n+1} - (\rho e)^{n} - \Delta t c\kappa_{0P}^{n}\left[E_0^{n+1} - \left(aT^4\right)^{n+1}\right] \tag{C.22}$$

$$F_r = E_0^{n+1} - E_0^{n} - \Delta t\left\{\nabla\cdot\left(\frac{c\lambda^n}{\chi_{0R}^{n}}\nabla E_0^{n+1}\right) - c\kappa_{0P}^{n}\left[E_0^{n+1} - \left(aT^4\right)^{n+1}\right]\right\} \tag{C.23}$$

The system update to the Newton iterations are then

$$\left[\begin{array}{cc} \left(\partial F_e/\partial T\right)^{(k)} & \left(\partial F_e/\partial E_0\right)^{(k)} \\ \left(\partial F_r/\partial T\right)^{(k)} & \left(\partial F_r/\partial E_0\right)^{(k)} \end{array}\right]\left[\begin{array}{c} \delta T^{(k+1)} \\ \delta E_0^{(k+1)} \end{array}\right] = \left[\begin{array}{c} -F_e^{(k)} \\ -F_r^{(k)} \end{array}\right] \tag{C.24}$$

where $\delta T^{(k+1)} = T^{n+1,(k+1)} - T^{n+1,(k)}$ and $\delta E_0^{(k+1)} = E_0^{n+1,(k+1)} - E_0^{n+1,(k)}$. By forming the Schur's complement of the Newton iteration, we can eliminate δT from the iteration update to get the $(k+1)$ update for the radiation energy density as

$$\begin{gathered} \left[(1-\eta)\, c\kappa_{\mathrm{0P}} + \frac{1}{\Delta t}\right] E_0^{(k+1)} - \nabla\cdot\left(d^n \nabla E_0^{(k+1)}\right) = \\ (1-\eta)\, c\kappa_{\mathrm{0P}}\left(aT_g^4\right)^{(k)} + \frac{1}{\Delta t}\left\{E_0^{n} - \eta\left[(\rho e)^{(k)} - (\rho e)^{n}\right]\right\} \end{gathered} \tag{C.25}$$

where $d^n = c\lambda^n/\chi_{\mathrm{0R}}^{n}$,

$$\eta = 1 - \frac{1}{1 + \beta^{(k)} c\kappa_{0P}\Delta t} \tag{C.26}$$

and

$$\beta^{(k)} = \frac{4\left(a_r T_g^3\right)^{(k)}}{\rho c_v} \tag{C.27}$$

At each iteration, the gas energy density is then updated as

$$(\rho e)^{(k+1)} = \eta\,(\rho e)^{(k)} + (1-\eta)\,(\rho e)^{n} + (1-\eta)\, c\kappa_{0P}\Delta t\left[E_0^{(k+1)} - \left(a_r T_g^4\right)^{(k)}\right] \tag{C.28}$$

We can write this into a form of

$$A^{(k)} E_0^{(k+1)} - \nabla \cdot \left[D^{(k)} \nabla E_0^{(k+1)} \right] = rhs^{(k)} \tag{C.29}$$

where

$$A^{(k)} = \left(1 - \eta^{(k)}\right) c\kappa_{0P} + \frac{1}{\Delta t^n} \tag{C.30}$$

$$D^{(k)} = \frac{c\lambda^{(k)}}{\chi_{0R}} \tag{C.31}$$

$$rhs^{(k)} = \left(1 - \eta^{(k)}\right) c\kappa_{0P} \left(a_r T_g^4\right)^{(k)} + \frac{1}{\Delta t^n} \left\{ E_0^n - \eta^{(k)} \left[(\rho e)^{(k)} - (\rho e)^n \right] \right\} \tag{C.32}$$

Implicit System in 1D

In one dimension, the system to be solved is

$$A_i E_i - \frac{1}{\Delta r_i} \left[D_{i+1/2} \left(\frac{E_{i+1} - E_i}{r_{i+1} - r_i} \right) - D_{i-1/2} \left(\frac{E_i - E_{i-1}}{r_i - r_{i-1}} \right) \right] = rhs \tag{C.33}$$

where we have dropped the (k) superscript and 0 subscript for brevity; whole indices denotes cell-centered quantities, and half indices denote face-centered quantities. Rewriting this as

$$\left[A_i + \frac{1}{\Delta r_i} \left(\frac{D_{i+1/2}}{r_{i+1} - r_i} + \frac{D_{i-1/2}}{r_i - r_{i-1}} \right) \right] E_i - \left[\frac{1}{\Delta r_i} \frac{D_{i+1/2}}{(r_{i+1} - r_i)} \right] E_{i+1} - \left[\frac{1}{\Delta r_i} \frac{D_{i-1/2}}{(r_i - r_{i-1})} \right] E_{i-1} = rhs \tag{C.34}$$

For the face-centered coefficients, we take two approaches for constructing a face-centered coefficient from cell-centered values. The first is a simple averaging of the two cells

$$D_{i+1/2} = \frac{D_{i+1} + D_i}{2} \tag{C.35}$$

Another option is to do a weighted average based on the distance of the face to each of the cell centers.

$$D_{i+1/2} = \frac{\Delta r_{i+1} D_i + \Delta r_i D_{i+1}}{\Delta r_i + \Delta r_{i+1}} \tag{C.36}$$

For equal-sized cells, this reduces to a simple averaging of the two cell coefficients. For unequally-spaced cells, the coefficient is weighted more heavily for the cell closest to the face.

We can write this as a linear system of equations

$$\mathbf{Mx} = \mathbf{b} \tag{C.37}$$

where $\mathbf{x} = E_i^{(k+1)}$, $\mathbf{b} = rhs^{(k)}$, and the matrix coefficients are given by

$$\mathbf{M}_{i,i-1} = -\frac{1}{\Delta r_i}\frac{D_{i-1/2}}{(r_i - r_{i-1})} \tag{C.38}$$

$$\mathbf{M}_{i,i} = A_i + \frac{1}{\Delta r_i}\left[\frac{D_{i+1/2}}{(r_{i+1} - r_i)} + \frac{D_{i-1/2}}{(r_i - r_{i-1})}\right] \tag{C.39}$$

$$\mathbf{M}_{i,i+1} = -\frac{1}{\Delta r_i}\frac{D_{i+1/2}}{(r_{i+1} - r_i)} \tag{C.40}$$

In spherical symmetry, all the coefficients and right-hand side are multiplied by a metric factor of r^2.

Comparison with Implicit Monte Carlo Simulations

The flux-limited diffusion (FLD) approximation has the advantage of being computationally inexpensive compared to other more accurate methods for radiation hydrodynamics, such as moment-based [232], discrete ordinates [233], variable Eddington tensor [234], and Monte Carlo methods [154]. FLD is particularly well-suited for optically thick problems, where the diffusion approximation is valid. However, the approximation breaks down once we enter the optically thin regions, which FLD addresses in an ad-hoc manner with a flux limiter. This situation is of particular concern in the $\xi < 1$ interaction models.

To test the validity of our FLD results, we run the same interaction problem using the implicit Monte Carlo method of [154], which is a much more accurate but also costly approach to solving the equations of radiation hydrodynamics. We use the same finite-volume moving mesh hydrodynamics method of [152] for the implicit Monte Carlo simulations, and adopt identical model parameters as the FLD runs.

In Fig. 18 we show the numerical light curves of the AT2018cow ($\xi > 1$) and OGLE-2014-SN-131 ($\xi < 1$) models (parameters listed in Table 1) for the two different transport methods. Overall we find excellent agreement across the different light curve phases in both cases, although FLD overpredicts the shock cooling tail in the Cow model by about $\sim 10 - 20\%$ at early times.

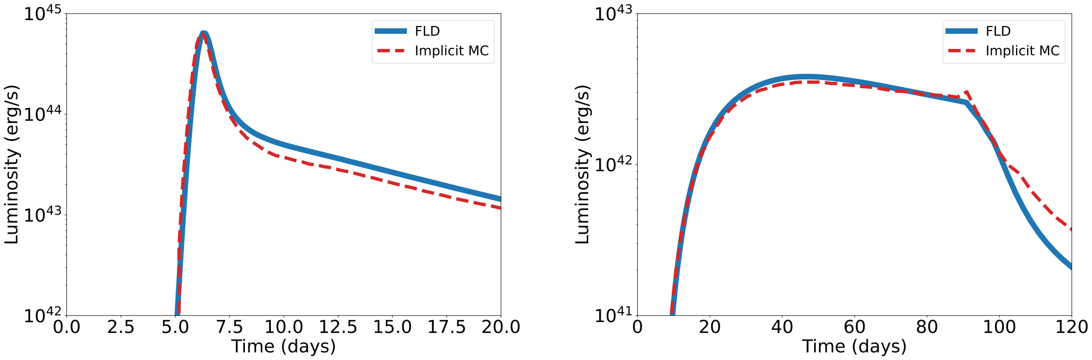

Figure C.1: Numerical light curve comparison using the AT2018cow (left) and OGLE-2014-SN-131 (right), using flux-limited diffusion (solid blue line) and implicit Monte Carlo radiation hydrodynamics (dashed red line).

Appendix D

Atomic Data

D.1 Configuration-Averaged Atomic Structure

There are various levels of fidelity in which the atomic structure is calculated. The balancing act is in having both completeness of atomic states (i.e. configurations, levels, and terms) and accuracy of individual state information (level energies, transition rates, etc.). This is a highly problem-dependent task, as greater degrees of completeness and accuracy come at the cost of a larger computational burden.

For our purposes, we are interested in getting the ion charge states and temperature coupling correct and to extract time-dependent broadband continuum emission. Namely, we are *not* seeking a fully spectrally-resolved atomic model set. Thus, we use configuration-averaged atomic models provided by Cretin, which averages atomic levels by their principal quantum number only. We therefore only consider super-transitions $n \rightarrow n'$, where each n represents the sum of all levels and/or terms described by principal quantum number n.

D.2 Radiative Rates

Photoionization/Radiative Recombination

Photoionization and radiative recombination refer to the forward and inverse processes

$$X_i + h\nu \Longleftrightarrow X_{i+1} + e^- \tag{D.1}$$

The left process is referred to as photoionization, which is when a photon with energy above the ionization energy χ_i of the X_i state is absorbed and ejects a free electron into the continuum with kinetic energy

$$\frac{1}{2} m_e v_e^2 = \chi_i - h\nu \tag{D.2}$$

which acts to heat the plasma. The reverse process, referred to as radiative recombination, occurs when a free electron is captured by an ion in charge state $i + 1$ into a bound level of charge state i. The sum of the free electron kinetic energy and the ionization energy is carried away as a photon with energy

$$h\nu = \frac{1}{2} m_e v_e^2 + \chi_i \tag{D.3}$$

As such, recombination is generally viewed as a "cooling" process if the photons are able to escape.

The radiative ionization, or photionization, rate is parameterized by a frequency-dependent bound-free cross-section $\sigma_{ij}(\nu)$ for level j of charge state i. The cross-section is zero below the threshold frequency $h\nu_{ij} = \chi_{ij}$, where χ_{ij} is the ionization energy of state (i, j).

The photoionization rate of level j of ion i to ion $i+1$ is expressed as

$$\mathcal{P}_{ij} = 4\pi \int_{\nu_{ij}}^{\infty} \frac{J_\nu}{h\nu} \sigma_{ij}(\nu)\, d\nu \tag{D.4}$$

The final state in ion $i+1$ is usually taken to be the ground state. However, in certain cases it can also represent an inner-hole excited state (i.e. K- or L-shell states). These are particularly important when interested in Fe K-shell fluorescence at X-ray energies.

The inverse rate, known as radiative recombination, contains the sum of both a spontaneous and stimulated term and can be obtained from the photoionization rate through the principle of detailed balance. Assuming a Maxwellian distribution of free electrons with nubmer density n_e at temperature T_e, it is expressed as

$$\mathcal{R}_{ij} = 4\pi \left[\frac{n_{ij}}{n_{i+1,c}}\right]_\star \int_{\nu_{ij}}^{\infty} \frac{\sigma_{ij}(\nu)}{h\nu} \left(J_\nu + \frac{2h\nu^3}{c^2}\right) e^{-h\nu/k_b T_e}\, d\nu \tag{D.5}$$

where

$$\left[\frac{n_{ij}}{n_{i+1,c}}\right]_\star = \lambda^3 n_e \frac{g_{ij}}{2g_{i+1,c}} e^{\tilde{\chi}_{ij}/k_b T_e} \tag{D.6}$$

g_{ij} is the statistical weight/degeneracy, $\tilde{\chi}_{ij} = \chi_{ij} + \epsilon_{i+1,c}$ with χ_{ij} the ionization energy of the (i, j) state, and $\epsilon_{i+1,c}$ is the excitation energy above ground of the continuum state (which is 0 if the continuum/recombining state is the ground state); and

$$\lambda = \left(\frac{h^2}{2\pi m_e k_b T_e}\right)^{1/2} \tag{D.7}$$

is the thermal electron de Broglie wavelength. We can rewrite the recombination rate as

$$\mathcal{R}_{ij} = \frac{2\pi n_e \lambda^3 g_{ij}}{g_{i+1,c}} \int_{\nu_{ij}}^{\infty} \frac{\sigma_{ij}}{h\nu} \left(J_\nu + \frac{2h\nu^3}{c^2}\right) e^{-(h\nu - \tilde{\chi}_{ij})/k_b T_e}\, d\nu \tag{D.8}$$

Photo-(De)excitation

The radiative excitation and de-excitation rates are given by the combined processes of absorption (excitation), spontaneous emission (de-excitation), and stimulated emission (de-excitation). The process of photo-excitation and spontaneous emission is described by

$$X_l + h\nu_0 \Longleftrightarrow X_u \tag{D.9}$$

Stimulated emission refers to the process

$$X_u + h\nu_0 \Rightarrow X_l + 2h\nu_0 \tag{D.10}$$

Note that radiative excitation processes do not themselves directly alter the thermal state of the gas, as the energy is trapped in the bound states of the ion. What is often referred to as "line cooling" is actually the combined process of collisional excitation extracting energy from the thermal pool of free electrons (or ions to a lesser extent), followed by spontaneous emission of a photon carrying energy away from the system.

Conversely, line thermalization refers to when a resonant photon excites a bound state, which is then collisionally de-excited before decaying back down (or fluorescing), adding the photon's energy into the thermal pool.

The spontaneous emission rate is given by the Einstein-A coefficient $\mathcal{A}_{ul}$ from the upper to lower state u and l, respectively. We can rewrite the Einstein A values in terms of a dimensionless quantity known as the *oscillator strength*

$$f_{lu} = \frac{g_u}{g_l}\frac{m_e c^3}{8\pi^2 e^2 \nu_0^2}\mathcal{A}_{ul} \tag{D.11}$$

where $\nu_0 = (E_u - E_l)/h$ is the transition frequency. The radiative excitation rate from photoabsorption is given by

$$\mathcal{B}_{lu}\bar{J} = \frac{1}{h\nu_0}\frac{4\pi^2 e^2}{m_e c} f_{lu}\bar{J} \tag{D.12}$$

where

$$\bar{J} = \int J_\nu \phi_{lu}(\nu)\, d\nu \tag{D.13}$$

is the radiation intensity averaged over the transition line profile $\phi_{lu}(\nu)$.

The radiative de-excitation rate comes from both spontaneous and stimulated emission:

$$\mathcal{A}_{ul} + \mathcal{B}_{ul}\bar{J} = \mathcal{B}_{lu}\left[\frac{2h\nu_0^3}{c^2} + \bar{J}\right] \tag{D.14}$$

where we have made use of the Einstein relations of the three coefficients and assumed complete redistribution in the line in writing the last expression, as

$$g_l \mathcal{B}_{lu} = g_u \mathcal{B}_{ul} \tag{D.15}$$

$$\mathcal{A}_{ul} = \frac{2h\nu_0^3}{c^2} \mathcal{B}_{ul} \tag{D.16}$$

In our numerical implementation, when the frequency grid is too coarse to resolve individual line profiles, we instead replace the radiation field averaged over the line profile with the geometric mean

$$\bar{J} = \sqrt{J_{g-1} J_{g+1}} \tag{D.17}$$

where $J_{g\pm1}$ is the radiation field in the groups to the left and right of the bin g the transition falls in. This allows us to approximately capture the effect of excitation by a continuum radiation field, and will also roughly get LTE radiative excitation.